University of Alberta

An Investigation of Using n-Si Piezoresistive Behavior to Develop a Three-Dimensional Stress Sensing Rosette

by

Hossam Mohamed Hamdy Gharib

A thesis submitted to the Faculty of Graduate Studies and Research
in partial fulfillment of the requirements for the degree of

Doctor of Philosophy

Mechanical Engineering Department

©Hossam Mohamed Hamdy Gharib

Fall 2013
Edmonton, Alberta

Permission is hereby granted to the University of Alberta Libraries to reproduce single copies of this thesis and to lend or sell such copies for private, scholarly or scientific research purposes only. Where the thesis is converted to, or otherwise made available in digital form, the University of Alberta will advise potential users of the thesis of these terms.

The author reserves all other publication and other rights in association with the copyright in the thesis and, except as herein before provided, neither the thesis nor any substantial portion thereof may be printed or otherwise reproduced in any material form whatsoever without the author's prior written permission.

To my mother and father whom my success would not have been possible without their endless support

Abstract

This work involves the design, microfabrication, calibration, and testing of a new silicon-based piezoresistive rosette capable of extracting the three-dimensional (3D) stresses in the silicon upon deformation. A new 10-element piezoresistive rosette was devised to extract all stress components with temperature compensation compared to the 8-element rosette developed by previous researchers, which delivers partially temperature-compensated stress output. The proposed rosette is made up of either dual- or single-polarity sensing elements through utilizing the unique behavior of the shear piezoresistive coefficient (π_{44}) in n-Si with impurity concentration. An analytical study was conducted to investigate the feasibility of the new approach. The analysis is based on solving the determinants of the coefficients of the matrices describing the resistance change versus stress and temperature for the sensing elements. The calculated determinants over a range of impurity concentrations showed non-zero regions, thus indicating the feasibility of the approach.

A full experimental study including the microfabrication, calibration and testing of the 10-element single-polarity rosette was conducted to demonstrate the actual behavior of the rosette in extraction of the 3D stresses. An early prototype, named *POC chip*, using diffusion doping was used to calibrate the piezoresistive coefficients and temperature coefficient of resistance and calculate the determinants to support the analytical study. The calibration process involved applying uni-axial and thermal loads on the sensing elements. The resulting

determinants from the calibration process indicated non-zero values, thus verified the experimental feasibility of the approach.

On the other hand, the second prototype, named *test chip*, using ion implantation doping was used for testing of the rosette after conducting a full calibration process involving uni-axial, thermal, and hydrostatic loads. The testing of the *test chip* was conducted by applying a four-point bending of a chip-on-beam specimen at room temperature. Three chip orientations and three rosette-sites were used to induce five stress components in a controlled manner, while the out-of-plane normal stress was not tested independently due to its low sensitivity in the current microfabrication run. A finite element model (FEM) of the chip-on-beam loading was developed to compare to the stress output from the experimental testing. The five stress components were extracted from the three rosette-sites and showed good correlation with the FEM.

Acknowledgment

First and above all, my thanks and gratitude are due to **God** for providing me with the strength, patience, inspiration and resources to pursue this degree.

I would like to thank deeply and gratefully my supervisor Dr. Walied Moussa for his continuous support on all levels. He has been a good listener, source of valuable advice, and understanding especially during the hard times. Also, I am thankful to my supervisory committee members, Dr. Ben Jar and Dr. Pierre Mertiny for providing me with valuable and constructive criticism to support my research.

I would like to thank all my labmates who have been providing me with continuous advice and recommendations. Specials thanks are due to my friend Mohamed El Gowini, who has been a good listener all the time. Definitely, his presence was a great support and assistance. Also, I would like to thank Dr. Edmond Lou, Fraaz Kamal, and my labmate Suzan El-Shaer for their technical advice with the electrical aspects of the research. Special thanks are due to Dr. David Benfield and Florian Müllebner for their help with the testing setup.

The financial support of the many parties who invested in this research is greatly appreciated. Thanks to the National Science and Engineering Research Council (NSERC), Alberta Innovates Technology Futures (AITF), Auto21, CMC Microsystems, Syncrude R&D Centre, Petro-Canada, and Chevron Canada.

No words will ever be sufficient enough to describe my thankfulness, gratitude, and appreciation to my mother and father who have been a source of inspiration, support, and strength during my whole life. I would like to thank my beloved wife Radwa and sons; Yaseen and Malik for providing me with the determination to overcome difficulties during the course of this research.

I would like to thank the professors in the school of engineering at the University of Alberta who provided me with valuable knowledge during my coursework; Dr. Peter Schiavone, Dr. Steve Dew, and Dr. Xiaodong Wang.

Also, I appreciate the valuable microfabrication knowledge provided by Dr. Ken Westra and all the nanoFab staff who have been of great help and support. Moreover, the help of the machine shop staff has been of great value especially from Roger Marchand, Bernie Faulkner, and Rick Conrad. Finally, I appreciate the help of the administrative team at the Mechanical Engineering Department, especially Gail Dowler, Teresa Gray, and Donna Waring.

Table of Contents

Chapter 1: Introduction 1

1.1 Motivation 1

1.2 Load Transfer Loss... 7

1.3 Proposed Approach 7

1.4 Research Objectives 9

1.5 Thesis Organization... 10

Chapter 2: Literature Review 12

2.1 Overview 12

2.2 Piezoresistivity 12

2.3 Semiconductor Piezoresistive Stress/Strain Sensors 16

2.3.1 Piezoresistive Strain Sensors 16

2.3.2 Stress Sensing Rosettes 18

2.3.3 MOSFET Stress Sensors 20

2.3.4 Other Piezoresistive 3D Stress Sensing Techniques 22

2.4 Embedded Sensors 23

2.5 Calibration of the Piezoresistive Stress Sensors 26

2.6 Conclusions 29

Chapter 3: The Piezoresistive Three-Dimensional Stress Sensing Rosette ... 30

3.1 Theoretical Background 30

3.1.1 General Relations of an Arbitrary Piezoresistive Filament 30

3.1.2 Relations along (111) Silicon Plane 34

3.2 Three-dimensional (3D) Stress Sensing Rosette 37

3.2.1 The 8-Element Rosette 37

3.2.2 The Ten-Element Rosette 40

3.3 Fundamental Properties of the 10-Element Rosette 45

3.3.1 Effect of the Impurity Concentration on the Piezoresistive Coefficients 45

3.3.2 Effect of the impurity concentration on the Temperature Coefficient of Resistance (TCR) 49
3.4 Dual and Single-Polarity Rosettes 50
3.5 Temperature Effects 51
3.6 Analytical Verification 53
3.6.1 Behavior of D_1 and D_2 53
3.6.2 Behavior of B_i and TCR 59
3.7 Conclusions 62
Chapter 4: Microfabrication of the Sensing Chip 63
4.1 Overview 63
4.2 Silicon Doping 63
4.2.1 Diffusion 64
4.2.2 Ion Implantation 71
4.3 Microfabrication of the Proof-of-Concept (POC) Chip 74
4.3.1 Chip Design 74
4.3.2 Process flow 75
4.3.3 Characterization 83
4.4 Microfabrication of the Test Chip 88
4.4.1 Chip Design 88
4.4.2 Process Flow 91
4.4.3 Characterization 98
4.5 Noise in Piezoresistors 103
4.6 Challenges 105
4.6.1 Diffusion Process Control 105
4.6.2 Non-Ohmic Contacts 106
4.7 Conclusions 107
Chapter 5: Calibration of the Sensing Chip 108
5.1 Overview 108
5.2 Uni-axial loading 108
5.3 Thermal Loading 110

5.4 Hydrostatic Loading 110
5.5 Calibration of the Proof-of-Concept (POC) Chip 111
5.5.1 Approach and Setup 111
5.5.2 Calibration Results 114
5.6 Calibration of the Test Chip 117
5.6.1 Uni-Axial Stress Loading 119
5.6.2 Thermal Loading 127
5.6.3 Hydrostatic Loading 129
5.6.4 Calibration Results 134
5.7 Conclusions 136
Chapter 6: Testing of the Sensing Chip 137
6.1 Overview 137
6.2 Test Approach 137
6.3 Test Specimens 139
6.3.1 Stud Bumping 141
6.3.2 Flip-Chipping 144
6.3.3 Types of Specimens 145
6.4 Specimen Loading 147
6.5 Measurement Setup 148
6.6 Characterization of the Chip/PCB Interface 150
6.7 Finite Element Model 153
6.8 Drift and Hysteresis 158
6.9 Results 159
6.9.1 Resistance Change Output 160
6.9.2 Sensing chip output versus FEM 167
6.9.3 Experimental stress output at different loads 171
6.9.4 Loading/Unloading Cycles 183
6.10 Conclusions 184
Chapter 7: Conclusion and Future Work 186
7.1 Research Contributions 186

7.2 Future Work 188

Bibliography **190**

Appendix A: Derivation of the General Change in Resistance Relations of a Filamentary Conductor **204**

A.1 Formulation at Fixed Temperature 205

A.2 Formulation at Variable Temperature 205

A.3 Resistance Change Equations for One-Dimensional (1D) Filament along Crystallographic Directions 210

A.4 Resistance Change Equations for One-Dimensional (1D) Filament along Off-axis Coordinate System 212

Appendix B: Formulation of the Resistance-Strain Equations on the (111) Silicon Plane **215**

Appendix C: ANSYS Finite Element Code for the Four-Point Bending of the Calibration Beam **221**

Appendix D: ANSYS Finite Element Code for the Four-Point Bending of the Test Beam **222**

List of Tables

Table 3-1 Piezoresistive Coefficients for Lightly Doped Silicon, TPa^{-1} [19, 118]46
Table 3-2: Selected impurity types for each rosette 51
Table 4-1 Pre-deposition and drive-in parameters for the Proof-of-Concept Chip 87
Table 4-2 Analytical and experimental characterization of the doping parameters in the *POC chip* 88
Table 4-3 Ion Implantation and drive-in parameters for the *test chip* 101
Table 4-4 Analytical and experimental characterization of the doping parameters in the *test chip* 103
Table 5-1 Experimental values for B_i, α, D_1, and D_2 for the *POC chip* 116
Table 5-2. Geometry and loading conditions on 4PB silicon beam.................... 123
Table 5-3 Experimental values for B_i, α, D_1, and D_2 for the *test chip* 135
Table 6-1 Material properties and geometry of the chip-on-beam FEM 155

List of Figures

Figure 1-1 Local stress state 2

Figure 1-2 (a) single lap joint under un-axial load and (b) shear and peel stresses distribution along bond overlap (modified from [3]) 3

Figure 1-3 Potential application of the 3D stress sensor for monitoring adhesive debonding in (a) aircraft bonded repair patches and (b) pipeline repair wraps 5

Figure 2-1 Schematic of a strained conductor 13

Figure 2-2 8-element piezoresistive 3D stress sensing rosette developed by AMNSTC [66], Copyright © 2009 IEEE 19

Figure 2-3 MOSFET stress sensor developed by Baumann *et al.* [81], Copyright © 2010 IEEE 21

Figure 2-4 Schematic of a strain sensor embedded in a laminated composite along with auxiliary electronics [106], Copyright © 1999 IEEE 25

Figure 2-5 Cube measuring 10 mm x 10 mm x 10 mm for 3D strain measurement [108], Copyright © 2012 IEEE 26

Figure 2-6 The addition of probe forces changes the loading state from 4-point to 6-point loading 27

Figure 2-7 Application of an out-of-plane shear stress [81], Copyright © 2010 IEEE 28

Figure 3-1 Filamentary silicon conductor 31

Figure 3-2 Orientation of the (111) coordinate system with the crystallographic coordinate system 35

Figure 3-3 (111) silicon wafer with filament orientation 36

Figure 3-4 8-element rosette on (111) silicon 37

Figure 3-5 Ten-element rosette on (111) silicon 42

Figure 3-6 Piezoresistive factor P(N,T) as a function of impurity concentration and temperature in n-Si (re-plotted from [26]), Copyright © 1982 IEEE 47

Figure 3-7 Piezoresistive factor *P(N,T)* as a function of impurity concentration and temperature for p-Si (re-plotted from [26]), Copyright © 1982 IEEE 47

Figure 3-8 Measured variation of π_{44} with impurity concentration in phosphorus doped silicon at 300 K (modified from [23]) 48
Figure 3-9: TCR as a function of the surface concentration in a diffused resistor for n- and p-type silicon at room temperature [38] Copyright © 1978, Elsevier.. 50
Figure 3-10 Surface plot of the effect of impurity concentration of groups *a* and *b* on $|D_1|$ for the *dual-polarity* rosette 55
Figure 3-11 Contour plot of the effect of impurity concentration of groups *a* and *b* on $|D_1|$ for the *dual-polarity* rosette (values in 1x10^3 TPa^{-2}) 55
Figure 3-12 Surface plot of the effect of impurity concentration of groups *a* and *b* on $|D_2|$ for the *dual-polarity* rosette with impurity concentration of group *c* set at 5x10^{18} cm^{-3} 56
Figure 3-13 Contour plot of the effect of impurity concentration of groups *a* and *b* on $|D_2|$ for the *dual-polarity* rosette with impurity concentration of group *c* set at 5x10^{18} cm^{-3} (values in TPa^{-2} °C^{-1}) 56
Figure 3-14 Surface plot of the effect of impurity concentration of groups *a* and *b* on $|D_1|$ for the *single-polarity* rosette 57
Figure 3-15 Contour plot of the effect of impurity concentration of groups *a* and *b* on $|D_1|$ for the *single-polarity* rosette (values in 1x10^3 TPa^{-2}) 57
Figure 3-16 Surface plot of the effect of impurity concentration of groups *a* and *b* on $|D_2|$ for the *single-polarity* rosette with impurity concentration of group *c* set at 5x10^{18} cm^{-3} 58
Figure 3-17 Contour plot of the effect of impurity concentration of groups *a* and *b* on $|D_2|$ for the *single-polarity* rosette with impurity concentration of group *c* set at 5x10^{18} cm^{-3} (values in TPa^{-2} °C^{-1}) 58
Figure 3-18 Effect of impurity concentration on B_i in n-Si 60
Figure 3-19 Effect of impurity concentration on B_i in p-Si 60
Figure 3-20 Effect of impurity concentration on TCR in n-Si and p-Si [23] 61
Figure 4-1 Constant source diffusion profile with different *Dt* product 67
Figure 4-2 A Gaussian distribution for a limited-source diffusion 69
Figure 4-3 Process flow of the three-stage pre-deposition 71

Figure 4-4 Gaussian distribution for an ion implantation process (modified from [123]) 73
Figure 4-5 Layout of the *POC chip* 75
Figure 4-6 Microfabrication process flow of the proof-of-concept chip 76
Figure 4-7 Phosphorus diffusion furnace 78
Figure 4-8 Photograph of the microfabricated *POC chip* 81
Figure 4-9 Microscopic image of the fabricated *POC chip* showing the 10-element rosette with numbers indicating the different sensing elements 82
Figure 4-10 Microscopic image of the fabricated *POC chip* showing a characterization group *a* resistor 82
Figure 4-11 I-V Characteristic curves of the three groups of piezoresistors on the *POC chip* 83
Figure 4-12 The transfer line width (TLM) test structure; (a) schematic and (b) Microscopic image 84
Figure 4-13 Resistances of each group along the TLM structure on the *POC chip* 85
Figure 4-14 Net impurity concentration after pre-deposition steps 86
Figure 4-15 Net impurity concentration after drive-in step 86
Figure 4-16 Layout of the test chip showing the three rosette-sites 90
Figure 4-17 Microfabrication process flow of the test chip 92
Figure 4-18 Photograph of the final test wafer after annealing 97
Figure 4-19 Microscopic image of the fabricated 10-element sensing center rosette 97
Figure 4-20 Microscopic image of the fabricated (a) edge rosette 1 and (b) edge rosette 2 98
Figure 4-21 Sample I-V curves of the three groups of piezoresistors 99
Figure 4-22 Resistances of each group along the TLM structure on the test chip 100
Figure 4-23 Impurity concentrations profiles after ion implantation for the three groups 102
Figure 4-24 Impurity concentrations profiles after drive-in for the three groups 102

Figure 4-25 Diced silicon chip sent for SRP characterization 103
Figure 4-26 I-V Characteristic curves of two piezoresistors with Aluminum traces sputtered using two different equipment 107
Figure 5-1 Forces and moments acting on the silicon beam undergoing four point bending 109
Figure 5-2 Four-point bending (4PB) loading with probes 112
Figure 5-3 Probing of the piezoresistors under 4PB 113
Figure 5-4 *POC chip* calibration results for uni-axial stress versus resistance change for 0 degrees oriented piezoresistors (slopes equal to B_1) 114
Figure 5-5 *POC chip* calibration results for uni-axial stress versus resistance change for 90 degrees oriented piezoresistors (slopes equal to B_2) 115
Figure 5-6 *POC chip* calibration results for the thermal loading (slopes equal to α) 115
Figure 5-7. Silicon beam (a) before and (b) after connection to a ZIF connector 118
Figure 5-8 Measurement Setup for the calibration of the *Test Chip* 119
Figure 5-9. Four-point bending loading fixture; (a) schematic and (b) actual setup 120
Figure 5-10. Bending moment diagram with ZIF end connectors 121
Figure 5-11. Schematic of possible error in beam longitudinal position 123
Figure 5-12 Applied boundary conditions on the FEM of the silicon beam 124
Figure 5-13 FEM contour plot of (a) σ_{11} over the beam's length, and (b) σ_{11} over the beam's center region at translational misalignment s = 0 124
Figure 5-14. The non-uniformity and error in the stress at the calibration rosette given a longitudinal translation misalignment of the beam 125
Figure 5-15. *Test chip* calibration results for uni-axial stress versus resistance change for 0 degrees oriented piezoresistors (slopes equal to B_1) 126
Figure 5-16. *Test chip* calibration results for uni-axial stress versus resistance change for 90 degrees oriented piezoresistors (slopes equal to B_2) 126
Figure 5-17 Calibration chip fixture inside the environmental chamber 127

Figure 5-18 Thermal load calibration setup including environmental chamber, source meter, and switch box 128
Figure 5-19. Calibration results for temperature versus resistance change (slopes equal to α) 128
Figure 5-20 Hydrostatic pressure vessel calibration setup 131
Figure 5-21 Pressure vessel head with fluid inlets, wire-gland and RTD connection 131
Figure 5-22 Calibration chip connectivity in the pressure vessel 132
Figure 5-23. Pressure-temperature relationship of the hydraulic fluid inside the pressure vessel 133
Figure 5-24. Calibration results for hydrostatic pressure versus resistance change 133
Figure 5-25. Adjusted results for hydrostatic pressure versus resistance change without temperature effects (slopes equal π_p) 134
Figure 5-26. Effect of impurity concentration on B_i and α 136
Figure 6-1 Schematic of testing setup and specimens 140
Figure 6-2 Micro-fabricated test chip 141
Figure 6-3 Microscopic image of the stud bumping process 142
Figure 6-4 The final *Test Chips* with coined stud bumps 142
Figure 6-5 SEM image of the stud bumps before and after coining 143
Figure 6-6 SEM image of the 5 stud bumps on an Aluminum pad before coining 143
Figure 6-7 SEM image of the 5 stud bumps on an Aluminum pad after coining 144
Figure 6-8 Image showing the flip-chipping process of the chip on the PCB beam 145
Figure 6-9 Schematic showing the three chips orientations on the PCB beam .. 146
Figure 6-10 The three types of test specimens; S0, S45, and S90 146
Figure 6-11 PCB orientation during 4PB to induce (a) tensile stresses or (b) compressive stresses at the fibers in contact with the *test chip* 147
Figure 6-12 Test measurement setup 149
Figure 6-13 Experimental test setup 149

Figure 6-14 SEM image of the PCB/Chip cross-section showing the gold bump, copper trace and ACA spew fillet 150
Figure 6-15 SEM image of the PCB/Chip cross-section showing a different angle for the spew fillet and structure of the PCB composite 151
Figure 6-16 SEM image of the PCB/Chip cross-section showing ACA spew fillet 151
Figure 6-17 SEM image of the PCB/Chip cross-section showing the ACA, gold bump and copper trace thicknesses 152
Figure 6-18 SEM image of the PCB/Chip cross-section showing the width of one coined gold bump.. 152
Figure 6-19 Overall mesh and boundary conditions of the finite element model156
Figure 6-20 Cross-section view of the modeled chip/PCB interface.................. 156
Figure 6-21 Finite element mesh of the chip, ACA and PCB 157
Figure 6-22 Planar view of the finite element mesh of the (a) center rosette, (b) edge rosette 1, and (c) edge rosette 2 157
Figure 6-23 Loading setup for hysteresis testing (not to scale) 158
Figure 6-24 Typical output from the load-cell due to the applied vertical load increments on the beam 159
Figure 6-25 Resistance changes in the sensing elements of the center 10-element rosette in the S0-speciemen.. 162
Figure 6-26 Resistance changes in the sensing elements of the edge1 4-element rosette in the S0-speciemen.. 163
Figure 6-27 Resistance changes in the sensing elements of the edge2 4-element rosette in the S0-speciemen.. 163
Figure 6-28 Resistance changes in the sensing elements of the center 10-element rosette in the S45-speciemen.. 164
Figure 6-29 Resistance changes in the sensing elements of the edge1 4-element rosette in the S45-speciemen.. 164
Figure 6-30 Resistance changes in the sensing elements of the edge2 4-element rosette in the S45-speciemen.. 165

Figure 6-31 Resistance changes in the sensing elements of the center 10-element rosette in the S90-speciemen 165
Figure 6-32 Resistance changes in the sensing elements of the edge1 4-element rosette in the S90-speciemen 166
Figure 6-33 Resistance changes in the sensing elements of the edge2 4-element rosette in the S90-speciemen 166
Figure 6-34 Difference between the change in resistance from (R_2 and R_4) and (R_6 and R_8) due to applied load for the edge2 4-element rosette in the S90-speciemen 167
Figure 6-35 Specimen S0 - Stress field of σ'_{11} on chip surface at a nominal axial stress of 27.1 MPa 168
Figure 6-36 Specimen S0 - Stress field of σ'_{13} on chip surface at a nominal axial stress of 27.1 MPa 169
Figure 6-37 Specimen S45 - Stress field of σ'_{12} on chip surface at a nominal axial stress of 28.7 MPa 169
Figure 6-38 Specimen S90 - Stress field of σ'_{22} on chip surface at a nominal axial stress of 29.0 MPa 170
Figure 6-39 Specimen S90 - Stress field of σ'_{23} on chip surface at a nominal axial stress of 29.0 MPa 170
Figure 6-40 Extracted stresses from the 0 degrees oriented chip at the center rosette 174
Figure 6-41 Extracted stresses from the 0 degrees oriented chip at the edge rosettes 175
Figure 6-42 Extracted temperature from the 0 degrees oriented chip at the center rosette 176
Figure 6-43 Extracted stresses from the 45 degrees oriented chip at the center rosette 177
Figure 6-44 Mohr's circle representing the stress transformation for the S45 Specimen 177

Figure 6-45 Extracted stresses from the 45 degrees oriented chip at the edge rosettes 178
Figure 6-46 Extracted temperature from the 45 degrees oriented chip at the center rosette 179
Figure 6-47 Extracted stresses from the 90 degrees oriented chip at the center rosette 180
Figure 6-48 Extracted stresses from the 90 degrees oriented chip at the edge rosettes 181
Figure 6-49 Extracted temperature from the 90 degrees oriented chip at the center rosette 182
Figure 6-50 Stress $\left(\sigma'_{11} - \sigma'_{22}\right)$ from the center rosette under 10 cycles tensile/compressive loading 184

List of Symbols, Abbreviations, and Nomenclature

4PB	: Four-point bending
a, b, c	: The three groups of piezoresistors of the 10-element rosette representing three impurity concentration levels
ACA	: Anisotropic conductive adhesive
ADL	: Advanced Design Laboratory
Al	: Aluminum
α	: First order TCR
$\alpha_1, \alpha_2, \ldots$	: First and higher order temperature coefficients of resistance (*TCR*)
t_i^p and T_i^p	: Time and temperature for the pre-deposition process *i* if more than one pre-deposition steps are implemented
$B_{1(\mathrm{eff})}$ and $B_{2(\mathrm{eff})}$	: Effective values of B_1 and B_2 coefficients, respectively
B_i	: Coefficients representing functions of the crystallographic piezoresistive coefficients, i=1,2,3
B_i	: Coefficients representing functions of the crystallographic piezoresistive coefficients, i=1,2,3
BOE	: Buffered oxide etch
C_{11}, C_{12}, and C_{44}	: Stiffness constants
D	: Diffusion coefficient
d	: Distance between the middle supports in the 4PB
D_0	: Diffusion constant
D_1, D_2	: Functions of the determinants of the coefficients' matrices representing the stresses and temperature versus resistance change equations
$(Dt)_{tot}^p$	: Product of diffusion coefficient and time for the pre-deposition step

$\left(Dt\right)_{tot}^{d}$	: Product of diffusion coefficient and time for the drive-in step
$\frac{\Delta R}{R}$	: Change in resistance
DI	: De-ionized
$\left(Dt\right)_{tot}^{d}$	: Product of the diffusion coefficient and time for the dopants drive-in step
E	: Elastic modulus
E_A	: Arrhenius activation energy
E_{f}	: Fermi energy
erfc	: Complementary error function
f	: frequency
F	: Force applied during 4PB
F_c	: Force of the ZIF connector applied in the 4PB
F_d	: Force of the dead weight applied in the 4PB
FEA	: Finite element analysis
FEM	: Finite element model
G	: Gauge factor
γ	: Ratio of the axial section to the sum of the axial and transverse sections of a serpentine resistor
h	: Thickness of the 4PB beam
HMDS	: Hexamethyldisilazane
I	: Current supply in the piezoresistor
IPA	: Isopropyl Alcohol
J	: Particle flux
k	: Boltzmann constant
l, m, n	: Direction cosines with respect to the unprimed coordinate system, i.e. x_1, x_2, and x_3 axes
l', m', n'	: Direction cosines with respect to the primed coordinate system, i.e. x_1', x_2', and x_3' axes

L	: Distance between the applied forces in 4PB
L_c	: Distance between the two end ZIF connectors in the 4PB
L_d	: Distance between the dead weights in the 4PB
m	: Electron mass
M	: Electron mobility anisotropy
MEMS	: Micro-Electro Mechanical Systems
min.	: Minutes
$\mu(x)$	: Majority-carrier mobility
N	: Impurity concentration
N_0	: Impurity concentration at the wafer surface
N_B	: Background concentration
NEMS	: Nano-Electro Mechanical Systems
ν	: Poisson's ratio
N_p	: Peak impurity concentration of the ion implantation profile
n-Si	: n-type silicon
PCB	: Printed circuit board
PECVD	: Plasma Enhanced Chemical Vapor Deposition
π_{11}, π_{12}, and π_{44}	: Principal crystallographic piezoresistive coefficients
π_{p}	: Piezoresistive pressure coefficient
$\pi'_{\gamma\beta}$	: off-axis temperature dependent piezoresistive coefficients with γ, β equals 1,2,…6
$P(N,T)$	: Piezoresistance factor
POC	: Proof-of-concept
PR	: piezoresistive
PSG	: Phosphosilicate Glass
p-Si	: p-type silicon
Q	: Dose or total number of impurity atoms per unit area
q	: charge of an electron
R	: Electrical resistance
RIE	: Reactive Ion Etching

ρ	: Electrical resistivity
R_p, ΔR_p	: Projected range of incident ions and straggle (spread of distribution), respectively during ion implantation process
R_s	: Sheet resistance
RTD	: Resistance temperature detector
s_{44}	: Compliance shear constant
S_I	: Shot noise power spectral density
SEM	: Scanning electron microscope
σ'_{ij}	: Stresses in the primed coordinate system with, *i, j* = 1,2,3
σ'_{β}	: Stresses in the primed coordinate system with reduced notation, $\beta = 1,2,..,6$
σ_{ij}	: Stresses in the unprimed coordinate system with, *i, j* = 1,2,3
SRP	: Spreading Resistance Profiling
$T=T_c-T_{ref}$	: Difference between the current measurement temperature (T_c) and reference temperature (T_{ref})
t_i^p	: Time for the pre-deposition process *i* if more than one pre-deposition steps are implemented in seconds
T_i^p	: Temperature for the pre-deposition process *i* if more than one pre-deposition steps are implemented in Kelvin
t^d	: Time for the drive-in step in seconds
T^d	: Temperature for the drive-in step in Kelvin
T_k	: Absolute temperature in Kelvin
TEOS	: Tetraethylorthosilicate
TLM	: Transfer line method
ToF-SIMS	: Time of Flight Secondary Ion Mass Spectrometry
w	: Width of the 4PB beam
V_b	: Bias voltage across the resistor
V_j	: Thermal (Johnson) noise on voltage
$V_{1/f}$	: 1/*f* noise on voltage

V_s : Voltage source to the Wheatstone bridge

x : Distance into the bulk silicon from the surface

X_j^p : Junction depth after the pre-deposition steps or ion implantation step

X_j^d : Junction depth after the drive-in step

ZIF : Zero Insertion Force

CHAPTER 1: INTRODUCTION

"*Truth is sought for its own sake. And those who are engaged upon the quest for anything for its own sake are not interested in other things. Finding the truth is difficult, and the road to it is rough*" *Abu Ali Ibn al-Haytham (Alhazen) 965-1040 AD* [1]

Stress analysis has been considered a unique branch of engineering, which determines and improves the mechanical strength of structures and machines. There are two types of stress analysis; the conceptual and the real. In the conceptual type, the structure does not exist and in many cases the definition of the geometry, material and loads have to be assumed. This type is usually carried out using analytical or numerical analysis like the finite element method. In the real type, the structure or prototype that must be analyzed exists. It is in the real type that experimental stress analysis provides actual information and data about the behavior of the structure. With experimental stress analysis it is possible to monitor experimentally the stress distribution in a machine component in actual operation without knowing the applied forces acting on the part under these conditions, which is not possible with analytical or numerical methods. This led experimental stress analysis to be a critical and essential part of Structural Health Monitoring (SHM), which deals with damage detection, condition-based maintenance, failure prevention and non-destructive evaluation of structures. Therefore, problems can be detected and solved during the processing of the structure or during its service cycles.

1.1 Motivation

During the recent years, a significant development of the Micro/Nano Electro-Mechanical Systems (MEMS/NEMS) technology has occurred that revolutionized the field of SHM. Due to their small size and ease of integration with other

electronics, this technology enables micro/nano sensors to be integrated into different structures. Sensors embedded in structures are useful in monitoring and optimizing the manufacturing process of the structure and/or their performance during operation. Their major advantage is being embedded in the host material, thus they are not affected by external environments like chemicals, moisture and contamination. Also, embedded sensors add intelligence to structures and enable real-time monitoring at critical locations not accessible to surface mounted ordinary sensors. Micro stress and strain sensors have been developed using different techniques including optical fibers, piezoelectricity, piezoresistivity, and capacitance. An embedded sensor in a strained material is usually exposed to a state of three-dimensional (3D) stresses. A 3D stress state is defined by six stress components; σ_{ij} (i, j = 1,2,3), which is shown in the local stress state in Figure 1-1. In-plane stresses are defined as those over the 1-2 plane, i.e. σ_{11}, σ_{22}, and σ_{12}, while the out-of-plane stresses are the remaining σ_{33}, σ_{13}, and σ_{23}.

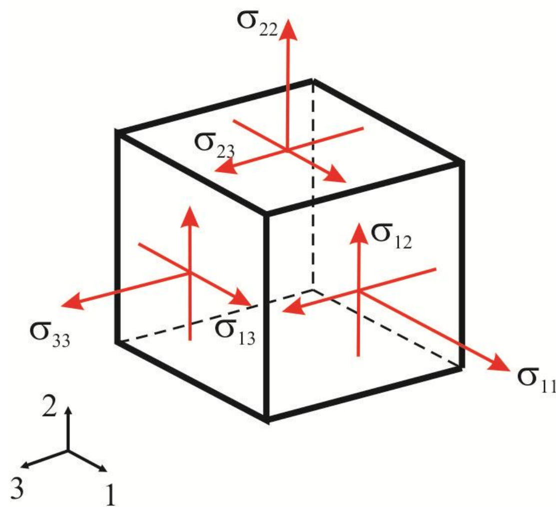

Figure 1-1 Local stress state

In a simple two members (adherends) bonded with an adhesive layer, their debonding initiates at the edges of the bond overlap through an adhesive shearing, or adhesive/adherend peeling [2]. This structure, called single-lap joint, is shown in Figure 1-2(a) under tensile loading. The shear (σ_{13}) and peel (σ_{33}) stresses

distribution along the bond overlap is shown in Figure 1-2(b) as modeled using finite element analysis (FEA) by Adams *et al*. [3]. The maximum out-of-plane stresses in terms of the shear and peel stresses are located at the edges of the bond overlap as shown in Figure 1-2(b). Moreover, in-plane stresses are induced at the center of the overlap length.

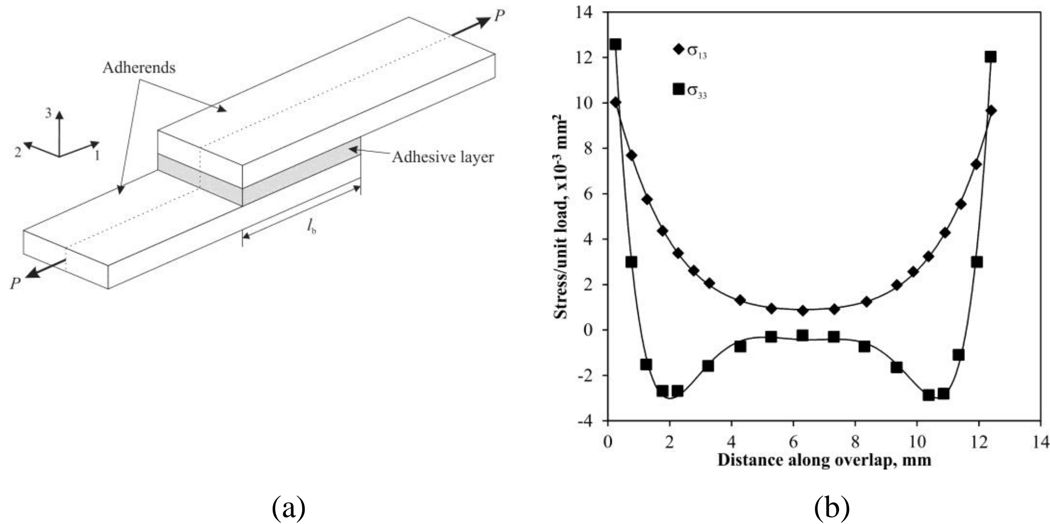

(a) (b)

Figure 1-2 (a) single lap joint under un-axial load and (b) shear and peel stresses distribution along bond overlap (modified from [3])

The stress behavior at the bond interface of a single-lap joint is observed in many bonded structures. One example is the adhesively bonded repair patches. Failure of large scale metallic structures, like aircrafts, ships and pipelines, could be catastrophic, cause leakage of hazardous materials to the environment, and put human life at great risk. A common mode of failure of large metallic structures is cracking, which is mainly due to fatigue and aging of the structure. A direct approach to avoid the propagation of minor cracks is to replace the cracked part. However, such decision can be costly in the case of large and sophisticated structures. An alternative approach is using repair patches which are fixed over the crack using either mechanical fasteners or adhesives. The use of adhesively

bonded patches has many advantages over mechanically fastened ones like reduced installation cost, increased strength and fatigue life, and elimination of the stress concentrations due to the fastener holes [4]. However, the adhesively bonded patches are prone to adhesive degradation that leads to the loss of its elastic modulus and high shear and peel stresses, which ultimately cause patch debonding. Hence, it is unpredictable if the bonded repair patch is suffering from bond degradation or debonding initiation.

A fair amount of research has been taking place for over a decade to develop a bonded patch that is "smart", such that it can provide *in-situ* monitoring of potential debonding of the adhesively bonded repair patches. This monitoring will minimize the need for visual and non-destructive testing techniques through the use of remote SHM of the available patches on the structure, which will reduce the maintenance cost and time. Also, in aircraft, a smart patch will accelerate the certification process of the bonded patch in civilian aircraft instead of its limited use to military aircraft [4]. A number of traditional sensing methods have been employed for damage detection of the adhesive bond in bonded patches. Some of these techniques are based on piezoelectricity [5], optical fibers [6-8], and electrochemical impedance spectroscopy (EIS) [9]. Most of these approaches rely on conventional macro-sized sensors that require large installation areas and measurement equipment and complicated signal processing.

A MEMS-based stress sensor capable of monitoring the 3D stress state can be a valuable alternative to detect debonding of bonded structures compared to the conventional sensors. An array of micro 3D stress sensors can be placed along the periphery of the patch at the adhesive bond-line. The out-of-plane shear and peel stresses occurring at the edges of the patch will be monitored by the sensor array and diagnosed for potential debonding if they exceeded the adhesive and adhesive/adherend strengths. Moreover, another array can be installed at the center of the patch to monitor the in-plane stresses that can indicate potential crack propagation. Auxiliary electronics in terms of computation, telemetry and power can be installed on the patch surface or integrated within its composite

material. A conceptual schematic of the approach is shown in Figure 1-3 for aircraft and pipeline repair patches. This approach can also be implemented in most of the adhesively bonded structures.

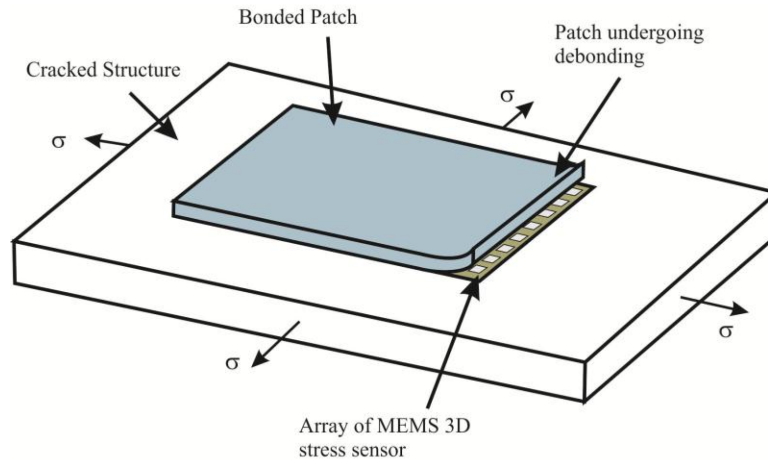

(a)

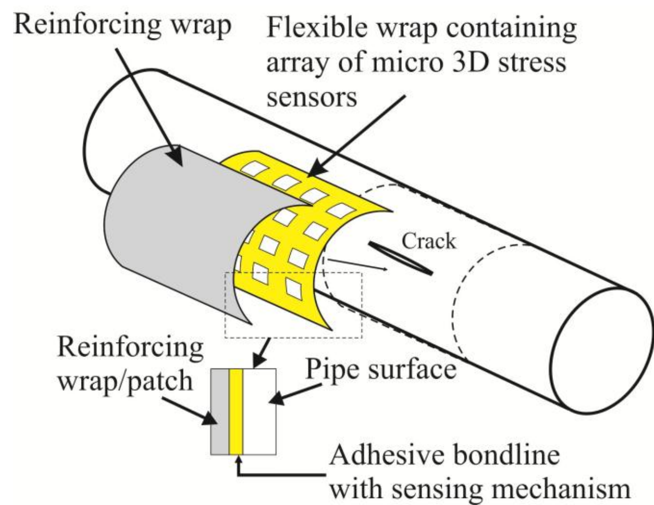

(b)

Figure 1-3 Potential application of the 3D stress sensor for monitoring adhesive debonding in (a) aircraft bonded repair patches and (b) pipeline repair wraps

Moreover, a 3D stress sensor can have a number of potential applications in the bio-medical field, like monitoring implant loosening, stresses induced during intra-cortical recording, and forces induced in dental brackets. People with joint implants suffer from implant loosening over time, which is believed to be due to stress shielding in which the process of fusion of the bone osseous tissues into the implant (osseointegration) is disturbed. An array of the 3D stress sensor embedded at the implant/bone interface can be used to monitor the stress field around the implant. Also, an inter-cortical electrode with surface mounted stress sensors can help surgeons during an operation to determine the amount of stresses being applied on a spinal cord or a nerve. In dentistry, an array of the 3D stress sensors can be embedded in a dental correction bracket as an indication of the amount of stress being applied on the teeth, which can reduce pain to dental correction patients. Some of the efforts in developing stress sensors for bio-medical applications include the works of Alfaro *et al*. [10] to develop a MEMS piezoresistive bone 3D stress sensor, Seidel *et al*. [11] to develop a silicon microprobe for stress mapping in intra-cortical applications, Lapatki *et al*. [12] to develop a smart bracket for 3D stress measurement to determine the forces and moments applied on the teeth brackets. The bio-medical application of the 3D stress sensor involves extra details compared to industrial applications in terms of its design and integration, especially with the material selection to guarantee appropriate bio-compatibility.

In electronic packaging, the semiconductor die is bonded to a packaging material, which is usually ceramic or polymer-based. An IC chip is affected by thermal loads that induce 3D stresses in the semiconductor die and its bond-line causing potential delamination and failure of the packaged chip [13]. A 3D stress sensor integrated with the semiconductor die can be used to monitor the thermally-induced stresses in electronic packaging. A number of piezoresistive 3D stress sensors have been developed for electronic packaging applications using piezoresistivity, which will be discussed in the next chapter.

1.2 Load Transfer Loss

The load transmitted to a bonded sensor from a loaded structure, whether embedded or surface mounted, occurs through the adhesive bond. If the monitored structure and sensor are of high stiffness, like a steel structure and silicon sensor, compared to the adhesive, there will be a relatively high load loss or change, which is known as the far/near field effect. For example, Hautamaki *et al*. bonded a 500 μm thick strain gauge silicon chip to an aluminum specimen with a 200 μm thick epoxy layer with modulus of elasticity of 4 GPa. The resulting load loss in the axial strain (800 με) transmitted from the loaded aluminum specimen to the silicon chip was 45% [14]. This load loss or change is solved through developing a coupling mechanism and calibration between the sensor and the surrounding medium or structure and through using sensors with high sensitivity to overcome the load losses. Therefore, a semiconductor stress sensor excels compared to a regular strain gauge through its high sensitivity which reaches 50 times that of strain gauges.

1.3 Proposed Approach

Piezoresistive stress sensors offer some very interesting advantages over other techniques like their direct linear relation with stress, simplicity of signal processing, low cost of support equipment, and possibility of subtracting the effect of temperature on evaluated stresses. Piezoresistive stress/strain sensing mechanisms have been investigated extensively during the past few decades. Most of these mechanisms are capable of evaluating limited number of stress or strain components while either surface mounted to or embedded in a structure. However, few researchers investigated the potential of developing a three-dimensional (3D) stress sensor that can measure the six stress components within a material, which is the primary goal of the current research.

Among the few developed piezoresistive 3D stress sensors, the one based on a rosette of diffused resistors developed by Suhling *et al*. [13] provides a simple and

direct relationship with the applied stresses. Their developed piezoresistive sensing rosette capable of 3D stress extraction is made up of 8 dual-polarity sensing elements of n- and p-type silicon and fabricated on the (111) silicon plane. The need for the dual-polarity elements is to produce a sufficient number of independent linear equations to solve for the stress components. This rosette is able to extract 4 stresses with temperature compensation; namely the difference of the in-plane normal stresses and the three shear stresses. On the other hand, the normal stress components are not temperature-compensated and require a known value of temperature to extract them. The inability to extract the normal stresses with temperature compensation is due to the limitation in the number of independent equations that hinders the ability to eliminate the effect of temperature on the change in electrical resistance of the sensing elements.

The current research adopts the piezoresistive sensing rosette approach to develop a 3D stress sensor. The *objective* is to extract the 6 stress components (full stress tensor) instead of just the 4 components achieved by previous researchers. This led to a close understanding and studying of the 8-element rosette to find an alternative solution approach. Accordingly, the special and unique behavior of the piezoresistive shear coefficient in n-type silicon (n-Si) was found to develop *single-polarity* and *dual-polarity* rosettes that extract all 6 stress components with temperature-compensation. The resulting 10-element rosette is based on coming up with sets of linear equations with independent coefficients to solve for the 6 stresses. A *single-polarity* rosette is found to be more appealing than a dual-polarity because it provides the following:

- A simpler micro-fabrication process without the need for the p-type doping equipment
- The potential of fabricating a rosette with a smaller footprint than the dual-polarity due to the absence of the n-well.
- The flexibility to select low doping concentrations for the sensing elements, which provides higher piezoresistive coefficients and sensitivity. On the other hand, either the p-type or n-type elements in a dual-polarity rosette are

confined to high doping concentrations, and consequently lower sensitivity, since the n-well or p-well needs to have a higher concentration than the background silicon and a lower concentration than the sensing elements to create appropriate junctions.

1.4 Research Objectives

The following are the overall objectives of the current research:

1. Devise a piezoresistive sensing rosette capable of 3D stress measurement through studying the operation of the sensing rosettes developed by previous researchers. A primary objective is to find an alternative approach to the available dual-polarity rosette to facilitate the microfabrication process through avoiding the use of both an n- and p-type doping equipment.
2. Study the developed approach and prove its feasibility both analytically and experimentally. Also, this study provides an understanding of the different parameters involved in the operation of the piezoresistive sensing rosettes. This includes the behavior of the piezoresistive coefficients and temperature coefficient of resistance (TCR) with impurity concentration and thermal loads. This understanding helps in the design of the rosette and selection of the appropriate microfabrication recipe especially for silicon doping.
3. Prototype a sensing-chip with the new developed rosette for experimental verification. This stage involves developing a microfabrication process flow utilizing bulk microfabrication techniques and available resources in the nanoFab and the MEMS/NEMS advanced design laboratory (ADL) at the University of Alberta. A number of runs need to be conducted to investigate the microfabrication processes and improve upon the process flow to achieve a desirable operational rosette. Two main stages of prototyping are performed. The first is intended for preliminary study through an early experimental testing to verify the feasibility of the approach and understand the behavior of the piezoresistive sensing elements. Once the approach is verified, the second prototyping deals with any shortcomings in the previous

prototypes and conduct experimental tests to verify the extraction of the 3D stresses from the rosette.

4. Calibrate the developed sensing rosette on the fabricated chip through applying known loads and measuring the output from the sensing elements. The calibration process involves applying know loads in terms of stresses and temperature and measuring the response of the sensing elements accordingly. This calibration process is an early experimental verification of the behavior of the sensing elements against known loads and provides an understanding of the different parameters affecting the operation of the rosette.
5. Test the sensing chip for extraction of the 3D stresses. This involves devising a test approach that can be used to induce the maximum number of stress components on the chip's surface for testing in a controlled manner. An exact known load is not required; however, achieving controlled stress components or combination of components is important to monitor the response of the rosette and judge its output based on a predicted behavior. The selected test approach needs to have an analytical and/or numerical solution that can provide an insight of the levels of expected stresses and which maximum components are expected. This research work limits the testing to room temperature conditions. Future research can deal with testing at variable thermal loads.

1.5 Thesis Organization

This thesis provides a detailed description of the new 10-element piezoresistive 3D stress sensing rosette in terms of its underlying theory, microfabrication, calibration and experimental testing. The thesis is divided into 7 chapters, where the following paragraphs describe the areas covered in each chapter.

Chapter 1 provides an introduction and overview of the presented research and highlights the motivation behind the current research and the approached methodology. Chapter 2 provides a literature review of the piezoresistivity including the theoretical and experimental efforts. Also, it presents the previous

efforts to develop piezoresistive stress sensors, especially for 3D stress monitoring. Moreover, it discusses the conducted efforts with embedded sensors for material characterization and the calibration techniques for 3D stress sensors.

Chapter 3 presents the theoretical background of the rosette-based piezoresistive stress sensors, which paves the way to the development of the new 10-element rosette. The fundamental concepts and approach of the 10-element rosette is presented. The behavior of the piezoresistive coefficients and TCR with impurity concentration and temperature is discussed to understand the potential use of n-Si to develop the 10-element rosette. An analytical study is provided to investigate the feasibility of the new approach.

Chapter 4 presents the microfabrication processes conducted to prototype two sensing chips; *POC chip* and *test chip*. The *POC chip* includes an early prototype of the 10-element rosette to conduct an experimental feasibility study of the new approach. On the other hand, the *test chip* is the final prototype chip that includes a number of rosettes for testing. The chapter presents the basic mathematical modeling of the doping processes conducted in this research and the full process flows and characterization of both sensing chips.

Chapter 5 presents the calibration of the *POC chip* and *test chip*. The three calibration setups including uni-axial, thermal, and hydrostatic loading are presented and the resulting coefficients are given to prove the feasibility of the approach.

Chapter 6 presents the experimental testing conducted to prove the operation of the 10-element rosette. The test setup using four-point-bending of a chip-on-beam assembly is discussed and analyzed using finite element analysis (FEA). The experimental results from a set of loaded sensing chips are presented and compared to the FEA model.

Chapter 7 provides concluding remarks and future work for the current research.

CHAPTER 2: LITERATURE REVIEW

"The seeker after the truth is not one who studies the writings of the ancients and, following his natural disposition, puts his trust in them, but rather the one who suspects his faith in them and questions what he gathers from them, the one who submits to argument and demonstration, and not to the sayings of a human being whose nature is fraught with all kinds of imperfection and deficiency. Thus the duty of the man who investigates the writings of scientists, if learning the truth is his goal, is to make himself an enemy of all that he reads, and applying his mind to the core and margins of its content, attack it from every side. He should also suspect himself as he performs his critical examination of it, so that he may avoid falling into either prejudice or leniency." Abu Ali Ibn al-Haytham (Alhazen) 965-1040 AD [15]

2.1 Overview

In this chapter, the development of the piezoresistivity theory, one of the leading phenomena used for stress and strain measurements, is presented along with its application in stress and strain sensors. Moreover, an overview of the development of embedded sensors is presented. Finally, the available calibration techniques of piezoresistive stress sensors are discussed.

2.2 Piezoresistivity

The piezoresistive stress/strain sensor or the electrical resistance strain gauge is commonly divided into the popular metallic foil strain gauge and the semiconductor strain gauge. The metallic foil strain gauge utilizes the strain-electrical resistance coupling to evaluate the in-plane strains when they are surface mounted to a structure. In 1843, Charles Wheatstone presented his first publication on the bridge circuit that he had invented, which revealed the working

principle of strain gauges [16]. He discovered that an electrical conductor changes its resistance upon an applied mechanical stress. Later, in 1856, William Thomson (Lord Kelvin) presented a paper showing similar conclusions, which was later referred to as the "Thomson effect" [17]. Not until the late 1930s, that serious attention was given to use this knowledge, which led to the development of the foil strain gauges [18]. For over 70 years, metallic foil strain gauges have been considered the *de facto* standard for the study of material deformations, whether a quick check or an exhaustive research.

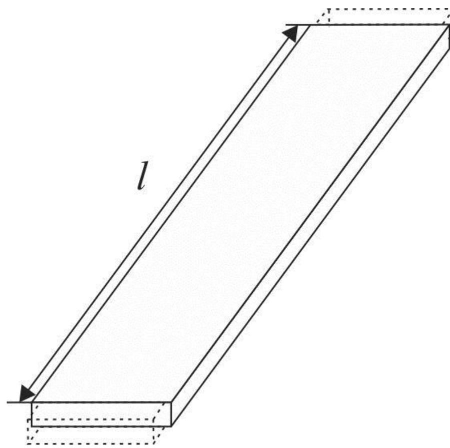

Figure 2-1 Schematic of a strained conductor

For a metal conductor shown in Figure 2-1, the change in resistance ($\Delta R/R_0$) from an initial unstrained state (R_0) is given by:

$$\frac{\Delta R}{R_0} = (1+2\upsilon)\frac{\Delta l}{l} + \frac{\Delta\rho}{\rho} \equiv G\varepsilon \tag{2-1}$$

Where, ν is Poisson's ratio of the material, l is the length of the conductor, ρ is the resistivity of the conductor, G is the relative change of resistance per unit strain (gauge factor), and ε is the mechanical strain in the conductor. In metals, the first term in equation (2-1) is high, while the change in resistivity ($\Delta\rho/\rho$) is negligible. However, in semiconductor materials like silicon or germanium, the second term ($\Delta\rho/\rho$) is the highest, which provides a gauge factor of around 50 times than that

of metal foil strain gauges. The change in resistivity due to the applied stress occurs due to the transfer of electrons between energy levels, which affect electron mobility and consequently resistivity.

The piezoresistive effect in semiconductors describes the change in electrical resistivity of a conductor upon application of a mechanical stress. It was first observed in silicon and germanium through experimental testing by Smith [19] and Paul *et al.* [20] in the 1950s. Since then, a lot of research work has been conducted to study the piezoresistive effect and its relation to other parameters like electrical resistivity, electrical mobility, impurity concentration and temperature.

The change in resistance of a piezoresistive filament is related to the applied stress and/or temperature through the piezoresistive coefficients and temperature coefficient of resistance (*TCR*) as follows:

$$\frac{\Delta R}{R_0} = \pi \times \sigma + \alpha T \qquad (2\text{-}2)$$

Where, $\Delta R = R_\sigma - R_0$, with R_σ and R_0 being the stressed and unstressed resistance, respectively, π is the piezoresistivity tensor, α is the TCR, and T is the difference between current and reference temperatures.

In 1961, Pfann and Thurston [21] formulated relations for the longitudinal and transverse piezoresistive coefficients for crystalline silicon in different directions. Piezoresistivity in silicon can be described through the fourth-order piezoresistive tensor, which due to the cubic symmetry of silicon has only three distinct principal coefficients (π_{11}, π_{12}, and π_{44}) describing the relationship between change in resistivity and applied stress. The principal piezoresistive coefficients were studied experimentally by Tufte *et al.* [22, 23], Morin *et al.* [24], and Richter *et al.* [25]. Analytical modeling of the piezoresistive coefficients and their relation to temperature and impurity concentration is attributed to Kanda [26]. He provided plots of the theoretical longitudinal and transverse piezoresistive

coefficients as a function of the crystal orientations (100), (110), and (211) at room temperature. Kanda *et al*. [27-31] studied analytically and experimentally the first and second order piezoresistive coefficients in both p-type (p-Si) and n-type (n-Si) silicon. Other theoretical modeling of the piezoresistive effect was introduced by Kozlovsky *et al.* [32], Toriyama *et al.* [33] and Richter *et al.* [34]. The piezoresistive characteristics of a diffused layer in silicon was investigated by Ker *et al*. [35].

The temperature dependence of the piezoresistivity in silicon and germanium was studied by Morin [24]. Lenkkeri [36] discussed the nonlinear effects on the piezoresistive coefficients at 77 K and 300 K. Temperature coefficient of resistance (TCR) in silicon was studied by Bullis *et al*. [37] and Norton *et al.* [38]. A study on the effect of doping concentration on the first and second order temperature coefficient of resistance was conducted by Boukabache *et al.* using the models for majority carriers mobility in silicon [39].

The behavior of the shear piezoresistive coefficient (π_{44}) in n-type silicon (n-Si) was highlighted by Tufte *et al*. in 1963 [22, 23]. They discovered that π_{44} is constant over most of the impurity concentration range and starts a steep change at concentrations above $1x10^{20}$ cm^{-3}. On the other hand, the other two coefficients π_{11} and π_{12} have an inter-dependent change at concentrations above $1x10^{16}$ cm^{-3}. This reflects a change in the symmetry of the piezoresistive effect in n-Si at high concentrations. This behavior was found to be distinct to the n-Si, while the p-Si had inter-dependence between the three coefficients over all concentration ranges. Years later, in 1991, Kanda proposed an explanation to the behavior of π_{44} with impurity concentration, which has been a long standing mystery. They reported that the electron transfer theory can be used to describe correctly the behavior of π_{11} and π_{12} in n-Si. However, when used to describe the behavior of π_{44} it suggested a zero value for the coefficient. In fact, π_{44} is small compared to the other two coefficients; however, it differs from zero beyond an experimental error. Also, an analytical expression was proposed, using the theory of effective

mass change, to describe the behavior of π_{44} with concentration and temperature [28, 29, 40], which satisfied the experimental results given by Tufte *et al*. [22, 23]. Extended analytical studies to prove the behavior of π_{44} were published in 2009 by Nakamura *et al*. [41], which further confirmed the previous analytical and experimental observations.

2.3 Semiconductor Piezoresistive Stress/Strain Sensors

The piezoresistive effect in semiconductors has been gaining wide interest among a number of researchers especially with the recent development in Micro Electro-Mechanical Systems (MEMS). A fairly large number of investigations have been conducted to develop semiconductor piezoresistive sensors to measure direct or indirect phenomena. Indirect piezoresistive measurement sensors like pressure sensors [42-44], flow sensors [45-47], force sensors [48-51], and accelerometers [52] correlate the measured phenomenon with the change in electrical resistance through the induced stress as an intermediate parameter. On the other hand, direct measurements systems are the stress or strain sensors which have a direct relationship with the change in electrical resistance of the piezoresistive filament. In a stress sensor, equation (2-2) is used to correlate between the change in resistance ($\Delta R/R$) and the applied mechanical stress (σ). In a strain sensor, on the other hand, $\sigma = C \times \varepsilon$ is substituted in equation (2-2), where C is the elastic stiffness and ε is the induced strain. Therefore, the resistance change is expressed in terms of ε by the gauge factor (G) as presented in equation (2-1). Therefore, depending on the application, a stress or strain sensor is developed.

2.3.1 Piezoresistive Strain Sensors

Piezoresistive strain sensors have been developed as an alternative technique to metallic foil strain gauges especially with applications that require high sensitivity, low hysteresis, and integration with chip electronics. Kuo *et al*. [53] developed a piezoresistive strain sensor utilizing high doping levels ($1\text{x}10^{20}$ cm^{-3}) and thin substrate (30 μm) and bonded to a stainless steel test specimen for load

testing. At high doping levels, the gauge factor of the sensors was less sensitive to temperature variation compared to lower doping levels of ($2x10^{18}$ cm^{-3}). Also, they discovered that the thinned substrate provided less drift in the measured strain over time compared to the usual 500 μm substrates. Substrate thickness effect was also studied by Hautamaki *et al.* [14], who noticed that a bonded strain sensor exhibits large strain loss (near/far field effect) due to the higher stiffness of the silicon chip compared to the bonding adhesive. To enhance the near/far field effect, Mohammed *et al*. developed a silicon-based piezoresistive strain sensor with surface trenches to act as stress concentration intensifiers [54]. This novel approach eliminates the need for signal amplification from the measurement circuitry. Although their full rosette sensor is intended for extracting the three in-plane strain components, the experimental testing was only conducted to test the sensor chip for extraction of the uni-axial strain. Similar approach in terms of using surface trenches to increase output sensitivity was later used by Baumann *et al*. to develop a pressure sensor [55].

Some efforts have been made to develop strain sensors using polysilicon. Although it has lower sensitivity than crystalline silicon, polysilicon is known to have low temperature dependence [56]. Cao *et al.* [57, 58] designed and fabricated a piezoresistive strain sensor based on doped n-polysilicon resistors on a 3 μm-thin Si_3N_4/SiO_2 membrane to amplify the measured output. The sensor had a gauge factor of up to 21 and TCR as low as 750 ppm/ °C.

At high temperatures, diffused piezoresistors will have current leakage above 125 °C. Therefore, for high temperature applications, Silicon-on-Insulator (SOI) wafers are used to isolate piezoresistors from the bulk material. SOI wafers, developed mainly to reduce parasitic device capacitance, are made of layers of silicon, insulator, and silicon instead of the conventional silicon substrates, which are made homogenously of one silicon layer. Fraga *et al*. [59] developed two types of piezoresistive strain sensors for high temperature applications. The first utilizes non-stoichiometric amorphous silicon carbide (a-Si_xC_y) thin film and the

second is made up of p-type resistors on SOI substrate. Both types were tested under thermal loads up to 250 °C. The TCR values of both types were smaller than that of diffused resistors and exhibited a quasi-constant behavior.

2.3.2 Stress Sensing Rosettes

The first piezoresistive stress sensing rosette capable of extracting four of the six stress components was designed by Miura *et al.* [60]. This sensing rosette is made up of two p-type and two n-type diffused piezoresistors on (100) silicon wafer plane and extracts four stresses; the three in-plane stress components and the out-of-plane normal stress component. The first comprehensive presentation of the theory of piezoresistive stress sensing rosettes was given by Bittle *et al*. [61] and later re-constructed by Suhling *et al*. to include the effect of temperature on the resistance change equations and study the application of stress sensing rosettes to electronic packaging [13]. They provided some of the most significant and valuable work related to developing piezoresistive stress sensors as part of the research conducted in the Alabama Micro/Nano Science and Technology Center (AMNSTC) at Auburn University. For almost two decades, AMNSTC have been working on establishing the theory of stress sensors on crystalline silicon for measuring both in-plane and 3D stresses for electronic packaging applications.

The stress sensing rosettes are developed on the (100) silicon plane to extract the in-plane stress components and the normal out-of-plane stress, and on the (111) silicon plane to extract the full 3D six stress components [13]. In developing the 8-element 3D stress sensing rosette, the extracted stresses were partially temperature-compensated, where only four stresses are temperature-compensated, namely the three shear stresses and the difference of the in-plane normal stresses. Their inability to extract all stresses with temperature-compensation is due to the limitation in the number of independent equations that hinders the ability to eliminate the effect of temperature on the change in electrical resistance of the sensing elements. Solution for the remaining stress components required accurate independent measurement of the temperature using a temperature sensor

fabricated on the same sensing chip. A microscopic image of their developed 8-element 3D stress rosette on (111) silicon is shown in Figure 2-2.

The research conducted by AMNSTC in the area of stress sensing rosettes dealt with a number of development areas. The optimal silicon planes to orient the piezoresistive sensing elements were studied by Cordes *et al*. [62] to maximize the number of extracted stresses with temperature compensation, which was found to be the (111) silicon plane. Jaeger *et al*. [63] studied the errors associated with the design and calibration of the piezoresistive stress sensors in the (100). Cho *et al*. [64] studied the temperature effects on the piezoresistive coefficients and TCR in the stress sensors. Hussain *et al*. [65] conducted an error analysis to study the effect of measurement and calibration errors on the output of the (111) stress sensors.

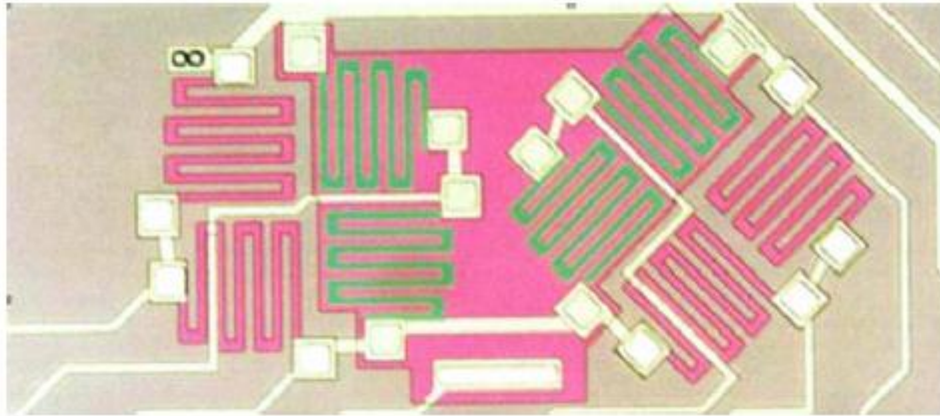

Figure 2-2 8-element piezoresistive 3D stress sensing rosette developed by AMNSTC [66], Copyright © 2009 IEEE

A number of researchers further investigated the use of the piezoresistive stress sensing rosettes developed by AMNSTC. Most of these efforts were towards using the (100) rosette that extracts the in-plane stresses. Lwo *et al.* [67, 68] investigated the use of all p-type or all n-type rosettes on the (100) silicon plane to

extract the in-plane stresses for electronic packaging applications. Although the n-type stress sensor had a lower sensitivity than the p-type, they suggested that the use of n-type piezoresistive sensors are highly recommended as *in-situ* stress sensing due to their lower standard deviation on the extracted coefficients compared to the p-type ones. Later, they utilized their developed stress sensor for measurement of moisture-induced stresses in electronic packaging [69] and thermal stresses in the low profile fine pitch ball grid array (LFBGA) packages [70]. Wang *et al.* [71] and Tian *et al.* [72] developed a piezoresistive stress sensing rosette using SOI wafer for in-plane stress measurement in electronic packaging. Their sensor is intended for high temperature applications up to 200 °C. Their dual-polarity rosette had non-linear TCR curves, which they attributed to the low thermal dissipation caused by the low thermal conductivity of the buried silicon dioxide (BOX) layer and the incomplete ionization of the n-type dopants. Tzeng *et al*. [73] designed, fabricated, and calibrated a stress sensor embedded in a Through Silicon Via (TSV) interposer. The sensor was intended to measure the strength of the TSV device and interposer wafer during the microfabrication process. Real-time stress measurement of an ultra-thin die (50 μm) during a drop test was conducted by Xiaowu *et al*. [74] through the use of a piezoresistive in-plane stress sensing rosette. This helped during the die packaging process to select the appropriate processes to enhance the final chip reliability. Other studies for the development of piezoresistive stress rosettes for electronic packaging applications include the works of Schwizer *et al*. [75], Lee *et al*. [76], and Shen *et al*. [77].

2.3.3 MOSFET Stress Sensors

In size-limited applications, a sensing rosette can become relatively large. Therefore, a stress sensor with a smaller footprint is required. Strained-silicon structures on Metal–Oxide–Semiconductor Field-Effect Transistor (MOSFET) have been studied extensively for years [78, 79]. The carrier mobility changes on MOSFET devices due to the applied stress or strain; therefore, the current

variations can be recorded at different channel directions [80]. This behavior allows MOSFETs or Piezo-FETs to act as chip stress sensors.

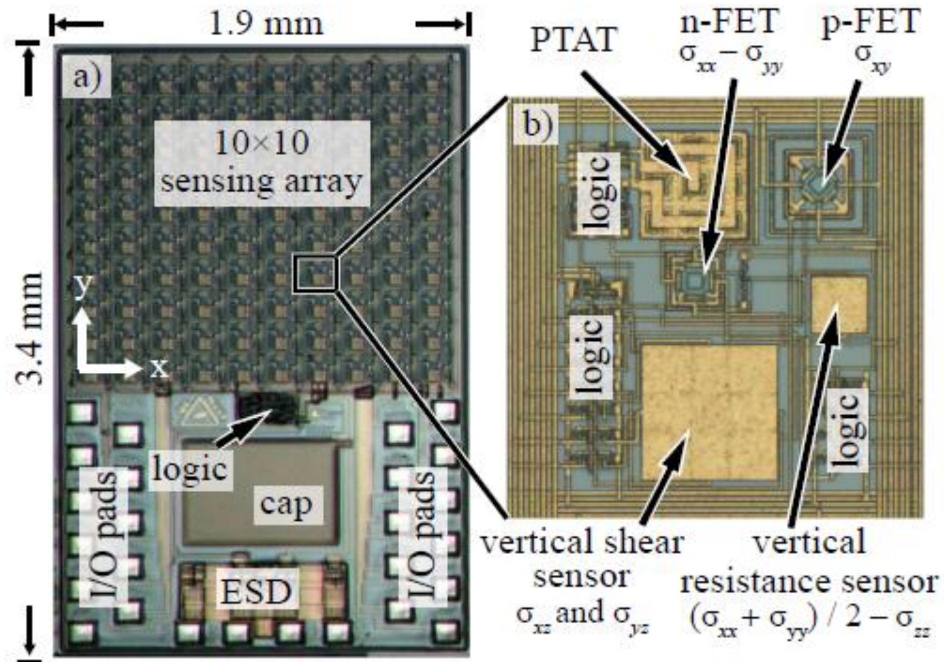

Figure 2-3 MOSFET stress sensor developed by Baumann *et al*. [81], Copyright © 2010 IEEE

MOSFET stress sensors have been developed by AMNSTC as an alternative to the (100) sensing rosette [82-85]. The sensors are able to extract the difference between the in-plane normal stresses and the in-plane shear stress. Another group at the department of Microsystems Engineering at the University of Freiburg in Germany [81, 86-88] developed a MOSFET stress sensor that can extract five stresses; namely the $(\sigma_{11} - \sigma_{22})$, σ_{12} , σ_{13} , σ_{23} , and $\sigma_{\Sigma} = (\sigma_{11} + \sigma_{22})/2 - \beta\sigma_{33}$. The sensor, shown in Figure 2-3, uses a pseudo-Hall contacts to extract the σ_{13} and σ_{23} components and a vertical resistance sensor formed by an n-doped silicon surrounded by a p-well to extract the σ_{Σ} component. Therefore, the extraction of the different stress components is performed from different sites on the silicon

die. They proposed using their technology in tactile sensors, smart dental brackets, and intra-cortical neural recording applications [11, 89].

2.3.4 Other Piezoresistive 3D Stress Sensing Techniques

Alfaro *et al*. [27] at Carnegie Mellon University developed an implantable piezoresistive sensor for measuring 3D stresses in bones. The sensor is comprised of an array of p- and n-type piezoresistive sensing elements implanted over square posts and oriented over the (100) silicon plane. A coupling scheme is developed to couple the in-plane stresses from the sensor to the 3D stresses in the bone material. This coupling scheme is case specific for certain bone geometry and properties. Also, the experimental testing results were given for tensile and compressive loading with no reference to loading conditions that induce shear stresses.

Another technique has been developed by Sutor *et al.* to measure the 3D stress distribution within a silicon chip [26]. This technique uses electrical impedance tomography (EIT) to map the resistivity change within a silicon chip by applying electrical current over surface contacts and measuring the voltage at other surface contacts. The method couples the effect of change in resistivity between different areas of the silicon chip to the stress distribution. However, this research was not continued because it was realized that the system becomes very sensitive to measurement errors.

An alternative approach for the sensing rosette was developed by Mian *et al*. [90] using van der Pauw structures. These structures are commonly used to measure sheet resistances as test structures during microfabrication processes. However, they discovered that it can also be used as a stress sensor with more than three times the sensitivity of the sensing rosettes. They used it to measure the in-plane or full 3D stresses by fabrication on a (100) or (111) planes, respectively.

2.4 Embedded Sensors

Embedding sensors in materials help monitor the stresses and strains generated during the fabrication or operation of the structures. Sensors can be embedded in different types of materials, including composites, polymers and metals. Also, investigations towards embedding different types of sensing mechanisms have been performed like piezoelectric, shape memory alloys (SMA), optical fibers, and piezoresistive.

One of the major research groups working in embedded sensors is the laboratory for rapid manufacturing of smart structures at University of Wisconsin-Madison [91-94]. Using rapid prototyping and layered manufacturing techniques, they investigated embedding sensors into different host materials including metals, polymers, composites, and ceramics.

Piezoelectric PZT sensors are used as a stress/strain sensor based on utilizing the generated voltage due to an applied strain to the crystal. However, their major disadvantage is that the output charge dissipates over time although the strain is still applied. So, they can work well at measuring transient loads, but not accurate enough for steady loads. Du *et al.* applied embedded PZT piezoelectric sensing elements below a tooling-workpiece interface to monitor the process loads [95, 96]. SMA is an alloy that changes its shape upon heating through returning to its original cold-forged form. Rogers *et al.* [97] introduced the idea of embedding SMA actuators in composite laminates for structural control. Osigu *et al.* performed a study on embedding SMA foil sensors and actuators in CFRP laminates with the objective to suppress the damage growth in the laminates [98, 99]. They were able to suppress the damage in composites such as transverse cracks and delamination using the embedded SMA actuators. Also, they developed an effective technique of surface treatment to improve the bonding properties between SMA and CFRP and manufacturing of CFRP laminates with embedded pre-strained SMA foils.

The use of optical fibers as embedded sensors has shown a great deal of research. There are many types of optical fiber sensors; however, fiber bragg gratings (FBGs) is the most successful due to its stable signal, capability for multiplexing, endurance against power fluctuation, and capacity for non-uniform strain field measurement [100]. FBGs strain sensors are based on the change in the wavelength of their reflected light beam when exposed to deformation or temperature. Murukeshan *et al*. investigated the use of embedded fiber Bragg grating to evaluate strains in composite specimens [101]. Also, Sirkis *et al.* employed embedded optical fibers as damage sensors to investigate the development of low velocity impact-induced delamination in composite laminates [102].

One major requirement for an embedded sensor is to have minimum effect on the structural integrity of the host material. This was studied by Paget *et al*. through embedding a piezoelectric ceramic transducer into a carbon/epoxy composite [103]. The transducer was embedded at the mid-plane of the composite material and tensile and compressive static loads were applied to the composite material. They found that the embedded sensor did not affect the strength of the composite and the final failure of the composite due to loading did not coincide with the position of the embedded sensor. Kim *et al.* carried out a similar research to examine the effect of embedding optical fiber sensors in composite materials in terms of initiating micro cracks and altering the composite strength [104]. They realized that composite laminates containing embedded optical fibers did not show change in strength due to applied in-plane compressive and three-point bend tests. On the other hand, Shivakumar *et al.* conducted a finite element study of an optical fiber embedded perpendicular to the reinforcing fibers of a composite. They showed that the embedded fiber caused an “eye”-shaped defect, which induced a maximum stress concentration of about 1.44 with failure occurring at the embedded optical fiber [105]. Moreover, Sirkis *et al*. realized that embedded optical fibers less than 100 μm in diameter do not alter the micro-cracks in the composite laminate [102].

In terms of embedded piezoresistive stress/strain sensors, Hautamaki *et al.* used MEMS piezoresistive strain sensors as embedded structures in fiber reinforced laminated composite plates [106]. Their approach was to embed a silicon-based strain sensor including signal conditioning and telemetry circuitry, and antenna as shown in Figure 2-4. They were able to evaluate strain values due to an applied uni-axial tension and bending loads. Also, Mahayotsanun *et al.* used thin-film force piezoresistive sensors embedded under the surface of the die cavity and flange in a deep drawing process to measure the contact pressure with the punch and holder tools [107]. Moore *et al*. [108] developed an embedded strain sensor in a cube form measuring 10 mm x 10 mm x 10 mm that can resolve the six strain components. The cube is made up of foil strain gauges on the outer sides and electronics consisting of signal conditioning circuitry, analog to digital converter (ADC), a microcontroller to send the data to a master device, and a temperature sensor for thermal compensation. Although, this novel sensor is appealing, its relatively thick size does not allow its deployment in thin interfaces between bonded structures.

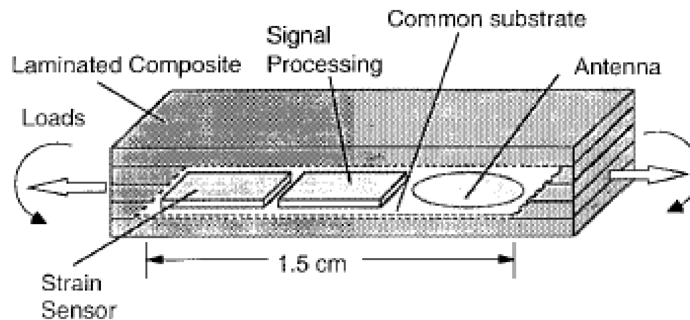

Figure 2-4 Schematic of a strain sensor embedded in a laminated composite along with auxiliary electronics [106], Copyright © 1999 IEEE

Figure 2-5 Cube measuring 10 mm x 10 mm x 10 mm for 3D strain measurement [108], Copyright © 2012 IEEE

2.5 Calibration of the Piezoresistive Stress Sensors

Accurate calibration of the piezoresistive coefficients is important to obtain correct stress measurements. A three-dimensional stress sensing rosette requires three calibration setups to calibrate the temperature coefficient of resistance (TCR) and the three piezoresistive coefficients B_1, B_2, and B_3. The B_1 and B_2 are related to the in-plane stresses, while the B_3 relates to the out-of-plane stress components [13]. The calibration of the temperature coefficient of resistance is usually carried out through placing the sensing chip in a stress-free varying temperature environment. However, different approaches have been adopted to calibrate the three piezoresistive coefficients B_1, B_2, and B_3, which are functions of the crystallographic piezoresistive coefficients. The calibration of B_1 and B_2, and the crystallographic piezoresistive coefficients in other applications, has mostly been performed using a four-point-bending fixture to apply a known uni-axial stress to a silicon beam; however, the resistance measurement has been performed differently among researchers. The most common approach has been contacting the contact pads on the silicon beam using micro-probes [13]. However, the probes when contacting the silicon beam create additional forces (shown as F_p in Figure 2-6), which can create a six-point bending instead of a four-point bending. Even if the location of the probes contact is known on the beam, the amount of force applied is unknown especially with manually probing techniques.

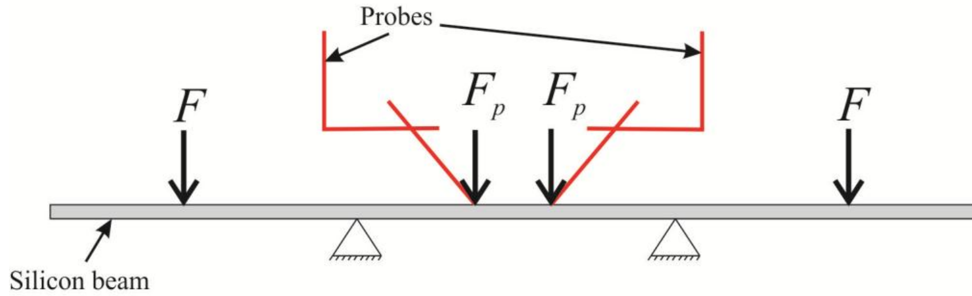

Figure 2-6 The addition of probe forces changes the loading state from 4-point to 6-point loading

To avoid the effect of probe forces, some researchers used a printed circuit board (PCB) bonded to the silicon beam and connected to the piezoresistors through wire bonds [72, 109]. Lwo *et al.* adopted a similar approach through connecting the wire bonds to enameled wires with silver-filled epoxy adhesive to avoid bonding a PCB to the silicon beam [110]. Tan *et al.* wire-bonded the chip pads to a flat flexible cable (FFC), which connects to the measurement instrument [111]. All of these techniques apply an additional load on the silicon beam, which either increases the beam's stiffness or adds stress concentration points on the beam. To Resolve the external load effects on the center of the beam, where the sensing elements being calibrated are located, Richter *et al.* [112] developed a new approach that uses zero insertion force (ZIF) connectors at the two ends of the silicon beam to connect to measurement circuitry. In this case, metal traces are fabricated on the wafer before dicing into beam shape, which connect on one side to the sensing elements and on the other side to a ZIF connector. A ZIF connector is commonly used in electronic assembly to connect to flat flexible cables (FFCs). Adopting ZIF connectors in the piezoresistive calibration process is useful, not only due to elimination of external loads on the center of the beam, but also because it expedites the calibration process. Moreover, it can be used for quick measurement of a variety of microfabricated devices without the need for probing, wire-bonding, or flip-chipping.

The third piezoresistive coefficient, B_3, can be calibrated either using a controlled out-of-plane shear or hydrostatic pressure loading, where in both cases a diced

sensing chip is wire-bonded to a PCB during calibration. The calibration process using a controlled out-of-plane shear has been carried out by Baumann *et al*. to calibrate a MOSFET stress sensor [86]. They fabricated a micro silicon two-point shear bridge and bonded it to the surface of the sensor and applied side force on the applicator to transmit out-of-plane shear stresses on the surface as shown in Figure 2-7. However, other stress components were found to be induced during the loading as simulated using finite element analysis. Moreover, this approach can only be used for one sensor element at a time.

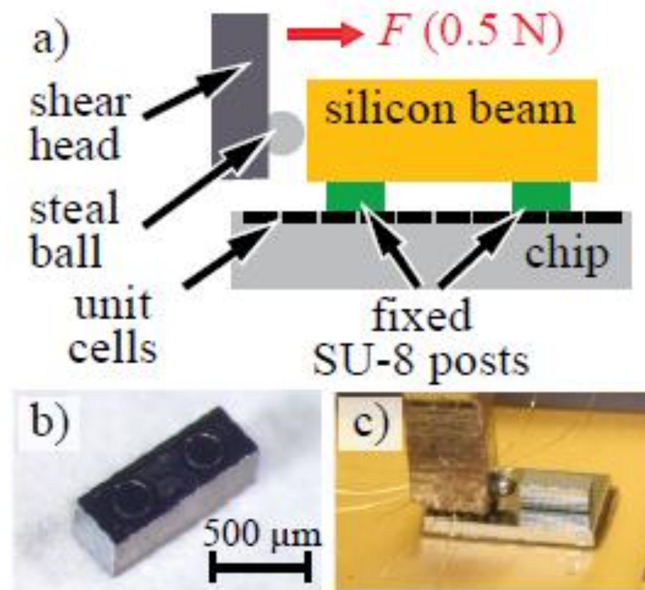

Figure 2-7 Application of an out-of-plane shear stress [81], Copyright © 2010 IEEE

On the other hand, the application of hydrostatic pressure has been commonly carried out by AMNSTC during their development of the stress sensors [113]. The calibration chip is immersed in a pressure vessel filled with hydraulic oil to apply a uniform hydrostatic pressure the chip. This allows the calibration of a number of sensing elements in the same setup. However, the extracted coefficient needs de-coupling from the thermal effects that are induced due to the applied pressure. An alternative approach was proposed by Hau *et al*. [114] for a wafer-level calibration using aluminum micro-beams deposited on top of the sensing element.

Upon thermal loading, the beams expand and create an out-of-plane shear enough for calibration of the $(B_2 - B_3)$. However, this approach also requires de-coupling of the temperature effects and is based on some stress field assumptions that are expected to affect the calibrated coefficient.

2.6 Conclusions

This chapter presented the development of the theory of piezoresistivity and specifically towards the design of piezoresistive stress sensors. The area of 3D stress sensor development using the theory of piezoresistivity has been discussed. The number of successful approaches to develop 3D piezoresistive stress sensors is limited. These approaches mainly utilized a dual-polarity rosette of diffused resistors on (111) silicon or MOSFETs on (100) silicon and are unable to extract all stress components with temperature compensation. An overview of the efforts to embed sensors in different materials was presented to demonstrate the potential use of the proposed 3D sensing chip as an embedded sensor. Finally, the available calibration techniques of piezoresistive 3D stress sensors have been discussed.

CHAPTER 3: THE PIEZORESISTIVE THREE-DIMENSIONAL STRESS SENSING ROSETTE[1]

3.1 Theoretical Background

3.1.1 General Relations of an Arbitrary Piezoresistive Filament

This section presents the fundamental equations relating the change in resistance of a piezoresistive filament due to an applied stress and thermal loads, which have been presented earlier by Bittle *et al*. [61] and Suhling *et al*. [117]. The behavior of a piezoresistive sensing rosette fabricated in crystalline silicon depends on the orientation of the sensing elements with respect to the crystallographic coordinates of the silicon crystal structure. An arbitrary oriented piezoresistive filament with respect to the silicon crystallographic axes is shown in Figure 3-1. The unprimed coordinates (on-axis) represent the principal crystallographic directions of silicon, i.e. X_1 = [100], X_2 = [010], and X_3 = [001], while the primed axes (off-axis) represent an arbitrary rotated coordinate system with respect to the principal crystallographic directions.

The change in electrical resistance of a piezoresistive filament due to an applied stress and temperature along the primed axes is given by [13]:

$$
\begin{aligned}
\frac{\Delta R}{R} &= \frac{R(\sigma,T)-R(0,0)}{R(0,0)} \\
&= \left(\pi'_{1\beta}\sigma'_{\beta}\right)l'^2 + \left(\pi'_{2\beta}\sigma'_{\beta}\right)m'^2 + \left(\pi'_{3\beta}\sigma'_{\beta}\right)n'^2 \\
&\quad + 2\left(\pi'_{4\beta}\sigma'_{\beta}\right)l'n' + 2\left(\pi'_{5\beta}\sigma'_{\beta}\right)m'n' + 2\left(\pi'_{6\beta}\sigma'_{\beta}\right)l'm' \\
&\quad + [\alpha_1 T + \alpha_2 T^2 + \ldots]
\end{aligned}
\tag{3-1}
$$

[1] Some of the material in this chapter has been previously published by Gharib *et al*. [115, 116].

Where,

$R(\sigma, T)$ = resistor value with applied stress and temperature change

$R(0, 0)$ = reference resistor value without applied stress and temperature change

$\pi'_{\gamma\beta}$ = off-axis temperature dependent piezoresistive coefficients with γ, β equals 1,2,…6

σ'_{β} = stress in the primed coordinate system, $\beta = 1,2,..,6$

$\alpha_1, \alpha_2, \ldots$ = first and higher order temperature coefficients of resistance (TCR)

$T=T_c-T_{ref}$ = difference between the current measurement temperature (T_c) and reference temperature (T_{ref})

l', m', n' = direction cosines of the filament orientation with respect to the x'_1, x'_2, and x'_3 axes

The derivation of equation (3-1) from the fundamental axiom of the current density/electric field relationship is presented in Appendix A.

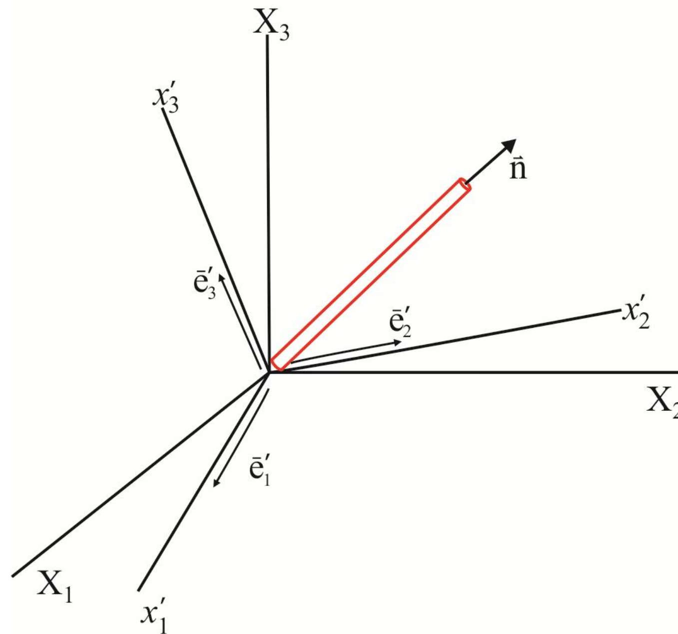

Figure 3-1 Filamentary silicon conductor

In equation (3-1), the stresses are given in reduced index notation, where:

$$\sigma'_1 = \sigma'_{11},\ \sigma'_2 = \sigma'_{22},\ \sigma'_3 = \sigma'_{33}$$
$$\sigma'_4 = \sigma'_{13},\ \sigma'_5 = \sigma'_{23},\ \sigma'_6 = \sigma'_{12} \qquad (3\text{-}2)$$

The crystallographic piezoresistivity tensor has 36 coefficients; however, due to cubic symmetry of the crystalline silicon structure, these coefficients are reduced to a matrix defined by the three unique on-axis piezoresistive coefficients π_{11}, π_{12}, and π_{44}.

$$\left[\pi_{\alpha\beta}\right] = \begin{bmatrix} \pi_{11} & \pi_{12} & \pi_{12} & 0 & 0 & 0 \\ \pi_{12} & \pi_{11} & \pi_{12} & 0 & 0 & 0 \\ \pi_{12} & \pi_{12} & \pi_{11} & 0 & 0 & 0 \\ 0 & 0 & 0 & \pi_{44} & 0 & 0 \\ 0 & 0 & 0 & 0 & \pi_{44} & 0 \\ 0 & 0 & 0 & 0 & 0 & \pi_{44} \end{bmatrix} \qquad (3\text{-}3)$$

The off-axis piezoresistive coefficients ($\pi'_{\alpha\beta}$) described in equation (3-1) are related to the crystallographic piezoresistive coefficients ($\pi_{\gamma\delta}$) through the following transformation:

$$\pi'_{\alpha\beta} = T_{\alpha\gamma}\pi_{\gamma\delta}T^{-1}_{\delta\beta} \qquad (3\text{-}4)$$

Where, the transformation matrix $T_{\alpha\gamma}$ is given by:

$$\left[T_{\alpha\beta}\right] = \begin{bmatrix} l_1^2 & m_1^2 & n_1^2 & 2l_1n_1 & 2m_1n_1 & 2l_1m_1 \\ l_2^2 & m_2^2 & n_2^2 & 2l_2n_2 & 2m_2n_2 & 2l_2m_2 \\ l_3^2 & m_3^2 & n_3^2 & 2l_3n_3 & 2m_3n_3 & 2l_3m_3 \\ l_1l_3 & m_1m_3 & n_1n_3 & l_1n_3+l_3n_1 & m_1n_3+m_3n_1 & l_1m_3+l_3m_1 \\ l_2l_3 & m_2m_3 & n_2n_3 & l_2n_3+l_3n_2 & m_2n_3+m_3n_2 & l_2m_3+l_3m_2 \\ l_1l_2 & m_1m_2 & n_1n_2 & l_1n_2+l_2n_1 & m_1n_2+m_2n_1 & l_1m_2+l_2m_1 \end{bmatrix} \qquad (3\text{-}5)$$

And the direction cosines of the primed axes are related to the unprimed axes through the vector:

$$a_{ij} = \cos(X_i^{'}, X_j) = \begin{bmatrix} l_1 & m_1 & n_1 \\ l_2 & m_2 & n_2 \\ l_3 & m_3 & n_3 \end{bmatrix} \tag{3-6}$$

Also, the stresses in the primed coordinate system are related to the unprimed system as follows:

$$\sigma'_{ij} = a_{ij}\sigma_{jk}a_{kl}^{-1}$$

$$\sigma'_{ij} = \begin{bmatrix} \sigma'_{11} & \sigma'_{12} & \sigma'_{13} \\ \sigma'_{21} & \sigma'_{22} & \sigma'_{23} \\ \sigma'_{31} & \sigma'_{32} & \sigma'_{33} \end{bmatrix} = \begin{bmatrix} l_1 & m_1 & n_1 \\ l_2 & m_2 & n_2 \\ l_3 & m_3 & n_3 \end{bmatrix} \times \begin{bmatrix} \sigma_{11} & \sigma_{12} & \sigma_{13} \\ \sigma_{21} & \sigma_{22} & \sigma_{23} \\ \sigma_{31} & \sigma_{32} & \sigma_{33} \end{bmatrix} \times \begin{bmatrix} l_1 & l_2 & l_3 \\ m_1 & m_2 & m_3 \\ n_1 & n_2 & n_3 \end{bmatrix} \tag{3-7}$$

Accordingly, in reduced index notation, the off-axis stress is related to the on-axis crystallographic stress by:

$$\sigma'_{\alpha} = T_{\alpha\beta}\sigma_{\beta}$$

Or

$$\begin{bmatrix} \sigma'_1 \\ \sigma'_2 \\ \sigma'_3 \\ \sigma'_4 \\ \sigma'_5 \\ \sigma'_6 \end{bmatrix} = \begin{bmatrix} l_1^2 & m_1^2 & n_1^2 & 2l_1n_1 & 2m_1n_1 & 2l_1m_1 \\ l_2^2 & m_2^2 & n_2^2 & 2l_2n_2 & 2m_2n_2 & 2l_2m_2 \\ l_3^2 & m_3^2 & n_3^2 & 2l_3n_3 & 2m_3n_3 & 2l_3m_3 \\ l_1l_3 & m_1m_3 & n_1n_3 & l_1n_3+l_3n_1 & m_1n_3+m_3n_1 & l_1m_3+l_3m_1 \\ l_2l_3 & m_2m_3 & n_2n_3 & l_2n_3+l_3n_2 & m_2n_3+m_3n_2 & l_2m_3+l_3m_2 \\ l_1l_2 & m_1m_2 & n_1n_2 & l_1n_2+l_2n_1 & m_1n_2+m_2n_1 & l_1m_2+l_2m_1 \end{bmatrix} \begin{bmatrix} \sigma_1 \\ \sigma_2 \\ \sigma_3 \\ \sigma_4 \\ \sigma_5 \\ \sigma_6 \end{bmatrix} \tag{3-8}$$

If the primed coordinate system coincides with the unprimed coordinate system, the transformation matrix $T_{\alpha\beta}$ reduces to a 6x6 identity matrix, which results in $\pi'_{\alpha\beta} = \pi_{\gamma\delta}$. Thus, equation (3-1) simplifies to the following relation for the resistance change along the crystallographic directions:

$$\begin{aligned}\frac{\Delta R}{R} &= \left[\pi_{11}\sigma_{11} + \pi_{12}\left(\sigma_{22} + \sigma_{33}\right)\right]l^2 + \left[\pi_{11}\sigma_{22} + \pi_{12}\left(\sigma_{11} + \sigma_{33}\right)\right]m^2 \\ &+ \left[\pi_{11}\sigma_{33} + \pi_{12}\left(\sigma_{11} + \sigma_{22}\right)\right]n^2 \\ &+ 2\pi_{44}\left[\sigma_{12}lm + \sigma_{13}ln + \sigma_{23}mn\right] + [\alpha_1 T + \alpha_2 T^2 + ...]\end{aligned} \tag{3-9}$$

Where, l, m, and n are the direction cosines of the piezoresistive filament with respect to the crystallographic coordinate system. Equation (3-9) demonstrates that an arbitrarily oriented piezoresistive conductor depends on the six stress components, the three piezoresistive coefficients and temperature. Orientation of this conductor on a specific silicon plane controls the number of stress components that can be extracted.

3.1.2 Relations along (111) Silicon Plane

The orientation defined by the primed axes for a set of piezoresistive filaments forming a rosette determines the number of stress components that can be extracted. The feasibility of utilizing a specific orientation is governed by the commonly available orientations of the silicon wafers. The two most common orientations, which provide two different combinations of stresses are the (001) and (111) silicon wafers. A rosette oriented over the (001) plane can be used to measure the in-plane stress components and the out-of-plane normal component. On the other hand, a rosette oriented over the (111) plane can extract the six stress components. Moreover, a (001) rosette can extract two temperature-compensated stress components, while the (111) rosette can extract four temperature-compensated stress components by eliminating the component (αT) in equation (3-1) [62]. In this research, the (111) wafer plane is used to develop the 3D stress sensing rosette.

The (111) plane (primed axes) is oriented relative to the silicon crystallographic coordinate system (unprimed axes) as shown in Figure 3-2. The direction cosines describing this relation are given by the vector:

$$\left[a_{ij}\right] = \cos(X_i', X_j) = \begin{bmatrix} l_1 & m_1 & n_1 \\ l_2 & m_2 & n_2 \\ l_3 & m_3 & n_3 \end{bmatrix} = \begin{bmatrix} -\frac{1}{\sqrt{2}} & \frac{1}{\sqrt{2}} & 0 \\ -\frac{1}{\sqrt{6}} & -\frac{1}{\sqrt{6}} & \frac{2}{\sqrt{6}} \\ \frac{1}{\sqrt{3}} & \frac{1}{\sqrt{3}} & \frac{1}{\sqrt{3}} \end{bmatrix} \tag{3-10}$$

Therefore, the piezoresistive coefficients along the (111) plane is obtained through the matrix transformation in equation (3-4) and using the direction cosines in equation (3-10).

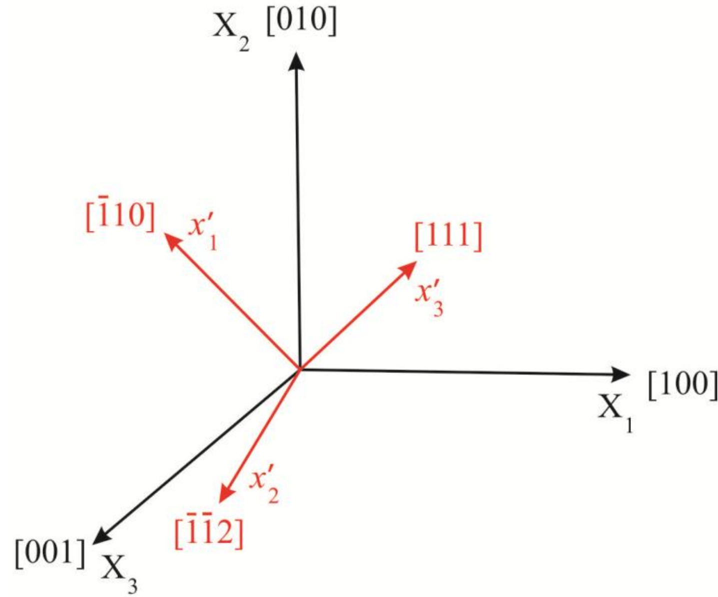

Figure 3-2 Orientation of the (111) coordinate system with the crystallographic coordinate system

The resistance change equation relating a sensing element (filamentary conductor) oriented along the (111) plane is derived from equation (3-1) by substituting the off-axis oriented piezoresistive coefficients from equation (3-4), which leads to:

$$\begin{aligned} \frac{\Delta R}{R} &= (B_1 \cos^2\phi + B_2 \sin^2\phi)\sigma_{11}^{'} + (B_2 \cos^2\phi + B_1 \sin^2\phi)\sigma_{22}^{'} + B_3\sigma_{33}^{'} \\ &+ 2\sqrt{2}(B_2 - B_3)(\cos^2\phi - \sin^2\phi)\sigma_{23}^{'} + 2\sqrt{2}(B_2 - B_3)\sin\left(2\phi\right)\sigma_{13}^{'} \\ &+ (B_1 - B_2)\sin\left(2\phi\right)\sigma_{12}^{'} + \left[\alpha_1 T + \alpha_2 T^2 + \ldots\right] \end{aligned} \tag{3-11}$$

Where ϕ is the angle defining the orientation of a piezoresistive filament over the (111) plane as shown in Figure 3-3 and related to the direction cosines l', m', n' in equation (3-1) through:

$$l' = \cos(\phi)\,,\; m' = \cos(90-\phi)\,,\text{ and } n' = \cos(90) \tag{3-12}$$

B_i (i=1,2,3) is a function of the crystallographic piezoresistive coefficients as follows:

$$B_1 = \frac{\pi_{11}+\pi_{12}+\pi_{44}}{2}\,,\quad B_2 = \frac{\pi_{11}+5\pi_{12}-\pi_{44}}{6}\,,\quad \text{and} \quad B_3 = \frac{\pi_{11}+2\pi_{12}-\pi_{44}}{3} \tag{3-13}$$

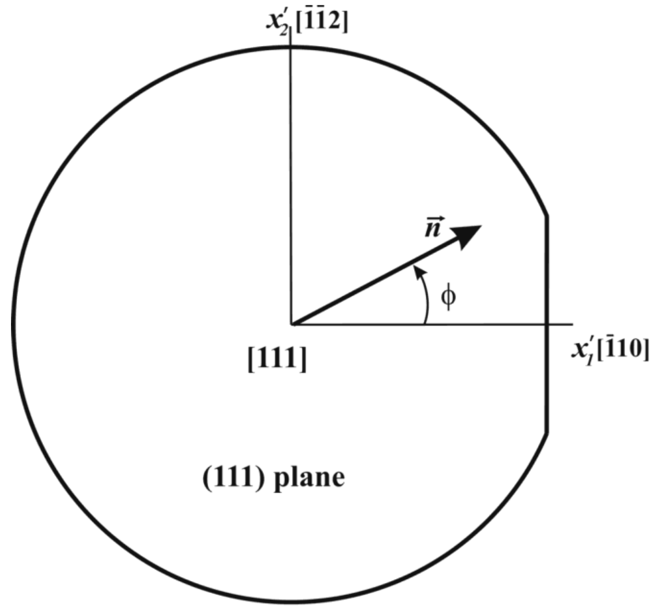

Figure 3-3 (111) silicon wafer with filament orientation

The mathematical formulation presented in this chapter focuses on the use of the piezoresistivity to extract the stress components. However, if strain components are the targeted output, resistance change versus strain relationships can be derived from equation (3-11) through considering the silicon stiffness constants. Derivation of the resistance change versus strain is presented in Appendix B.

3.2 Three-dimensional (3D) Stress Sensing Rosette

3.2.1 The 8-Element Rosette

The orientation of a sufficient number of sensing elements on the (111) silicon plane creates a sensing rosette that can extract the 3D stresses. The first 3D stress sensing rosette utilizing piezoresistive elements on the (111) silicon plane was proposed by Bittle *et al*. in 1991 [61] and later modified by Suhling *et al*. [13] to include the effect of temperature. This rosette is made up of eight sensing elements with dual-polarity (n- and p-type), where four n-type and four p-type elements were used. According to their analysis, a (111) sensing rosette fabricated from identically doped sensing elements (single-polarity) can only extract three stress components. On the other hand, a (111) dual-polarity rosette can extract the six stress components. The 8-element rosette developed by Suhling *et al*. is shown in Figure 3-4, where the elements from R_1 to R_8 are oriented at 45 degrees increments starting from R_1 at $\left[\bar{1}10\right]$ direction. Solution of the six stress components is still possible by using only 6 elements by omitting the two -45 degrees elements. However, the 8-element rosette provides reduced equation forms for some stress components and better stress localization.

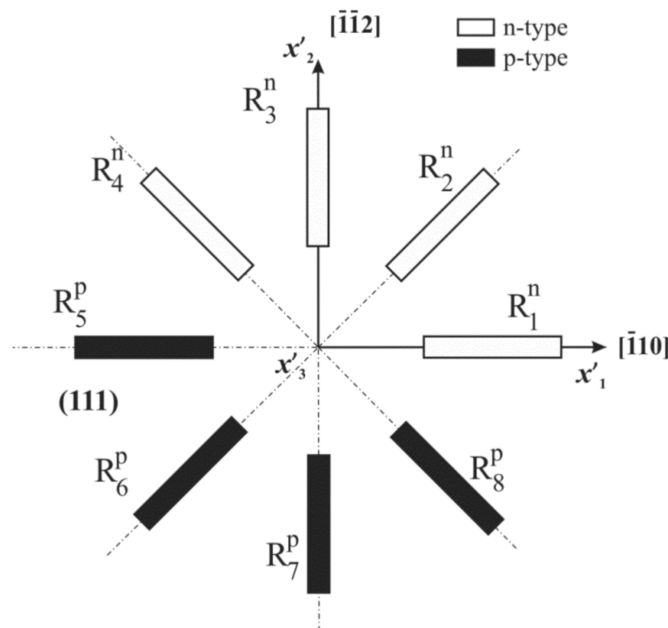

Figure 3-4 8-element rosette on (111) silicon

Orientation of equation (3-11) along the 8 angular directions and assuming the higher order temperature coefficients of resistance (α) are negligible generates the following equations for the 8-elements:

$$\left(\frac{\Delta R_1}{R_1}\right) = B_1^n \sigma'_{11} + B_2^n \sigma'_{22} + B_3^n \sigma'_{33} + 2\sqrt{2}(B_2^n - B_3^n)\sigma'_{23} + \alpha^n \mathrm{T}$$

$$\left(\frac{\Delta R_2}{R_2}\right) = \left(\frac{B_1^n + B_2^n}{2}\right)\sigma'_{11} + \left(\frac{B_1^n + B_2^n}{2}\right)\sigma'_{22} + B_3^n \sigma'_{33} + 2\sqrt{2}(B_2^n - B_3^n)\sigma'_{13} + (B_1^n - B_2^n)\sigma'_{12} + \alpha^n \mathrm{T}$$

$$\left(\frac{\Delta R_3}{R_3}\right) = B_2^n \sigma'_{11} + B_1^n \sigma'_{22} + B_3^n \sigma'_{33} - 2\sqrt{2}(B_2^n - B_3^n)\sigma'_{23} + \alpha^n \mathrm{T}$$

$$\left(\frac{\Delta R_4}{R_4}\right) = \left(\frac{B_1^n + B_2^n}{2}\right)\sigma'_{11} + \left(\frac{B_1^n + B_2^n}{2}\right)\sigma'_{22} + B_3^n \sigma'_{33} - 2\sqrt{2}(B_2^n - B_3^n)\sigma'_{13} - (B_1^n - B_2^n)\sigma'_{12} + \alpha^n \mathrm{T}$$

$$\left(\frac{\Delta R_5}{R_5}\right) = B_1^p \sigma'_{11} + B_2^p \sigma'_{22} + B_3^p \sigma'_{33} + 2\sqrt{2}(B_2^p - B_3^p)\sigma'_{23} + \alpha^p \mathrm{T}$$

$$\left(\frac{\Delta R_6}{R_6}\right) = \left(\frac{B_1^p + B_2^p}{2}\right)\sigma'_{11} + \left(\frac{B_1^p + B_2^p}{2}\right)\sigma'_{22} + B_3^p \sigma'_{33} + 2\sqrt{2}(B_2^p - B_3^p)\sigma'_{13} + (B_1^p - B_2^p)\sigma'_{12} + \alpha^p \mathrm{T}$$

$$\left(\frac{\Delta R_7}{R_7}\right) = B_2^p \sigma'_{11} + B_1^p \sigma'_{22} + B_3^p \sigma'_{33} - 2\sqrt{2}(B_2^p - B_3^p)\sigma'_{23} + \alpha^p \mathrm{T}$$

$$\left(\frac{\Delta R_8}{R_8}\right) = \left(\frac{B_1^p + B_2^p}{2}\right)\sigma'_{11} + \left(\frac{B_1^p + B_2^p}{2}\right)\sigma'_{22} + B_3^p \sigma'_{33} - 2\sqrt{2}(B_2^p - B_3^p)\sigma'_{13} - (B_1^p - B_2^p)\sigma'_{12} + \alpha^p \mathrm{T} \quad (3\text{-}14)$$

Where, the subscripts 1 to 8 on the left hand side refer to the number of the sensing element shown in Figure 3-4 and the superscripts *n* and *p* refer to the n- and p-type doping, respectively. Through addition and subtraction of equations (3-13), the following stress equations are generated [13]:

$$\sigma'_{11}=\frac{\left(B_3^p-B_2^p\right)\left(\frac{\Delta R_1}{R_1}-\frac{\Delta R_3}{R_3}\right)-\left(B_3^n-B_2^n\right)\left(\frac{\Delta R_5}{R_5}-\frac{\Delta R_7}{R_7}\right)}{2\left[\left(B_2^p-B_1^p\right)B_3^n+\left(B_1^p-B_3^p\right)B_2^n+\left(B_3^p-B_2^p\right)B_1^n\right]}+\frac{B_3^p\left[\frac{\Delta R_1}{R_1}+\frac{\Delta R_3}{R_3}-2\alpha_1^nT\right]-B_3^n\left[\frac{\Delta R_5}{R_5}+\frac{\Delta R_7}{R_7}-2\alpha_1^pT\right]}{2\left[\left(B_1^n+B_2^n\right)B_3^p-\left(B_1^p+B_2^p\right)B_3^n\right]}$$

$$\sigma'_{22}=-\frac{\left(B_3^p-B_2^p\right)\left(\frac{\Delta R_1}{R_1}-\frac{\Delta R_3}{R_3}\right)-\left(B_3^n-B_2^n\right)\left(\frac{\Delta R_5}{R_5}-\frac{\Delta R_7}{R_7}\right)}{2\left[\left(B_2^p-B_1^p\right)B_3^n+\left(B_1^p-B_3^p\right)B_2^n+\left(B_3^p-B_2^p\right)B_1^n\right]}+\frac{B_3^p\left[\frac{\Delta R_1}{R_1}+\frac{\Delta R_3}{R_3}-2\alpha_1^nT\right]-B_3^n\left[\frac{\Delta R_5}{R_5}+\frac{\Delta R_7}{R_7}-2\alpha_1^pT\right]}{2\left[\left(B_1^n+B_2^n\right)B_3^p-\left(B_1^p+B_2^p\right)B_3^n\right]}$$

$$\sigma'_{33}=\frac{-\left(B_1^p+B_2^p\right)\left[\frac{\Delta R_1}{R_1}+\frac{\Delta R_3}{R_3}-2\alpha_1^nT\right]+\left(B_1^n+B_2^n\right)\left[\frac{\Delta R_5}{R_5}+\frac{\Delta R_7}{R_7}-2\alpha_1^pT\right]}{2\left[\left(B_1^n+B_2^n\right)B_3^p-\left(B_1^p+B_2^p\right)B_3^n\right]}$$

$$\sigma'_{23}=\frac{\sqrt{2}}{8}\left[\frac{-\left(B_2^p-B_1^p\right)\left(\frac{\Delta R_1}{R_1}-\frac{\Delta R_3}{R_3}\right)+\left(B_2^n-B_1^n\right)\left(\frac{\Delta R_5}{R_5}-\frac{\Delta R_7}{R_7}\right)}{\left(B_2^p-B_1^p\right)B_3^n+\left(B_1^p-B_3^p\right)B_2^n+\left(B_3^p-B_2^p\right)B_1^n}\right]$$

$$\sigma'_{13}=\frac{\sqrt{2}}{8}\left[\frac{-\left(B_2^p-B_1^p\right)\left(\frac{\Delta R_2}{R_2}-\frac{\Delta R_4}{R_4}\right)+\left(B_2^n-B_1^n\right)\left(\frac{\Delta R_6}{R_6}-\frac{\Delta R_8}{R_8}\right)}{\left(B_2^p-B_1^p\right)B_3^n+\left(B_1^p-B_3^p\right)B_2^n+\left(B_3^p-B_2^p\right)B_1^n}\right]$$

$$\sigma'_{12}=\left[\frac{\left(B_3^p-B_2^p\right)\left(\frac{\Delta R_2}{R_2}-\frac{\Delta R_4}{R_4}\right)-\left(B_3^n-B_2^n\right)\left(\frac{\Delta R_6}{R_6}-\frac{\Delta R_8}{R_8}\right)}{2\left[\left(B_2^p-B_1^p\right)B_3^n+\left(B_1^p-B_3^p\right)B_2^n+\left(B_3^p-B_2^p\right)B_1^n\right]}\right] \qquad (3\text{-}15)$$

The solution of equations (3-15) is based on the independent coefficients of the n-type sensing elements from those of the p-type elements. This provides enough linearly independent responses from the sensing elements that make the solution of equations (3-15) possible. Although the 8-element rosette is capable of solving the 6 stress components, it provides partial temperature compensation to the output stresses. The 8-element rosette only solves for 4 stresses with temperature-compensation and 3 stresses with temperature-dependence. The 4 temperature-compensated stresses are the difference between the in-plane normal stresses $\left(\sigma'_{11} - \sigma'_{22}\right)$ and the shear stresses σ'_{23}, σ'_{13}, and σ'_{12}, while the 3 temperature-dependent stresses are the normal stress components σ'_{11}, σ'_{22}, and σ'_{33}.

3.2.2 The Ten-Element Rosette

The dual-polarity rosette provides two sets of independent piezoresistive coefficients (π) and temperature coefficients of resistance (α), which generate linearly independent equations to extract the six stresses with partial temperature-compensation. Therefore, if it is possible to have two groups of sensing elements (not necessarily dual-polarity) with independent π and α, the partially temperature-compensated six stress components can be extracted. Moreover, if a third group with different π and α is added, temperature-compensation of the normal stress components is achievable; therefore, coming up with a fully temperature compensated stress output.

The rosette developed in this research is based on adding two more sensing elements to the 8-element rosette developed by Suhling *et al*. Therefore, the new rosette is made up of 10 sensing elements developed over the (111) wafer plane as shown in Figure 3-5 and is divided into three groups (*a*, *b*, and *c*), where each group has linearly independent π and α. Eight of these elements, forming groups *a* and *b*, are used to solve for the four temperature-compensated stresses similar to the dual-polarity rosette of Suhling *et al.* The extra two sensing elements forming the third group *c* is used to solve for the remaining temperature-compensated

stress components. The following mathematical analysis is not based on using a specific doping type for the sensing elements; rather it deals with the equations from a solution feasibility approach. In sections 3.3 and 3.4, specific application of the doping type will be discussed. Application of equation (3-11) to the 10-element rosette gives ten equations describing the resistance change with the applied stress and temperature:

$$\left(\frac{\Delta R_1}{R_1}\right) = B_1^a\sigma'_{11} + B_2^a\sigma'_{22} + B_3^a\sigma'_{33} + 2\sqrt{2}(B_2^a - B_3^a)\sigma'_{23} + \alpha^a T$$

$$\left(\frac{\Delta R_2}{R_2}\right) = \left(\frac{B_1^a + B_2^a}{2}\right)\sigma'_{11} + \left(\frac{B_1^a + B_2^a}{2}\right)\sigma'_{22} + B_3^a\sigma'_{33} + 2\sqrt{2}(B_2^a - B_3^a)\sigma'_{13} + (B_1^a - B_2^a)\sigma'_{12} + \alpha^a T$$

$$\left(\frac{\Delta R_3}{R_3}\right) = B_2^a\sigma'_{11} + B_1^a\sigma'_{22} + B_3^a\sigma'_{33} - 2\sqrt{2}(B_2^a - B_3^a)\sigma'_{23} + \alpha^a T$$

$$\left(\frac{\Delta R_4}{R_4}\right) = \left(\frac{B_1^a + B_2^a}{2}\right)\sigma'_{11} + \left(\frac{B_1^a + B_2^a}{2}\right)\sigma'_{22} + B_3^a\sigma'_{33} - 2\sqrt{2}(B_2^a - B_3^a)\sigma'_{13} - (B_1^a - B_2^a)\sigma'_{12} + \alpha^a T$$

$$\left(\frac{\Delta R_5}{R_5}\right) = B_1^b\sigma'_{11} + B_2^b\sigma'_{22} + B_3^b\sigma'_{33} + 2\sqrt{2}(B_2^b - B_3^b)\sigma'_{23} + \alpha^b T$$

$$\left(\frac{\Delta R_6}{R_6}\right) = \left(\frac{B_1^b + B_2^b}{2}\right)\sigma'_{11} + \left(\frac{B_1^b + B_2^b}{2}\right)\sigma'_{22} + B_3^b\sigma'_{33} + 2\sqrt{2}(B_2^b - B_3^b)\sigma'_{13} + (B_1^b - B_2^b)\sigma'_{12} + \alpha^b T$$

$$\left(\frac{\Delta R_7}{R_7}\right) = B_2^b\sigma'_{11} + B_1^b\sigma'_{22} + B_3^b\sigma'_{33} - 2\sqrt{2}(B_2^b - B_3^b)\sigma'_{23} + \alpha^b T$$

$$\left(\frac{\Delta R_8}{R_8}\right) = \left(\frac{B_1^b + B_2^b}{2}\right)\sigma'_{11} + \left(\frac{B_1^b + B_2^b}{2}\right)\sigma'_{22} + B_3^b\sigma'_{33} - 2\sqrt{2}(B_2^b - B_3^b)\sigma'_{13} - (B_1^b - B_2^b)\sigma'_{12} + \alpha^b T$$

$$\left(\frac{\Delta R_9}{R_9}\right) = B_1^c\sigma'_{11} + B_2^c\sigma'_{22} + B_3^c\sigma'_{33} + 2\sqrt{2}(B_2^c - B_3^c)\sigma'_{23} + \alpha^c T$$

$$\left(\frac{\Delta R_{10}}{R_{10}}\right) = B_2^c\sigma'_{11} + B_1^c\sigma'_{22} + B_3^c\sigma'_{33} - 2\sqrt{2}(B_2^c - B_3^c)\sigma'_{23} + \alpha^c T$$

(3-16)

Subscripts (1, 2, 3, ... 10) on the left hand side represent the sensing elements shown in Figure 3-5, while the superscripts *a*, *b*, and *c* indicate the different groups of elements.

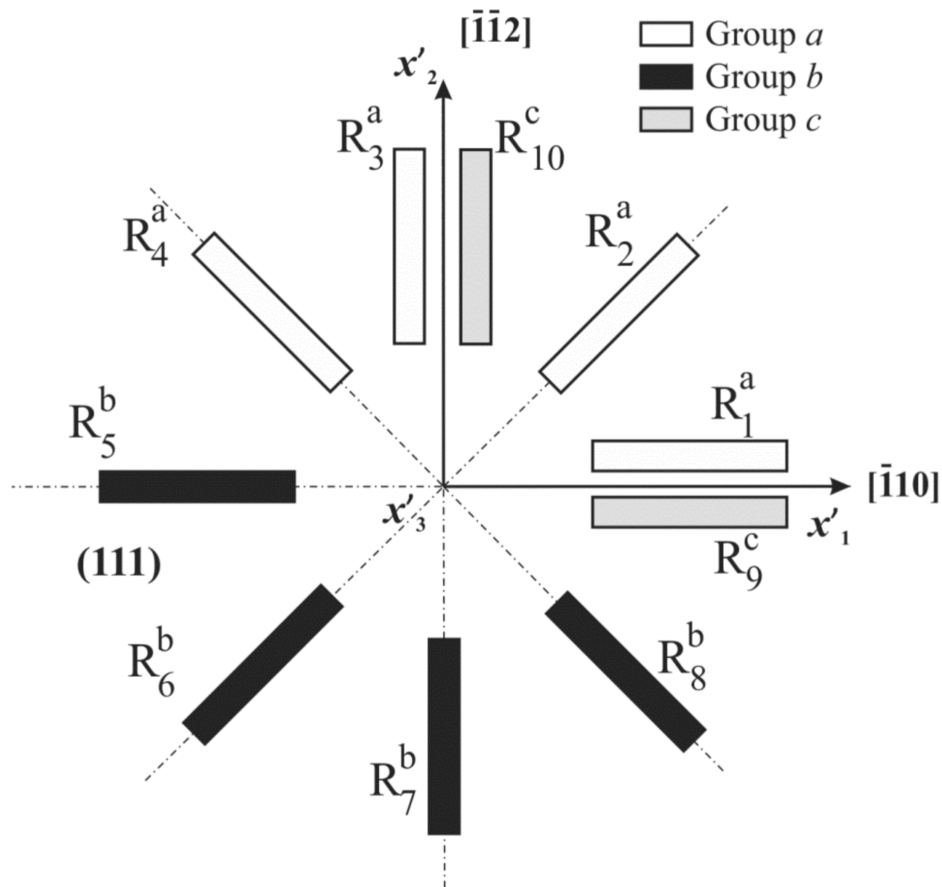

Figure 3-5 Ten-element rosette on (111) silicon

The evaluation of the stresses and temperature is carried out by the subtraction and addition of equations (3-16) to give:

(i) Equations for the evaluation of $\left(\sigma'_{11}-\sigma'_{22}\right)$ *and* σ'_{23}

$$\begin{bmatrix} \dfrac{\Delta R_1}{R_1}-\dfrac{\Delta R_3}{R_3} \\ \dfrac{\Delta R_5}{R_5}-\dfrac{\Delta R_7}{R_7} \end{bmatrix} = \begin{bmatrix} \left(B_1^a-B_2^a\right) & 4\sqrt{2}\left(B_2^a-B_3^a\right) \\ \left(B_1^b-B_2^b\right) & 4\sqrt{2}\left(B_2^b-B_3^b\right) \end{bmatrix} \begin{bmatrix} \left(\sigma'_{11}-\sigma'_{22}\right) \\ \sigma'_{23} \end{bmatrix} \tag{3-17}$$

(ii) Equations for the evaluation of σ'_{13} *and* σ'_{12}

$$\begin{bmatrix} \dfrac{\Delta R_2}{R_2}-\dfrac{\Delta R_4}{R_4} \\ \dfrac{\Delta R_6}{R_6}-\dfrac{\Delta R_8}{R_8} \end{bmatrix} = \begin{bmatrix} 4\sqrt{2}\left(B_2^a-B_3^a\right) & 2\left(B_1^a-B_2^a\right) \\ 4\sqrt{2}\left(B_2^b-B_3^b\right) & 2\left(B_1^b-B_2^b\right) \end{bmatrix} \begin{bmatrix} \sigma'_{13} \\ \sigma'_{12} \end{bmatrix} \tag{3-18}$$

(iii) Equations for the evaluation of $\left(\sigma'_{11}+\sigma'_{22}\right)$*,* σ'_{33}*, and T*

$$\begin{bmatrix} \dfrac{\Delta R_1}{R_1}+\dfrac{\Delta R_3}{R_3} \\ \dfrac{\Delta R_5}{R_5}+\dfrac{\Delta R_7}{R_7} \\ \dfrac{\Delta R_9}{R_9}+\dfrac{\Delta R_{10}}{R_{10}} \end{bmatrix} = \begin{bmatrix} \left(B_1^a+B_2^a\right) & 2B_3^a & 2\alpha^a \\ \left(B_1^b+B_2^b\right) & 2B_3^b & 2\alpha^b \\ \left(B_1^c+B_2^c\right) & 2B_3^c & 2\alpha^c \end{bmatrix} \begin{bmatrix} \left(\sigma'_{11}+\sigma'_{22}\right) \\ \sigma'_{33} \\ T \end{bmatrix} \tag{3-19}$$

The expressions in (3-17)-(3-19) are inverted to solve for the stresses and temperature in terms of the measured resistance changes, where D_1 describes the determinants of the coefficients in (3-17) and (3-18), and D_2 describes the determinant of the coefficients in (3-19).

$$\sigma'_{11} = \frac{1}{2D_2}\left[\left(B_3^c\alpha^b - B_3^b\alpha^c\right)\left(\frac{\Delta R_1}{R_1} + \frac{\Delta R_3}{R_3}\right) + \left(B_3^a\alpha^c - B_3^c\alpha^a\right)\left(\frac{\Delta R_5}{R_5} + \frac{\Delta R_7}{R_7}\right)\right.$$
$$\left. + \left(B_3^b\alpha^a - B_3^a\alpha^b\right)\left(\frac{\Delta R_9}{R_9} + \frac{\Delta R_{10}}{R_{10}}\right)\right]$$
$$+ \frac{1}{2D_1}\left[\left(B_2^b - B_3^b\right)\left(\frac{\Delta R_1}{R_1} - \frac{\Delta R_3}{R_3}\right) - \left(B_2^a - B_3^a\right)\left(\frac{\Delta R_5}{R_5} - \frac{\Delta R_7}{R_7}\right)\right]$$

$$\sigma'_{22} = \frac{1}{2D_2}\left[\left(B_3^c\alpha^b - B_3^b\alpha^c\right)\left(\frac{\Delta R_1}{R_1} + \frac{\Delta R_3}{R_3}\right) + \left(B_3^a\alpha^c - B_3^c\alpha^a\right)\left(\frac{\Delta R_5}{R_5} + \frac{\Delta R_7}{R_7}\right)\right.$$
$$\left. + \left(B_3^b\alpha^a - B_3^a\alpha^b\right)\left(\frac{\Delta R_9}{R_9} + \frac{\Delta R_{10}}{R_{10}}\right)\right]$$
$$- \frac{1}{2D_1}\left[\left(B_2^b - B_3^b\right)\left(\frac{\Delta R_1}{R_1} - \frac{\Delta R_3}{R_3}\right) - \left(B_2^a - B_3^a\right)\left(\frac{\Delta R_5}{R_5} - \frac{\Delta R_7}{R_7}\right)\right]$$

$$\left(\sigma'_{11} - \sigma'_{22}\right) = \frac{1}{D_1}\left[\left(B_2^b - B_3^b\right)\left(\frac{\Delta R_1}{R_1} - \frac{\Delta R_3}{R_3}\right) - \left(B_2^a - B_3^a\right)\left(\frac{\Delta R_5}{R_5} - \frac{\Delta R_7}{R_7}\right)\right]$$

$$\sigma'_{33} = \frac{1}{2D_2}\left[\left((B_1^b + B_2^b)\alpha^c - (B_1^c + B_2^c)\alpha^b\right)\left(\frac{\Delta R_1}{R_1} + \frac{\Delta R_3}{R_3}\right)\right.$$
$$+ \left((B_1^c + B_2^c)\alpha^a - (B_1^a + B_2^a)\alpha^c\right)\left(\frac{\Delta R_5}{R_5} + \frac{\Delta R_7}{R_7}\right)$$
$$\left. + \left((B_1^a + B_2^a)\alpha^b - (B_1^b + B_2^b)\alpha^a\right)\left(\frac{\Delta R_9}{R_9} + \frac{\Delta R_{10}}{R_{10}}\right)\right]$$

$$\sigma'_{23} = \frac{1}{D_1}\left[-\frac{\left(B_1^b - B_2^b\right)}{4\sqrt{2}}\left(\frac{\Delta R_1}{R_1} - \frac{\Delta R_3}{R_3}\right) + \frac{\left(B_1^a - B_2^a\right)}{4\sqrt{2}}\left(\frac{\Delta R_5}{R_5} - \frac{\Delta R_7}{R_7}\right)\right]$$

$$\sigma'_{13} = \frac{1}{D_1}\left[\frac{-\left(B_1^b - B_2^b\right)}{4\sqrt{2}}\left(\frac{\Delta R_2}{R_2} - \frac{\Delta R_4}{R_4}\right) + \frac{\left(B_1^a - B_2^a\right)}{4\sqrt{2}}\left(\frac{\Delta R_6}{R_6} - \frac{\Delta R_8}{R_8}\right)\right]$$

$$\sigma'_{12} = \frac{1}{D_1}\left[\frac{\left(B_2^b - B_3^b\right)}{2}\left(\frac{\Delta R_2}{R_2} - \frac{\Delta R_4}{R_4}\right) - \frac{\left(B_2^a - B_3^a\right)}{2}\left(\frac{\Delta R_6}{R_6} - \frac{\Delta R_8}{R_8}\right)\right]$$

$$T = \frac{1}{2D_2}\Bigg[\left((B_1^c + B_2^c)B_3^b - (B_1^b + B_2^b)B_3^c\right)\left(\frac{\Delta R_1}{R_1} + \frac{\Delta R_3}{R_3}\right) + \left((B_1^a + B_2^a)B_3^c - (B_1^c + B_2^c)B_3^a\right)\left(\frac{\Delta R_5}{R_5} + \frac{\Delta R_7}{R_7}\right) + \left((B_1^b + B_2^b)B_3^a - (B_1^a + B_2^a)B_3^b\right)\left(\frac{\Delta R_9}{R_9} + \frac{\Delta R_{10}}{R_{10}}\right)\Bigg] \quad (3\text{-}20)$$

Where,

$$D_1 = B_1^a\left(B_2^b - B_3^b\right) + B_2^a\left(B_3^b - B_1^b\right) + B_3^a\left(B_1^b - B_2^b\right) \quad (3\text{-}21)$$

$$D_2 = B_3^a\left[(B_1^b + B_2^b)\alpha^c - (B_1^c + B_2^c)\alpha^b\right] + B_3^b\left[(B_1^c + B_2^c)\alpha^a - (B_1^a + B_2^a)\alpha^c\right] + B_3^c\left[(B_1^a + B_2^a)\alpha^b - (B_1^b + B_2^b)\alpha^a\right] \quad (3\text{-}22)$$

3.3 Fundamental Properties of the 10-Element Rosette

This section highlights some of the fundamental properties of the p- and n-type piezoresistors that shape the design and operation of the 10-element rosette. These properties are the effect of the impurity concentration on (1) the principal piezoresistive coefficients π_{11}, π_{12}, and π_{44} and (2) the temperature coefficient of resistance (TCR) for both p- and n-type piezoresistors.

3.3.1 Effect of the Impurity Concentration on the Piezoresistive Coefficients

The values of the on-axis piezoresistive coefficients (π_{11}, π_{12}, and π_{44}) in silicon vary with impurity concentration and temperature as analytically modeled by Kanda [26]:

$$\pi\left(N,T\right) = P\left(N,T\right) \times \pi\left(300\text{ K}\right) \quad (3\text{-}23)$$

Where,

π (300 K) is the piezoresistive coefficient at lightly doped levels and 300 degrees Kelvin (K) and $P(N,T)$ is the piezoresistive factor given by:

$$P(N,T) = \frac{300}{T} \frac{1}{\left(1+e^{-E_f/kT}\right)\ln\left(1+e^{E_f/kT}\right)} \tag{3-24}$$

Where, E_f = Fermi energy which is dependent on the impurity concentration and the valence band energy and k = Boltzmann constant = $1.3806504\text{x}10^{-23}$ J/K = $8.617343\text{x}10^{-5}$ eV/K

The on-axis piezoresistive coefficients for lightly doped silicon are given in Table 3-1 as experimentally tested by Smith [19] and Mason *et al*. [118]. The analytically modeled *P(N,T)* factor by Kanda [26] as a function of impurity concentration for n- and p-Si is shown in Figure 3-6 and Figure 3-7, respectively.

Table 3-1 Piezoresistive Coefficients for Lightly Doped Silicon, TPa^{-1} [19, 118]

Piezoresistive Coefficient	n-type Silicon	p-type Silicon
π_{11}	-1022	66
π_{12}	534	-11
π_{44}	-136	1381

The relation in equation (3-23) assumes that all the on-axis piezoresistive coefficients vary with impurity concentration and temperature with the same factor *P(N,T)*. This is found to be experimentally true for the p-Si [22, 35]. Similarly, in n-Si, π_{11} and π_{12} are related to the impurity concentration and temperature with a common factor. On the other hand, the shear piezoresistive coefficient π_{44} in n-Si behaves in a different manner than the other two coefficients. Tufte *et al*. [22, 23] reported that upon change in impurity concentration, the absolute value of π_{44} shows no change until an impurity concentration of around 10^{20} cm^{-3}, then it starts showing a logarithmic increase of its absolute value as shown in Figure 3-8 compared to the decreasing π_{11} and π_{12}.

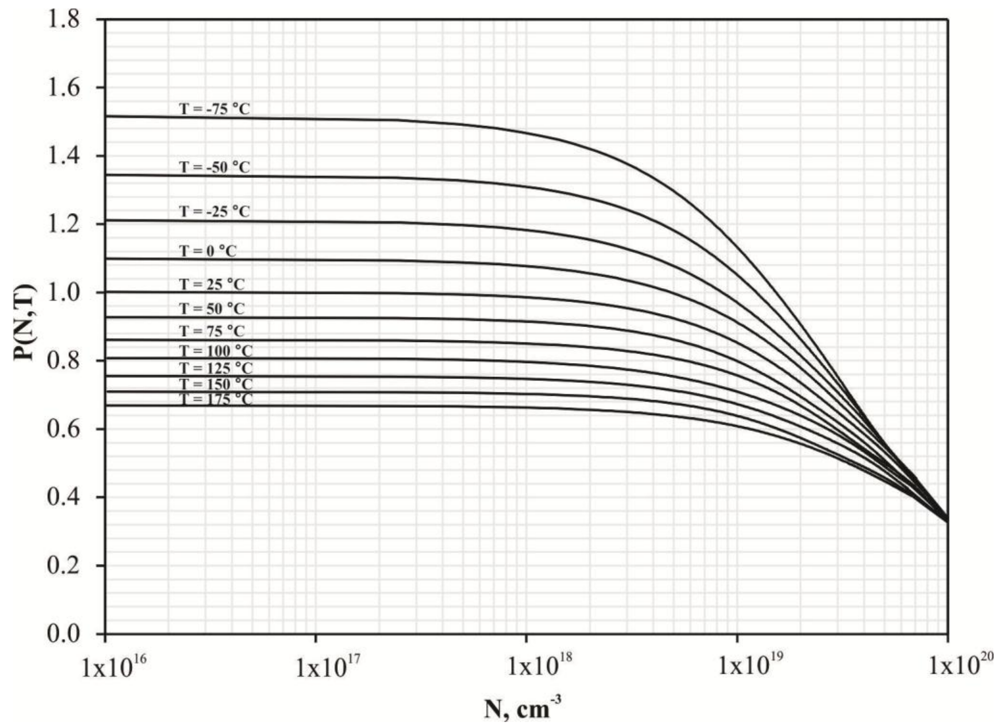

Figure 3-6 Piezoresistive factor P(N,T) as a function of impurity concentration and temperature in n-Si (re-plotted from [26]), Copyright © 1982 IEEE

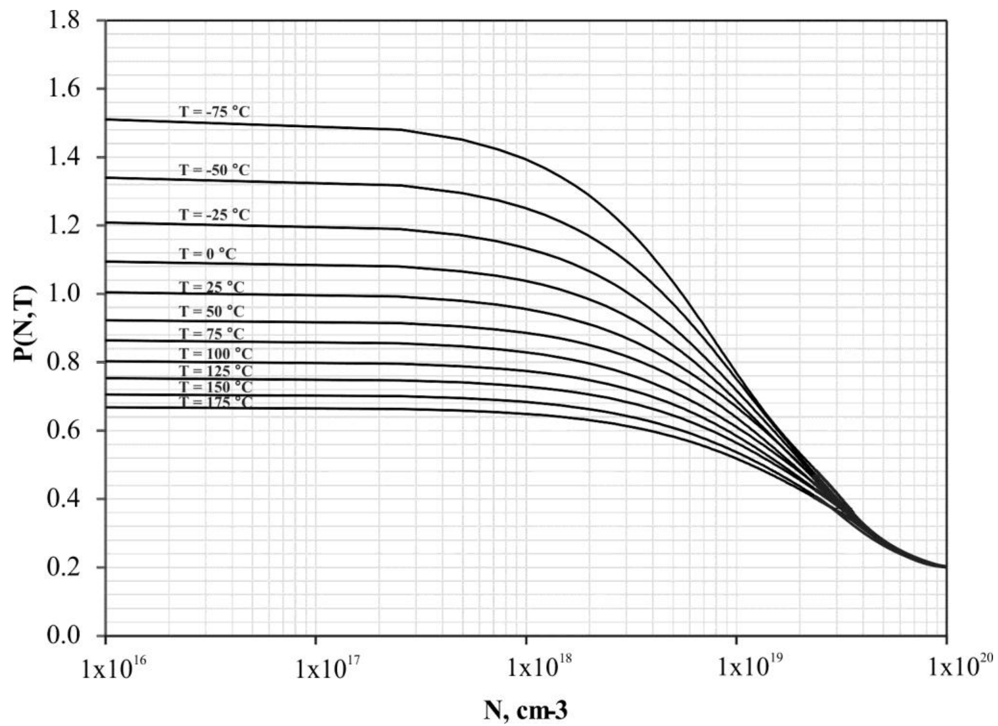

Figure 3-7 Piezoresistive factor *P(N,T)* as a function of impurity concentration and temperature for p-Si (re-plotted from [26]), Copyright © 1982 IEEE

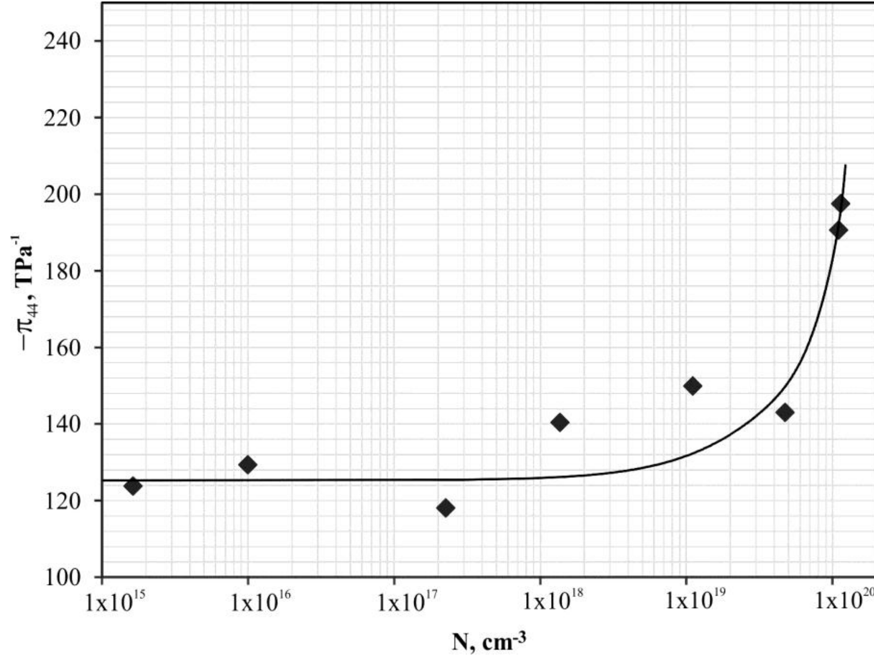

Figure 3-8 Measured variation of π_{44} with impurity concentration in phosphorus doped silicon at 300 K (modified from [23])

Kanda *et al*. provided an analytical model to describe this behavior of π_{44} with impurity concentration. The electron transfer theory can be used to describe correctly the behavior of π_{11} and π_{12} in n-Si. However, when used to describe the behavior of π_{44} it suggested a zero value for the coefficient [28, 29]. Therefore, they proposed using the theory of effective mass change to describe the behavior of π_{44} and it was found to satisfy the experimental results given by Tufte *et al*. [23]. They provided an analytical model to describe this behavior of the π_{44} coefficient with impurity concentration as follows.

$$\pi_{44} = \frac{-\beta m_l s_{44}}{1+2M} \tag{3-25}$$

Where,

s_{44} = compliance shear constant = $1.26\text{x}10^{-11}$ Pa^{-1}

β = $86.8 \pm 5.0/m$

m = electron mass

m_l/m = 0.9163

M = electron mobility anisotropy = 4.81 at low impurity concentration and decreases with concentration increase

Equation (3-25) shows that the shear piezoresistive coefficient π_{44} is independent of temperature change and varies proportionally with the increase in impurity concentration. Similar observance was reported by Nakamura *et al.*, who analytically modeled the n-Si piezoresistive behavior and discovered that π_{44} hardly depends on concentration over the range from 1×10^{18} to 1×10^{20} cm^{-3} [41]. Such realization is paramount in the design of the 10-element rosette.

3.3.2 Effect of the impurity concentration on the Temperature Coefficient of Resistance (TCR)

The linear TCR (α) is function of the resistivity of silicon for both n- and p-type silicon, as confirmed experimentally by Bullis *et al*. [37]. Since, resistivity of silicon is a function of impurity concentration, a direct relation between TCR and the impurity concentration can be reached, which was studied analytically by Norton *et al.* [38] for a range of temperatures from -50 °C to 125 °C and compared to the experimental work of Bullis *et al*. [37]. The curves for impurity concentration versus TCR for n- and p-Si for Gaussian profile diffused resistors are shown in Figure 3-9 at room temperature. Similar trends for TCR have been reported by other researchers [39, 119-121].

The impurity concentration-TCR relationship is shown to decrease with impurity concentration to a minimum value, then starts increasing slightly afterwards. For p-Si, the minimum TCR is around 600ppm/°C and is located at around a surface concentration of 2×10^{19} cm^{-3}. For n-Si, the minimum TCR is around 200ppm/°C at a surface concentration of 7×10^{18} cm^{-3}. This behavior of the TCR with impurity concentration (N) is another fundamental parameter for the operation of the 10-element rosette.

In summary, the difference in behavior of the piezoresistive coefficients and TCR with impurity concentration provides independent coefficients in equations (3-17) to (3-19). For example, for two sensing elements with different impurity concentrations (*a* and *b*), the coefficients are related as follows:

For p-Si,

$$\frac{B_1^a}{B_1^b} = \frac{B_2^a}{B_2^b} = \frac{B_3^a}{B_3^b} \neq \frac{\alpha^a}{\alpha^b} \tag{3-26}$$

And for n-Si,

$$\frac{B_1^a}{B_1^b} \neq \frac{B_2^a}{B_2^b} \neq \frac{B_3^a}{B_3^b} \neq \frac{\alpha^a}{\alpha^b} \tag{3-27}$$

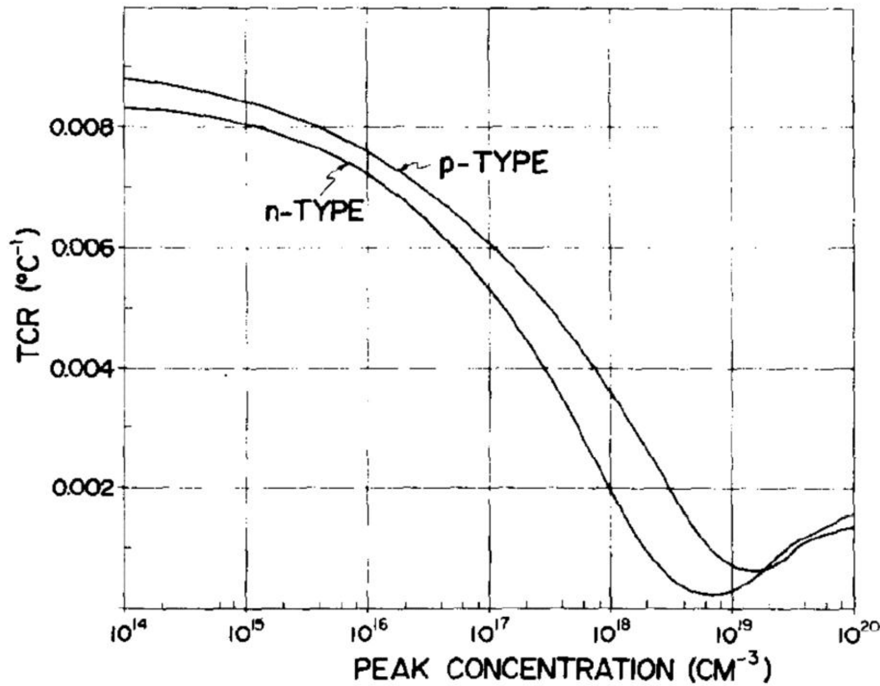

Figure 3-9: TCR as a function of the surface concentration in a diffused resistor for n- and p-type silicon at room temperature [38] Copyright © 1978, Elsevier

3.4 Dual and Single-Polarity Rosettes

The solution of (3-20) requires non-zero D_1 and D_2, which means that each of the three sets of equations (3-17)-(3-19) must be linearly independent. This is achieved in two ways; using a dual-polarity rosette or a single-polarity rosette designated as *dual-polarity* and *single-polarity* respectively as shown in Table 3-2.

The *dual-polarity* rosette has n-type group *a* elements, and p-type groups *b* and *c* elements but with a different impurity concentration designated as (1) and (2) in Table 3-2. This selection of the sensing elements offers different and independent coefficients as shown in the relations (3-26) and (3-27), thus independency of the equations in (3-17)-(3-19).

Table 3-2: Selected impurity types for each rosette

Rosette	Group *a*	Group *b*	Group *c*
dual-polarity	n-type	p-type (1)	p-type (2)
single-polarity	n-type (1)	n-type (2)	n-type (3)

The *single-polarity* rosette has n-type sensing elements for all three groups, but with different impurity concentration designated as (1), (2) and (3) in Table 1. This selection of the sensing elements is attributed to the unique piezoresistive properties of n-Si compared to p-Si discussed, where the shear piezoresistive coefficient π_{44} in n-Si is independent from the other two coefficients as presented in section 3.3. This creates groups *a*, *b*, and *c* with independent *B* and α coefficients as given in the relation (3-27), thus providing independent equations (3-17)-(3-19).

3.5 Temperature Effects

Piezoresistors are sensitive to temperature variation, which changes the mobility and number of carriers. These temperature variations affect the values of (1) the resistance of the sensing element by the temperature function [$f(T)=\alpha_1 T+\alpha_1 T^2+\ldots$], (2) the piezoresistive coefficients (π), and (3) the temperature coefficient of resistance, TCR (α). The reduction of these unwanted variations on the calculated stresses is addressed in this section.

The temperature function f(T) in piezoresistive sensors is usually eliminated by the addition of an unstressed resistor, which is used to subtract the temperature effect from the stress sensitivity equations. However, this approach would be

difficult to implement in applications that do not have an unstressed region in close proximity to the sensing rosette like in cases of embedded sensors. The other option, which is adopted in this study, is to use two resistors of the same impurity level and type to subtract the temperature effects. This method is implemented in equations (3-17) and (3-18), therefore, the stresses extracted from (3-17) and (3-18) are independent of temperature effect on resistance. On the other hand, f(T) is included in (3-19) in order to be evaluated and compensate for its effect in the remaining stress equations, i.e. σ'_{11}, σ'_{22}, and σ'_{33}.

Experimental studies on the effect of temperature and impurity concentrations on π were conducted by Tufte *et al*. [22] for a large range of temperatures and concentrations and compiled from the literature by Cho *et al*. [64]. It is noticeable that at high impurity concentrations, the effect of temperature on π is decreased, which is verified analytically by Kanda *et al*. [26]. Similarly, at high impurity levels the *TCR* value remains constant with temperature variations, thus giving a linear f(T) function. Cho *et al*. studied the effect of temperature on the *TCR* value on heavily doped n-type resistors from -180°C to 130°C. They concluded that a first order *TCR* is adequate to model the f(T) function at high impurity concentrations [113]. A similar conclusion is reached by Olszacki *et al*. for p-type silicon, where the quadratic terms in f(T) were found to approach zero at high impurity levels [120].

Based on the previous behavior of π and TCR, the impurity level of the proposed rosettes is selected to be at high concentrations to minimize the effect of temperature on both π and *TCR*. In order to better enhance the accuracy of the extracted stresses, calibration of π and *TCR* can be carried out over the operating temperature range of the rosette.

3.6 Analytical Verification

The analytical verification of the presented approach is based on evaluating D_1 and D_2 at different impurity concentrations for the three groups of sensing elements (*a*, *b*, and *c*) in order to study the behavior of D_1 and D_2 with concentration and their range of non-zero values. The analysis is based on the analytical values of π for n- and p-Si given by Kanda [26], the experimental values of π_{44} for n-Si given by Tufte *et al*. [23], and the experimental values of α for n- and p-Si given by Bullis *et al*. [37] for uniformly doped piezoresistors. A Matlab code was developed to solve for D_1 and D_2 given a combination of concentrations for groups *a*, *b*, and *c*. The analysis is carried out over a range of concentrations from $1\text{x}10^{18}$ to $1\text{x}10^{20}$ cm^{-3} to avoid the constant behavior of the piezoresistive coefficients at low impurity concentrations (as shown in Figure 3-6 and Figure 3-7) which will affect the linear independency of (3-17)-(3-19) and to minimize the effect of temperature on π and α. The analysis does not include impurity levels above $1\text{x}10^{20}$ due to the limited data available in the literature over this high concentration.

3.6.1 Behavior of D_1 and D_2

The evaluation of D_1 and D_2 at different concentrations for the *dual-polarity* and *single-polarity* rosettes are shown in Figure 3-10 through Figure 3-17, where N_a and N_b are the impurity concentrations of groups *a* and *b* respectively. The concentration of group *c* for both rosettes is set at $5\text{x}10^{18}$ cm^{-3}. Each coefficient is presented as both a surface plot and a contour plot for clarity purposes.

In the case of the *dual-polarity* rosette, D_1 has a maximum at the low impurity concentration ($1\text{x}10^{18}$ cm^{-3}) for both groups *a* and *b* of the analyzed range as shown in Figure 3-10 and Figure 3-11. On the other hand, D_2 is shown to have a maximum at (N_a, N_b) = ($1\text{x}10^{18}$ cm^{-3}, $1\text{x}10^{18}$ cm^{-3}) and ($1\text{x}10^{18}$ cm^{-3}, $1\text{x}10^{20}$ cm^{-3}) as shown in Figure 3-12 and Figure 3-13. It is noticed that $|D_1|$ is always positive because groups *a* and *b* have independent π and α. Contrarily, $|D_2|$ reaches a zero

value at two concentrations. The first is when group *b* has the same impurity concentration as group *c*, i.e. $5x10^{18}$ cm^{-3} and the second when group *b* has the same *TCR* value of group *c* at $1x10^{19}$ cm^{-3}.

For the *single-polarity* rosette, D_1 shown in Figure 3-14 and Figure 3-15 has a maximum at the boundaries of the range, i.e. at (N_a, N_b) = ($1x10^{18}$ cm^{-3}, $1x10^{20}$ cm^{-3}) and ($1x10^{20}$ cm^{-3}, $1x10^{18}$ cm^{-3}) and reaches zero when both groups *a* and *b* have the same impurity concentration. The zero value occurs when groups *a* and *b* have the same coefficients, thus giving dependent equations (3-17)-(3-18). On the other hand, as shown in Figure 3-16 and Figure 3-17, $|D_2|$ has two peaks at (N_a, N_b) = ($1x10^{20}$ cm^{-3}, $2x10^{19}$ cm^{-3}) and ($2x10^{19}$ cm^{-3}, $1x10^{20}$ cm^{-3}) and reaches zero when: (1) both groups *a* and *b* have the same concentration and (2) any of groups *a* or *b* has the same concentration as group *c* (i.e. $5x10^{18}$ cm^{-3}). These many zero valleys found in the D_2 of the *single-polarity* rosette requires more caution in the selection of the appropriate concentrations for groups *a*, *b*, and *c*. It is important to note that if a different concentration for group *c* is selected, the contour plots of D_2 will be different, but a non-zero solution can still be achieved.

It is clear that finding non-zero D_1 and D_2 is possible for both *dual-polarity* and *single-polarity* rosettes by selecting different impurity concentration for each group. The relatively large range of non-zero D_1 and D_2 facilitates the process of doping by allowing larger tolerance on the concentration of the doped sensing elements. This is important in cases where the accuracy and reproducibility of the doping process is low as in the case of diffusion as compared to ion implantation.

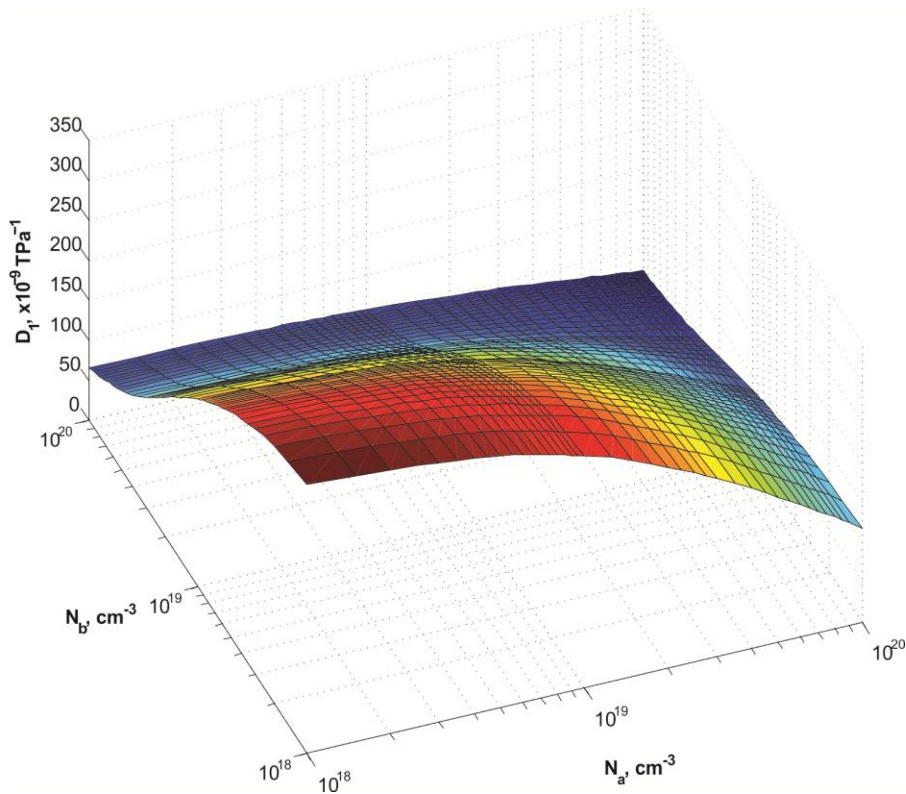

Figure 3-10 Surface plot of the effect of impurity concentration of groups *a* and *b* on $|D_1|$ for the *dual-polarity* rosette

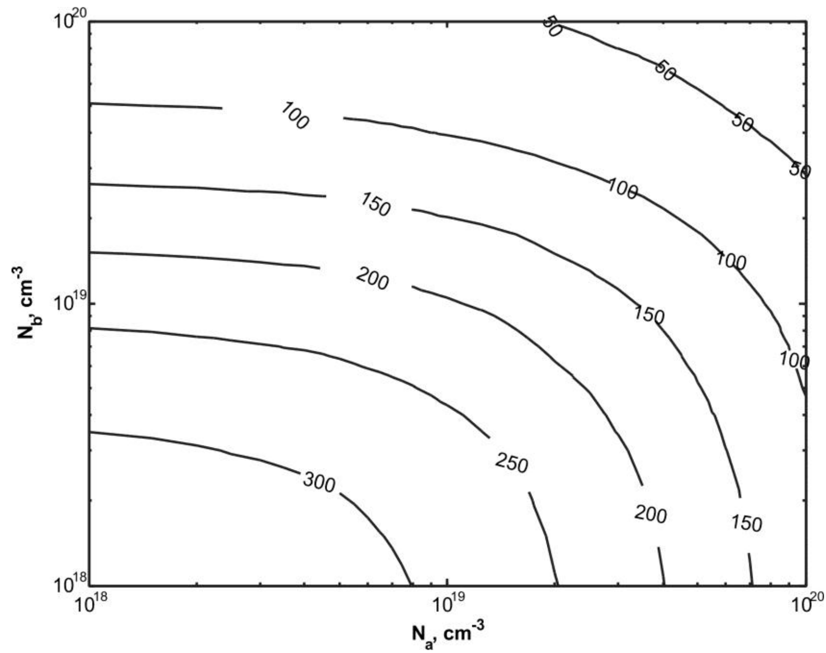

Figure 3-11 Contour plot of the effect of impurity concentration of groups *a* and *b* on $|D_1|$ for the *dual-polarity* rosette (values in 1x10^3 TPa^{-2})

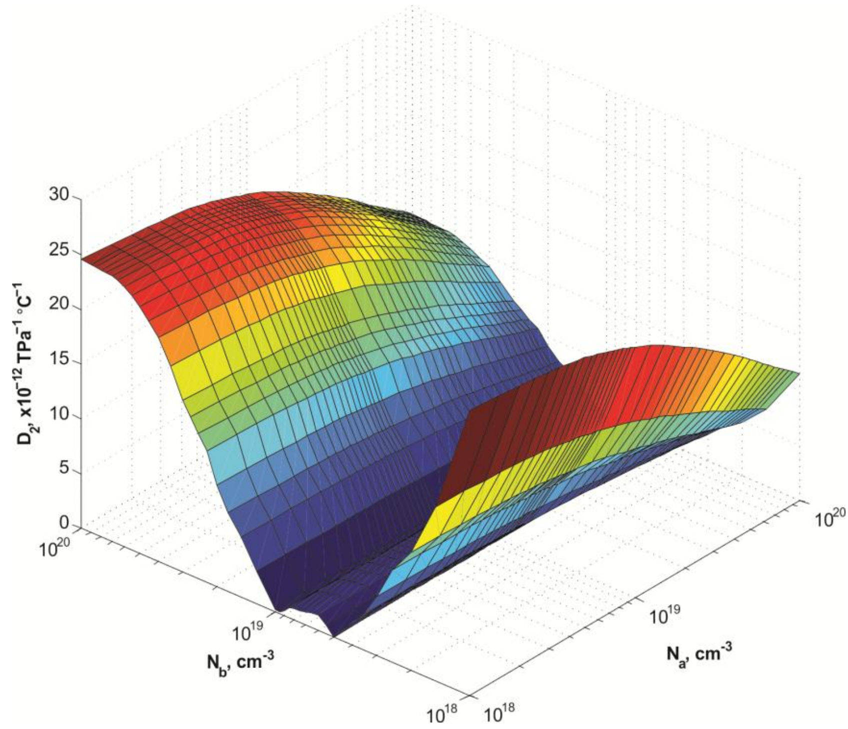

Figure 3-12 Surface plot of the effect of impurity concentration of groups *a* and *b* on $|D_2|$ for the *dual-polarity* rosette with impurity concentration of group *c* set at $5x10^{18}$ cm^{-3}

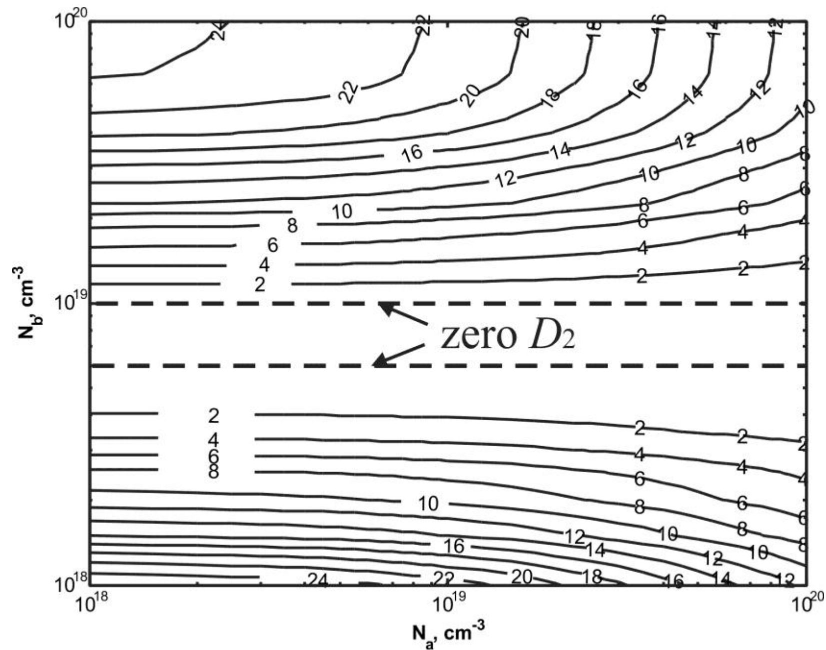

Figure 3-13 Contour plot of the effect of impurity concentration of groups *a* and *b* on $|D_2|$ for the *dual-polarity* rosette with impurity concentration of group *c* set at $5x10^{18}$ cm^{-3} (values in TPa^{-2} °C^{-1})

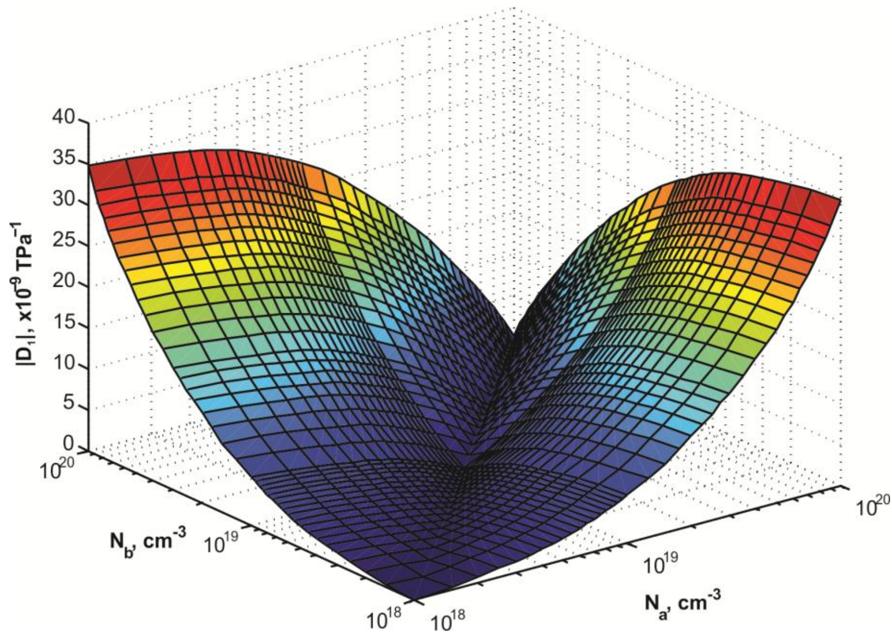

Figure 3-14 Surface plot of the effect of impurity concentration of groups *a* and *b* on $|D_1|$ for the *single-polarity* rosette

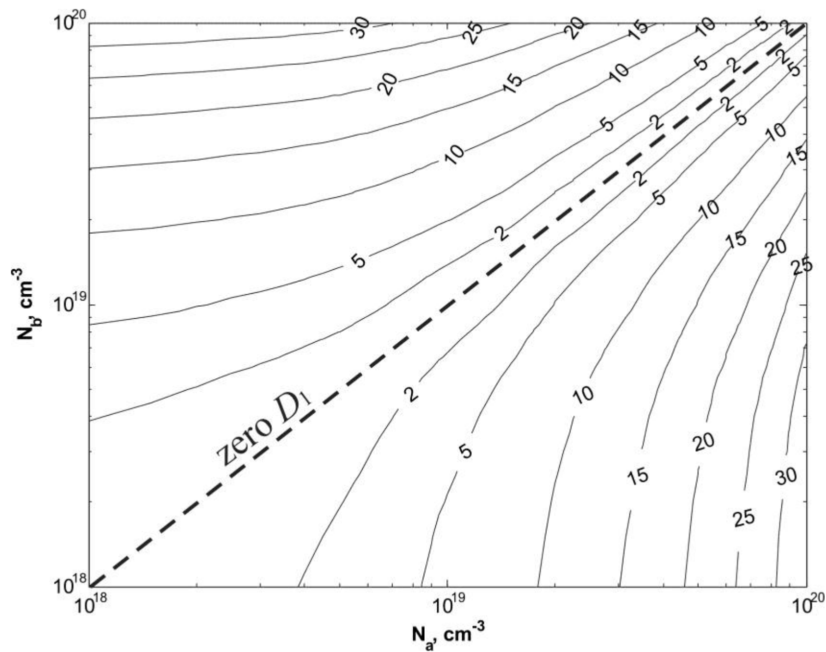

Figure 3-15 Contour plot of the effect of impurity concentration of groups *a* and *b* on $|D_1|$ for the *single-polarity* rosette (values in 1x10^3 TPa^{-2})

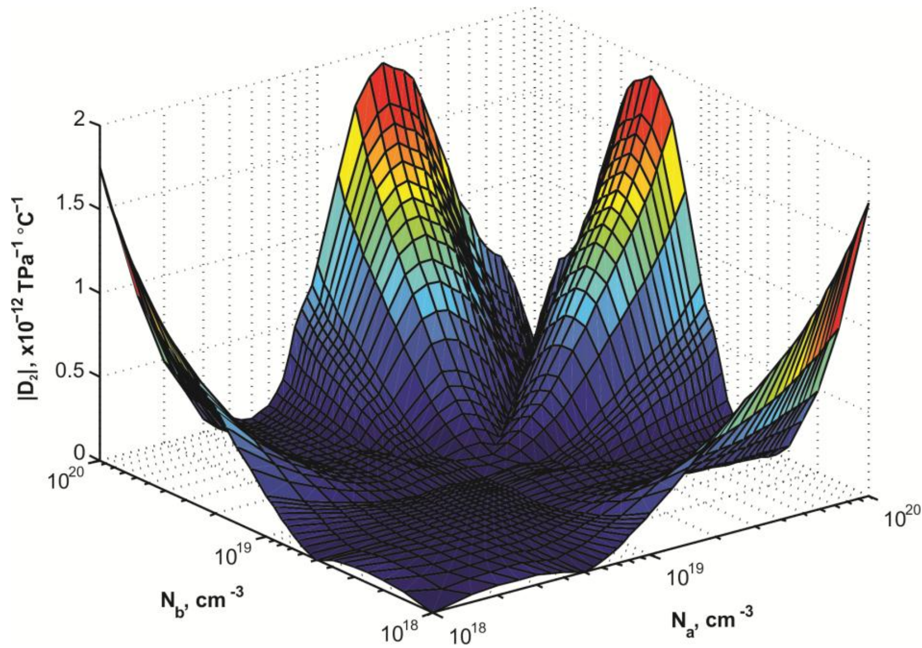

Figure 3-16 Surface plot of the effect of impurity concentration of groups *a* and *b* on $|D_2|$ for the *single-polarity* rosette with impurity concentration of group *c* set at $5x10^{18}$ cm^{-3}

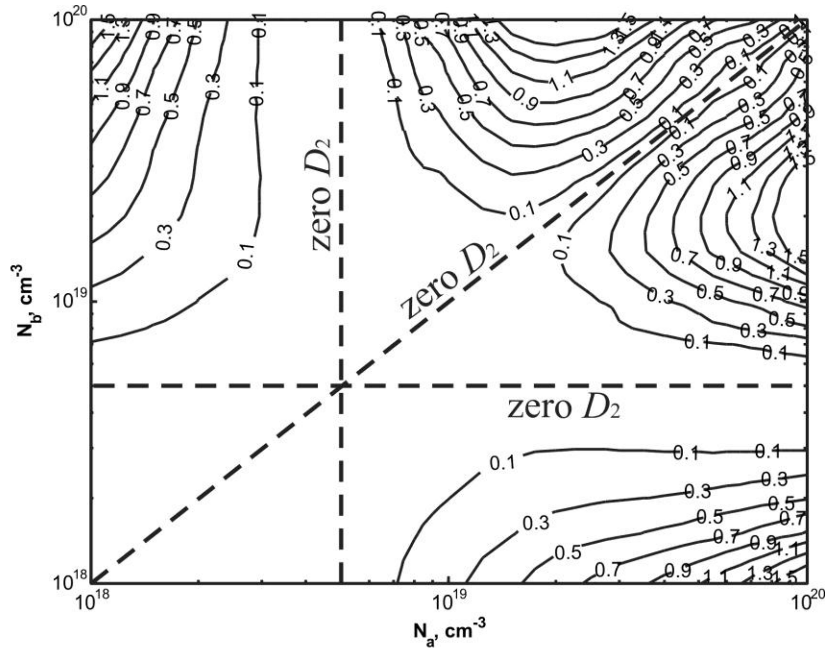

Figure 3-17 Contour plot of the effect of impurity concentration of groups *a* and *b* on $|D_2|$ for the *single-polarity* rosette with impurity concentration of group *c* set at $5x10^{18}$ cm^{-3} (values in TPa^{-2} $°C^{-1}$)

3.6.2 Behavior of B_i and TCR

The selection of the impurity concentrations of groups *a*, *b* and *c* is based primarily on finding non-zero D_1 and D_2. However, another condition is still important to analyze, which is maximizing *B* and α. These coefficients determine the sensitivity and output of the sensing elements for each of the seven components (six stress components and temperature). It is important to maximize the values of these coefficients to maximize the sensitivity and to avoid running into measurement errors during calibration. However, maximizing these coefficients means lowering the impurity concentration, which maximizes the variation of the piezoresistive coefficients and *TCR* due to temperature changes. Therefore, it is required to select the optimum impurity concentration that maximizes *B* and α, while minimizing the effect of temperature on the coefficients.

The B_i coefficients for n-Si in Figure 3-18 decrease with impurity concentration except for B_3, which shows an almost constant behavior with impurity concentration. This constant trend of B_3 is due to its primary dependence on π_{44}, which as noted earlier is independent of impurity concentration up to $1\text{x}10^{20}$ cm^{-3}. The relationship between π_{11} and π_{12} in n-Si is approximately given by $\pi_{12} \approx -1/2\pi_{11}$ as observed from their values in Table 3-1 and confirmed experimentally by Tufte *et al*. [23]. This when substituted in equation (3-13) shows that B_3 is dependent on π_{44}. On the other hand, the B_i coefficients for p-Si, shown in Figure 3-19, show a mutual decrease with the increase in impurity concentration due to the common factor, *P(N,T)*, relating the piezoresistive coefficients with impurity concentration.

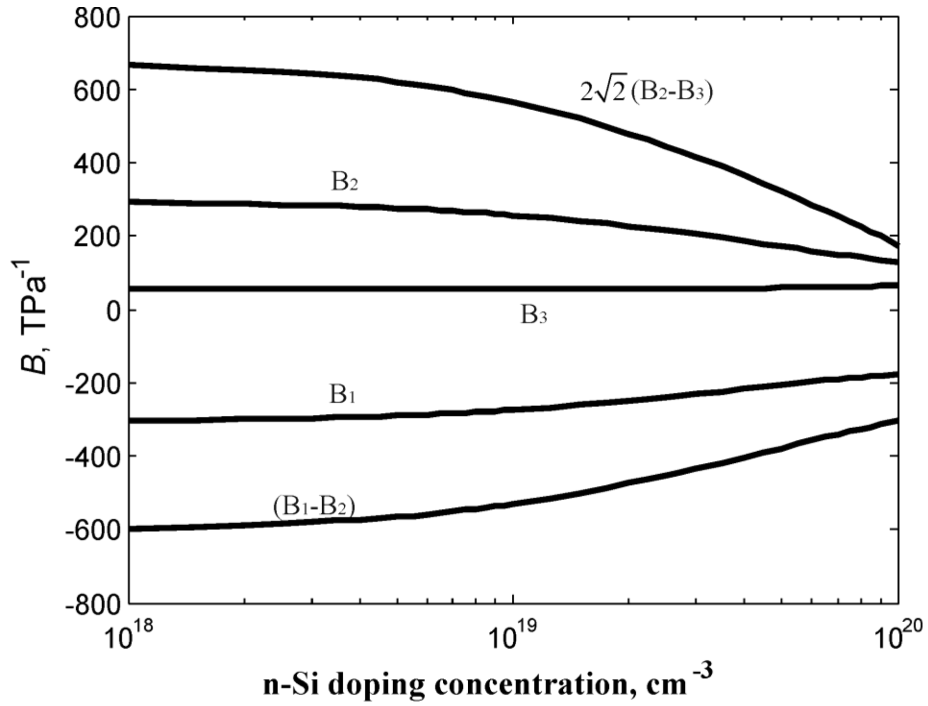

Figure 3-18 Effect of impurity concentration on B_i in n-Si

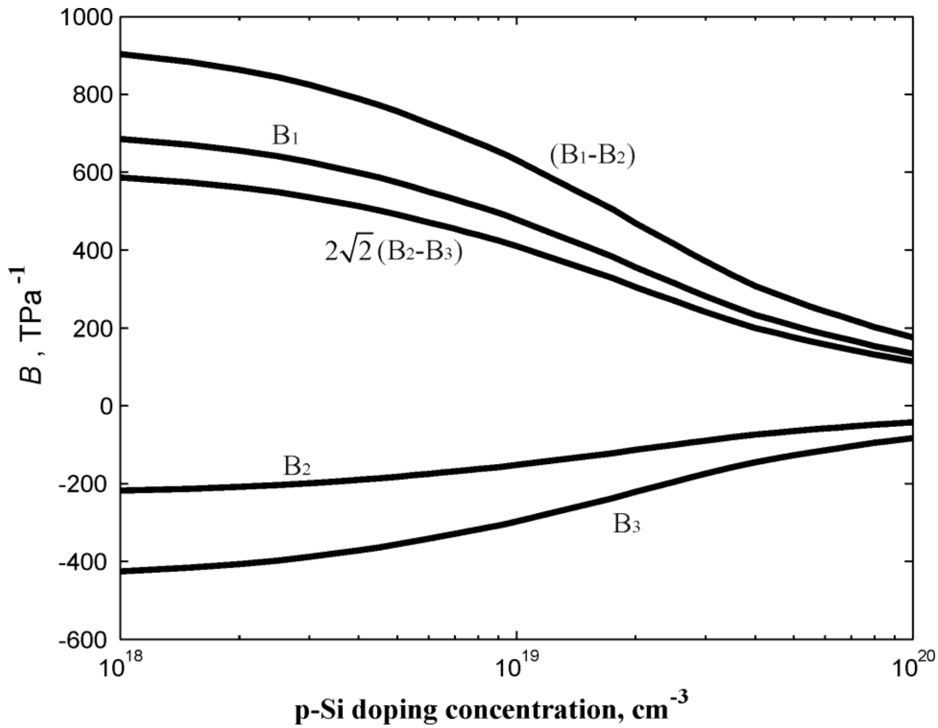

Figure 3-19 Effect of impurity concentration on B_i in p-Si

The *TCR* curves for p- and n-Si with impurity concentration are shown in Figure 3-20 as extracted from Figure 3-9 over the range from 1×10^{18} to 1×10^{20} cm^{-3}. It is noticed that TCR for n-Si is zero at around 1.5×10^{18} and 7×10^{18} cm^{-3}. Therefore, it is important to avoid those values in order to avoid measurement errors during calibration.

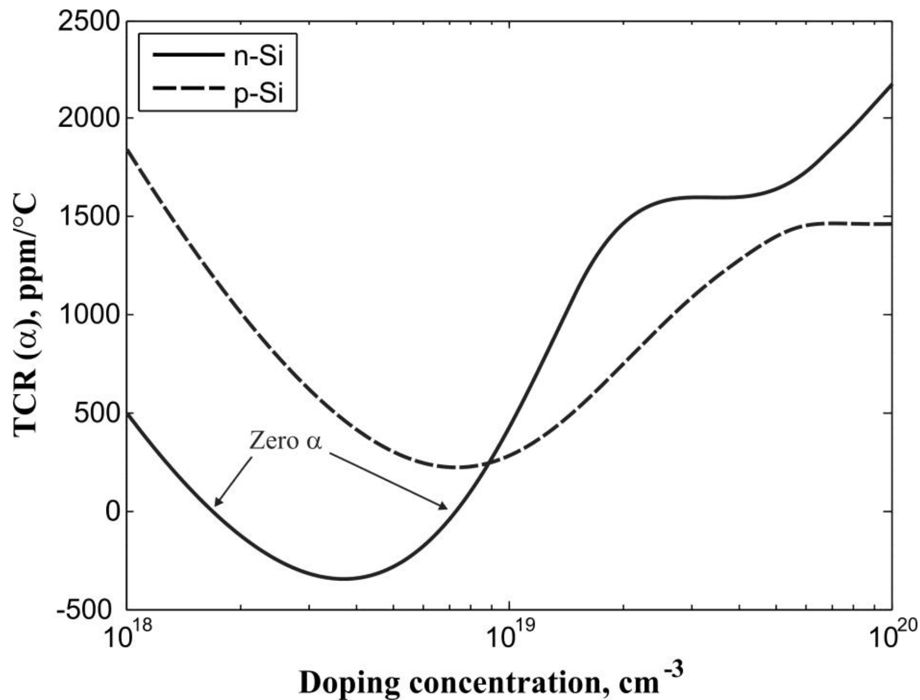

Figure 3-20 Effect of impurity concentration on TCR in n-Si and p-Si [23]

The present analysis is based on assuming uniform impurity concentration of the sensing elements. For actual sensor rosette fabricated using diffusion or ion implantation, the sensing elements will have non-uniform distribution of dopants across the thickness of the chip which follows either a Gaussian or complementary error function profile. This non-uniform impurity concentration of the sensing elements was not considered in the presented analysis due to the unavailability of enough experimental or analytical data for non-uniformly doped

piezoresistors. However, according to Kerr *et al.*, the surface dopant concentration could be used as an average effective concentration to model the piezoresistivity of diffused layers [35].

3.7 Conclusions

This chapter presented the theoretical background of the piezoresistive stress sensing rosette and application to the (111) silicon plane. The equations relating stresses with the resistance change in the new 10-element rosette are discussed to show the fundamental approach for the rosette operation. This was followed by a discussion of the piezoresistive properties that shape the operation of two types of the 10-element rosette; the *dual-polarity* and the *single-polarity*. An analytical study was performed to prove that non-zero determinants are achievable for the sets of linear equations for both types of rosettes.

CHAPTER 4: MICROFABRICATION OF THE SENSING CHIP[2]

4.1 Overview

The 10-element single-polarity rosette was prototyped using bulk microfabrication techniques. A number of microfabrication runs were conducted to prototype a silicon chip with the developed rosette. The early runs focused on devising the suitable fabrication recipe of the chip in the University of Alberta Micro and Nano-Fabrication Facility (nanoFab) and the MEMS/NEMS Advanced Design Laboratory (ADL). Once an acceptable fabrication approach was reached, two major microfabrication runs were used to support the feasibility of the current research. The first was a preliminary run for prototyping of a *proof-of-concept (POC) chip*, where the B_i and TCR coefficients of the rosette were calibrated to prove that non-zero determinants are achievable with the single-polarity rosette. On the other hand, the second run involved the fabrication of a final *test chip*, which was fully calibrated and tested for extraction of the six stress components. This chapter presents the microfabrication processes involved in the development of the two sensing chips. First, an account of the mathematical modeling of the two doping methods, diffusion and ion implantation, used in this research is presented. Then, the chip design, process flow, and characterization of each of the two fabricated chips are presented.

4.2 Silicon Doping

Doping of silicon is the introduction of a controlled amount of impurity dopants into silicon in order to change the electrical properties of the semiconductor. The two most widely used processes are diffusion and ion implantation. Both

[2] Some of the material in this chapter has been previously published by Gharib *et al*. [115, 122].

processes have been used in the present research to introduce phosphorus ions into boron-doped crystalline silicon. Diffusion was used in the fabrication of the *POC chip* as a cheap and accessible method of doping, while ion-implantation was used in the fabrication of the *test chip* to provide a more controlled and uniform impurity levels.

4.2.1 Diffusion

The diffusion process is a technique of introducing dopant atoms like phosphorus or boron into the silicon lattice. It is typically done by placing the silicon wafers in a quartz-tube furnace with controlled high temperature and passing a mixture of impurities and carrier gas on the wafer surface. The areas of silicon which need to be doped are exposed to the impurities source, while all other areas on the wafer surface is masked using a masking material like thermal silicon dioxide (SiO_2). The source of impurities can either be gas, liquid or solid sources. In our case, a phosphorus solid source (PhosPlus® TP-250) from TechneGlas Inc. was used.

The diffusion process was carried on in two steps; pre-deposition and drive-in steps. Pre-deposition introduces the phosphorus ions at high concentrations and temperatures (800 °C - 900 °C) to the surface of the silicon. The second step, dopants drive-in, is used to move the surface impurities to the desired depth at high temperature.

The diffusion process creates a profile of impurity concentration within the thickness of the doped area. The basic modeling of the diffusion profile is based on a one-dimensional diffusion process that follows Fick's first law of diffusion [123]:

$$J = -D\frac{\partial N\left(x,t\right)}{\partial x} \tag{4-1}$$

Where, J is the particle flux of the impurity species, D is the diffusion coefficient, N is the concentration of the impurity, and x is the distance from the silicon surface. The continuity equation for the particle flux states that the rate of increase

of concentration with time is equal to the negative of the divergence of the particle flux [123]:

$$\frac{\partial N(x,t)}{\partial t} = -\frac{\partial J}{\partial x} \tag{4-2}$$

Then, combining equations (4-1) and (4-2), the expression for Fick's second law is given by:

$$\frac{\partial N(x,t)}{\partial t} = D\frac{\partial^2 N(x,t)}{\partial x^2} \tag{4-3}$$

Equation (4-3) assumes that the diffusion coefficient D is constant and independent of position. This assumption is valid as long as the impurity concentration is lower than the intrinsic-carrier concentration at the diffusion temperature. Above this concentration, the diffusion coefficient D is concentration dependent. The intrinsic-carrier concentration of relatively low doped silicon ranges between 3×10^{18} cm^{-3} and 1.3×10^{19} cm^{-3} over the temperature range from 820 °C to 1050 °C, respectively [124]. In the current research, the final targeted impurity concentrations are in the 1×10^{19} cm^{-3} to 2×10^{20} cm^{-3} ranges with diffusion temperatures from 820 °C to 1050 °C. Therefore, it is expected that the diffusion coefficient will vary over the impurity concentration profile. However, for the sake of simplicity and since accurate modeling of the diffusion profile is outside the scope of this work, the diffusion coefficient is assumed to be constant. Moreover, the objective of the diffusion modeling conducted in this research is to provide an approximate guidance to select the diffusion parameters.

The solution of the differential equation (4-3) requires the knowledge of at least two boundary conditions. There are two sets of boundary conditions that solve this equation to determine the diffusion profile; the constant source diffusion and the limited source diffusion.

4.2.1.1 Constant source diffusion

The constant source diffusion refers to the pre-deposition stage which introduces a high concentration of dopants to the silicon. Pre-deposition assumes the presence of a constant source of dopants and the dopants distribution in the silicon material follows a complementary error function (erfc) [123] as follows:

$$N(x,t) = N_0 erfc\left(\frac{x}{2\sqrt{(Dt)_{tot}^{p}}}\right) \tag{4-4}$$

In which, *N(x,t)* is the distribution of the impurity, N_0 is the impurity concentration at the wafer surface (x=0), which is independent of time and equals to the solid solubility limit for the dopants at the process temperature, and $(Dt)_{tot}^{p}$ is the product of the diffusion coefficient and time and is given as:

$$(Dt)_{tot}^{p} = \sum_i (Dt)_i^p \tag{4-5}$$

And

$$(Dt)_i^p = D_0 t_i^p \exp\left(\frac{-E_A}{kT_i^p}\right) \tag{4-6}$$

Where,

D_0 = diffusion constant = 10.5 cm^2/sec (phosphorus dopant)

E_A = Arrhenius activation energy = 3.69 eV (phosphorus dopant)

k = Boltzman constant = 8.62x10^{-5} eV/K

t_i^p and T_i^p = time and temperature for the pre-deposition process i if more than one pre-deposition steps are implemented.

The profile of the constant source diffusion is shown in Figure 4-1, where the increasing *Dt* product increases the depth of the profile at the same surface

concentration N_0. The total number of impurity atoms per unit area, known as the dose, is given by:

$$Q = \int_0^\infty N(x,t)dx = 2N_0\sqrt{\frac{(Dt)_{tot}^p}{\pi}} \tag{4-7}$$

Then, the junction depth X_j^p of the impurity profile is calculated from equation (4-4) when $N(x,t)$ equals the background doping (N_B) of the wafer:

$$X_j^p = 2\sqrt{(Dt)_{tot}^p}\, erf^{-1}\left(1 - \frac{N_B}{N_0}\right) \tag{4-8}$$

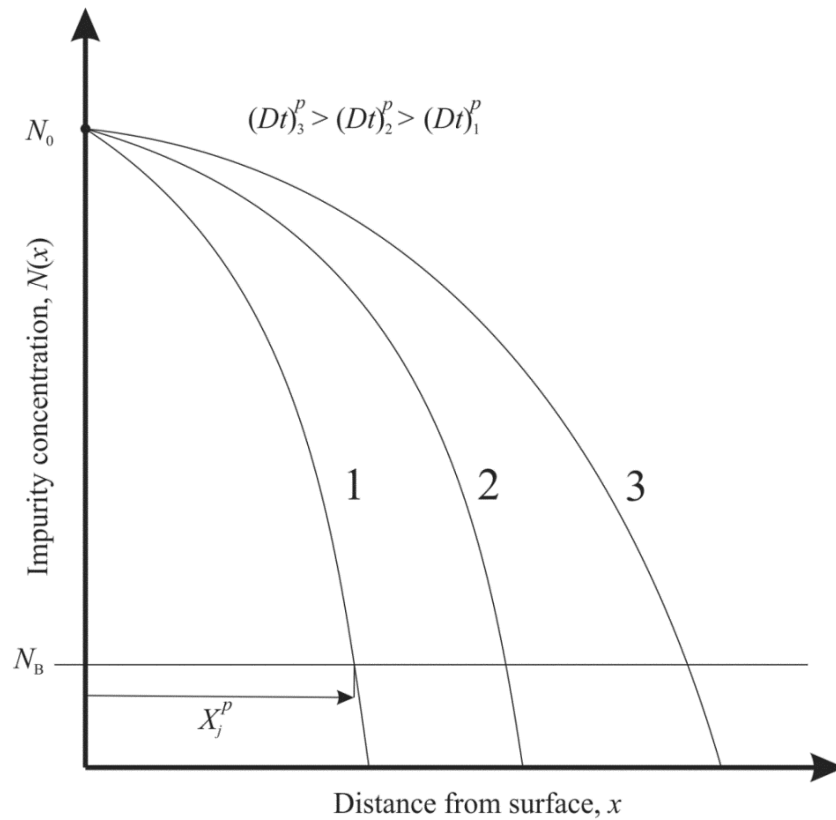

Figure 4-1 Constant source diffusion profile with different *Dt* product

4.2.1.2 Limited Source Diffusion

The second boundary condition based on limited source diffusion refers to the drive-in diffusion stage. In this stage, the doping source is not present, thus only the pre-deposited impurities are allowed to diffuse. The impurity concentration is given as a Gaussian distribution function [123] as follows:

$$N(x,t) = \frac{Q}{\sqrt{\pi (Dt)_{tot}^{d}}} \exp\left(\frac{-x^2}{4\left(Dt\right)_{tot}^{d}} \right) \tag{4-9}$$

In which, Q is the dose calculated from the pre-deposition step from equation (4-7), and $\left(Dt\right)_{tot}^{d}$ is the product of the diffusion coefficient and time for the drive-in step. This product can include the effects of all subsequent high temperature processes like thermal oxidation. The profile of the limited source diffusion is shown in Figure 4-2 for three cases of different $\left(Dt\right)_{tot}^{d}$ product, where the junction depth increases and the surface concentration decreases for a higher drive-in time and temperature.

Considering only one drive-in step, the $\left(Dt\right)_{tot}^{d}$ product is given by:

$$\left(Dt\right)_{tot}^{d} = D_0 t^d \exp\left(\frac{-E_A}{kT^d} \right) \tag{4-10}$$

Where, t^d and T^d are the time and temperature of the drive-in step, respectively. The junction depth is calculated from equation (4-9) at $N(x,t) = N_B$:

$$X_j^d = \sqrt{-4\left(Dt\right)_{tot}^{d} \ln\left(\frac{N_B \sqrt{\pi \left(Dt\right)_{tot}^{d}}}{Q} \right)} \tag{4-11}$$

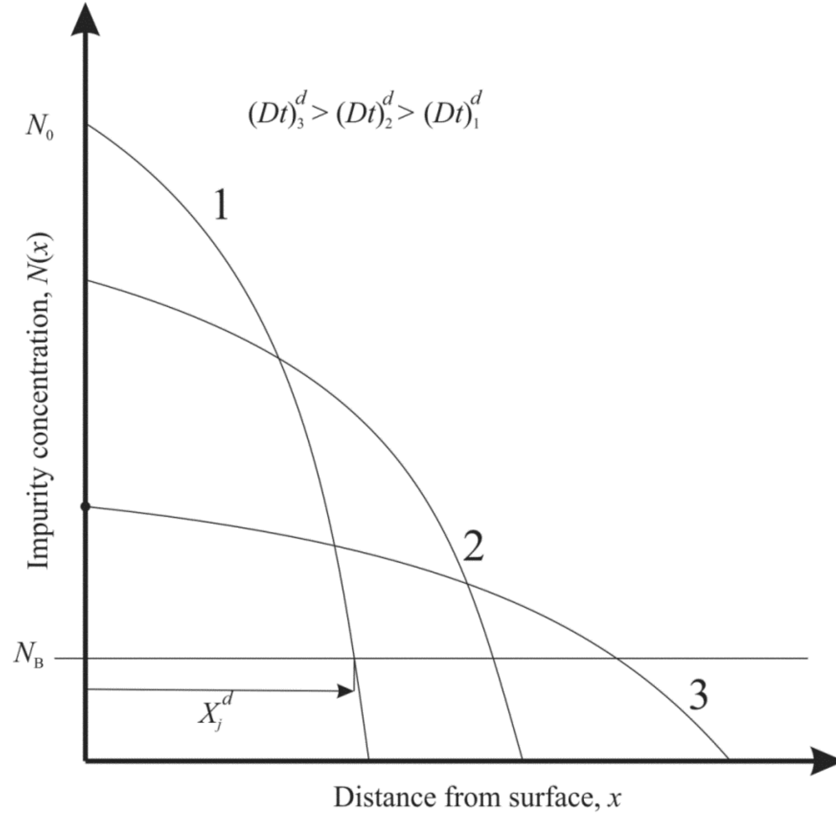

Figure 4-2 A Gaussian distribution for a limited-source diffusion

The resulting sheet resistance is calculated as [125]:

$$R_s = \frac{1}{\int_0^{x_j} q\mu(x)N(x)dx} \tag{4-12}$$

In which, x_j is the metallurgical junction depth, q is the charge of an electron, and $\mu(x)$ is the majority-carrier mobility given by:

$$\mu(x) = \mu_{\min} + \frac{\mu_{\max} - \mu_{\min}}{\left[1 + \left(N(x)/N_{ref}\right)^{\kappa}\right]} \tag{4-13}$$

Where the values of the fit parameters are $\mu_{\min}$ = 68.5 cm^2/Vs, $\mu_{\max}$ = 1414 cm^2/Vs, N_{ref} = 9.2x10^{16} cm^{-3}, and κ = 0.711. Equation (4-12) is valid for the pre-

deposition and drive-in steps and also for the ion implantation profile, which will be presented in section 4.2.2.

4.2.1.3 Three Stages Pre-deposition

The three groups of sensing elements of the single-polarity rosette are at different surface concentrations to guarantee different and independent piezoresistive coefficients. One approach to fabricate three concentration resistors is to use three steps of pre-deposition, where at each step a thermal oxide layer is grown before the pre-deposition process to act as a masking layer and etched after the doping step. This will require three steps of thermal oxidation. Another approach, which is adopted in this research, is to use three pre-deposition steps using the same masking thermal oxide layer. In this case, the first pre-deposition step will dope group *a* resistors, the second pre-deposition step will dope groups *a* and *b* resistors and the third pre-deposition step will dope groups *a*, *b*, and *c* resistors as shown in the process flow in Figure 4-3. In each pre-deposition step, a preceding optical photolithography step is carried out to pattern a photoresist layer to etch the diffusion windows through the thermal oxide layer. The three pre-deposition steps are succeeded with a drive-in process.

The final profiles of the doped resistors can be predicted based on the diffusion equations described in section 4.2.1.1 and section 4.2.1.2. In this case, the Dt value is calculated for each pre-deposition step, where the final $(Dt)_{tot}^{p}$ for each group is:

Group *a*: $(Dt)_{tot}^{p} = (Dt)_{1}^{p} + (Dt)_{2}^{p} + (Dt)_{3}^{p}$

Group *b*: $(Dt)_{tot}^{p} = (Dt)_{2}^{p} + (Dt)_{3}^{p}$

Group *c*: $(Dt)_{tot}^{p} = (Dt)_{3}^{p}$

In which subscripts 1, 2, and 3 designate the first, second, and third pre-deposition step, respectively. A solution of the concentrations profiles and sheet resistances using the analytical equations for the specific diffusion process conducted to

develop the *POC chip* is presented in section 4.3. Also, the resulting experimental characterization data is used to compare to the analytical solution.

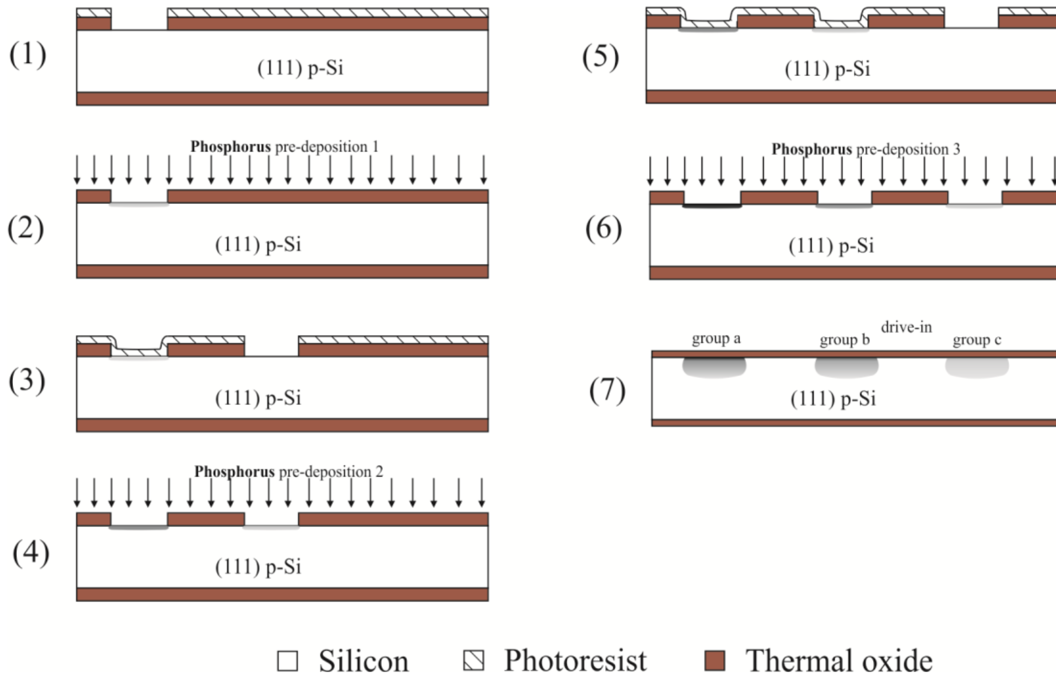

Figure 4-3 Process flow of the three-stage pre-deposition

4.2.2 Ion Implantation

Ion implantation today is the most common doping method of semiconductors. It is the process where accelerated ions are bombarded onto the substrate surface to penetrate the semiconductor and come to rest due to collisions with the electrons and nuclei in the substrate within femtoseconds. An ion beam is used to accelerate implantation ions at energies between 1 keV and 1 MeV, resulting in ion distributions with average depth of 10 nm to 10 μm. The amount of ions bombarded is expressed as ion doses which vary from 10^{12} ions/cm^2 to 10^{18} ions/cm^2. The ion implantation process is usually divided into an implantation step followed by a high temperature annealing step to regain the crystal structure and drive-in the dopants. The main advantages of ion implantation over diffusion

are its more precise control and reproducibility of impurity ions and its lower processing temperature.

The following equations present the basic equations of modeling the phosphorus concentration profiles and sheet resistance for the ion implantation and annealing processes. The implanted impurity profile is approximated by a Gaussian distribution profile [81]:

$$N(x) = N_p \exp\left[\frac{-\left(x - R_p\right)^2}{2\Delta R_p^2}\right] \tag{4-14}$$

Where, x is the distance along the axis of incidence and R_p and ΔR_p are the projected range of incident ions and the straggle or spread of distribution, respectively, which are dependent on the implantation energy in keV. Values R_p and ΔR_p are available in the literature for a range of ion acceleration energies [123]. Finally, N_p is the peak concentration at $x = R_p$ and is given by (for an implant completely contained with the silicon):

$$N_p = \frac{Q}{\sqrt{2\pi}\Delta R_p} \tag{4-15}$$

Where, Q is the ion dose and is given in cm^{-2}. The Gaussian distribution from the ion implantation is shown in Figure 4-4 for a profile completely below the wafer surface. The junction depth after ion-implantation is calculated by equating the impurity concentration in equation (4-14) by the background doping. Therefore, the junction depth equals:

$$X_j^p = R_p \pm \Delta R_p \sqrt{2 \ln\left(\frac{N_p}{N_B}\right)} \tag{4-16}$$

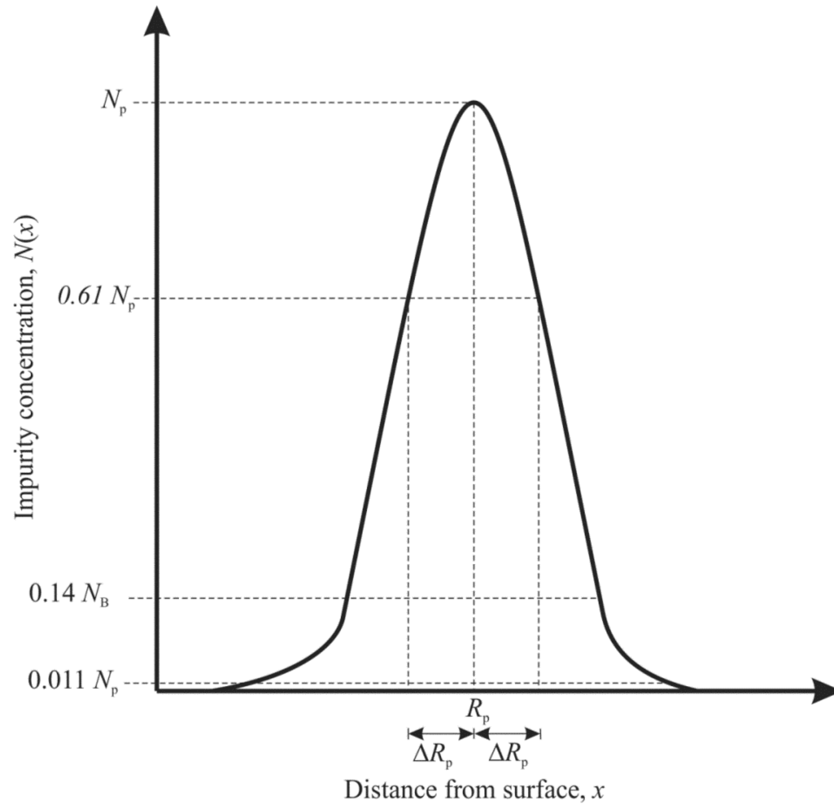

Figure 4-4 Gaussian distribution for an ion implantation process (modified from [123])

The two roots in equation (4-16) indicate that two junctions can occur at two different depths. This is possible for deep subsurface implants as shown in Figure 4-4. An additional drive-in step for time t and diffusion coefficient D creates a concentration profile given by:

$$N(x) = \frac{Q}{\sqrt{2\pi\left(\Delta R_p^2 + 2Dt\right)}} \exp\left[\frac{-\left(x - R_p\right)^2}{2\left(\Delta R_p^2 + 2Dt\right)}\right] \tag{4-17}$$

The junction depth is calculated by equating the impurity concentration in equation (4-17) with the background doping:

$$X_j^d = R_p \pm \sqrt{-2\left(\Delta R_p^2 + 2Dt\right)\ln\left(\frac{N_B}{N_P}\frac{\sqrt{\Delta R_p^2 + 2Dt}}{\Delta R_p}\right)} \tag{4-18}$$

The sheet resistance for the concentration profile is calculated using equation (4-12). The above equations were used to predict the resulting impurity profiles for the three groups of the sensing elements in the *test chip* and were compared to the experimental results as discussed in section 4.4.

4.3 Microfabrication of the Proof-of-Concept (POC) Chip

4.3.1 Chip Design

The layout of the *POC chip* measuring 7 mm x 7 mm x 0.525 mm is shown in Figure 4-5. The chip had 6 typical 10-element rosettes, each measuring 1 mm x 1 mm, located in the center with their contact pads oriented along two edges of the chip. These multi-rosettes were developed to maximize the yield of the available sensing elements for calibration. The piezoresistors were designed in a serpentine shape to increase the total resistance value. The width of an axial section of the piezoresistor was 7, 9, and 15 μm for groups *a*, *b*, and *c* sensing elements, respectively. This difference in width was used to control the final resistance of all sensing elements. The number of turns were 9, 7, and 5 for groups *a*, *b*, and *c* sensing elements, respectively with an average total resistor dimensions of 200 μm x 110 μm. Contact pads measured 350 μm x 350 μm with spacing of 170 μm. Test structures on the chip including cross-bridges and kelvin crosses were used for measurement of resistivity and contact resistance, respectively. There were other test structures on the wafer for measurement of contact resistance using the transfer line method (TLM), which will be discussed later in this chapter. Large open windows measuring 7 mm x 2 mm were used for characterization of the phosphorus doping through measurement of the sheet resistance using a four-point probe and characterization of the doping profile using Secondary Ion Mass Spectrometry (SIMS).

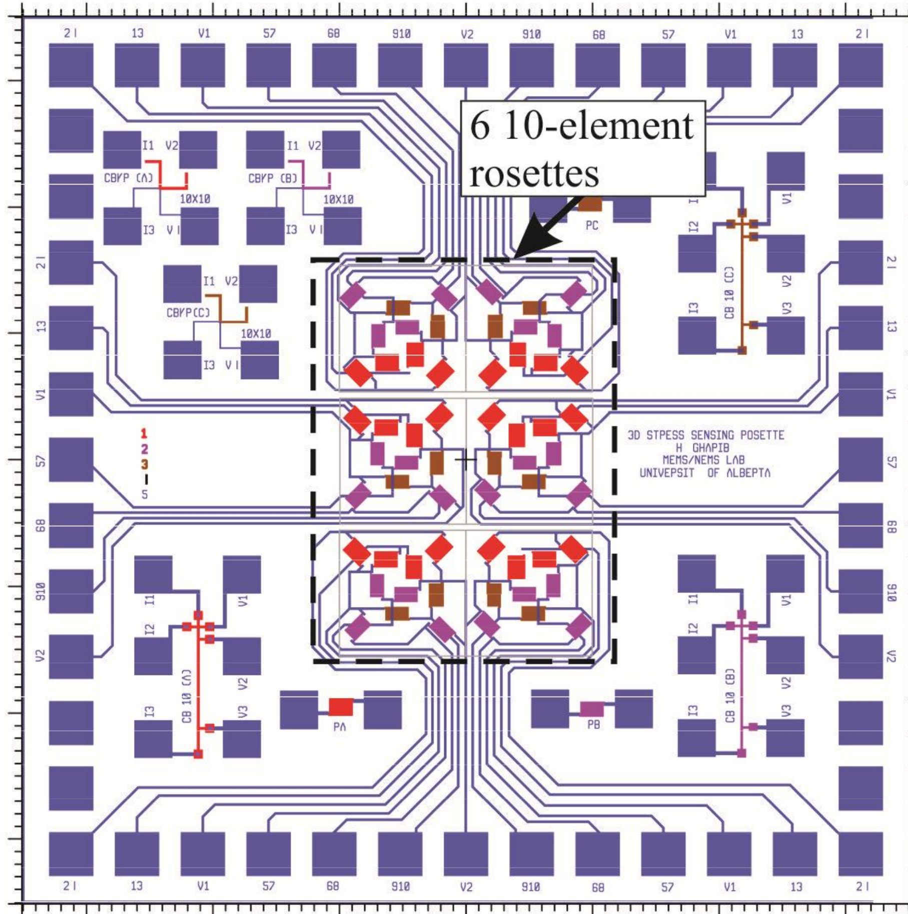

Figure 4-5 Layout of the *POC chip*

4.3.2 Process flow

The process flow developed to fabricate the *POC chip* is shown in Figure 4-6. All processes were conducted in the nanoFab except for diffusion, which was conducted in the MEMS/NEMS ADL. This process included 5 masks; three for the *a*, *b*, and *c* groups of sensing elements, one for the contact vias, and one for the patterning of the metal layer.

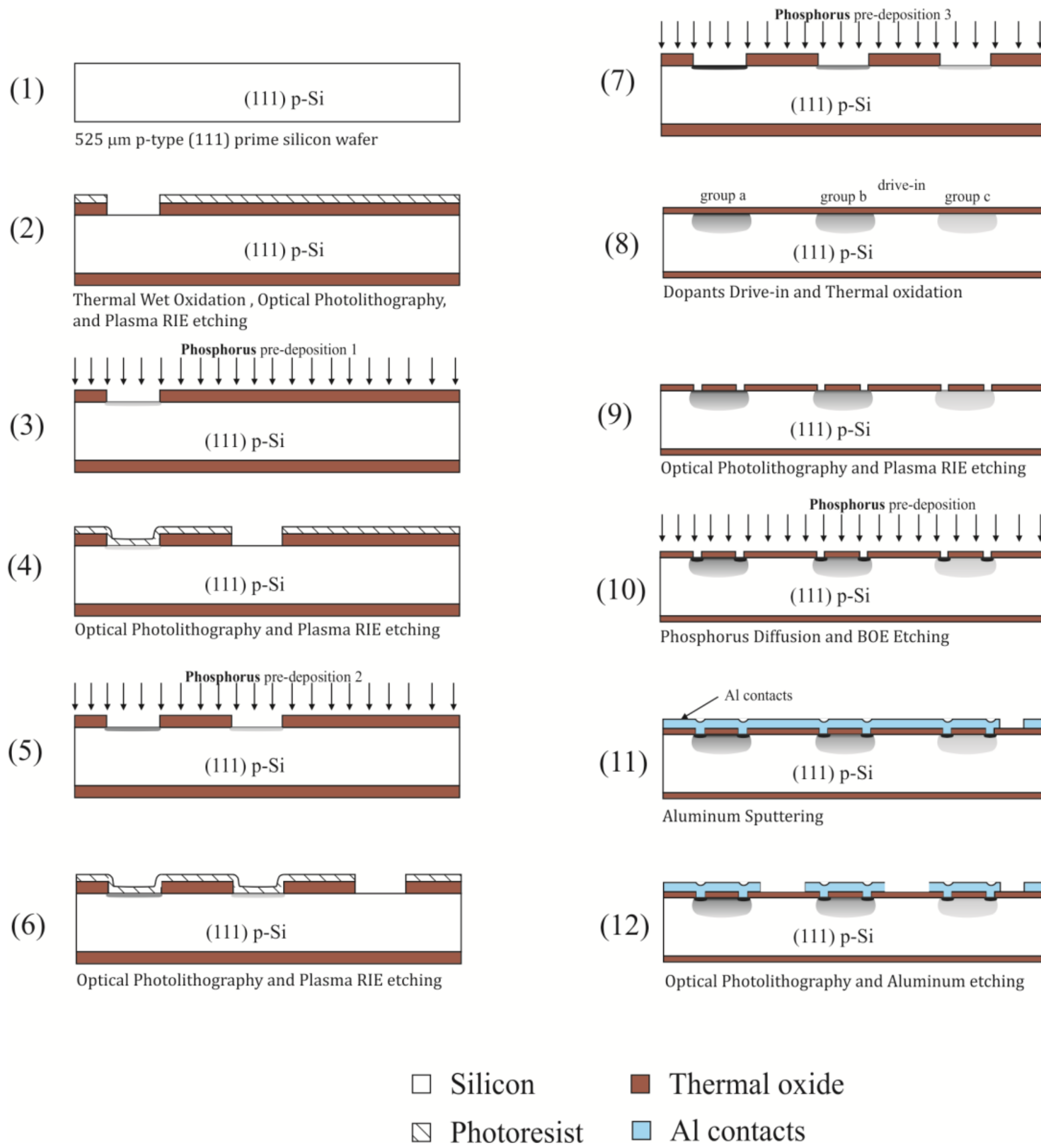

Figure 4-6 Microfabrication process flow of the proof-of-concept chip

The following are the details of the process, where each paragraph number describes the corresponding stage in Figure 4-6:

1. The initial starting material was a p-type (111) single-sided polished prime silicon wafer with a diameter and thickness of 100 mm and 525±25 μm, respectively. The wafer is boron doped with bulk resistivity of 7 Ω-cm, which corresponds to a background impurity concentration of 2 x 10^{15} cm^{-3}. The

wafer was initially cleaned using piranha cleaning (3 H_2SO_4: 1 H_2O_2) followed by buffered oxide etch (BOE) to remove traces of native oxide.

2. This step prepared the wafer for the first doping level to create the group *a* piezoresistors:
   a. A thermal silicon dioxide (SiO_2) layer was grown using wet thermal oxidation process. The wafer was placed in a tube furnace at 1000 °C for 2 hours with wet vapor inlet from a bubbler set at 95 °C and a nitrogen carrier gas at 5 liter/min flow rate. The final oxide thickness is around 650 nm.
   b. This was followed by an optical photolithography to open windows for doping of group *a* piezoresistors. First, the wafer was placed in an oven that deposits a layer of Hexamethyldisilazane (HMDS) to enhance the photoresist adhesion to the oxide layer. The use of HMDS is primarily essential with features that are close to 1 μm. A photoresist layer (HPR 504) was spread for 10 seconds at 500 rpm and spun for 40 seconds at 4000 rpm on the device side of the wafer. This was followed by soft baking at 115 °C for 90 seconds and leaving the wafer to cool and re-hydrate for 15 mins before exposure. The soft baking process removes some of the water content in the photoresist layer, which is essential for proper development. The first mask was used to expose ultraviolet (UV) light on the photoresist using an exposure energy of 195 mJ/cm^2. The wafer with the exposed photoresist was gently agitated in a MICROPOSIT 354 developer (an aqueous alkaline solution) for 25 seconds and then sprayed with deionized (DI) water and dried with nitrogen. The final photoresist layer was measured using an Alpha Step IQ surface profiler to be around 1.2 μm.
   c. Oxide etching to open diffusion windows for group *a* piezoresistors was performed using an STS machine utilizing Reactive Ion Etching (RIE). The etch rate for the 650 nm thermal oxide layer was 4 nm/s.

   d. The photoresist was stripped by rinsing the wafer in an acetone sonic bath for 15 mins followed by Isopropyl Alcohol (IPA) cleaning and DI water rinse and dry.

3. The wafer was placed on a quartz boat in a diffusion tube furnace utilizing solid doping sources for phosphorus pre-deposition. The solid sources are PhosPlus® TP-250 from TechneGlas Inc., which contains Phosphorus PentaOxide (P_2O_5) combined with Lanthanum Oxide (La_2O_3) that evolves the P_2O_5 when the sources are heated to the diffusion temperature. The furnace was heated to 845 °C for 60 mins with ramping up and down at 7 °C/min from an initial standby temperature of 700 °C. The diffusion furnace used in this study is shown in Figure 4-7.

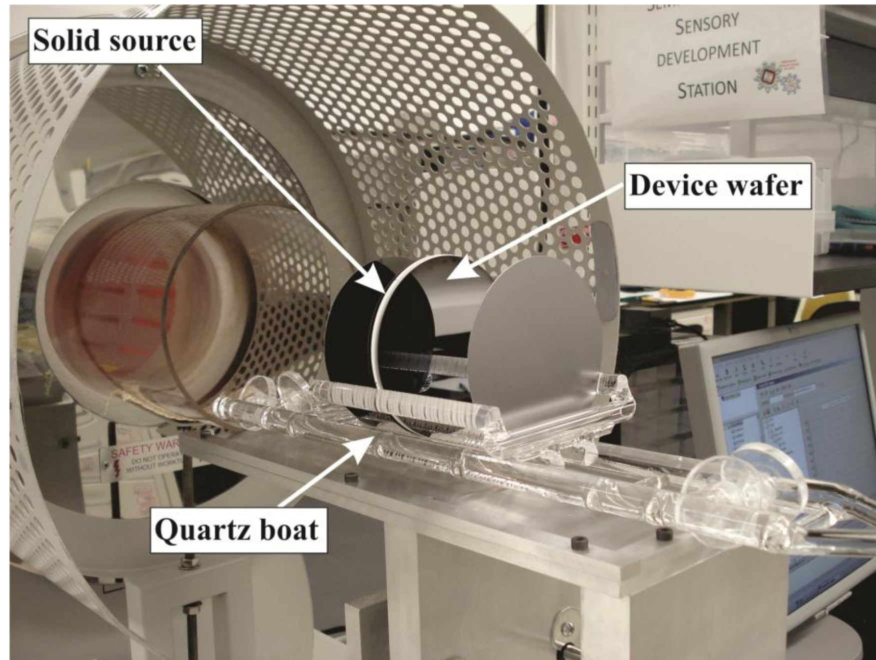

Figure 4-7 Phosphorus diffusion furnace

4. The wafer was cleaned using acetone and IPA followed by photolithography to prepare the second diffusion windows for group *b* piezoresistors. The same photolithography process in step 2.b was conducted, but an alignment process was used to align the second mask to the previous features on the wafer. Also, the same oxide etching procedure in step 2.c was used to open diffusion windows for group *b* piezoresistors.

5. The wafer was placed in the diffusion furnace at 830 °C for 75 mins using the same solid sources and procedure described in step 3. This step dopes both groups *a* and group *b*, where group *a* is getting a second dose of dopants, while group *b* is getting its first dose of dopants.
6. The wafer was cleaned using acetone and IPA followed by photolithography to prepare the third diffusion windows for group *c* piezoresistors. The same photolithography process in step 2.b was conducted, but an alignment process was used to align the third mask to the previous features on the wafer. Also, the same oxide etching procedure in step 2.c was used to open diffusion windows for group *c* piezoresistors.
7. The wafer was placed in the diffusion furnace at 820 °C for 105 mins using the same solid sources and procedure described in step 3. This step dopes the three groups, where group *a* is getting a third dose of dopants, group *b* is getting a second dose of dopants, and group *c* is getting its first dose of dopants.
8. Once the 3 pre-deposition steps are finished, drive-in of dopants was performed.
   a. The thermal masking oxide and Phosphosilicate Glass (PSG) layer created from diffusion was etched using BOE and the wafer was cleaned using Piranha.
   b. The wafer was placed in a tube furnace for dopants drive-in and growing the thermal oxide layer in one step. The process temperature and time was 1050 °C for 60 mins. The first 50 mins was carried out in an inert nitrogen environment for dopants drive-in, while the final 10 mins were used to grow a wet thermal oxide layer of around 300 nm, while continuing the dopants drive-in process.
9. The contact vias through the insulating oxide layer was created.
   a. Photolithography was used to define the contact vias. The same photolithography procedure in step 2.b is used with aligning mask 4 to the previous features on the wafer.
   b. The SiO_2 layer was etched using RIE similar to step 2.c

10. Right after the etching of the oxide layer in step 9, phosphorus doping is carried out to dope the silicon surface at the contact vias with a high concentration layer of phosphorus (n+). This step is important to guarantee a good Ohmic contact and minimize the Schottky barrier [126]. The effect of the Schottky barrier can be more evident with piezoresistors under $5x10^{19}$ cm^{-3} peak concentration. The intended impurity concentrations in this run were in the range of $1x10^{19}$ to $1x10^{20}$ cm^{-3}; therefore, an n+ diffusion step was needed. The same diffusion furnace used in doping the piezoresistive elements was used at 875 °C for 60 mins. The constant diffusion rate from a diffusion solid source is dependent on the diffusion temperature that was used for aging the source. Therefore, if a different diffusion temperature is required, a different solid source should be aged at the new temperature to guarantee a constant diffusion rate. In this case, a second solid source was used to create the n+ contacts.
11. Sputtering of an aluminum layer for metal contacts
    a. First the wafer was placed in BOE for 1:50 mins to etch the insulating phosphosilicate layer and lower the final insulating oxide layer to 150 nm. Then, the wafer was cleaned with acetone, IPA and DI-water before drying with a nitrogen gun. Then, the wafer was heated at 115 °C for 90 seconds to remove any traces of vapor at the contact vias.
    b. Before a potential layer of native oxide is created, the wafer is brought directly into the sputtering chamber within 30 mins of the previous step. “BOB” sputtering machine in the nanoFab was used for 1 hr and 30 mins to sputter a 700 nm layer of aluminum.
12. The patterning of the sputtered aluminum was conducted in a two-step process.
    a. Photolithography was used to pattern a layer of masking photoresist on top of the sputtered aluminum. The same procedure in step 2.b was used; however, the HMDS layer was not deposited since it is not effective with aluminum and the minimum feature size was in the 20 μm range.

b. The wafer was placed in an aluminum etchant (phosphorus-acetic-nitric acid) with gentle agitation. Based on an etch rate of 35 nm/min, the aluminum layer was etched in around 20 mins. The wafer was inspected under an optical microscope for any traces of aluminum before the photoresist layer is stripped using acetone. Then, the wafer was cleaned with IPA and DI-water and dried with nitrogen

c. The final device wafer was placed in an annealing furnace at 450 °C for 30 mins. The annealing step is important to ensure a good contact formation between the aluminum and the underlying silicon.

A photograph of the final diced POC chip is shown in Figure 4-8, while microscopic images of the fabricated *POC chip* are shown in Figure 4-9 and Figure 4-10.

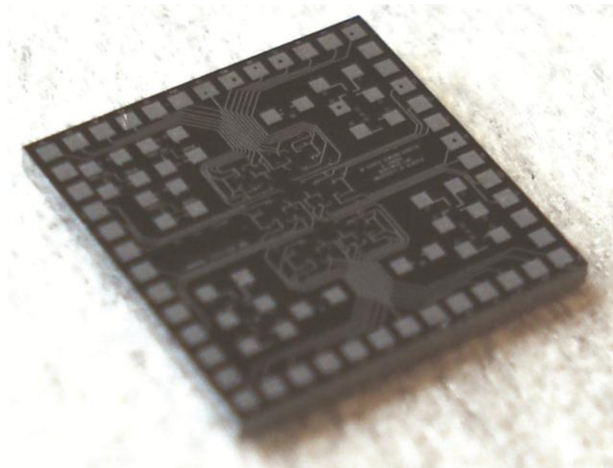

Figure 4-8 Photograph of the microfabricated *POC chip*

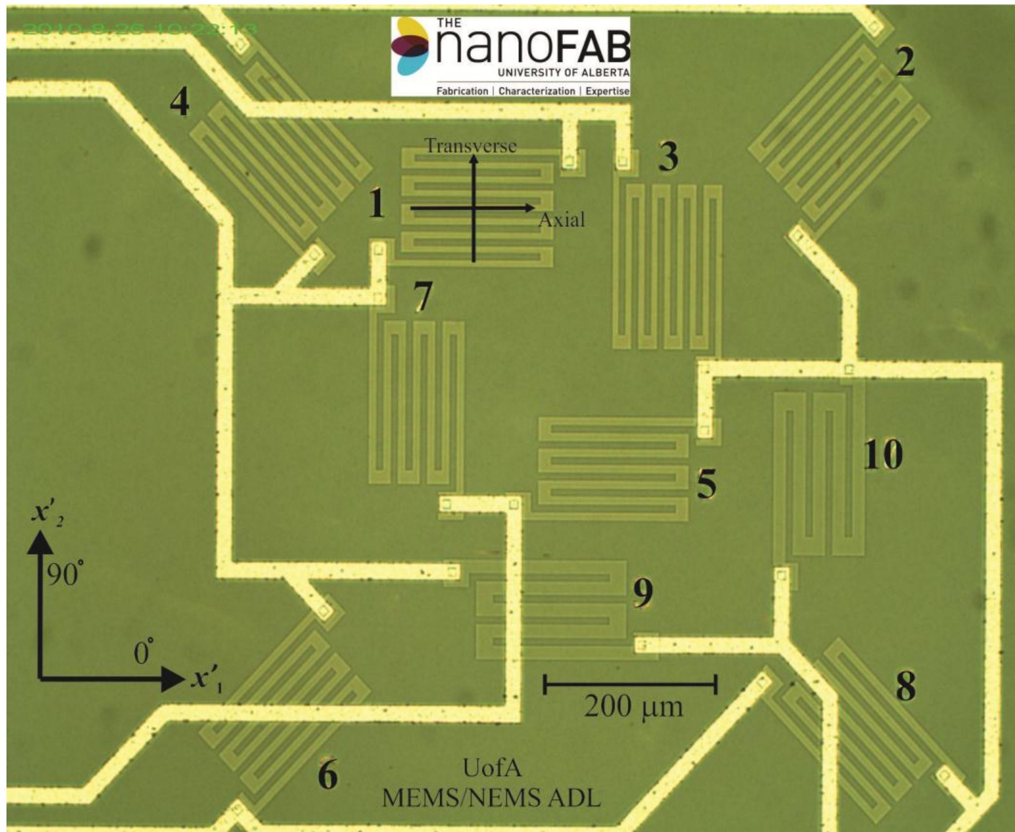

Figure 4-9 Microscopic image of the fabricated *POC chip* showing the 10-element rosette with numbers indicating the different sensing elements

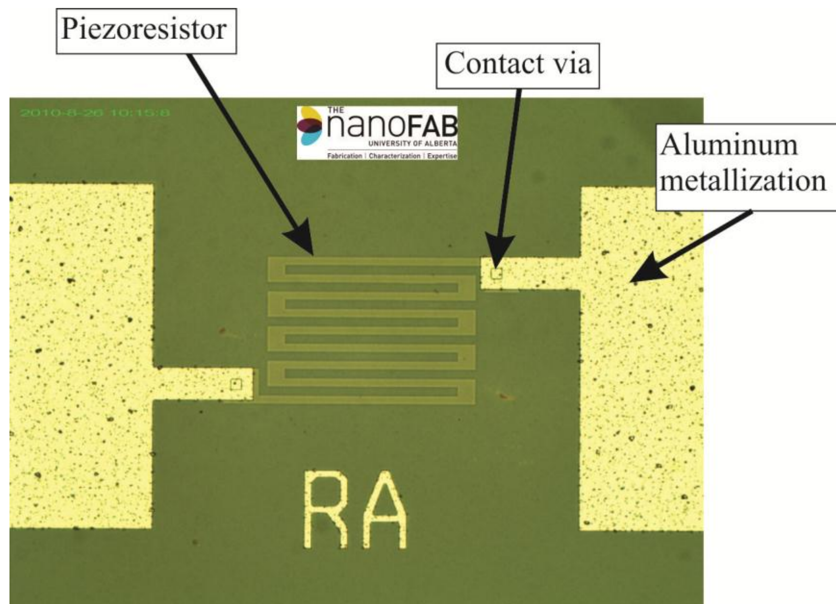

Figure 4-10 Microscopic image of the fabricated *POC chip* showing a characterization group *a* resistor

4.3.3 Characterization

The characterization of the microfabricated chip focused on three major aspects. The first is the current-voltage relationship (I-V characteristics) of the piezoresistor; the second is the contact resistance of the piezoresistor, while the third is the level of impurity concentrations and sheet resistances for the three groups.

4.3.3.1 I-V Characteristics

An important property of a piezoresistor is to have a linear I-V characteristic curve which provides constant resistance. This linear relationship is known as the Ohmic behavior, which is important to guarantee a current-voltage relationship that is only dependent on the applied load. A current sweep process over the range of -200 μA to 200 μA while recording the voltage response was carried out for each group of piezoresistors using a Keithley 2400 source meter. The resulting I-V behavior is shown in Figure 4-11, which shows the good linearity of the piezoresistors.

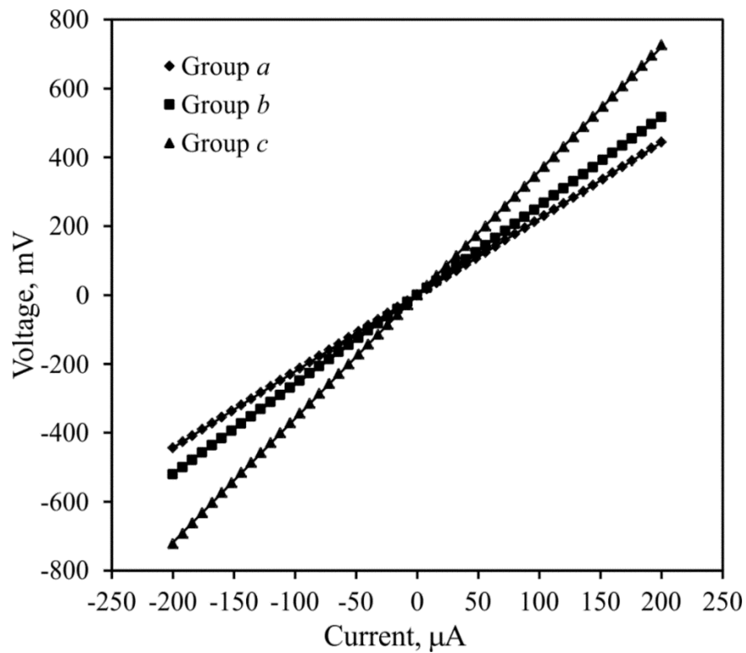

Figure 4-11 I-V Characteristic curves of the three groups of piezoresistors on the *POC chip*

4.3.3.2 Contact Resistance

A contact resistance is generated for each piezoresistor at the metal-silicon interface. Measurement of the contact resistance of a piezoresistor is important to determine if a correction is needed to the actual resistance value. Also, it is an indication of the quality of the metal-silicon interface. A transfer line method (TLM) was used to calculate the contact resistance of the fabricated piezoresistors. A TLM test structure was created on the wafer for each of the three groups of piezoresistors. The structure is made up of a straight doped region with 8 contact points along its length. The distance (d) between the contact points keeps increasing from the first point to the last as shown in Figure 4-12. A resistance measurement between each two points is made and plotted in Figure 4-13, where the intercept of the lines correspond to the total contact resistance at the two contact vias of a piezoresistor. The contact resistance of the developed piezoresistors was found to be around 0.5 Ω, which is relatively small compared to the resistor value that is above 2 kΩ.

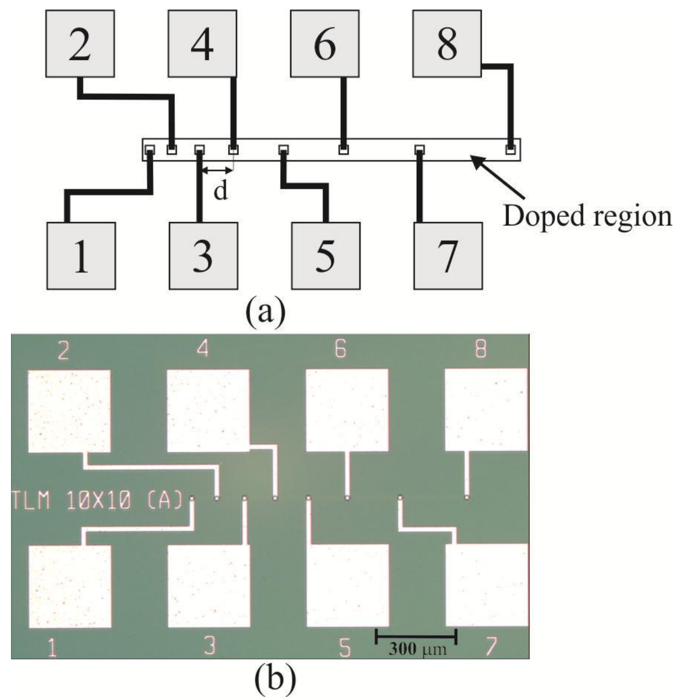

Figure 4-12 The transfer line width (TLM) test structure; (a) schematic and (b) Microscopic image

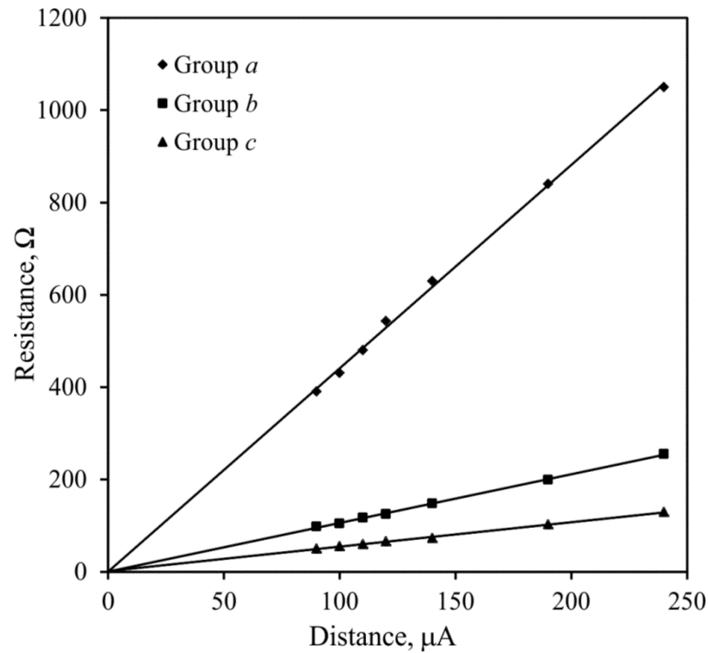

Figure 4-13 Resistances of each group along the TLM structure on the *POC chip*

4.3.3.3 Impurity Concentrations and Sheet Resistances

The impurity profiles of the three groups were modeled using the mathematical equations in section 4.2.1 by implementing them in a MATLAB® code. The diffusion parameters in terms of the temperature and time for the pre-deposition and drive-in steps are given in Table 4-1. The resulting profiles are shown in Figure 4-14 for the three pre-deposition steps and in Figure 4-15 for the final drive-in step. The net impurity concentrations shown in the figures is the difference between the phosphorus concentration and the boron background doping. It helps identifying the location of the junction depth on the impurity profile.

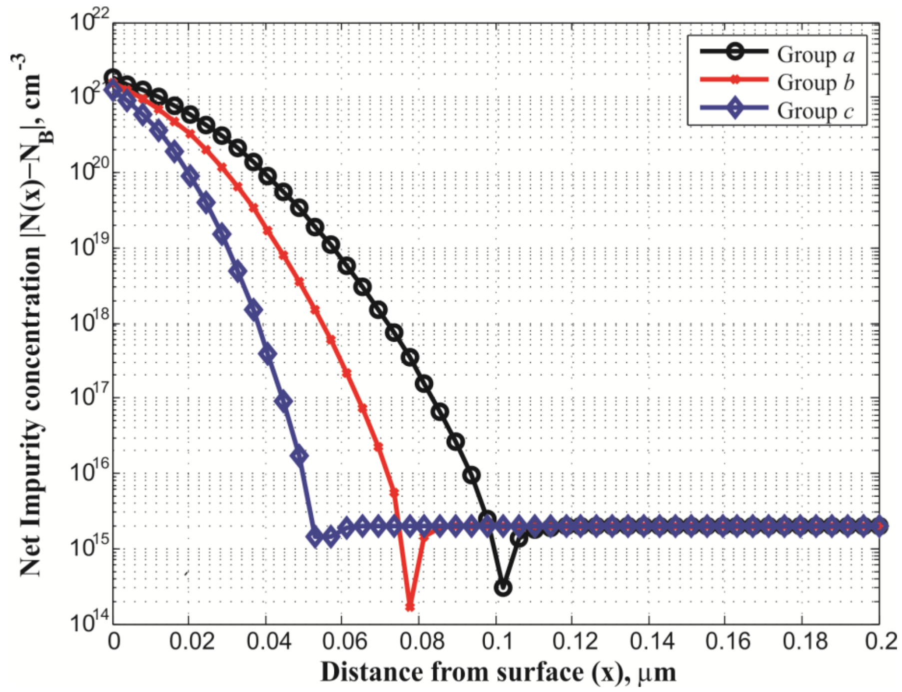

Figure 4-14 Net impurity concentration after pre-deposition steps

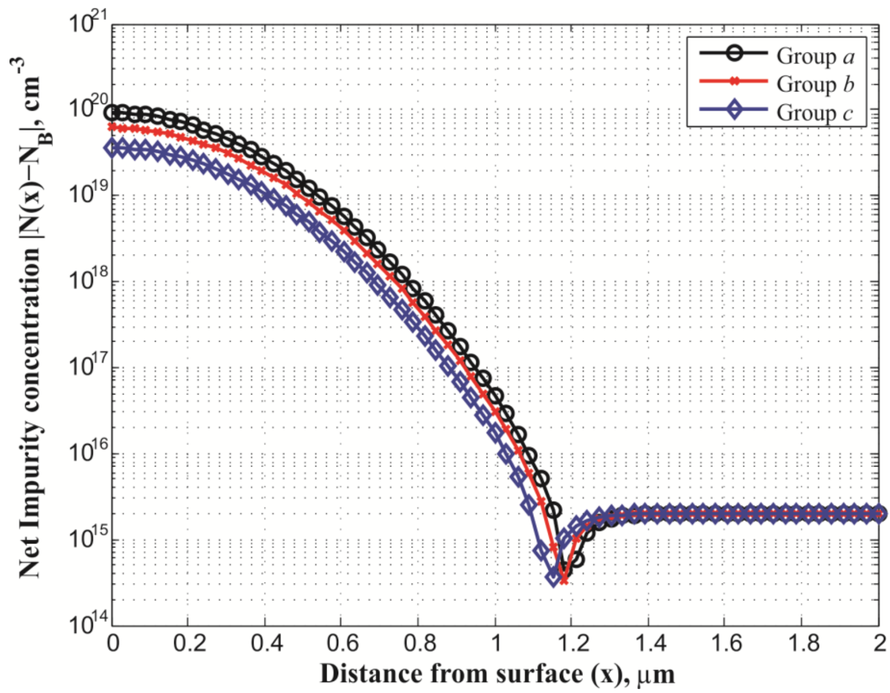

Figure 4-15 Net impurity concentration after drive-in step

Table 4-1 Pre-deposition and drive-in parameters for the Proof-of-Concept Chip

Pre-deposition						Drive-in	
t_1^p, hrs	T_1^p, °C	t_1^p, hrs	T_2^p, °C	t_1^p, hrs	T_3^p, °C	t^d, hrs	T^d, °C
1	845	1.25	830	1.75	820	1	1050

The fabricated wafer had three open windows with phosphorus concentrations corresponding to groups *a*, *b* and *c*. The three windows, measuring 7 mm x 2 mm each, were diced and sent to the Alberta Center for Surface and Engineering and Science (ACSES) laboratory at the University of Alberta for Time of Flight Secondary Ion Mass Spectrometry (ToF-SIMS). This characterization technique at ACSES laboratory was sensitive to impurity concentrations above 5×10^{18} cm^{-3}. Therefore, full concentration profiles were not extracted; however, surface concentrations were enough to correlate to the calibration coefficients. Also, sheet resistances of the three diced chips were measured prior to the SIMS characterization using a four-point probe available at the MEMS/NEMS ADL. The average resistances of the three groups of sensing elements in the 10-element rosette were 2.2 kΩ, 2.6 kΩ and 3.5 kΩ for groups *a*, *b*, and *c*, respectively. The results of the calculated and measured surface concentrations (N_0) and sheet resistances (R_s) are shown in Table 4-2. The analytical values correspond to the calculated surface concentrations from equation (4-9) at $x = 0$ and the sheet resistances from equation (4-12) after drive-in.

The results indicate that the analytical equations are under-estimating the surface concentrations. Also, there seemed to be large variation in the sheet resistances between the analytical calculations and experimental results. This discrepancy is assumed to be attributed to the assumption made earlier that the diffusion coefficient is constant over the impurity concentration profile. At high concentrations above the intrinsic-carrier concentration of silicon, the impurity

concentration of phosphorus differs from the Gaussian or complementary error-function. The phosphorus diffusion profiles at a non-constant diffusion coefficient was studied by Fair *et al*. [127] to have three regions known as the high concentration region, low concentration region, and the transition (kink) region. The solution of such problem is complicated and solved numerically. The diffusion modeling adopted in the current research was intended to give an estimate of the required diffusion temperature and time to come up with a certain range of surface concentrations, which was achieved with the basic equations described in section 4.2.1. The design of the 10-element rosette requires non-equal surface concentrations for the three groups. The difference between the concentrations of the three groups selected in the analytical model is consistent with experimental results in terms of their ratio, which is around 1.5 to 1.7.

Table 4-2 Analytical and experimental characterization of the doping parameters in the *POC chip*

	Analytical		Experimental	
	N_0, [cm^{-3}]	Rs, [Ω/sq]	N_0, [cm^{-3}]	Rs, [Ω/sq]
Group *a*	9.2×10^{19}	26.3	2.0×10^{20}	11.1
Group *b*	6.2×10^{19}	36.7	1.2×10^{20}	20.7
Group *c*	3.6×10^{19}	57.3	7.0×10^{19}	100.6

4.4 Microfabrication of the Test Chip

4.4.1 Chip Design

The main objective of the *test chip* is testing the 10-element single-polarity rosette for extraction of the stress components. Therefore, the design of the chip was based on the adopted testing approach that will induce enough stress components for testing. The selected testing setup was bonding the chip on a PCB beam undergoing four-point-bending, which has a stress field that is well defined by the analytical methods. Details of the testing process will be discussed later in chapter

6; however, the design of the chip was based on having a number of sensing rosettes on the surface that can detect different stress components. The sensing chip, measuring 7 mm x 7 mm x 0.3 mm, has three rosette-sites; center rosette and two edge rosettes as shown in Figure 4-16. The center rosette, measuring 500 µm x 1000 µm, is made up of the full 10-element rosette capable of extracting the six stress components, while the edge rosettes are reduced rosettes used primarily to extract the shear stresses. Edge rosette 1, measuring 450 µm x 250 µm, located along the chip's x_2'-direction, is made up of the normal sensing elements formed from groups *a* and *b* to extract $\left(\sigma_{11}' - \sigma_{22}'\right)$ and σ_{23}'. On the other hand, edge rosette 2, measuring 200 µm x 900 µm, located along the chip's x_1'-direction, is made up of the 45 degrees oriented sensing elements formed from groups *a* and *b* to extract σ_{12}' and σ_{13}'. Edge rosette 1 has two extra elements, R_9 and R_{10}, which were designed to extract the normal stress σ_{33}' using equations (3-19). However, due to the low sensitivity of σ_{33}' in the microfabricated rosette, those two elements were not tested as will be explained in the next chapter. All piezoresistors have the same length of 200 µm, but different width of 10 µm, 13 µm, and 17 µm for groups *a*, *b*, and *c*, respectively. Test structures made up of the three groups of piezoresistors are located around the center rosette for characterizing the I-V behavior of the individual piezoresistors.

The sensing elements were designed as straight resistors compared to the serpentine design utilized in the previous *POC chip*. The selection of the straight resistor design has a number of reasons. First, the calibration of the B_i coefficients is directly related to the crystallographic piezoresistive coefficients in a straight resistor. However, the values of the calibrated B_i coefficients in a serpentine resistor are effective values and have to be corrected for the actual crystallographic B_i coefficients due to the effect of the transverse-sensitivity of the piezoresistor. This will be discussed in the calibration of the *POC chip* in chapter 5. Also, for the same line width, a serpentine resistor will take more foot-print

compared to a straight resistor, unless the individual line width is decreased. It was an important factor in the rosette design on the chip to have a minimum foot-print to lay on an area with least stress field non-uniformities. In addition, smaller line width was not used due to the limitation on the optical photolithography process. It was noticed that higher non-uniformity in a resistor value occurs for features less than 10 μm in width. Therefore, it was decided to design all piezoresistors as straight structures with minimum width of 10 μm to obtain B_i coefficients directly related to the crystallographic piezoresistive coefficients and minimize the non-uniformities on the resistance values.

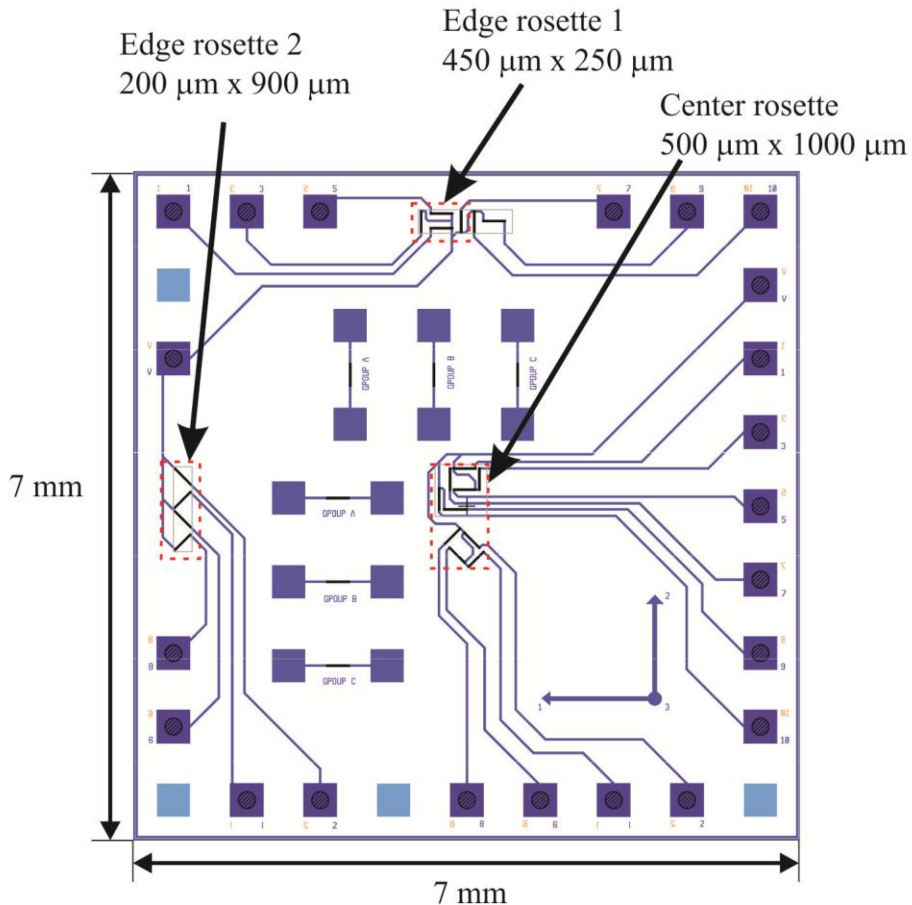

Figure 4-16 Layout of the test chip showing the three rosette-sites

4.4.2 Process Flow

The process flow developed to fabricate the *test chip* is shown in Figure 4-17. All processes were conducted in the nanoFab except for ion implantation, used to dope the piezoresistors, was out-sourced to INNOViON. Also, diffusion process, used to create the n+ contacts, was conducted in the MEMS/NEMS ADL. This process uses 6 masks with three masks for the *a*, *b*, and *c* groups of sensing elements, one mask for an alignment mark, one mask for the contact vias, and one mask for the patterning of the metal layer.

The selection of ion implantation over diffusion to dope the sensing elements is made based on two reasons. The first is the wide range of impurity concentrations that can be achieved using ion implantation, especially at concentrations below $1x10^{20}$ cm^{-3}. Although the available solid sources was able to achieve concentrations in the $1x10^{19}$ cm^{-3} range, deep junction depths and low sheet resistances were evident, which led to a very low resistance values. The second reason is the higher uniformity of concentrations achievable on the surface of the wafer using ion implantation compared to diffusion. A test was conducted to compare the results from a diffused resistor fabricated using diffusion and another using ion implantation. The resistor measuring 200 μm x 10 μm (20 squares) was doped using diffusion pre-deposition at 820 °C for 90 mins and drive-in at 1050 °C for 60 mins to achieve a sheet resistance of 25 Ω/sq. On the other hand, the ion implanted resistor was phosphorus implanted at a dose of 1.5 $x10^{15}$ cm^{-2} and energy of 100 keV and annealed at 950 °C for 60 mins to achieve a sheet resistance of 42 Ω/sq. The same wafer was used for both doping methods, which was a (111) 100 mm diameter prime silicon double-sided polished wafer with 300±25 μm thickness and resistivity of 10 Ω-cm. The resistances of 5 typical resistors at different points on the wafer fabricated using diffusion showed a variation of 70% compared to 12% variation for the same resistor fabricated using ion implantation.

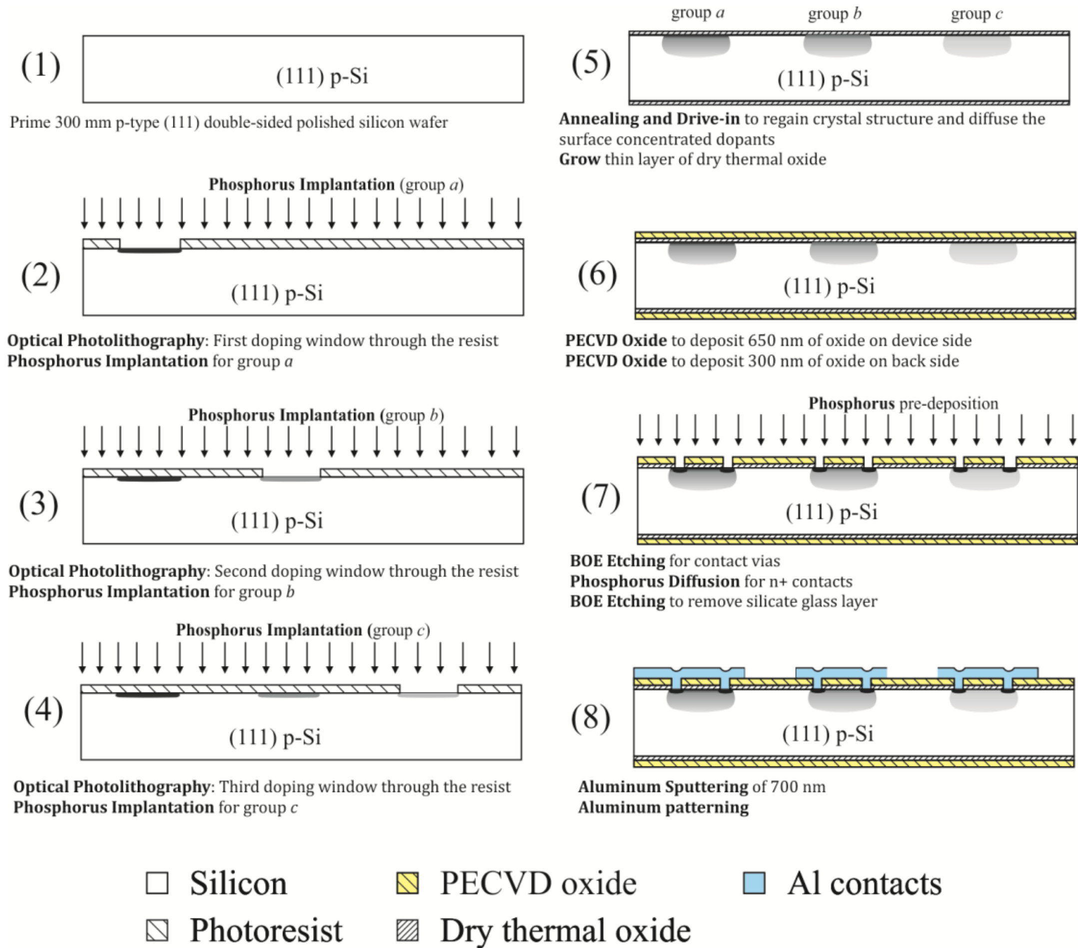

Figure 4-17 Microfabrication process flow of the test chip

The following are the details of the process, where each paragraph number describes the corresponding stage in Figure 4-17:

1. The initial starting material was a p-type boron doped (111) double-sided polished prime silicon wafer with a diameter and thickness of 100 mm and 300±25 μm, respectively. The double-sided polished wafer was selected to include through silicon vias (TSVs) in the wafer. However, it was not incorporated into the process due to microfabrication challenges. Also, the selection of a 300 μm wafer thickness is made to accommodate the use of commercially available Zero Insertion Force (ZIF) connectors during the

calibration process, will be discussed in the next chapter. The wafer is boron doped with bulk resistivity of 10 Ω-cm, which corresponds to a background impurity concentration of 1.35 x 10^{15} cm^{-3}. A batch of 13 wafers was prepared in this microfabrication run to optimize the cost of the fabrication per wafer and have enough samples for the fabrication trials. The wafers was initially cleaned using piranha cleaning (3 H_2SO_4: 1 H_2O_2) followed by buffered oxide etch (BOE) to remove traces of native oxide.

2. Ion implantation of group *a* piezoresistors:
   a. Optical photolithography was performed to pattern a layer of masking photoresist for the implantation windows of group *a* piezoresistors. The same photolithography process and photoresist HPR 504 with a thickness of 1.2 µm adopted in the *POC chip* is used in this process flow. The steps included depositing an HMDS adhesion promoter layer, spinning the photoresist, soft baking, exposure, and developing. However, an extra step included a final hard baking process of the photoresist to withstand the ion bombardment during implantation. The hard baking was performed at 115 °C in an oven for 20 mins.
   b. Oxide etching using BOE was performed to remove any traces of native oxide before sending the wafers for implantation. The wafers were dipped in BOE for 1 min followed by rinsing in DI-water and nitrogen drying.
   c. The wafers were sent to INNOViON for implantation at energy of 80 keV and dose of 1.7×10^{15} cm^{-2}.
   d. The returned wafers were placed in an oxygen plasma etcher (Branson etcher) to strip off the photoresist. Then, the wafers were cleaned using Piranha and followed by BOE etching to remove traces of oxide that are deposited during the oxygen plasma etching.
3. Ion implantation of group *b* piezoresistors: The same process in step 2 is used to implant group *b* piezoresistors. The ion implantation energy and dose were 80 keV and 1.1×10^{15} cm^{-2}.
4. Ion implantation of group *c* piezoresistors: The same process in step 2 is used to implant group *c* piezoresistors. The ion implantation energy and dose were

80 keV and $7.5x10^{14}$ cm^{-2}. The total time for the ion implantation of the three groups was around 1 month, which included the micro-fabrication processes at the nanoFab, shipping, and ion-implantation processing.

5. Annealing, drive-in and growing thermal oxide:
   a. The ion implanted regions transformed the crystalline structure of silicon into an amorphous layer, which has a different color than the surrounding crystalline silicon. However, after annealing the crystal structure is restored and the implanted regions can hardly be noticed on the surface of the wafer. Therefore, alignment of the subsequent mask for the contact vias is hard to achieve. An alignment mask that create etch marks on the silicon surface is used at this point to facilitate the subsequent contact vias mask alignment. A photolithography step similar to step 2.a is used to pattern a photoresist layer with the etch marks. Then, deep reactive ion etching (DRIE) process is performed to etch around 400 nm from the silicon surface. This is followed by a stripping of the photoresist in acetone sonic bath and cleaning with IPA and DI-water and drying with nitrogen. A final cleaning before annealing the wafer was done using Piranha followed by BOE etching to remove any traces of oxide on the silicon surface.
   b. The annealing and drive-in step was followed at 950 °C for 35 mins, which included a 20 mins annealing in an N_2 atmosphere followed by 15 mins dry thermal oxidation period to grow a very thin layer (~15 nm) of high quality thermal oxide for insulation. The 20 mins annealing period in N_2 is important to reduce the dislocation lines originating from the amorphous surface layer created due to ion implantation. If annealing was performed directly in an oxidizing atmosphere, the dislocation lines can grow deeply into the silicon and seriously degrade the electrical properties of the p-n junction [128]. A longer thermal oxidation process was avoided to prevent excessive drive-in of the dopants, which consequently drops the sheet resistance and resistance values of the piezoresistors.

6. A layer of silicon dioxide (SiO_2) using Plasma Enhanced Chemical Vapor Deposition (PECVD) is deposited for electrical insulation and as a masking layer for the next diffusion step. Tetraethylorthosilicate (TEOS) compound was decomposed at 300 °C in PECVD chamber from Trion Technology Inc. to deposit the oxide film, which has a good uniformity and step coverage. The final oxide thicknesses were 650 nm and 300 nm on the front and back side of the wafer, respectively with a non-uniformity of 7.5%. The oxide created from TEOS is known to have a high density (2.2 g/cm^3) and dielectric strength (10x10^6 V/cm) enough for electrical insulation [129].
7. Etching of contact vias and n+ layer doping:
    a. Photolithography was used to define the contact vias. The same photolithography procedure in step 2.a, but without the hard baking step is used with mask 5 to pattern the contact vias on the photoresist.
    b. The SiO_2 layer was etched using RIE with an etch rate of 7 nm/s
    c. The photoresist is stripped using acetone sonic bath followed by cleaning with IPA and DI-water.
    d. An n+ phosphorus layer is diffused at the contact vias to create a high concentration layer that lowers the Schottky barrier at the silicon-metal interface. The same diffusion furnace used in doping the piezoresistive elements in the *POC chip* was used at 860 °C for 40 mins.
8. Metallization:
    a. First the wafer was placed in BOE for 1.2 mins to etch the insulating phosphosilicate layer and lower the final insulating oxide layer to 550 nm on the device surface and 200 nm on the back side of the wafer. Then, the wafer was cleaned with acetone, IPA and DI-water before drying with a nitrogen gun. At the end, the wafer was heated at 115 °C for 90 seconds to remove any traces of vapor at the contact vias.
    b. Before a potential layer of native oxide is created, the wafer is brought directly into the sputtering chamber within 30 mins of the previous step. "FLOYD" sputtering machine in the nanoFab was used for 45 mins to sputter a 700 nm layer of aluminum. FLOYD machine was selected in this

run due to its load lock mechanism, which limits chamber contamination compared to the open chamber used in BOB machine and probably due an inefficient pumping mechanism. The switch to FLOYD machine is discussed in section 4.6.

c. Photolithography was used to pattern a layer of masking photoresist on top of the sputtered aluminum. The same procedure in step 2.a was used; however, the HMDS layer deposition and hard baking steps were not performed.

d. The wafer was placed in an aluminum etchant (phosphorus-acetic-nitric acid) with gentle agitation. Based on an etch rate of 35 nm/min, the aluminum layer was etched in around 20 mins. The wafer was inspected under an optical microscope for any traces of aluminum before the photoresist layer is stripped using acetone. Then, the wafer was cleaned with IPA and DI-water and dried with nitrogen

e. The final device wafer was placed in an annealing furnace at 450 °C for 15 mins.

The total time required for this process was around two months including the ion implantation time. The final fabricated wafer is shown in Figure 4-18 with annotations for the test chip, test structure chips for sheet and contact resistances measurement, doped regions for characterization of the surface concentration, and the aluminum traces used for rosette calibration. A microscopic image of the 10-element sensing center rosette is shown in Figure 4-19 and the two edge rosettes are shown in Figure 4-20 with numbers corresponding to each piezoresistor in the rosette.

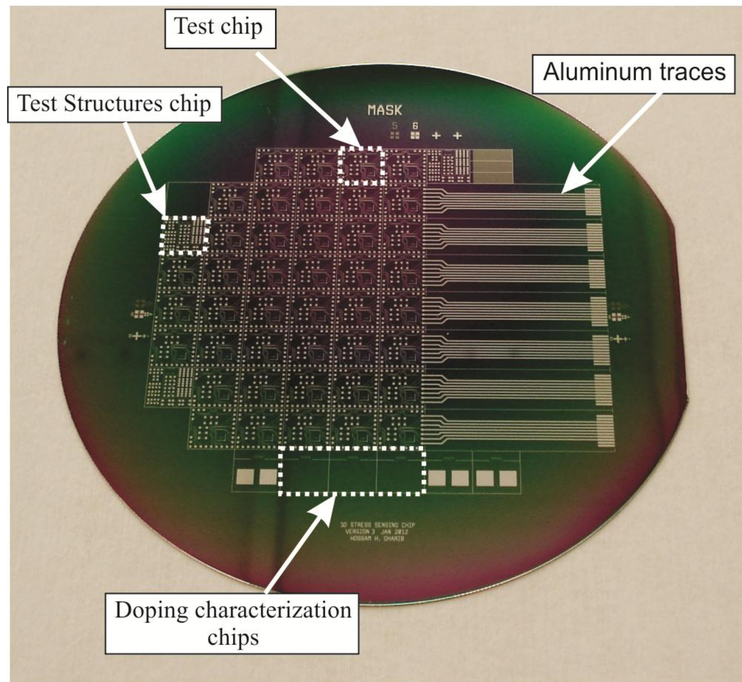

Figure 4-18 Photograph of the final test wafer after annealing

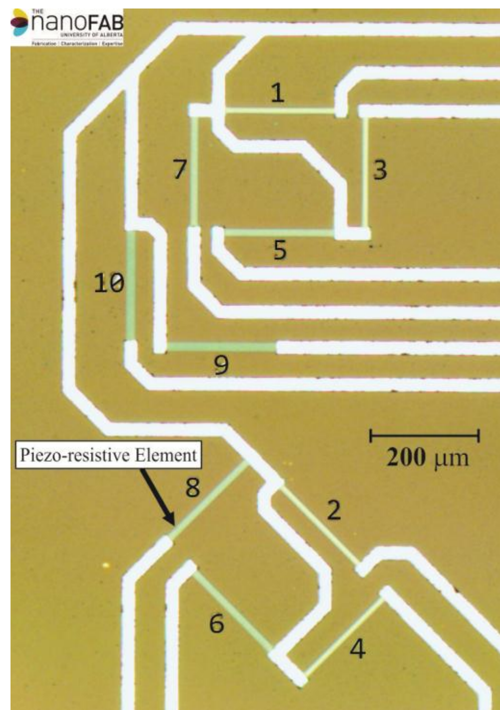

Figure 4-19 Microscopic image of the fabricated 10-element sensing center rosette

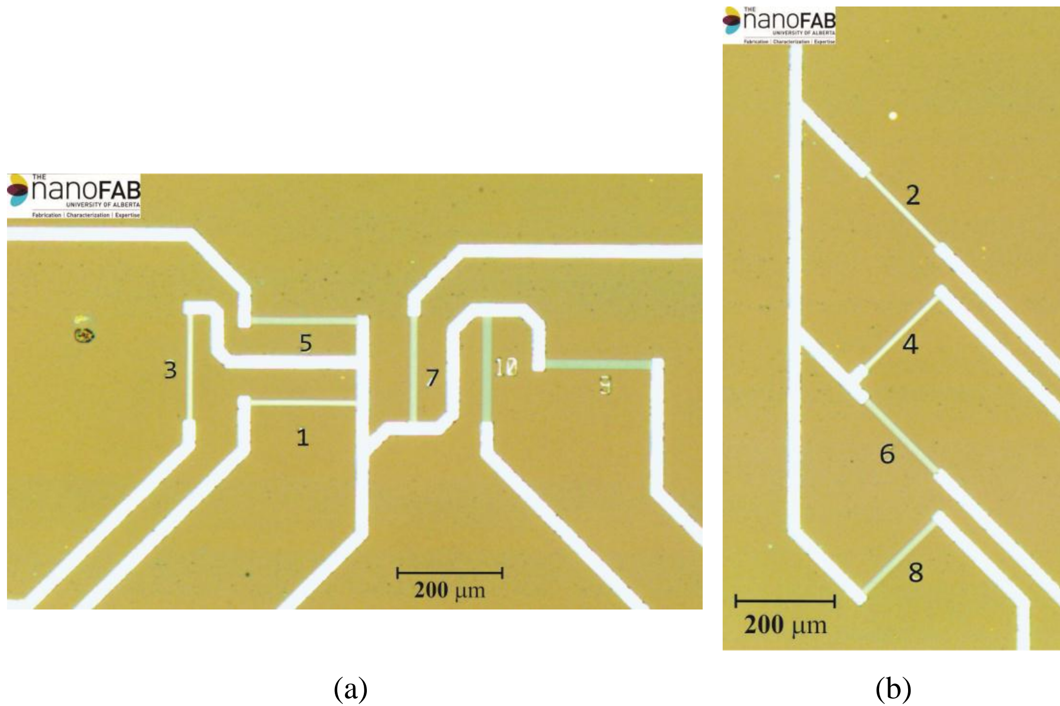

(a) (b)

Figure 4-20 Microscopic image of the fabricated (a) edge rosette 1 and (b) edge rosette 2

4.4.3 Characterization

Similar to the characterization of the *POC chip*, three aspects were characterized in the *test chip*. These are the current-voltage relationship (I-V characteristics) of the piezoresistor; the contact resistance of the piezoresistor, and the impurity concentration profiles and sheet resistances for the three groups.

4.4.3.1 I-V Characteristic Curve

The I-V characteristic curves of the three piezoresistors for groups *a*, *b*, and *c* are shown in Figure 4-21. The current was swept from -200 μA to 200 μA and the output voltage is recorded with two wire measurement using Keithley 2400 source meter. The I-V curves demonstrate good linearity over the tested range indicating good Ohmic behavior. The average resistances of the piezoresistors were 820 Ω, 950 Ω, and 1150 Ω, for groups *a*, *b*, and *c*, respectively.

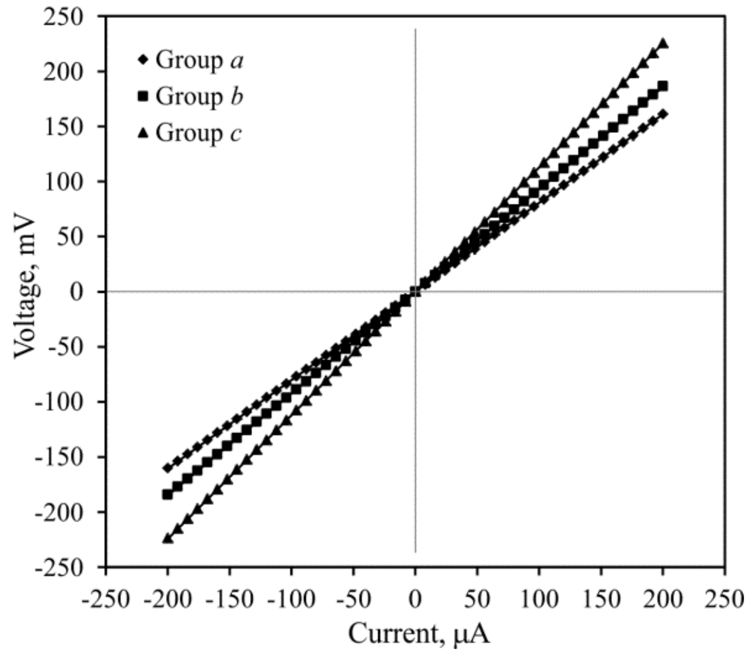

Figure 4-21 Sample I-V curves of the three groups of piezoresistors

4.4.3.2 Contact Resistance

The contact resistances for the three groups were characterized with the on-wafer TLM test structures shown earlier in Figure 4-12. The resulting resistance behavior over the changing resistor length is shown in Figure 4-22, which indicates a contact resistance close to zero. The calculated contact resistance ranged from 0.5 to 3 Ω, which is considered acceptable compared to the resistances of the sensing elements which were around 1 k Ω.

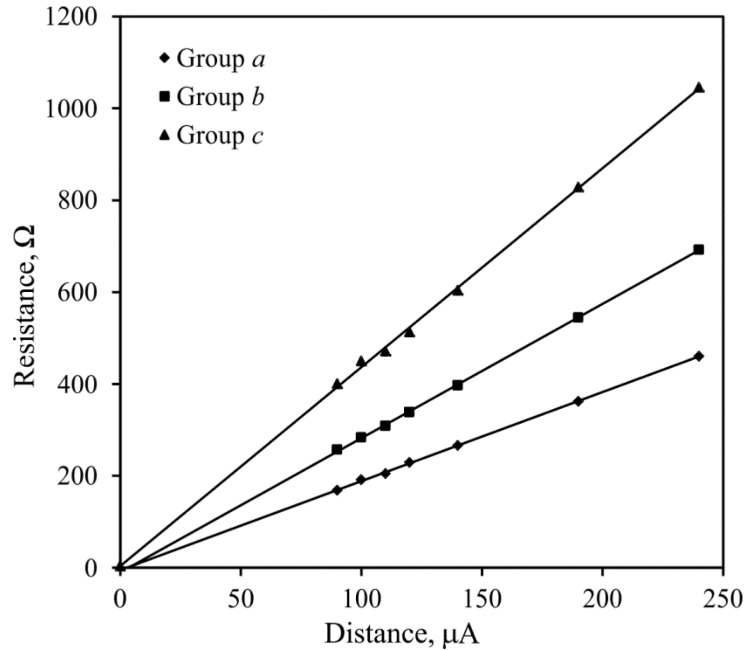

Figure 4-22 Resistances of each group along the TLM structure on the test chip

4.4.3.3 Impurity Concentrations and Sheet Resistances

An analytical solution utilizing the equations in section 4.2.2 in a MATLAB® code was used to solve for the impurity profiles after the three ion implantation steps and the drive-in step. The calculated profiles are shown in Figure 4-23 and Figure 4-24. The ion implantation parameters in terms of dose (Q) and acceleration energy (E) and the drive-in parameters in terms of time (t_d) and temperature (T_d) are given in Table 4-3, where the subscripts *a*, *b*, and *c* denote the three different implantation steps. Three diced chips from the wafer with final doped regions after drive-in for the three groups were sent to Solecon Laboratories for Spreading Resistance Profiling (SRP). A photograph of one of the sent chips is shown in Figure 4-25 with marking of the doped region. The measured impurity concentration profiles for the three groups are shown in Figure 4-24 in comparison with the analytical solution after the drive-in step. The resulting peak concentrations and sheet resistances of the three groups are presented in Table 4-4 for the analytical solution and experimental measurements.

The experimental sheet resistances were measured using four-point probe at Solecon Laboratories. It is noticed that there is an acceptable correlation between the analytical and experimental results, especially in terms of the sheet resistances. However, it is noticed that the experimental SRP results demonstrate a deeper diffusion into the silicon compared to the analytical calculations as shown in Figure 4-24. This is assumed to be due to the same assumption made in the diffusion modeling, which is assuming the diffusion coefficient D is constant over the concentration profile. However, this assumption is still invalid in the analytical modeling of the dopants drive-in given by equation (4-17). Therefore, a more accurate solution to the problem should assume a non-constant diffusion profile. However, similar to the diffusion modeling, the purpose of this analysis is to guide the selection of the ion implantation and drive-in parameters that provide a window of peak concentrations.

Table 4-3 Ion Implantation and drive-in parameters for the *test chip*

Ion Implantation						Drive-in	
Q_a, cm^{-2}	E_a, keV	Q_b, cm^{-2}	E_b, keV	Q_c, cm^{-2}	E_c, keV	t^d, mins	T^d, °C
1.7×10^{15}	80	1.1×10^{15}	80	7×10^{14}	80	35	950

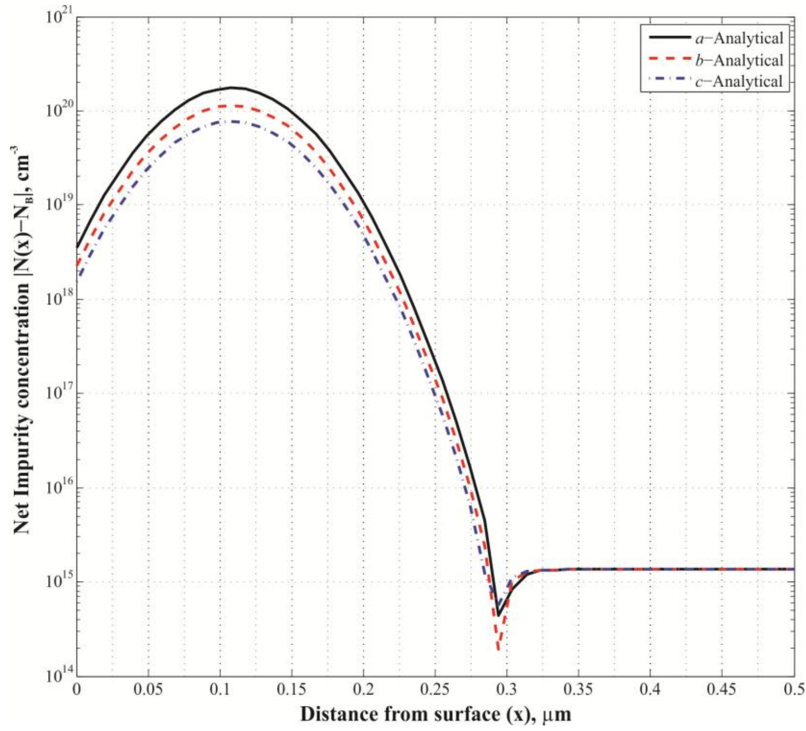

Figure 4-23 Impurity concentrations profiles after ion implantation for the three groups

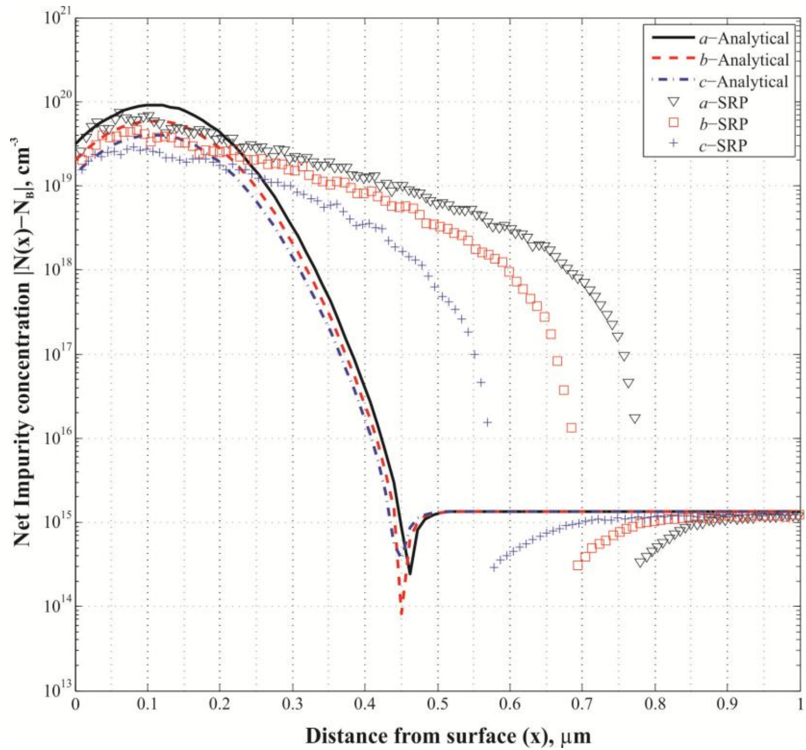

Figure 4-24 Impurity concentrations profiles after drive-in for the three groups

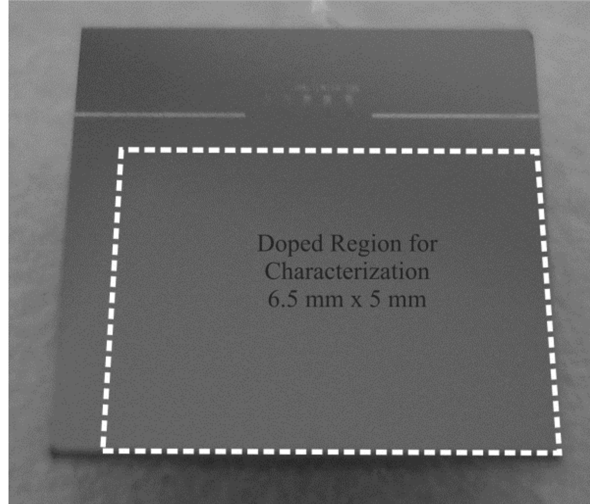

Figure 4-25 Diced silicon chip sent for SRP characterization

Table 4-4 Analytical and experimental characterization of the doping parameters in the *test chip*

	Analytical		Experimental	
	N_p, [cm^{-3}]	Rs, [Ω/sq]	N_p, [cm^{-3}]	Rs, [Ω/sq]
Group *a*	9.1×10^{19}	44.4	7.4×10^{19}	41
Group *b*	5.9×10^{19}	64.7	4.7×10^{19}	60
Group *c*	4.0×10^{19}	88.8	2.9×10^{19}	94

4.5 Noise in Piezoresistors

The electrical noise generated in piezoresistors is due to random variation in the potential of the conductor. In a diffused piezoresistor, noise is governed by to main sources; Johnson (thermal) noise and 1/*f* (flicker) noise. The thermal noise exists in all resistors and cannot be eliminated and is given by:

$$V_j = \sqrt{4kT_k R} \tag{4-19}$$

Where, k, T_k, and R are the Boltzmann's constant in J/K, absolute temperature in Kelvin, and resistance value in Ω, respectively.

The other source of noise is the 1/*f* noise, which as the name implies is inversely proportional to the frequency. Therefore, since piezoresistors usually operate at low frequency, this type of noise is significant. The 1/*f* noise is dependent on the microfabrication process parameters like implant dose and energy and anneal temperature and time. It is given by:

$$V_{1/f} = V_b \sqrt{\frac{\alpha}{Nf}} \tag{4-20}$$

Where, f, N, and V_b are the frequency, total number of impurity carriers in the piezoresistor, and the bias voltage across the resistor, respectively. The parameter α is a non-dimensional fitting parameter referring to the quality of the lattice, which ranges between 10^{-3} to 10^{-7} [130]. The microfabrication process can be used to reduce the 1/*f* noise specifically through using high doping concentrations, which consequently decreases the sensitivity. For example, a change in the peak doping concentration, N_p, from 10^{19} cm^{-3} to 10^{17} cm^{-3} increases the sensitivity of a piezoresistor by 65% and increases the noise by a factor of 10 [45]. In the current research, the piezoresistors have been doped at high concentrations in the 10^{19} cm^{-3} to avoid running into 1/f noise.

In a diffused resistor with a p-n junction, the charge carriers cross the junction independently and randomly causing fluctuations in the average current *I*. These fluctuations induce a shot noise, which is a white noise or frequency independent. The shot noise power spectral density is given by [131, 132]:

$$S_I = 2qI \tag{4-21}$$

Where, q and I are the electron charge and current, respectively. It is observed that the shot noise is proportional to the current *I*. In this research, a low constant current source of 100 μA was used to avoid shot noise and potential current leakages in the substrate.

4.6 Challenges

A number of challenges were faced during the microfabrication processes. Some of these challenges had to deal with building an appropriate hands-on experience with the microfabrication technology, where almost all processes were personally conducted except for the ion-implantation, which was out-sourced. Also, other challenges had to do with delays due to equipment downtime or process repetition due to some mal-functioning equipment. However, the primary microfabrication challenges had to do with the control of the diffusion process and achieving Ohmic contacts for the piezoresistors.

4.6.1 Diffusion Process Control

A great deal of time was spent to determine the appropriate approach to dope the three groups of piezoresistors using phosphorus diffusion. The initial setup of the diffusion furnace for phosphorus pre-deposition took on average few months to order the appropriate solid sources, condition them, test the nitrogen (N_2) quality inside the quartz tube, and test the resulting sheet resistances to the manufacturer's charts. The conditioning process required special Nitrogen/Oxygen mix (75% N_2 : 25% O_2) cylinders to clean the solid sources and condition them for around 20 hours to release dopants at a fixed rate. The Nitrogen operating carrier gas was supplied from an in-house supply; however, early in the process, it had a vapor content, which led to wafer oxidation. Therefore, Nitrogen cylinders were used for the process until the quality of the in-house Nitrogen was improved. Few tests were conducted on bare silicon wafers to ensure the absence of oxide growth.

The major challenge with the diffusion process was coming up with uniform final concentrations over the wafer surface without sacrificing the required surface concentrations and sheet resistances. At low pre-deposition temperatures, ~800 °C, the process requires longer time to produce acceptable uniformity across the wafer surface, which reduced the sheet resistances and added a higher dose to the

three groups. Therefore, there was a challenge to get relatively high sheet resistances, specifically for group *a*. A number of experimental trials were conducted to come up with the appropriate diffusion parameters.

4.6.2 Non-Ohmic Contacts

The Ohmic behavior is the primary characteristic of a resistor. Therefore, it was important to fabricate the piezoresistors with linear I-V curves. During the different microfabrication trials conducted, there was inconsistency in the Ohmic behavior of the resulting piezoresistors, where some runs provided linear Ohmic behavior and others did not. Few runs and tests were conducted to troubleshoot the problem. The two main expected reasons were: (1) having insufficient doping level for the n+ layer and (2) the presence of an interfacial insulating layer between the silicon and metallization layer. The level of impurity in the n+ layer was studied by testing the solid source that was used to give an appropriate sheet resistance and conditioning a new source to avoid any possible contamination in the old source. The possible presence of an interfacial insulating layer was studied by Piranha cleaning and BOE etching the silicon surface at the contact vias prior to sputtering to ensure a clean and oxide free interface. However, after a long period of trials, the problem still existed.

A switch was made to a different sputtering machine, called FLOYD, to eliminate any possible contamination from the microfabrication process. The resulting I-V curves were linear compared to the previously used equipment, BOB. A comparison between both I-V curves for the same piezoresistor with sputtered aluminum using BOB and FLOYD is shown in Figure 4-26. The non-Ohmic behavior from BOB is expected to be due cross-contamination of sputtered materials in the sputtering chamber. BOB has an open chamber system, which is exposed regularly to the 10 K rating clean room atmosphere. Also, the vacuum pump might not be efficient enough to remove all contaminants during the pump down process. On the other hand, FLOYD is a load-lock system, where the sputtering chamber is kept under vacuum all the time and rarely opened except for

maintenance. Also, FLOYD sputter only four types of materials compared to the uncontrolled amount used in BOB.

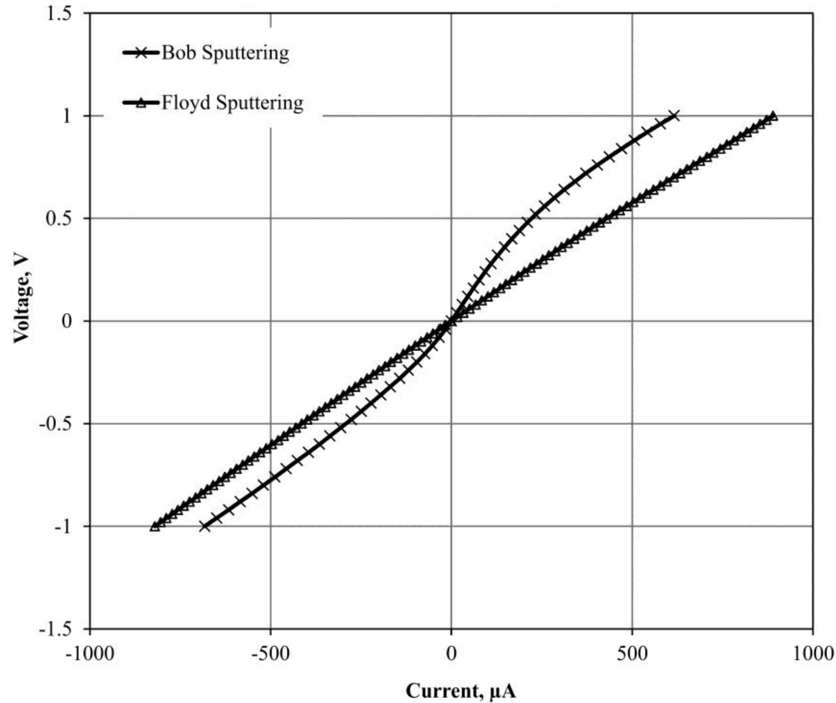

Figure 4-26 I-V Characteristic curves of two piezoresistors with Aluminum traces sputtered using two different equipment

4.7 Conclusions

This chapter presented the microfabrication processes conducted to prototype two silicon chips; the *POC chip* for the early feasibility study and the *test chip* for the full testing of the proposed 10-element rosette. An emphasis was given to the analytical modeling for both diffusion and ion implantation processes, which were used in this research. Also, the characterization of the fabricated chips were presented in terms of the piezoresistors' I-V characteristics, contact resistance, and impurity concentration profiles, which are the important characteristic parameters of the piezoresistors.

CHAPTER 5: CALIBRATION OF THE SENSING CHIP[3]

5.1 Overview

The calibration of the 10-element single polarity rosette involves the evaluation of 12 coefficients; the 3 piezoresistive coefficients (B_i) and TCR (α) for the three groups, *a*, *b*, and *c*. This involves three load applications on the rosette; uni-axial, thermal, and hydrostatic. The uni-axial loading is used to calibrate B_1 and B_2, while the thermal loading is used to calibrate α, and finally the hydrostatic loading is used to calibrate B_3. This chapter discusses the calibration processes for each load application, which are implemented to both the *POC chip* and *test chip*.

5.2 Uni-axial loading

Application of a known uni-axial stress (σ'_{11}) at the rosette site and measurement of the resulting resistance change of the sensing element is used to calibrate B_1 and B_2. The resistance change from the sensing elements oriented along 0 and 90 degrees from the x'_1 -direction in Figure 3-5, is evaluated from equations **Error! Reference source not found.** as follows:

$$\left(\frac{\Delta R_0}{R_0}\right) = B_1\,\sigma'_{11}$$

$$\left(\frac{\Delta R_{90}}{R_{90}}\right) = B_2\sigma'_{11} \qquad (5\text{-}1)$$

Therefore, elements R_1, R_5, and R_9 are used to calibrate B_1 for groups *a*, *b*, and *c*, respectively. On the other hand, elements R_3, R_7, and R_{10} are used to calibrate B_2 for groups *a*, *b*, and *c*, respectively.

---

[3] Some of the material in this chapter has been previously published by Gharib *et al*. [115, 116, 122]

A four-point bending (4PB) fixture is used to apply a known uni-axial stress on a rectangular beam diced from the fabricated wafer and contains a row of test chips. The four-point loading, shown in Figure 5-1, develops a state of uniform bending stress between the supports at the middle section of the beam, which develops a uni-axial stress field with a maximum tensile value at the upper fibers and maximum compressive value at the lower fibers of the beam [133]. The state of uni-axial stress is given by:

$$\sigma_{11} = \frac{3F(L-d)}{wh^2} \tag{5-2}$$

Where, F = applied force, L = distance between the applied forces, d = distance between the middle supports, w = width of rectangular strip, and h = thickness of rectangular strip. This equation is accurate if the beam is not significantly deformed due to the applied load and the dimensions w and h are small compared to L and d. The 4PB fixture has been successfully used by many researchers [110, 113, 133-135] to calibrate the piezoresistive coefficients and is found to have a maximum error of 5% in calculated stress by combining errors due to weight and length measurement, loading symmetry, beam rotation, and probe forces as investigated by Beaty *et al* [133].

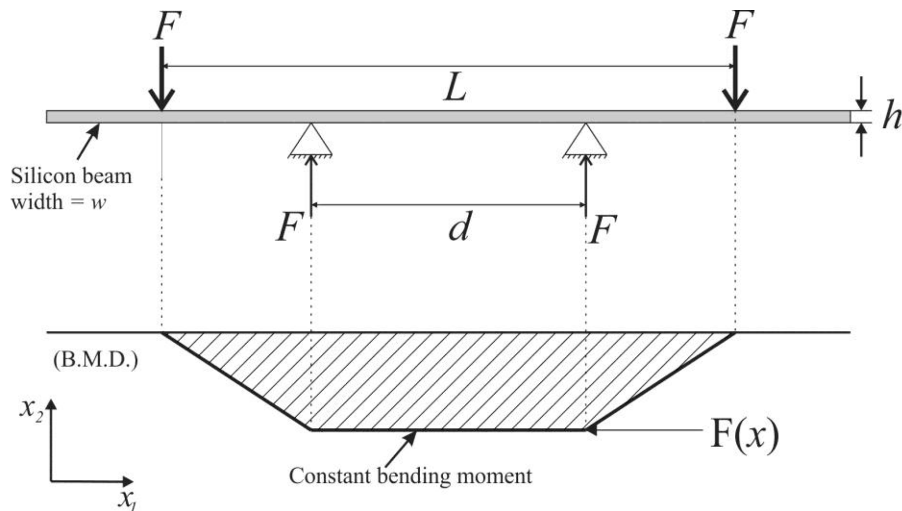

Figure 5-1 Forces and moments acting on the silicon beam undergoing four point bending

5.3 Thermal Loading

Calibration of TCR (α) requires application of a stress-free thermal load. This is usually performed in an enclosed chamber with a controlled temperature environment. Since α is isotropic across the 10 sensing elements, all piezoresistors can be used for α calibration. The resistance change of a sensing element at a stress-free condition with thermal load is given by:

$$\frac{\Delta R}{R} = \alpha T \tag{5-3}$$

5.4 Hydrostatic Loading

The piezoresistive coefficient B_3 can be calibrated through either a well-controlled out-of-plane shear stress (σ'_{13} or σ'_{23}) or hydrostatic pressure. The application of a controlled out-of-plane shear stress on a sensing element is difficult to achieve and requires accurate positioning of a load transfer applicator on the sensing element. However, hydrostatic loading can be applied using a pressure vessel with non-compressible fluid like hydraulic oil, where the applied pressure will be uniformly distributed on the sensing elements. The resistance change equation for a piezoresistor undergoing hydrostatic pressure is given by:

$$\left(\frac{\Delta R}{R}\right) = -\left(B_1 + B_2 + B_3\right) p + \alpha \mathrm{T} \tag{5-4}$$

Where, p = the applied hydrostatic pressure. The term $-\left(B_1 + B_2 + B_3\right)$ is referred to as the piezoresistive pressure coefficient, π_p. Therefore, B_3 is evaluated as:

$$B_3 = -\left(B_1 + B_2 + \pi_p\right) \tag{5-5}$$

The applied hydrostatic pressure induces a temperature increase in the compressible fluid, which increases the resistance of the piezoresistors by (αT) as

given in equation (5-4). Therefore, measurement of the temperature rise is essential to omit its effect using the previously calibrated α.

5.5 Calibration of the Proof-of-Concept (POC) Chip

The calibration process conducted for the *POC chip* was intended as a preliminary analysis to verify the feasibility of the 10-element rosette through the evaluation of the D_1 and D_2. Non-zero values for these two parameters indicates independency between the linear equations in (3-17), (3-18), and (3-19); therefore, a solution of stresses is possible. Preliminary simple calibration measurements were performed for this purpose as shown in the following paragraphs.

5.5.1 Approach and Setup

The B_1 and B_2 coefficients were calibrated by applying uni-axial loading on the sensing elements oriented at 0° and 90° through a 4PB fixture, which was specially fabricated for this study. Since the *POC chip* had a serpentine shaped piezoresistors, the evaluated B_1 and B_2 coefficients from the loading were considered effective values due to the transverse effect of the resistor arms. This gives the following normalized resistance change equations:

$$\left(\frac{\Delta R_0}{R_0}\right) = B_{1(eff)}\sigma'_{11}$$

$$\left(\frac{\Delta R_{90}}{R_{90}}\right) = B_{2(eff)}\sigma'_{11} \tag{5-6}$$

Where, $B_{1(eff)}$ and $B_{2(eff)}$ are the effective values of the B_1 and B_2 coefficients, respectively. In order to eliminate the transverse effect on the coefficients and extract the fundamental values of the piezoresistive coefficients of silicon, the following correction relationship proposed by Cho *et al*. is used [136]:

$$B_1 = \frac{\gamma B_{1(eff)} + (\gamma - 1) B_{2(eff)}}{2\gamma - 1}$$

$$B_2 = \frac{\gamma B_{2(eff)} + (\gamma - 1) B_{1(eff)}}{2\gamma - 1} \tag{5-7}$$

Where γ is the ratio of the axial section to the sum of the axial and transverse sections of the resistor, such that $\gamma = N_{ax}/(N_{ax} + N_{trans})$ and N_{ax} and N_{trans} are the number of squares in the axial and transverse sections of the resistor.

The 4PB fixture used to generate the uni-axial stress on the sensing elements incremented the applied force F using dead weights each weighing 12 grams. The fabricated wafer was diced into rectangular beams with a width of 7 mm and thickness of 0.525 mm. Measurement of the changes in resistance was performed under the microscope using micro probes contacting the contact pads on the beam. The forces F were applied at a distance L = 84 mm and the supports were located at a distance d = 28 mm, which generated uni-axial stress σ'_{11} in the beam that ranged from 0 to 82 MPa. A Keithley 2400 source meter was used to supply a constant current of 100 μA, while measuring the resistance across the sensing elements. A schematic of the 4PB fixture is shown in Figure 5-2 and the actual setup is shown in Figure 5-3.

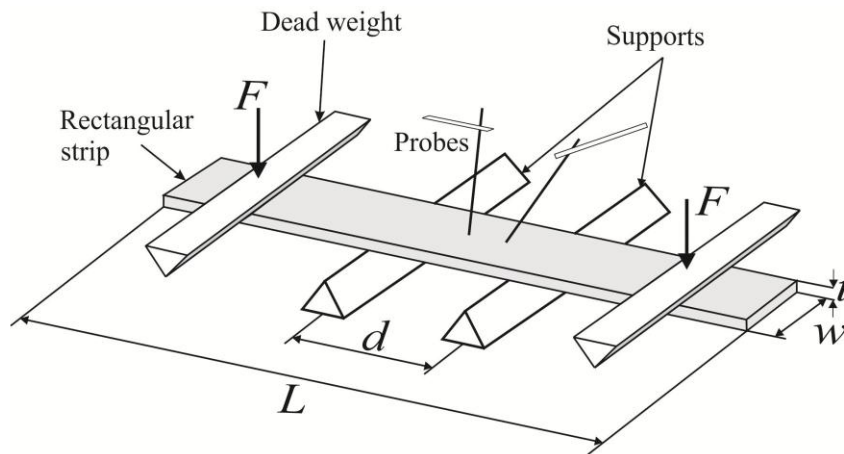

Figure 5-2 Four-point bending (4PB) loading with probes

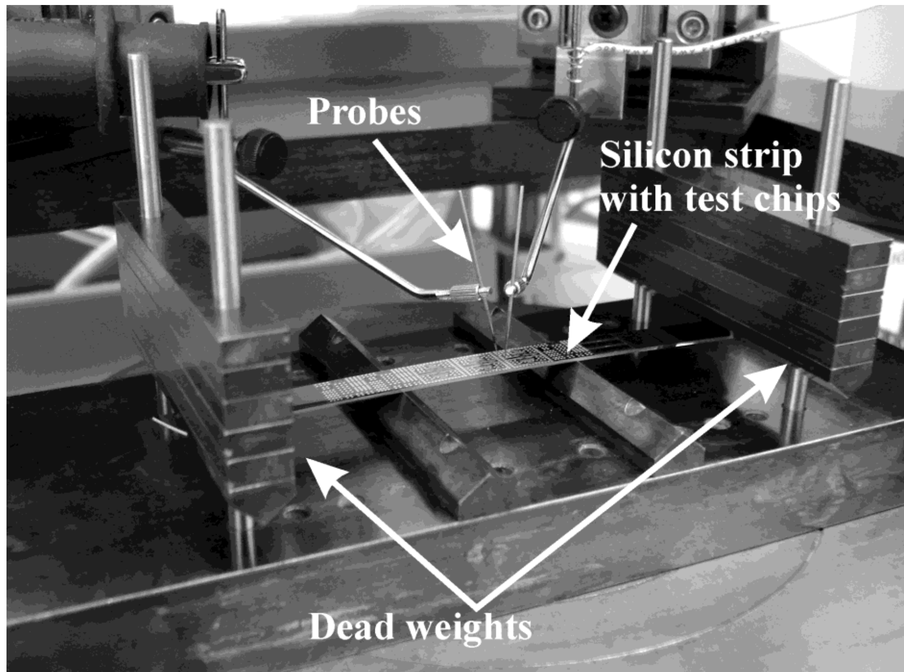

Figure 5-3 Probing of the piezoresistors under 4PB

The temperature coefficient of resistance (α) was calibrated by using a hot plate. The diced silicon beams with an array of sensing rosettes were placed on a hot plate and temperature was varied from room temperature at 23°C to 60°C. Due to the small thickness of the beam and the high thermal conductivity of silicon, the temperature at the set point of the hot plate is assumed to be equal to that at the top of the beam. Similar to the 4PB setup, resistance was measured using a Keithley 2400 source meter by supplying a constant current of 100 µA and contacting the sensing elements by micro probes under the microscope.

At this stage of the research, a simple approach to prove the proposed concept was required. Therefore, a pressure vessel was not used to calibrate B_3; however, evaluation of B_3 was based on the known relationship of the hydrostatic pressure coefficient (π_P) with B_1, B_2, and B_3 given in equation (5-5). Experimental values for π_P in n-Si is given by Tufte *et al.* [23] over a concentration range from 1×10^{15} to 2×10^{20} cm^{-3} and presented in Table 5-1 for each of the three groups of the current piezoresistors.

5.5.2 Calibration Results

The resistance change response under 4PB is shown in Figure 5-4 and Figure 5-5 for R_0 and R_{90} sensing elements, respectively. The slopes of the R_0 represent the B_1 coefficient for the three groups, while the slopes of R_{90} represent the B_2 coefficient for the three groups. The results for the resistance change due to thermal loads are shown in Figure 5-6, where T represent the change in temperature from the reference temperature at 23 °C and the slopes represent the TCR of the three groups.

The measured values of $B_{1(eff)}$, $B_{2(eff)}$, and α as well as the calculated B_i coefficients for the three groups are shown in Table 5-1 along with their corresponding D_1 and D_2 values. These values are averaged over 10 specimens with their standard deviations noted between parentheses in the table.

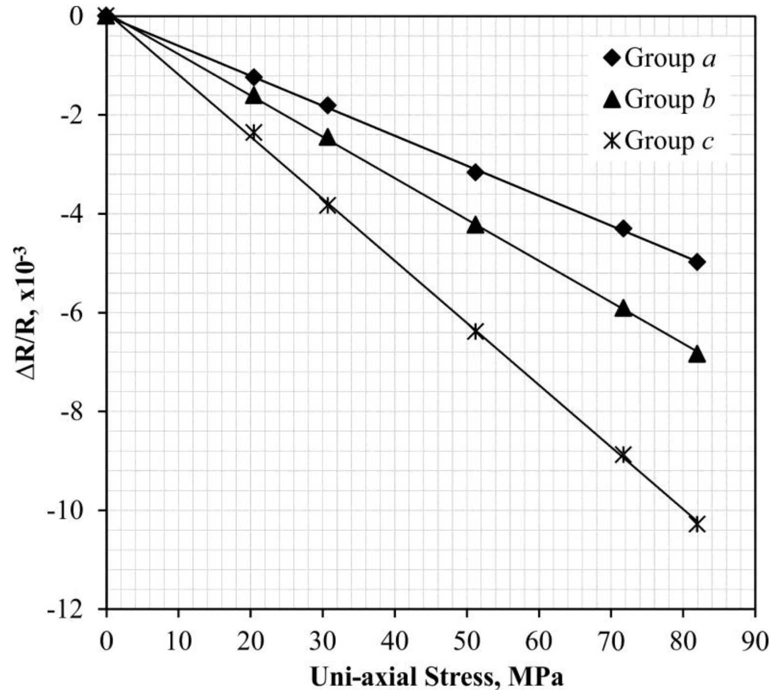

Figure 5-4 *POC chip* calibration results for uni-axial stress versus resistance change for 0 degrees oriented piezoresistors (slopes equal to B_1)

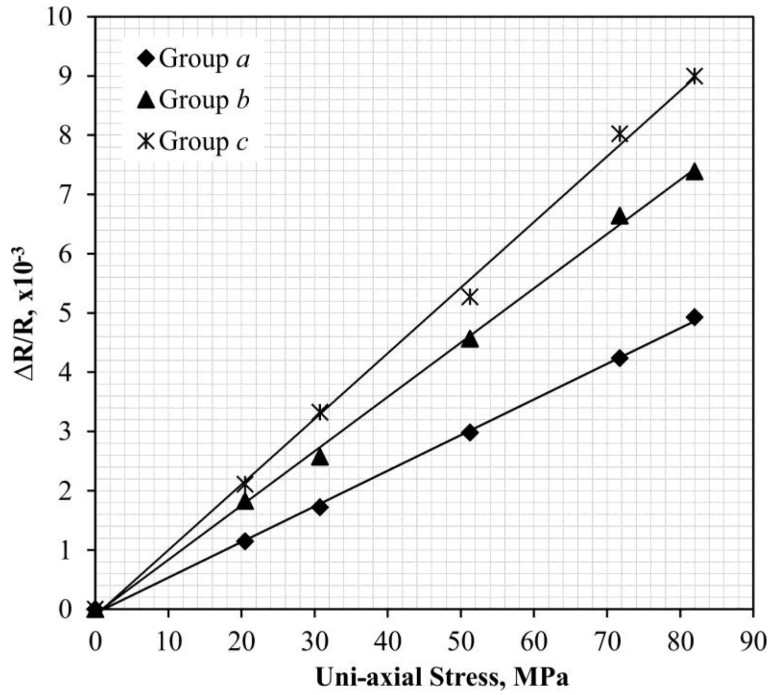

Figure 5-5 *POC chip* calibration results for uni-axial stress versus resistance change for 90 degrees oriented piezoresistors (slopes equal to B_2)

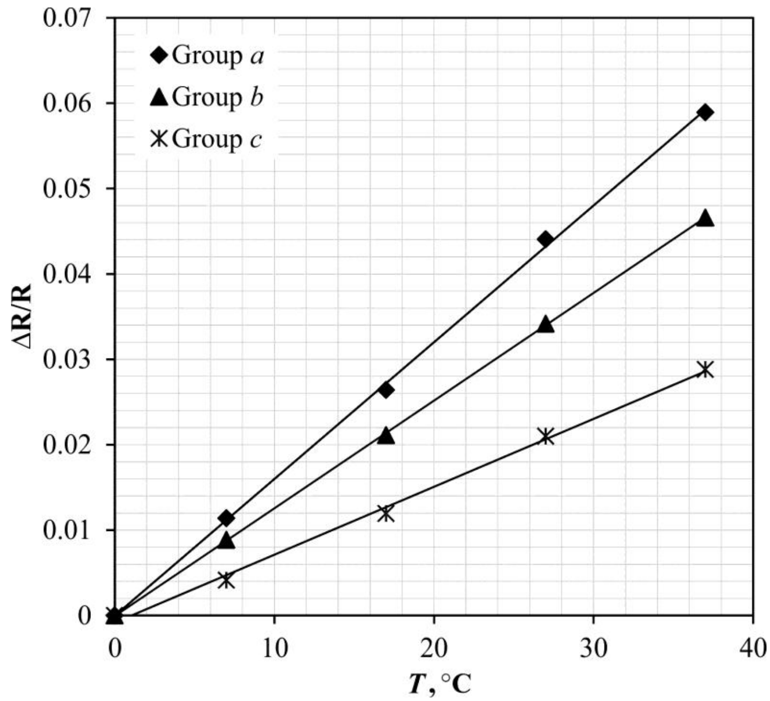

Figure 5-6 *POC chip* calibration results for the thermal loading (slopes equal to α)

Table 5-1 Experimental values for B_i, α, D_1, and D_2 for the *POC chip*

Group	*a*	*b*	*c*
N, cm^{-3}	$2x10^{20}$	$1.2x10^{20}$	$7x10^{19}$
π_p, TPa^{-1} [11]	27	26	25
$B_{1(eff)}$, TPa^{-1}	-72.0	-76.5	-116.3
	(13.5)	(10.4)	(13.6)
$B_{2(eff)}$, TPa^{-1}	64.7	69.0	108.1
	(11.1)	(10.4)	(4.5)
B_1, TPa^{-1}	-75.2	-80.8	-124.5
B_2, TPa^{-1}	67.8	73.3	116.4
B_3, TPa^{-1}	34.4	33.5	33.1
α, ppm/°C	1425.5	1208.6	1055.6
	(189)	(162)	(184)
$\|D_1\|$, TPa^{-2}		538.3	
$\|D_2\|$, $x10^{-3}$ TPa^{-2} $°C^{-1}$		3.1	

The results in Table 5-1 indicate that the present set of piezoresistors have non-zero D_1 and D_2 values, which prove the feasibility of the proposed approach. An important observation from the experimental results is that although the concentration levels of groups *a*, *b* and *c* are close, a solution is still possible for obtaining a non-zero D_1 and D_2. A larger difference between the concentrations of the three groups is expected to provide higher D_1 and D_2 values as indicated by the analytical study and illustrated in Figure 3-14 to Figure 3-17.

The B_i coefficients presented in Table 5-1 demonstrate similar trends to those presented in Figure 3-18, where B_1 and B_2 show a monotonic decrease from group *c* to group *a*, while B_3 shows almost no change. On the other hand, the values of *TCR* in Table 5-1 are seen to increase from 1055.6 ppm/°C at low concentration to 1425.5 ppm/°C at higher concentration. This trend agrees with the experimental behavior of TCR available in the literature and presented in Figure 3-9 and Figure

3-20. Moreover, the good linear fit of the *TCR*-resistance data proves that the assumption of neglecting the second order *TCR* is valid over the studied doping concentration and temperature ranges. Also, the increase in *TCR* compared to the decrease of B_i from group *c* to group *a* illustrate the independency of TCR and B_i which proves the feasibility of solving equations (3-20) for both *dual-polarity* and *single-polarity* rosettes.

5.6 Calibration of the Test Chip

The calibration of the *test chip* involved the three loading applications; uni-axial, thermal, and hydrostatic. As discussed earlier in Chapter 2, calibration of the piezoresistive devices has commonly been carried out through wire-bonding the sensing chip to a printed circuit board (PCB) and/or probing the metallic pads on the chip. The calibration of the *test chip* did not utilize the micro probes used in the *POC chip* calibration. However, the approach developed by Richter *et al.* [112], which utilizes a zero-insertion force (ZIF) connectors to connect the edges of the silicon beam to the measurement circuitry, was adopted in the calibration process. The microfabricated wafer was diced into straight beams containing a number of sensing chips and connected to a ZIF connector (TE Connectivity, part No. 1-1734839-3) that is connected to the measurement equipment. In all three calibration setups, only the 0° and 90° sensing elements are calibrated, i.e. the six sensing elements R_1, R_3, R_5, R_7, R_9, and R_{10}. The sensing rosette is connected to the ZIF connector through seven aluminum traces sputtered over the surface of the silicon beam, where 6 traces provide the bias voltage to the six sensing elements and the seventh is a common ground. The use of ZIF connectors is found to expedite the calibration process and eliminate the errors due to the applied forces from the contacting probes or attaching the silicon die to a PCB. The silicon beam used for calibration is shown in Figure 5-7 before and after attaching to the ZIF connector. A Keithley 2400 source meter is used to supply 100 μA to each piezoresistor and measure the voltage drop, while a rotary switch box is used to switch between each of the six piezoresistors. A schematic of the measurement

setup for the calibration is shown in Figure 5-8, which was used in the three load applications except with some modifications to fit the specific setup. Data logging was performed manually by recording the resistance changes from the source meter to a computer.

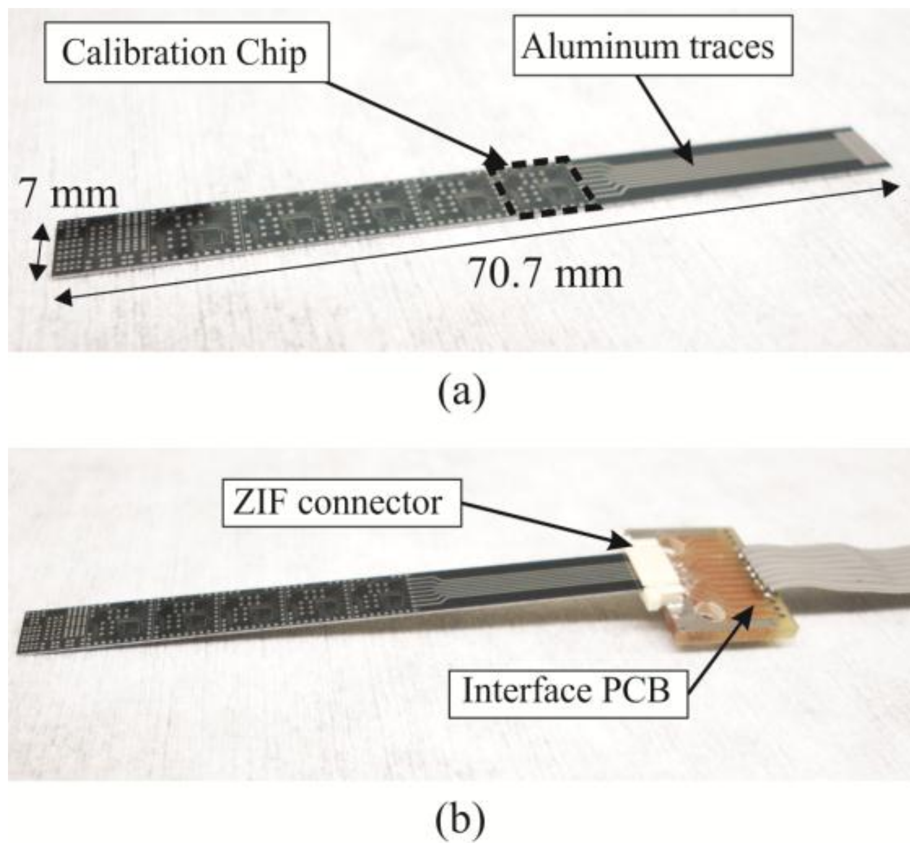

Figure 5-7. Silicon beam (a) before and (b) after connection to a ZIF connector

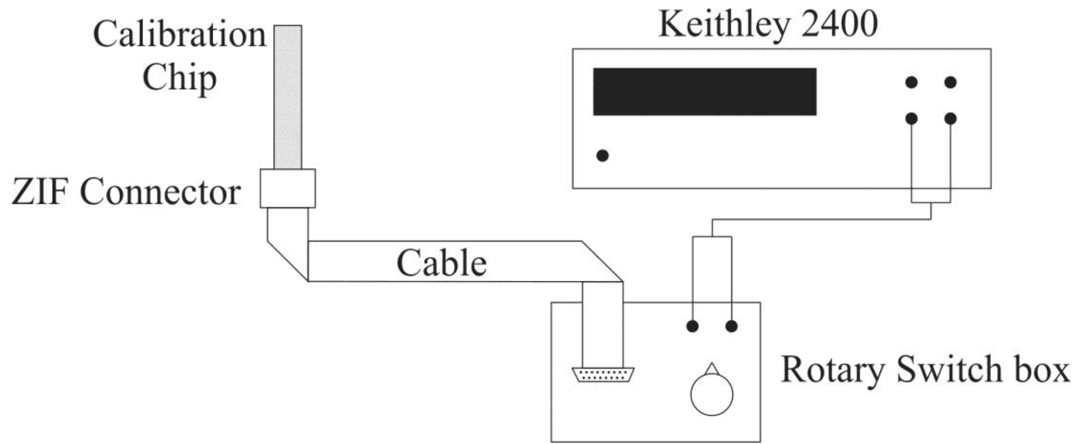

Figure 5-8 Measurement Setup for the calibration of the *Test Chip*

5.6.1 Uni-Axial Stress Loading

5.6.1.1 4PB Fixture Setup

The same 4PB fixture used in the calibration of the *POC chip* was adopted in this calibration process; however, with some modifications to accommodate the ZIF connectors. Each diced silicon beam was connected to two ZIF connectors at the end of the beam, where one is electrically connected to the calibration chip and the other is a dummy load for balancing. Both the active and dummy connectors were carefully matched in weight to 1.1 grams with a maximum variation of ±0.05 grams. The 4PB fixture is supported on a balance, sensitive to 0.1 grams, to measure the exact applied load at each dead weight increment. The electrically active ZIF connector is wired to an intermediate printed circuit board (PCB) through fine 42 AWG (~65 μm diameter) enameled copper wires to eliminate external uncontrolled loads transmitted to the silicon beam. The PCB is supported on an aluminum frame that does not contact the 4PB fixture or balance. At each dead weight load increment, the sensitive balance records the exact applied dead weights and the fine copper wires did not alter this load. The intermediate PCB is fixed to a support frame that does not contact the 4PB fixture as shown in figure 5-9.

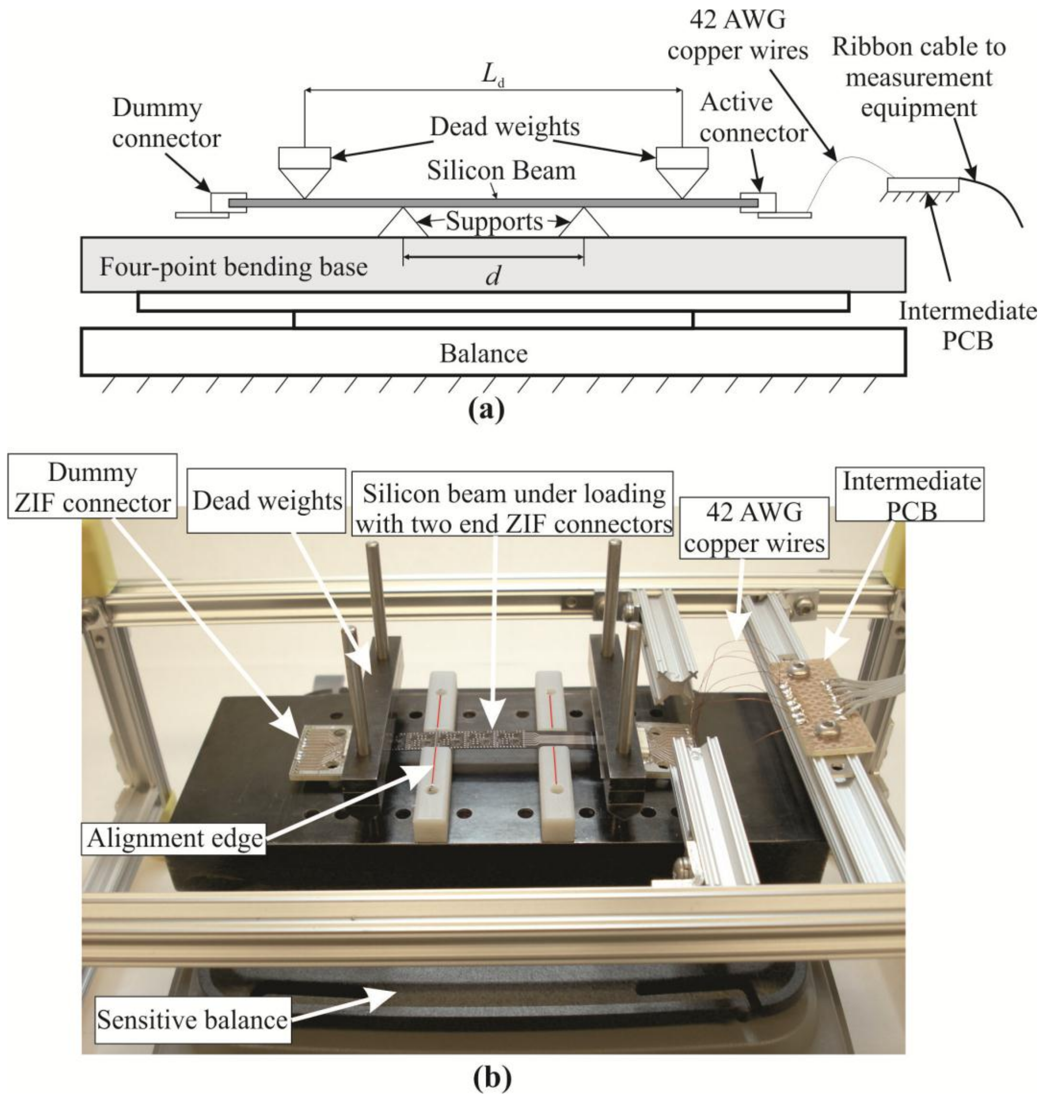

Figure 5-9. Four-point bending loading fixture; (a) schematic and (b) actual setup

The bending moment diagram generated from this loading setup is shown in figure 5-10, where F_c and F_d represent the forces from the ZIF connector and the dead weights, respectively. The force F_d is applied as a point load, while F_c is applied as a distributed load at the end of the beam, where the area of contact of the ZIF connector on the beam is measured to be 2 mm x 7 mm. The uniform uni-axial stress transmitted to the upper fibers of the beam between the two supports is given by:

$$\sigma = \frac{6\left(F_c x_1 + F_d x_2\right)}{wh^2} \tag{5-8}$$

Where, x_1 and x_2 = the distances to the middle support from the ZIF connector and dead weight, respectively, w = width of rectangular beam, and h = thickness of the rectangular beam. If the effect of the end connector load is eliminated from equation (5-8) assuming that the first incremental load is the first dead weight, then the equation reduces to:

$$\sigma = \frac{3F_d (L_d - d)}{wh^2} \tag{5-9}$$

Where, L_d = distance between the two dead weights and d = distance between the middle supports.

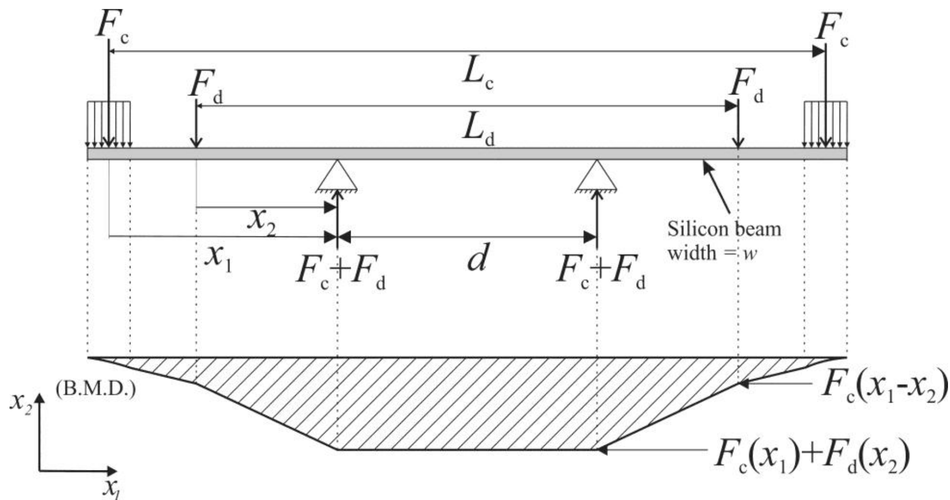

Figure 5-10. Bending moment diagram with ZIF end connectors

5.6.1.2 Analysis of Beam Misalignment

The current 4PB fixture setup utilizing ZIF connectors has lower percentage error in the calculated uni-axial stress compared to using micro probes, which produces high stress errors if the applied dead weight forces are small. For example, the percent error in stress can reach around 50% if the ratio between probe force and dead weight is 1/5 [133, 137]. The stress percentage error due to weight and length measurement, loading symmetry, and beam rotation is estimated to be a maximum of 1% compared to 5% if probe forces are added. However, an additional error in the current setup is due to the longitudinal position of the silicon beam on the 4PB fixture as shown in figure 5-11. In this case, the location of the ZIF connectors relative to the dead weights is unsymmetrical and is expected to affect the stress uniformity at the calibration rosette and introduce an additional error to the calculated stress.

A finite element model (FEM) was developed using the commercial software ANSYS® multiphysics release 13 to study the beam longitudinal translation error (s) from 0 to 2.5 mm under the ZIF connectors load. The model is based on linear structural analysis using Solid186 20-noded structural quadrilateral elements. The beam's geometry and ZIF connector force (F_c) are given in Table 5-2. The force F_c was applied at the ends of the beam as a distributed pressure covering the ZIF connector contact area of 7 mm x 2 mm. The beam's supports were modeled as displacement constraints in the x_3-direction as shown in Figure 5-12. Two point constraints at the center of the support lines in the x_2-direction and a constraint line along the centerline of the beam along the x_1-direction were applied to avoid free body motion of the beam. The beam's x_1-longitudinal position was varied from 0 to 2.5 mm over 5 increments and the stress field at the calibration rosette was recorded at each increment. The ANSYS code for this problem is presented in Appendix C.

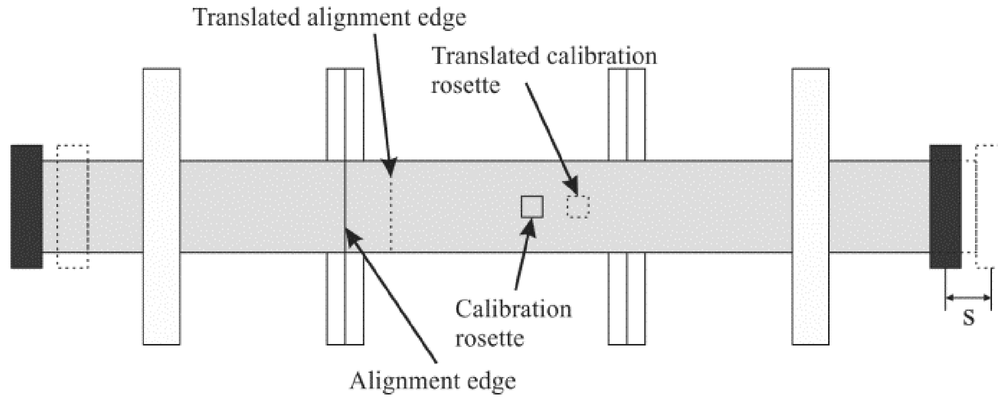

Figure 5-11. Schematic of possible error in beam longitudinal position

The resulting contour plots of σ_{11} over the surface of the beam are shown in Figure 5-13. The effect of the beam's longitudinal misalignment is shown in Figure 5-14, where the stress non-uniformity and error increases with the translation error. The stress non-uniformity is calculated as the difference between the minimum and maximum stress at the calibration rosette extracted from the FEM divided by the analytically calculated stress from equation (5-9). On the other hand, the stress error is the average stress at the calibration rosette divided by the analytically calculated stress from equation (5-9). An alignment edge on the silicon beam is used to correctly align the beam with the 4PB supports as shown in figure 5-11. The beam can be easily aligned within s=0.5 mm error, which is the width of the support centerline. Therefore, the maximum stress error due to the beam longitudinal misalignment is expected to be around 0.3%.

Table 5-2. Geometry and loading conditions on 4PB silicon beam

Geometry, mm		Loads, mN	
L_c	70.7	F_c	10.8
L_d	56	F_d (increment)	117.7
d	28		
w	7		
h	0.3		

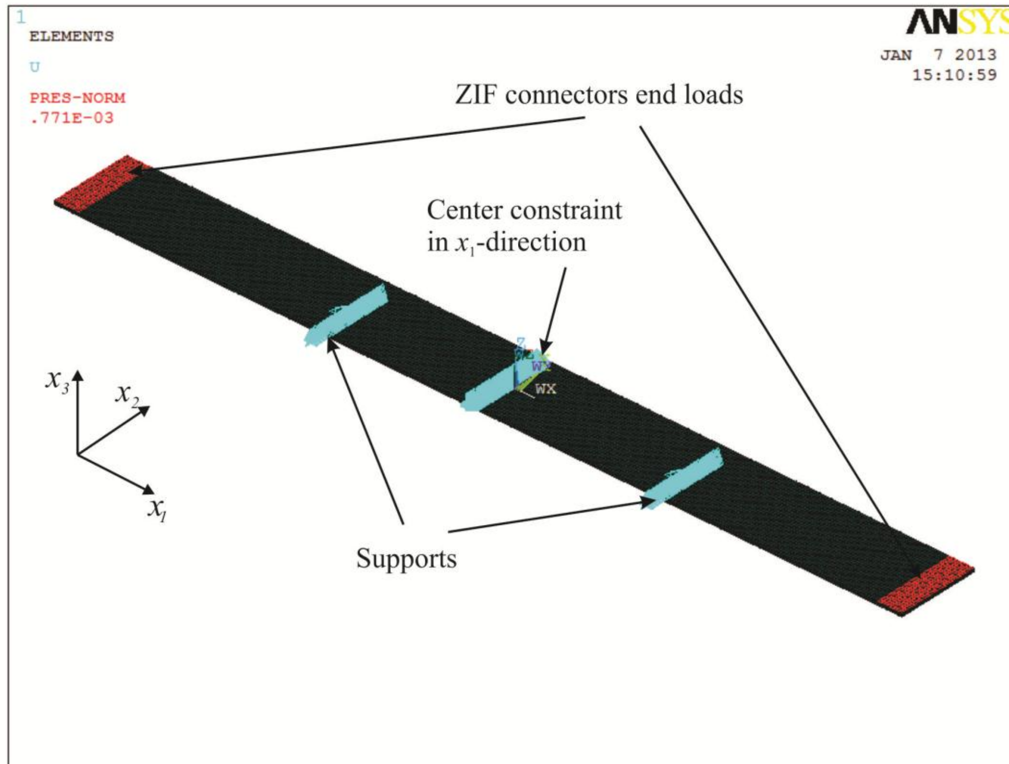

Figure 5-12 Applied boundary conditions on the FEM of the silicon beam

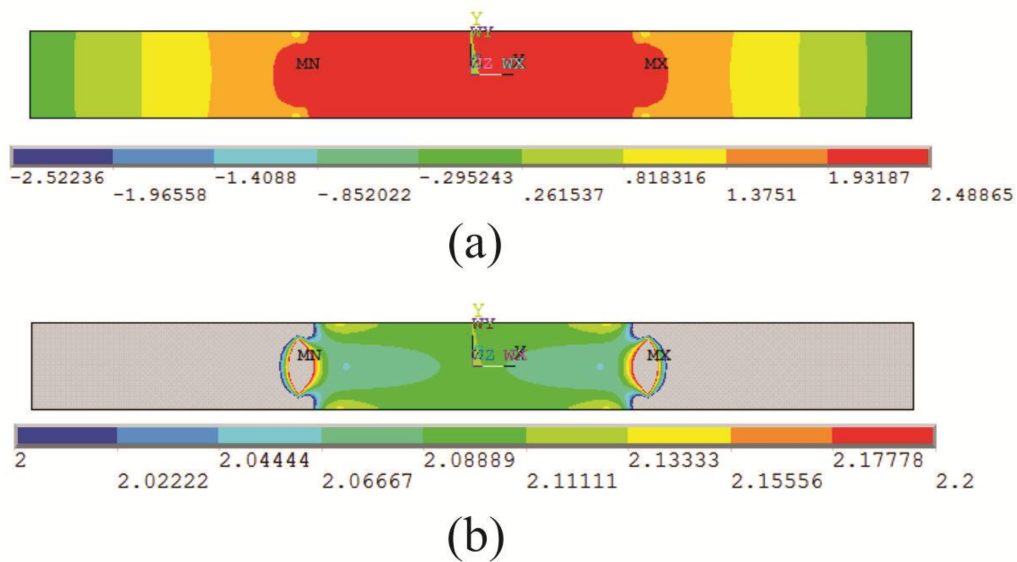

Figure 5-13 FEM contour plot of (a) σ_{11} over the beam's length, and (b) σ_{11} over the beam's center region at translational misalignment s = 0

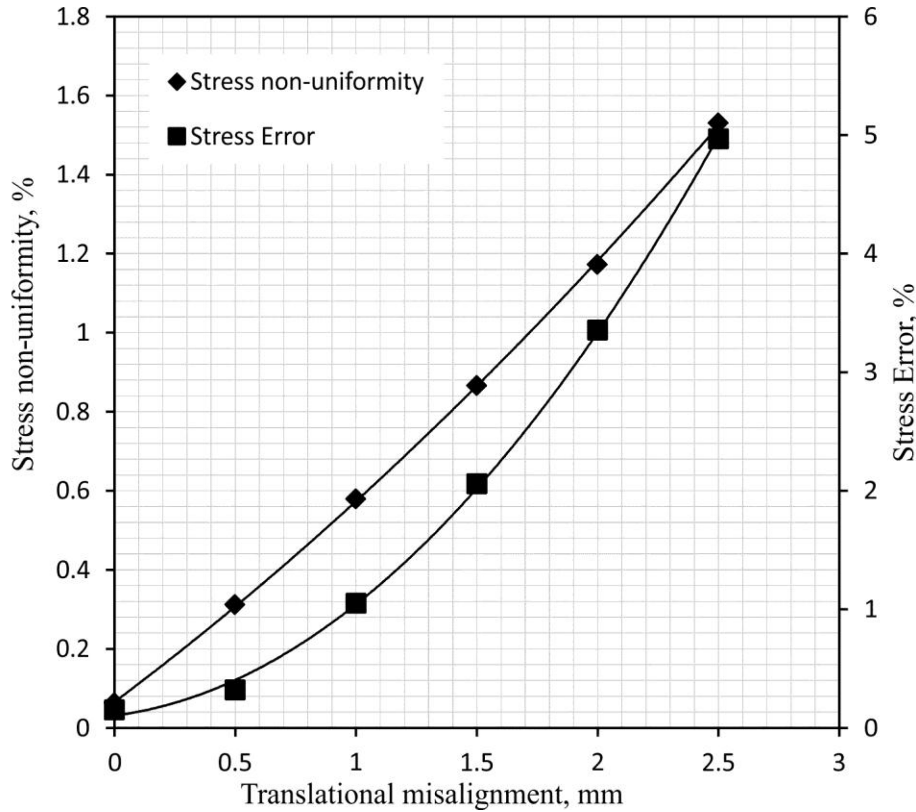

Figure 5-14. The non-uniformity and error in the stress at the calibration rosette given a longitudinal translation misalignment of the beam

The geometry and loading conditions specific to the current silicon beam under study is given in table 5-2. Solution of equations (5-8) and (5-9) gives a uni-axial stress of 17.8 MPa and 15.7 MPa, respectively for a single dead weight load, such that the stress applied due to the end ZIF connector is 2.1 MPa and the incremental applied stress is 15.7 MPa. Four dead weights were applied, which produces a total uni-axial stress of 62.8 MPa on the surface of the silicon beam. Sample stress sensitivity data from the 4PB measurements for the R_0 and R_{90} resistors are shown in figure 5-15. The resistance change response due to the applied uni-axial stress shows a good linear response, with the slopes of the lines in figure 5-15(a) correspond to B_1 and those in figure 5-15(b) correspond to B_2.

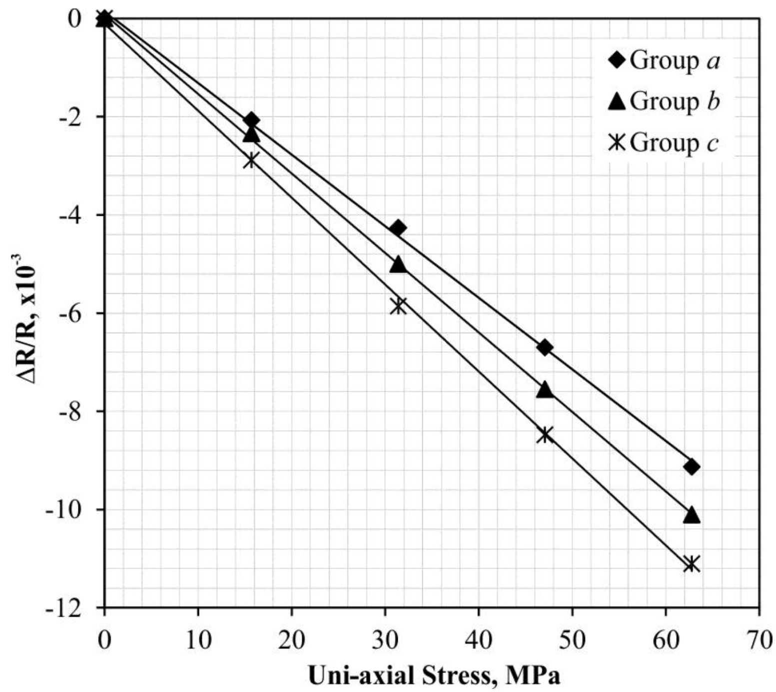

Figure 5-15. *Test chip* calibration results for uni-axial stress versus resistance change for 0 degrees oriented piezoresistors (slopes equal to B_1)

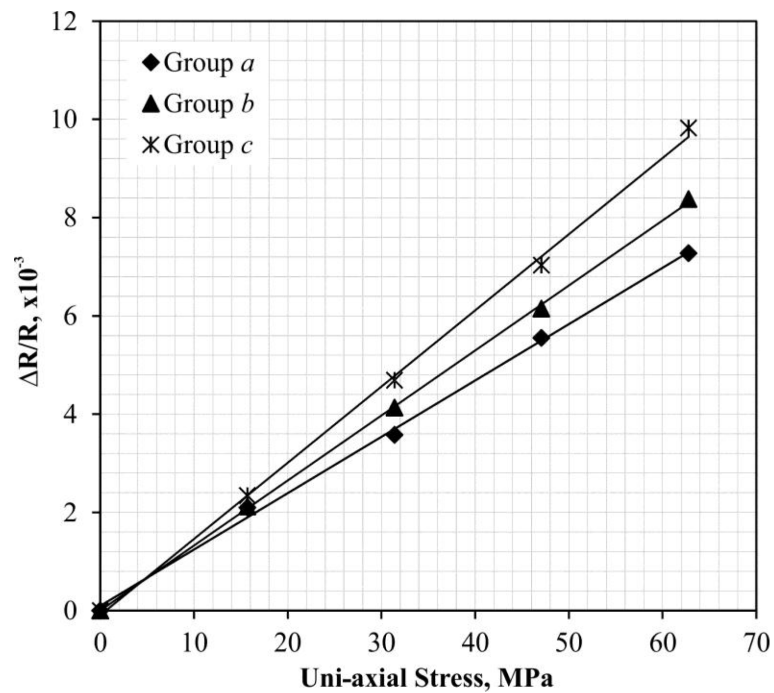

Figure 5-16. *Test chip* calibration results for uni-axial stress versus resistance change for 90 degrees oriented piezoresistors (slopes equal to B_2)

5.6.2 Thermal Loading

The TCR (α) was calibrated by applying thermal loads on the silicon beam connected to the ZIF connector using an environmental chamber. Temperature was varied from -40 °C to 60 °C and the change in resistance was recorded at each 10 °C increment for each piezoresistor. The environmental chamber used was an HP 6890 series GC system with compressed carbon dioxide (CO_2) cooling located at Syncrude Canada Ltd. Research Centre in Edmonton. The chip was held by a ZIF connector on a PCB and attached to an aluminum frame that was developed for the setup as shown in Figure 5-17. The thermal calibration setup is shown in Figure 5-18. A ribbon cable is connected from the PCB to the rotary switch box and connected to the Keithley 2400 source meter. A total of 4 sensing chips were calibrated where each has two sensing elements from each group. Therefore, a total of 8 sensing elements were calibrated from each group. Sample temperature sensitivity measurements are shown in figure 5-19, where T represents the temperature change from the reference temperature at 23°C and the slopes of the lines represent α for the three groups.

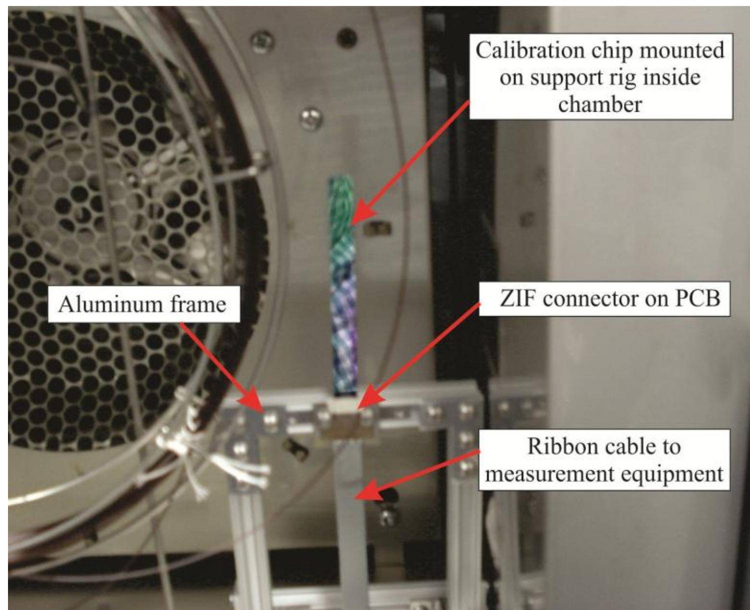

Figure 5-17 Calibration chip fixture inside the environmental chamber

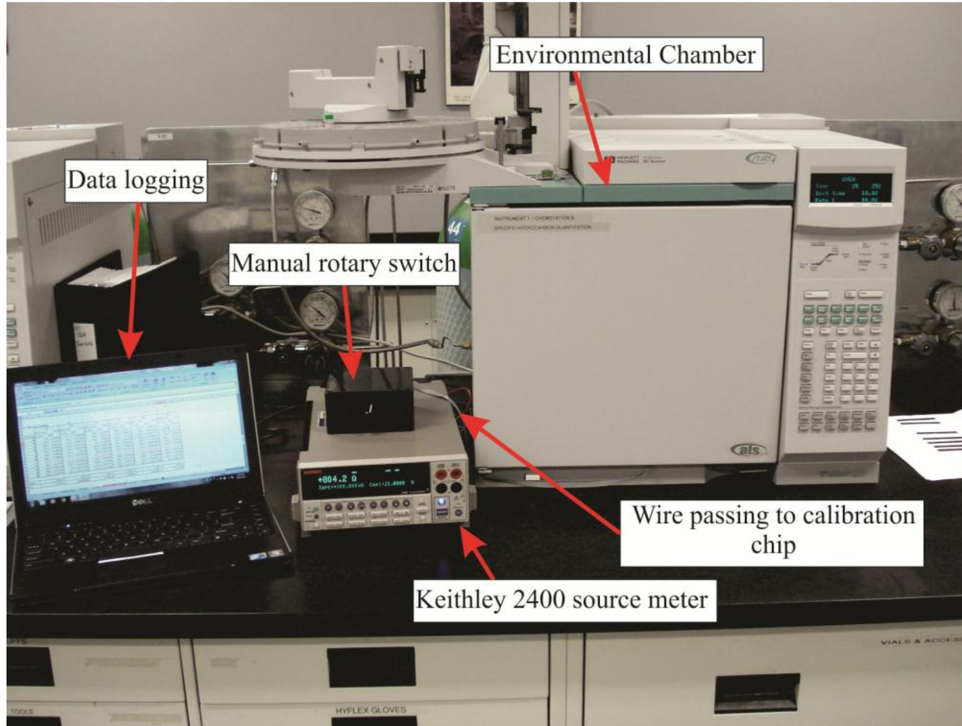

Figure 5-18 Thermal load calibration setup including environmental chamber, source meter, and switch box

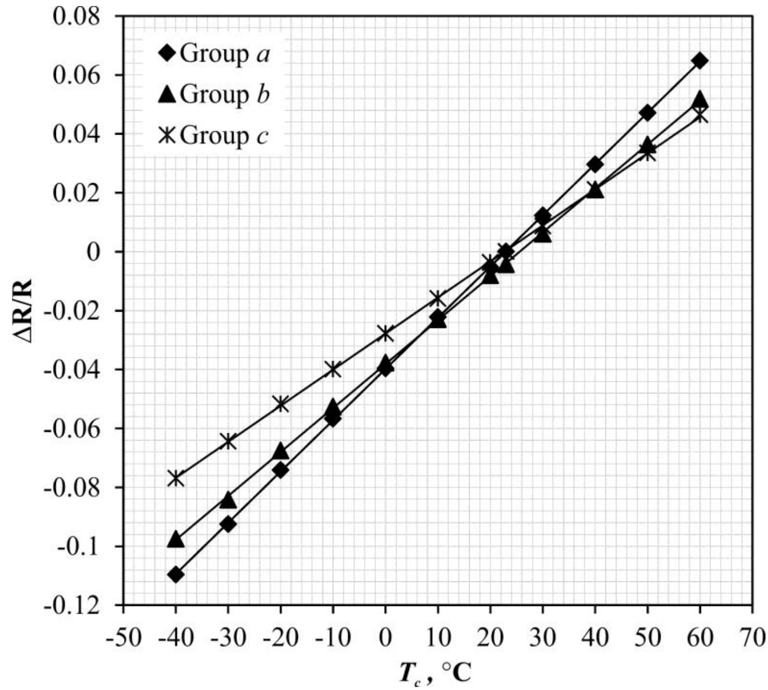

Figure 5-19. Calibration results for temperature versus resistance change (slopes equal to α)

5.6.3 Hydrostatic Loading

The piezoresistive coefficient B_3 is calibrated through a controlled hydrostatic loading. In this setup, a pressure vessel filled with hydraulic fluid is used to apply hydrostatic pressure on the sensing chip, which is connected through the ZIF connector to the measurement circuitry. A 1 L pressure vessel rated at 20.7 MPa was fabricated specifically for this research by Parr Instrument Company and includes a wire gland to pass 24 AWG wires to the sensing chip. The pressure vessel and auxiliary equipment are shown in Figure 5-20 to Figure 5-22. The hydraulic fluid inside the vessel is pressurized using a manual hydraulic pump to produce a maximum internal pressure of 18.6 MPa. An analog pressure gauge is connected to the pressure head to measure the internal pressure with a relief valve to discharge the internal fluid for pressure control. A rupture disc valve rated at 20.7 MPa is included on the head as a safety precaution. The calibration chip was connected to a ZIF connector with a PCB soldered to the wires in the vessel's wire gland as shown in Figure 5-20. The 7 wires from the vessel's head are connected to the rotary switch box, which in turn is connected to the current source meter. A Resistance Temperature Detector (RTD) sensor is installed in a thermo-well in the vessel's head to measure the temperature increase due to the applied pressure. The RTD is connected to a temperature monitor for display.

At each applied pressure increment, the resistance measurement is taken after 1 min to wait for the fluid temperature to stabilize. A plot of the pressure-temperature relationship inside the vessel is given in Figure 5-23, which shows the fluid temperature increases by around 1.2 °C due to the applied pressure of 18.6 MPa.

The resulting pressure versus resistance change is shown in Figure 5-24, where the "raw data" correspond to the resistance change output due to the hydrostatic and thermal loadings, while the "temperature effects" refer to the αT component in the resistance change. At each pressure loading increment, the effect of the increase in resistance due to temperature is subtracted from equation (5-4) using

the calibrated α specific to the calibration chip to come up with the adjusted pressure versus resistance data shown in figure 5-25 for the three groups of sensing elements; *a*, *b*, and *c*. The slopes of the lines in figure 5-25 represent the piezoresistive pressure coefficient (π_p), which is used along with the calibrated B_1 and B_2 from the 4PB to solve for B_3. A total of 8 sensing elements were calibrated under hydrostatic loading.

The resulting resistance change from the sensing elements due to the applied hydrostatic load of 18.6 MPa was around 2 Ω. The low resistance change is due to the low resistance of the sensing elements (~ 1 k Ω) and the low sensitivity of the elements to the hydrostatic pressure. Moreover, the αT component was negating the pressure sensitivity, thus decreasing the amount of resistance change. This small resistance change led to some difficulty in the measurements especially to capture the variations over 4 load increments. A higher applied pressure can induce a higher resistance change; however, a high pressure rating pressure vessel would have been required. On the other hand, having a larger resistance value can provide a better resolution, which is one limitation of the current fabricated chip that will require modification in the future prototypes.

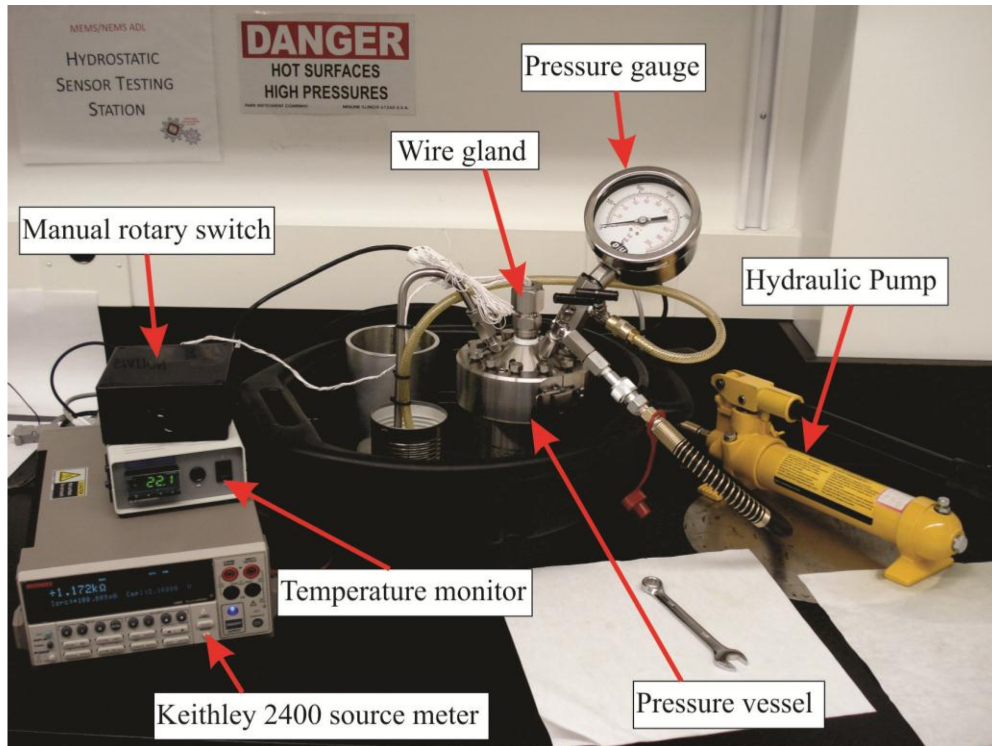

Figure 5-20 Hydrostatic pressure vessel calibration setup

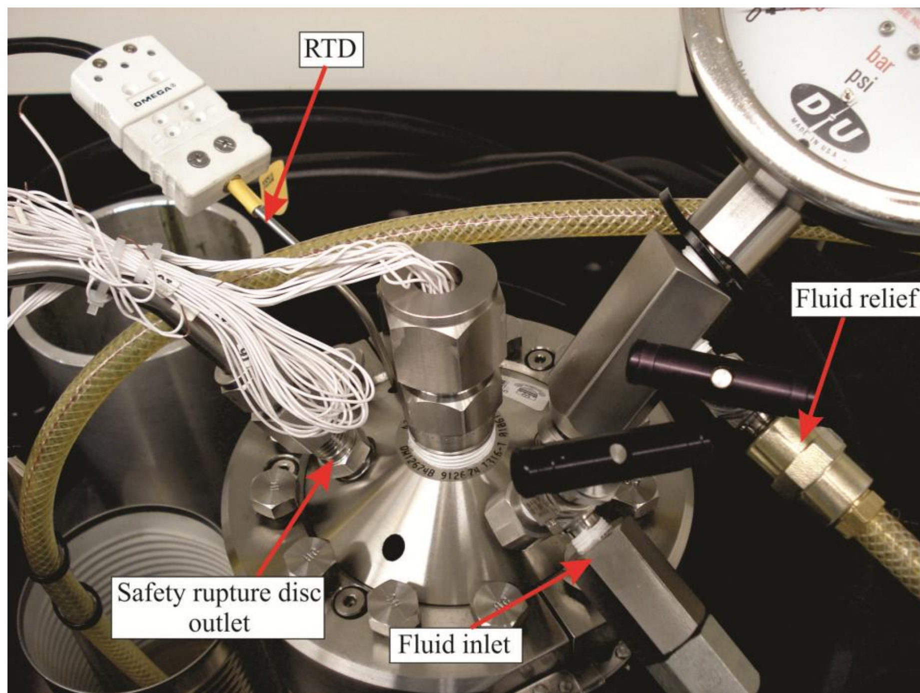

Figure 5-21 Pressure vessel head with fluid inlets, wire-gland and RTD connection

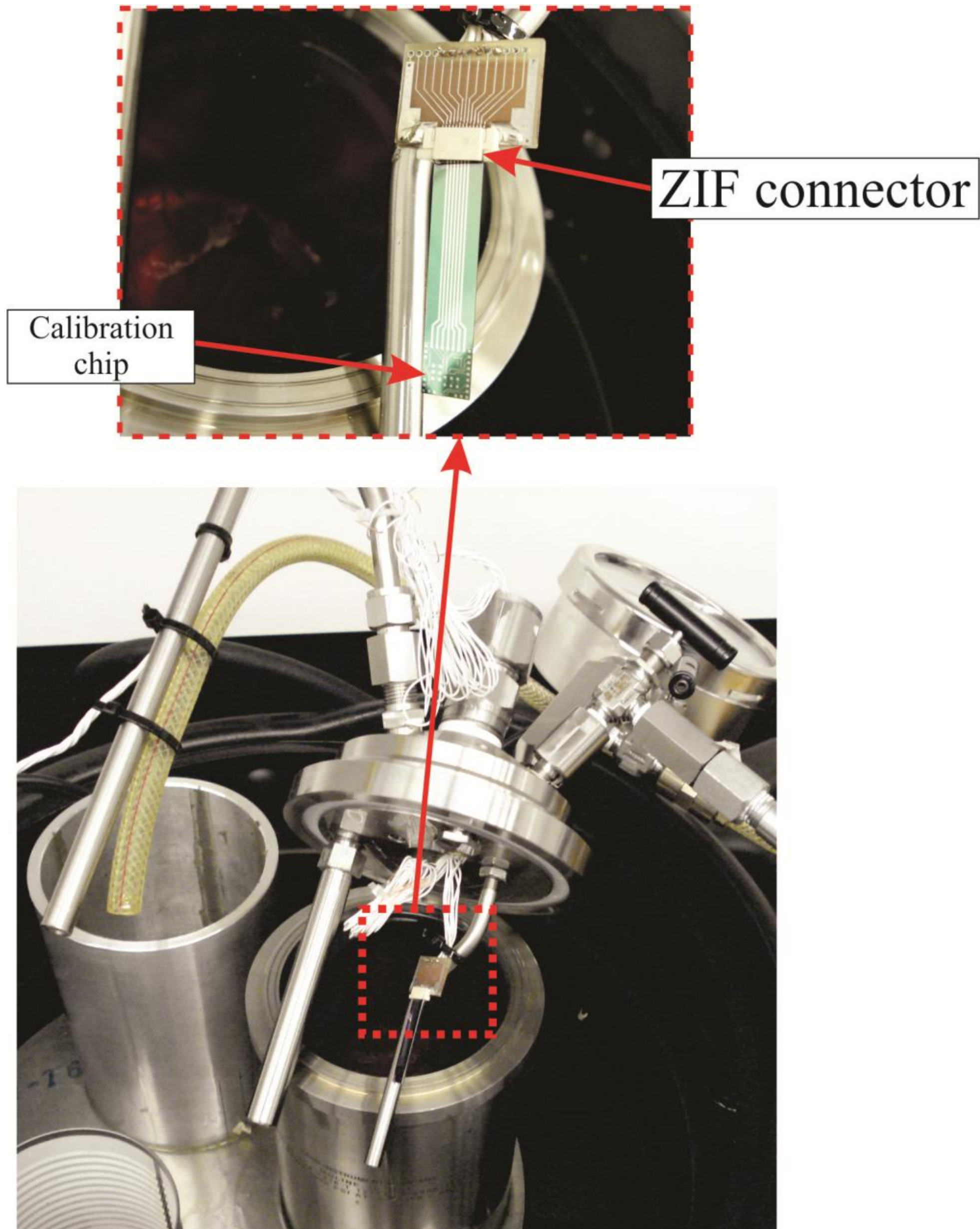

Figure 5-22 Calibration chip connectivity in the pressure vessel

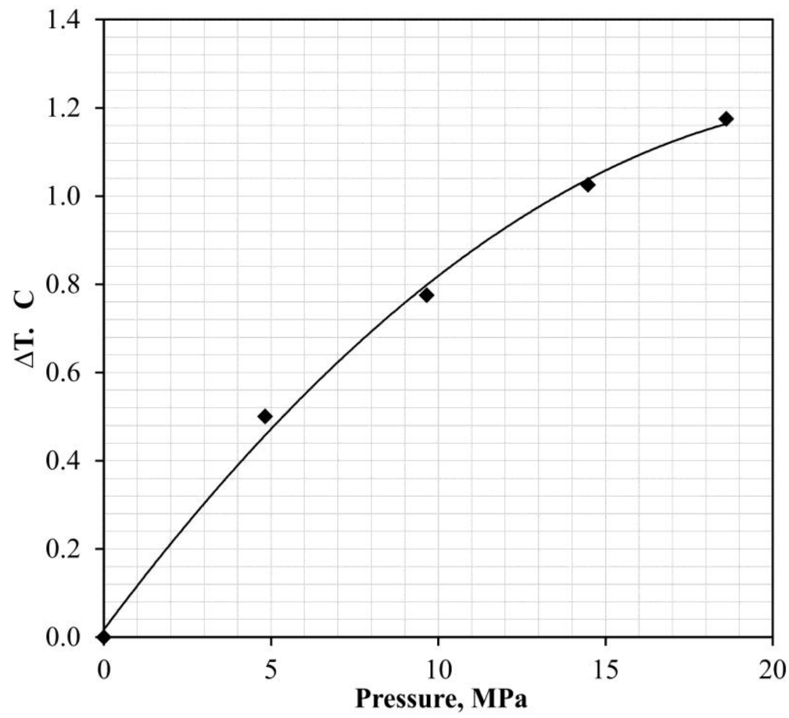

Figure 5-23. Pressure-temperature relationship of the hydraulic fluid inside the pressure vessel

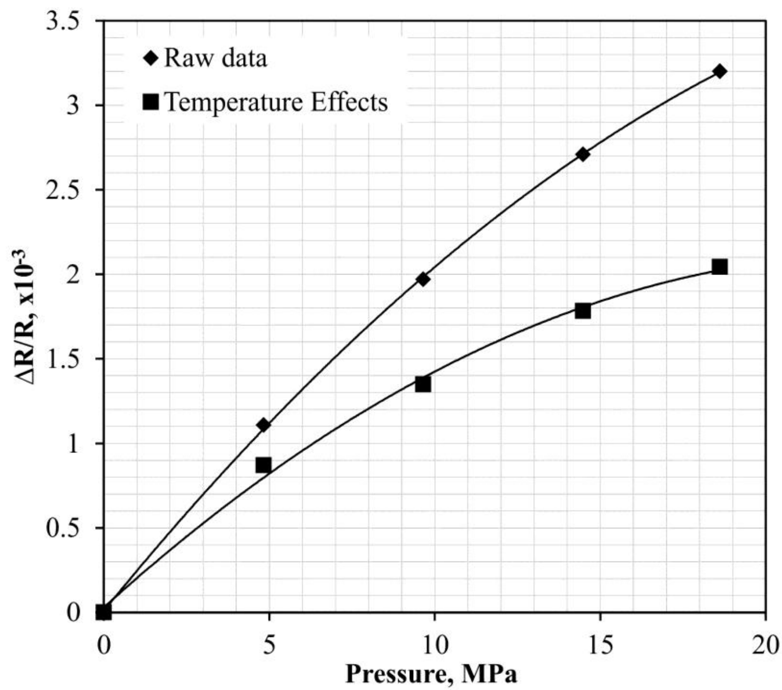

Figure 5-24. Calibration results for hydrostatic pressure versus resistance change

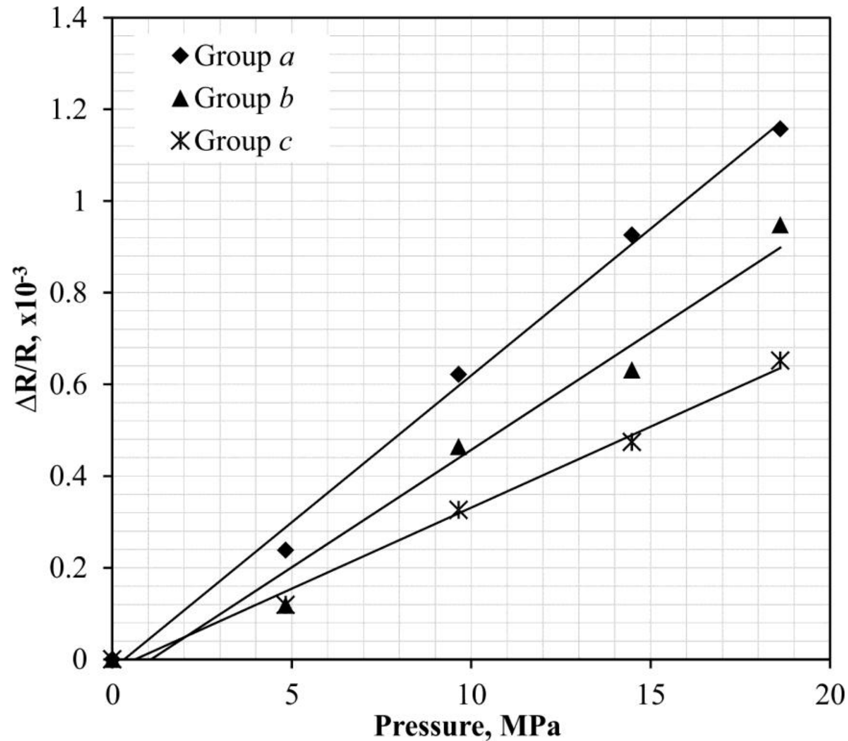

Figure 5-25. Adjusted results for hydrostatic pressure versus resistance change without temperature effects (slopes equal π_p)

5.6.4 Calibration Results

The final calibrated coefficients are given in table 5-3 along with their corresponding D_1 and D_2 values. The calibrated values are averages of 8 calibration elements with their standard deviations noted between parentheses. The results demonstrate the increase in the absolute values of B_1 and B_2 from low concentration to higher concentration. The piezoresistive pressure coefficient (π_p) is shown to increase from low to high concentration, thus verifying the trend presented by Tufte *et al.* [23] at this range of concentration. The calibrated B_3 is small compared to the other coefficients B_1 and B_2, which suggests that the sensitivity to the out-of-plane normal stress σ'_{33} is lower compared to the other stress components. The sensitivity of the different stress components is noted in the table, where the shear stresses have the highest sensitivity, followed by the in-

plane normal stresses σ'_{11} and σ'_{22} then σ'_{33} is the lowest. Also, σ'_{11} and σ'_{22} have low sensitivity with the ±45 degrees oriented sensing elements which are related to $(B_1+B_2)/2$ (i.e. R_2, R_4, R_6, R_8) as given by equations (3-16). More interestingly, the rate of change of B_1 and B_2 with concentration is almost the same as shown from their slopes in figure 5-26, while B_3 shows a different slope with impurity concentration due to its primary dependence on the shear PR coefficient π_{44}. Also, TCR is shown to increase with impurity concentration with a different slope than the B_i coefficients. Moreover, the calculated D_1 and D_2 are non-zero, which allows for independent equations (3-17) to (3-19).

Table 5-3 Experimental values for B_i, α, D_1, and D_2 for the *test chip*

Group	Relates to	*a*	*b*	*c*
N, cm^{-3}		7.4x10^{19}	4.7x10^{19}	2.9x10^{19}
B_1, TPa^{-1}	σ'_{11} and σ'_{22}	-153.7	-162.2	-170.7
		(3.7)	(3.1)	(3.2)
B_2, TPa^{-1}	σ'_{11} and σ'_{22}	116.1	125.2	132.7
		(5.1)	(5.1)	(4.9)
π_p, TPa^{-1}		50.1	38.4	31.8
		(6.0)	(6.2)	(5.1)
B_3, TPa^{-1}	σ'_{33}	-12.5	-1.4	6.2
α, ppm/°C		1780.6	1526.6	1223.0
		(43.02)	(53.56)	(48.78)
$(B_1+B_2)/2$	σ'_{11} and σ'_{22}	-18.8	-18.5	-19
(B_1-B_2)	σ'_{12}	-269.8	-287.4	-303.3
$2\sqrt{2}(B_2-B_3)$	σ'_{23} and σ'_{13}	363.9	357.8	357.8
D_1, TPa^{-2}			2825.9	
D_2 x 10^{-3}, TPa^{-2} °C^{-1}			50.6	

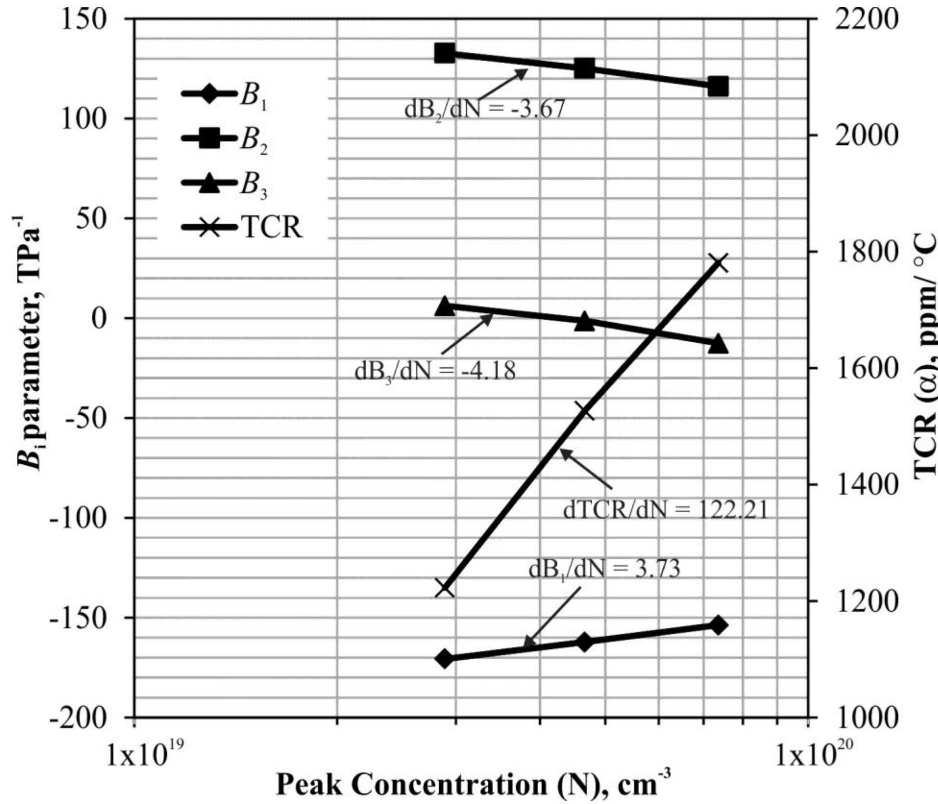

Figure 5-26. Effect of impurity concentration on B_i and α

5.7 Conclusions

This chapter presented the calibration processes conducted to extract the B_i coefficients and the TCR for the three groups of the sensing elements. The theoretical and experimental approaches for calibration of the coefficients were presented early in the chapter. Two major calibration processes were discussed; the first is the calibration of the *POC chip* and the second is the calibration of the *Test Chip*. The results demonstrate the independent behavior of the B_i coefficients and TCR with impurity concentration, especially the B_3 coefficient which is independent from B_1 and B_2. This confirms that the unique properties of the shear piezoresistive coefficient π_{44} in n-Si can be used to develop the 10-element rosette discussed in Chapter 3.

CHAPTER 6: TESTING OF THE SENSING CHIP[4]

6.1 Overview

The objective of the testing of sensing chip is to demonstrate its ability to extract the 3D stresses from the 10-element rosette. This chapter demonstrates the details pertaining to the testing of the microfabricated *test chip*. It presents the adopted test approach including the test setup, design of the specimens, packaging of the sensing chip, characterization of the interface between the chip surface and surrounding host material, test measurement, and finite element modeling of the stress output. The final results are presented in terms of the resistance change output from the sensing elements and the corresponding stress output, and a comparison with the stress output from the finite element model. Moreover, a preliminary test for hysteresis is presented to show that the stress output from the rosette has no drifts over 10 cycles of compressive and tensile loads.

6.2 Test Approach

The selection of the test approach was based on: (1) inducing the maximum number of stress components for testing and (2) ease of specimen preparation, setup, and measurement. The selected approach was the four-point bending of a chip-on-beam as shown in the schematic in Figure 6-1. The beam is a standard printed circuit board (PCB) connected to the measurement equipment using edge connectors and the chip is bonded to the PCB using anisotropic conductive adhesive (ACA). The bonded chip acts as a stiffener to the PCB beam, which creates stress fields in the adhesive and the chip that are well developed using the classical shear lag model developed by Volkersen in 1938 and later by Goland and Reissner in 1944 to include the effect of the bending moment [139]. There have been a number of analytical and numerical solutions to the bonded stiffener

[4] Some of the material in this chapter has been submitted for publication as a paper in the *Journal of Micromechanics and Microengineering [138].*

problem, specifically the stress analysis in rectangular composite patches, which resembles the current chip-on-beam problem [87, 140, 141]. These analyses provide an insight about the expected stress field at the chip/adhesive interface under the uni-axial loading induced from the four-point bending. At the center of the chip, the normal stress σ_{11} is the maximum induced stress with an opposite and lower σ_{22} developed due to transverse material deformation, while all other stress components are zero. On the other hand, at the edges of the chip/adhesive interface the out-of-plane shear stresses are maximum. This variation of the stress field over the chip/adhesive interface is utilized to test five stress components in a controlled manner, which are σ'_{11}, σ'_{22}, σ'_{23}, σ'_{13} and σ'_{12}.

The sensing chip, measuring 7 mm x 7 mm x 0.3 mm, was diced from the fabricated wafer using a precision dicing saw at the nanoFab with a width of cut of 50 μm. The chip has three rosette-sites; center rosette and two edge rosettes as shown in Figure 6-2. The center rosette is made up of the full 10-element rosette capable of extracting the six stress components, while the edge rosettes are reduced rosettes used primarily to extract the shear stresses. Edge rosette 1, located along the chip's x'_2-direction, is made up of the normal sensing elements formed from groups *a* and *b* to extract $\left(\sigma'_{11}-\sigma'_{22}\right)$ and σ'_{23} from the set of equations (3-17). On the other hand, edge rosette 2, located along the chip's x'_1-direction, is made up of the 45 degrees oriented sensing elements formed from groups *a* and *b* to extract σ'_{12} and σ'_{13} from the set of equations (3-18).

The 4PB of the chip-on-beam specimen induces high out-of-plane normal stress σ'_{33} very close to the edge of the chip where it is physically hard to include a rosette for its extraction. Therefore, a controlled normal pressure on the chip is needed to induce enough σ'_{33} at the center rosette for extraction. However, the low B_3 coefficient reported in Chapter 3 drops the sensitivity of σ'_{33} to levels that

can be hardly measured using the available equipment. For a normal pressure load of 20 MPa, which corresponds to around 1kN force on the chip surface, the changes in the resistance $\Delta R/R$ will be in the order of $1\text{x}10^{-5}$. This is translated in terms of change in the voltage drop across a sensing element in the range of 1 to 10 μV. This value is too low to capture using the available measurement equipment, especially if a number of load increments will be applied over the load range. Therefore, it was decided not to test σ'_{33} independently for the current fabricated sensing chip. However, higher B_3 values in n-Si are possible at different concentrations that reached by Suhling *et al*. 55 TPa^{-1} [13] and -75.5 TPa^{-1} [66], which would provide a change in the voltage drop across the current sensing element between 88 μV to 121 μV for the same loading.

6.3 Test Specimens

The chip is bonded to the PCB beam using an anisotropic conductive adhesive (ACA) such that the sensing surface is facing the board as shown in Figure 6-1. The ACA is made up of conductive micron-sized particles floating in an epoxy resin matrix. The adhesive is dispensed between the chip and PCB for electrical conduction and structural bonding. This is followed by an applied normal pressure and temperature to cure the adhesive and create electrical conduction between the conductive particles and the pads on the chip and PCB. Prior to bonding, metal bumps, usually gold, need to be bonded on the chip pads to provide good conduction in the vertical direction and avoid shortening other traces on the chip surface.

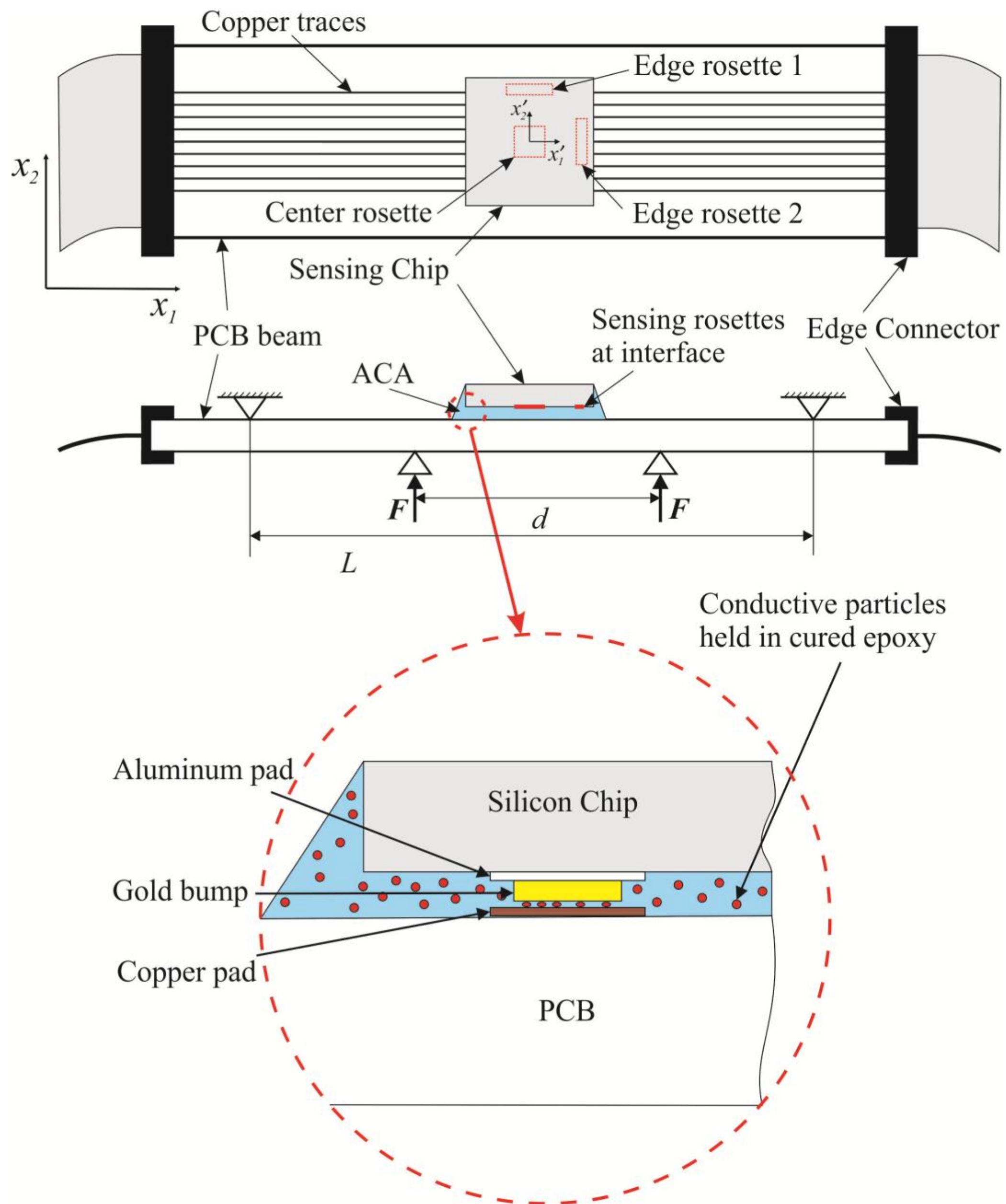

Figure 6-1 Schematic of testing setup and specimens

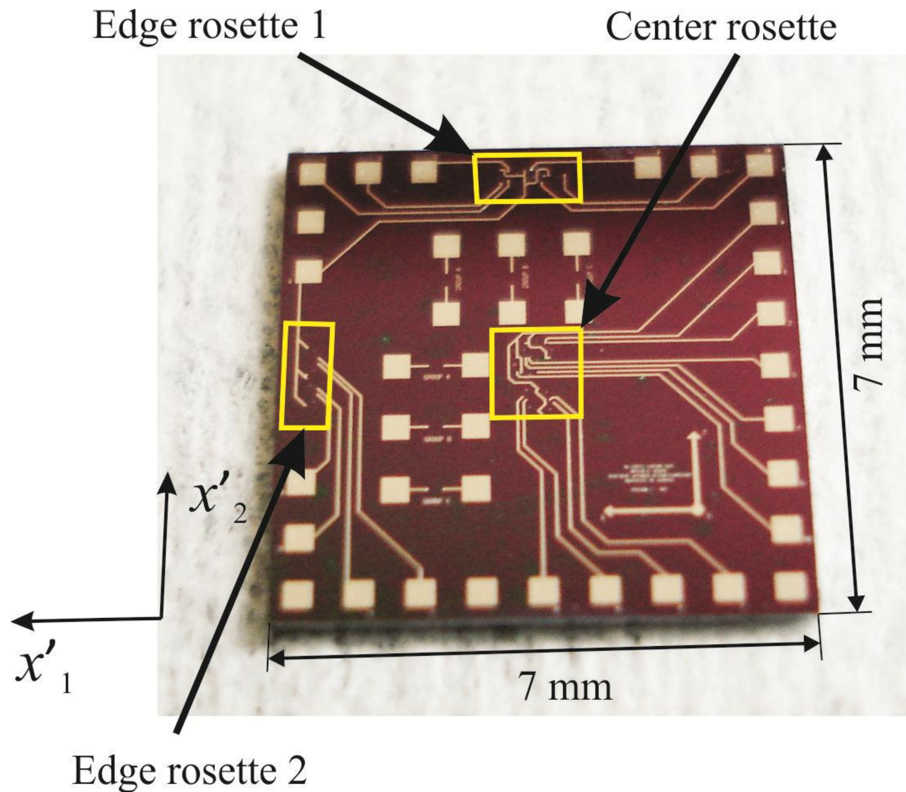

Figure 6-2 Micro-fabricated test chip

6.3.1 Stud Bumping

A wire-bonder, West.Bond® 7476E, available in the MEMS/NEMS ADL was used to bond a number of gold (Au) stud bumps on the chip's aluminum pads. On each pad, 5 stud bumps were bonded to cover the 350x350 μm pad area in order to provide large surface area for conduction. This is followed by a coining process to flatten the surface of the bump to enhance the electrical conduction with the conductive particles in the ACA. The stud bumping process is shown under the microscope in Figure 6-3, while the final *test chips* with coined stud bumps are shown in Figure 6-4. A Scanning Electron Microscope (SEM) image of the bumps before and after coining is shown in Figure 6-5 to Figure 6-7. It is noticed that the width of the bump increased from around 100 μm to around 125 μm after coining.

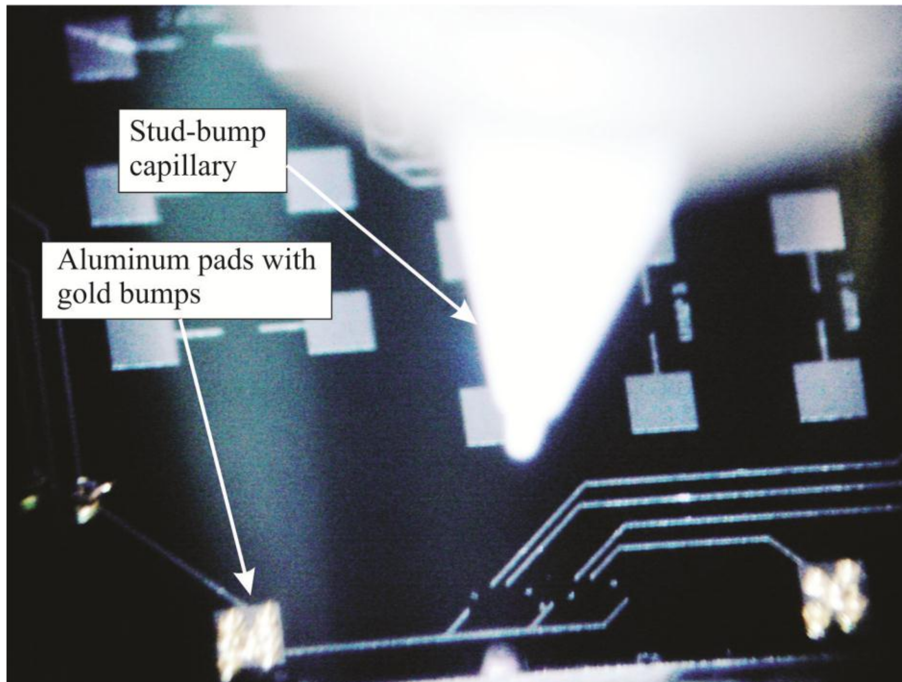

Figure 6-3 Microscopic image of the stud bumping process

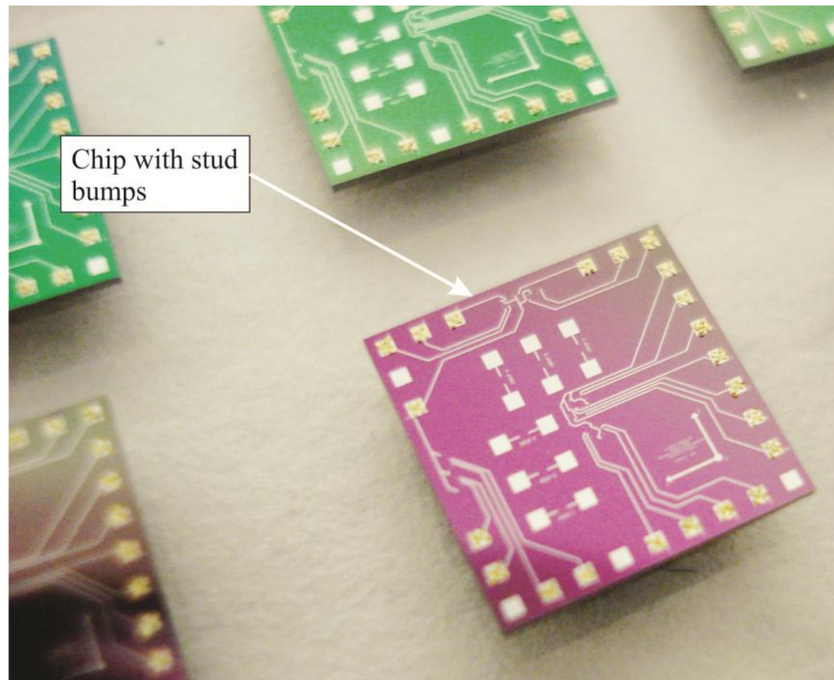

Figure 6-4 The final *Test Chips* with coined stud bumps

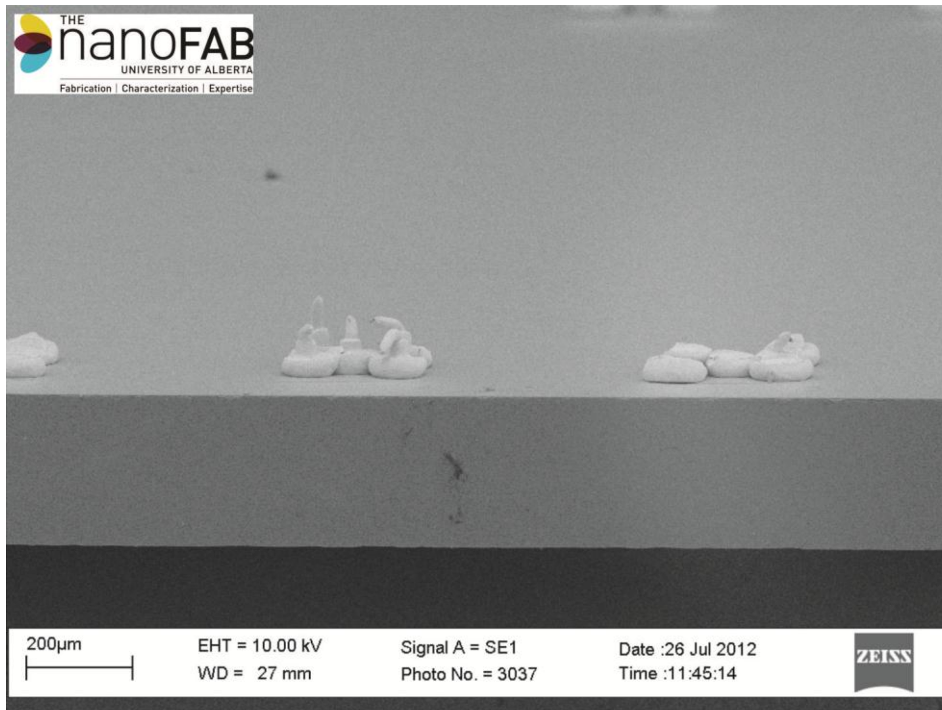

Figure 6-5 SEM image of the stud bumps before and after coining

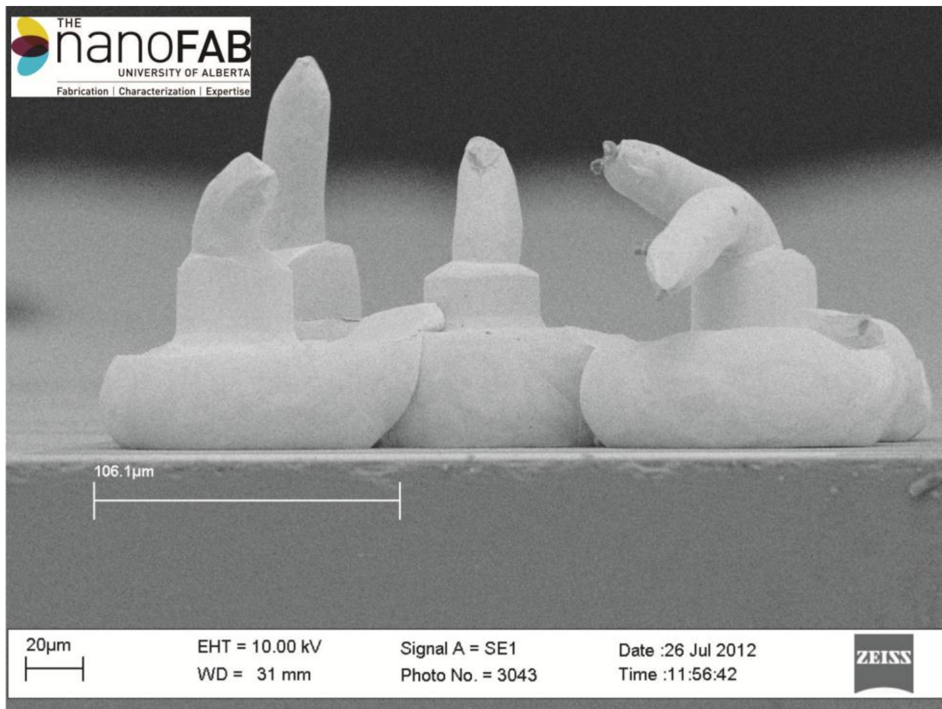

Figure 6-6 SEM image of the 5 stud bumps on an Aluminum pad before coining

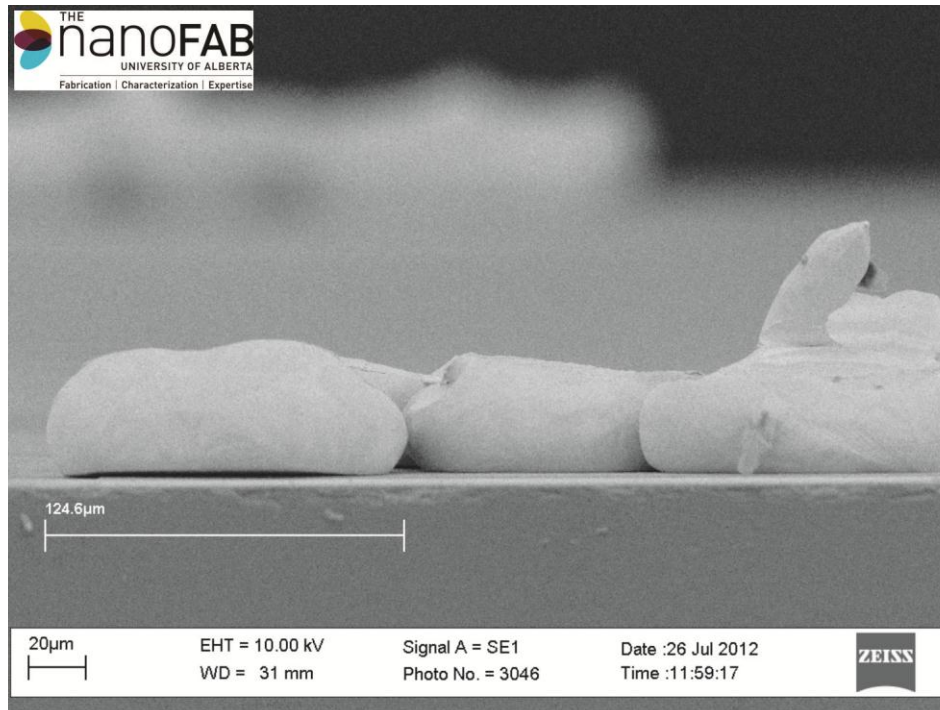

Figure 6-7 SEM image of the 5 stud bumps on an Aluminum pad after coining

6.3.2 Flip-Chipping

The flip-chipping process utilized to package the chip with the PCB beam used the DELOMONOPOX® AC265 ACA with Ni/Au conductive particles from DELO® Industrial adhesives [142] for bonding. A FinePlacer® pico flip-chipper available at the MEMS/NEMS ADL was used for the flip-chipping process. The ACA was prepared in 5 ml syringes and dispensed manually at the center area of the chip contact on the PCB and spread uniformly to cover the contact area including the pads. The chip, which was held using a chip contact heating module (thermode), was flipped on the PCB. A pressure of 0.5 MPa, using the flip-chipper pivot arm, and a temperature of 200 °C for 8 seconds (thermo-compression bonding) using the thermode were used to cure the ACA and create electrical contact between the conductive particles and the contact pads. This application process was recommended by the ACA manufacturer. An image showing the PCB beam and the thermode in contact with the chip during the curing process is shown in Figure 6-8.

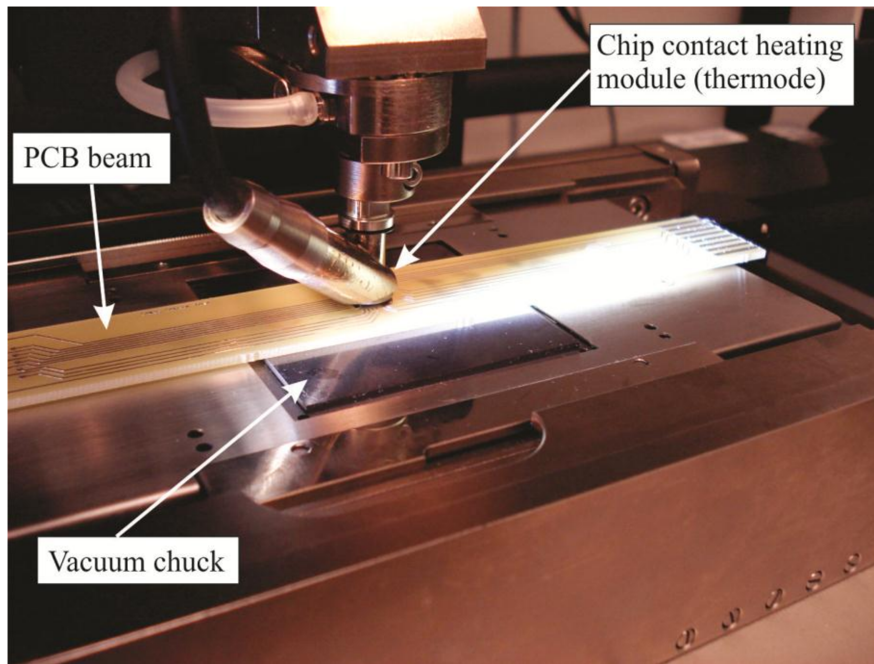

Figure 6-8 Image showing the flip-chipping process of the chip on the PCB beam

A few early test trials of the AC265 ACA were conducted on test PCBs to ensure good electrical conduction and bond between the chip and the PCB. The test PCBs were square sized with 2.5 x 2.5 cm footprint and edge pads for quick resistance measurement of each individual piezoresistor on the chip.

6.3.3 Types of Specimens

The test chip was oriented over the beam at three angles to induce different stress components at the rosettes. Three types of specimens were prepared for each chip orientation, where the chip's axial-direction, x_1', is oriented to the beam's axial-direction, x_1, at 0, 45, and 90 degrees designated as S0, S45, and S90 specimens, respectively as shown in Figure 6-9. The S0 specimen is used to induce σ_{11}' at the center rosette and σ_{13}' at the edge rosette 2. The S45 specimen is used to induce σ_{12}' at the center rosette and σ_{23}' and σ_{13}' at the edge rosettes 1 and 2, respectively.

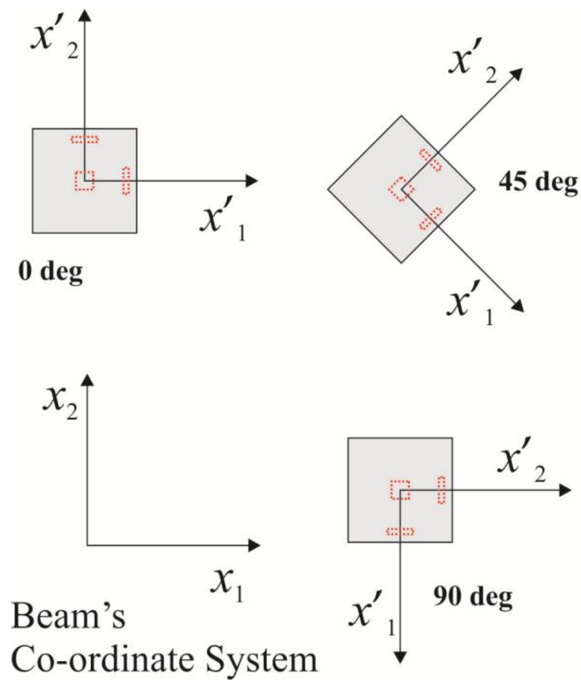

Figure 6-9 Schematic showing the three chips orientations on the PCB beam

Finally, the S90 specimen is used to induce σ'_{22} at the center rosette and σ'_{23} at the edge rosette 2. Using this combination of the 3 rosette-sites and the 3 chip orientations on the PCB, five stresses can be induced for testing. An image of the three specimens after packaging is shown in Figure 6-10.

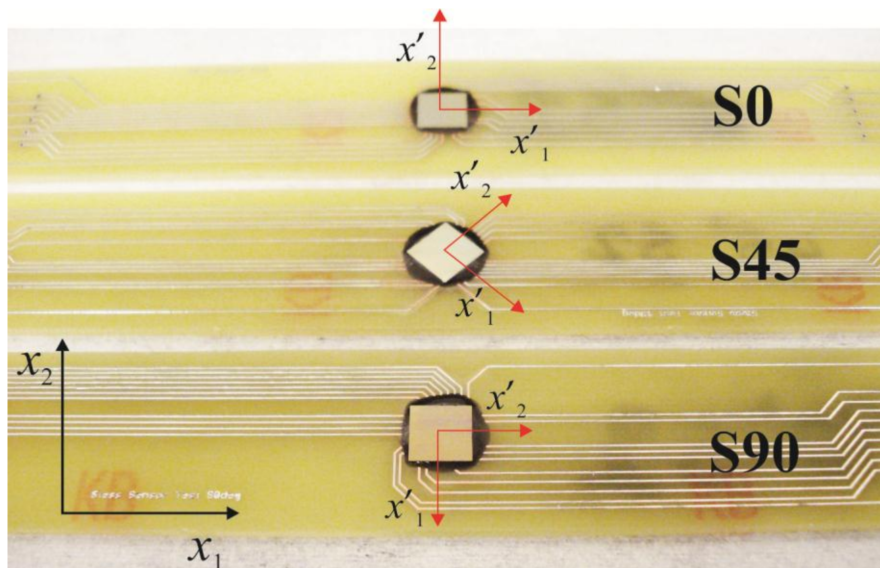

Figure 6-10 The three types of test specimens; S0, S45, and S90

6.4 Specimen Loading

Assuming a homogenous PCB beam, without the bonded sensing chip, undergoing four-point bending, a state of uni-axial stress is induced within distance *d* shown in Figure 6-1. The top surface of the beam undergoes tensile stress and the bottom surface undergoes compressive stress. In 4PB, the induced uni-axial stress, described earlier in equation (5-2) is re-stated again:

$$\sigma_n = \frac{3F(L-d)}{wh^2} \tag{6-1}$$

Where, F is the applied force, L is the distance between the outer supports, d is the distance between the middle supports, w is the width of the beam, and h is the thickness of the beam. This stress is referred to in the tests as the *nominal axial stress* in the beam. Three specimens of each orientation were loaded under four point bending at different loading increments to induce tensile and compressive axial stresses on the PCB beam surface, where the beam was flipped on the opposite side to create the compressive axial stresses at the chip location. A total of 10 tensile and compressive load increments were applied on the beam, where at each load increment the output force from a load cell is averaged over the loading period.

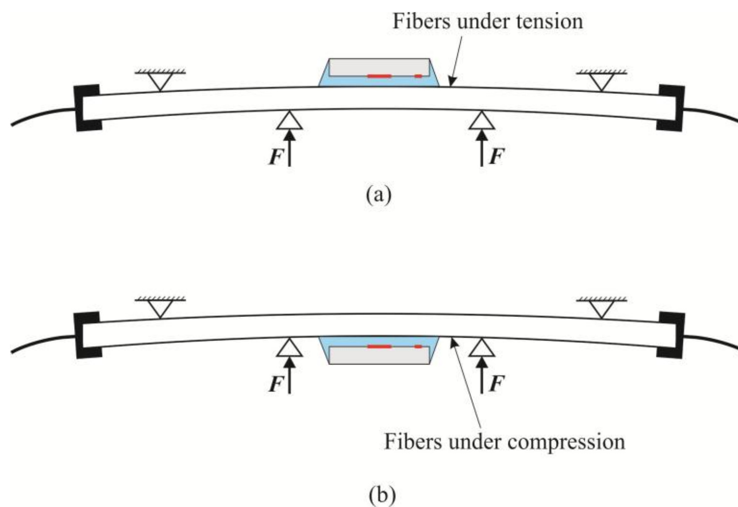

Figure 6-11 PCB orientation during 4PB to induce (a) tensile stresses or (b) compressive stresses at the fibers in contact with the *test chip*

6.5 Measurement Setup

The measurement setup shown in Figure 6-12 was used to measure the resistance change of the sensing elements and the applied load on the beam at each loading increment. The resistance measurement of each sensing element was carried out through supplying a constant current of 100 μA using a Keithley 2400 source meter and measuring the differential voltage change from 18 piezoresistive sensing elements using a 6½ digit multi-meter HP 34401A. The load (F) on the PCB beam was incremented from 0 to around 7.5 N over 5 increments using a manual jack and a load-cell is used to measure the applied load on the beam. At each load increment, the switching between the sensing elements was performed using a manual rotary switch, while the multi-meter is recording the differential voltage. The load-cell was connected to a data acquisition (DAQ) system and a LabVIEW SignalExpress program to record the applied force on the beam. On the other hand, the multi-meter was connected directly to the LabView SignalExpress through a GPIB cable to record the differential voltages at 3 seconds interval to allow for the manual switching between the piezoresistors. The measured changes in resistances along with the calibrated coefficients shown in Table 5-3 were used to calculate the stresses using equations (3-20). The actual experimental setup is shown in Figure 6-13.

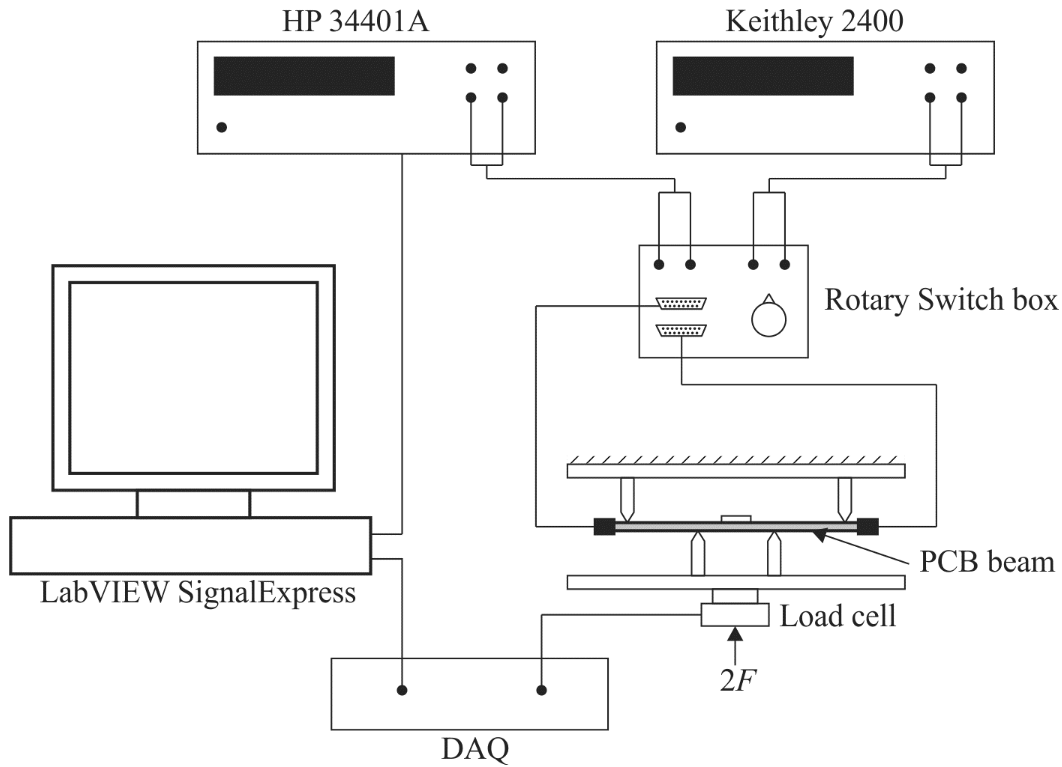

Figure 6-12 Test measurement setup

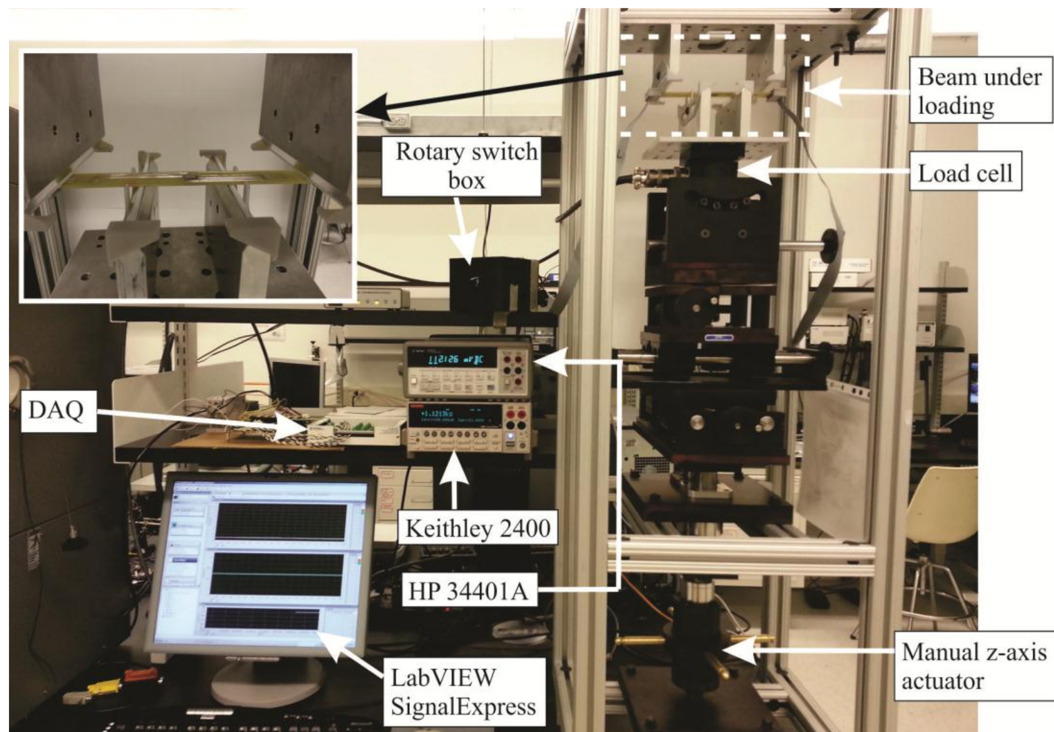

Figure 6-13 Experimental test setup

6.6 Characterization of the Chip/PCB Interface

The final thicknesses of the ACA, gold bumps, and the PCB copper traces were required to be quantified for use into the finite element model, which will be discussed in the next section. Three samples of the bonded chip/PCB assembly were diced along the copper traces and Aluminum pads to characterize the dimensions of the different materials at the interface. A dicing saw at the nanoFab utilizing a diamond blade with a width of cut of 325 μm was used. The testing PCBs, which were used for testing of the ACA electrical conduction, were used as characterization samples. The samples were inspected in an SEM to measure the interface thicknesses. Also, the spew fillet created due to the flow of the adhesive during bonding is inspected. A thin layer of gold (Au), measuring around 20 μm, was sputtered at the interface to prevent electrons accumulation at non-conductive surfaces like the PCB material, where the charge buildup causes a divergence of the electron beam and degrades the SEM image.

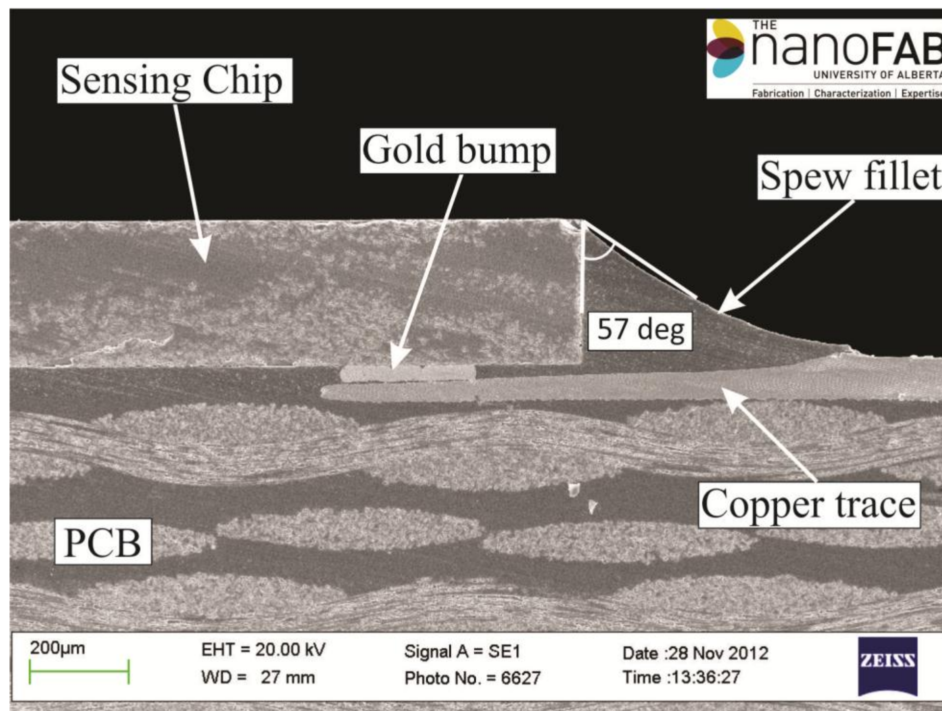

Figure 6-14 SEM image of the PCB/Chip cross-section showing the gold bump, copper trace and ACA spew fillet

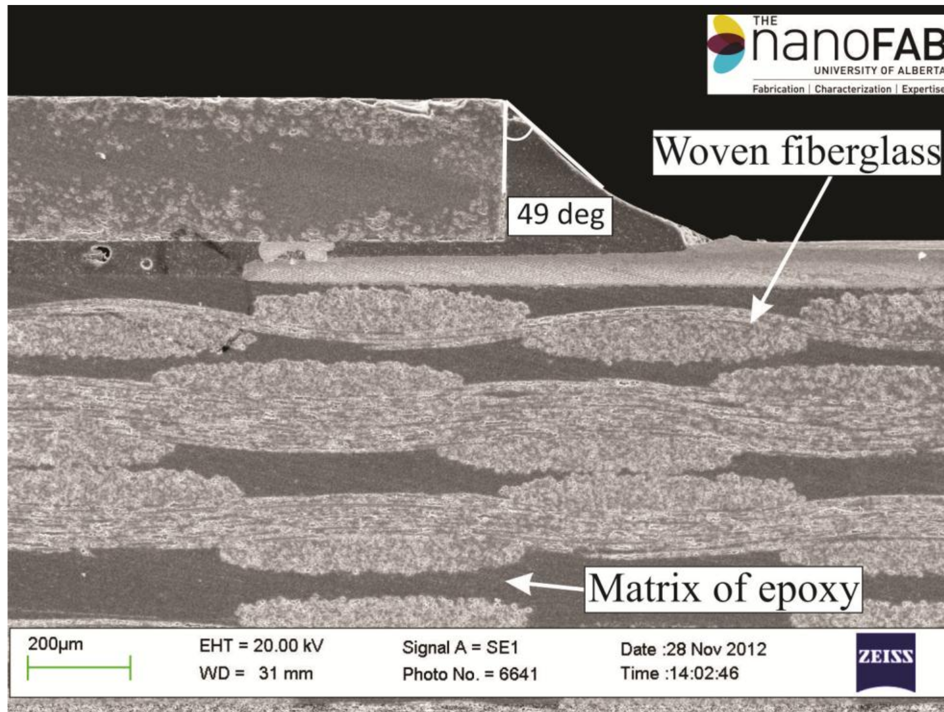

Figure 6-15 SEM image of the PCB/Chip cross-section showing a different angle for the spew fillet and structure of the PCB composite

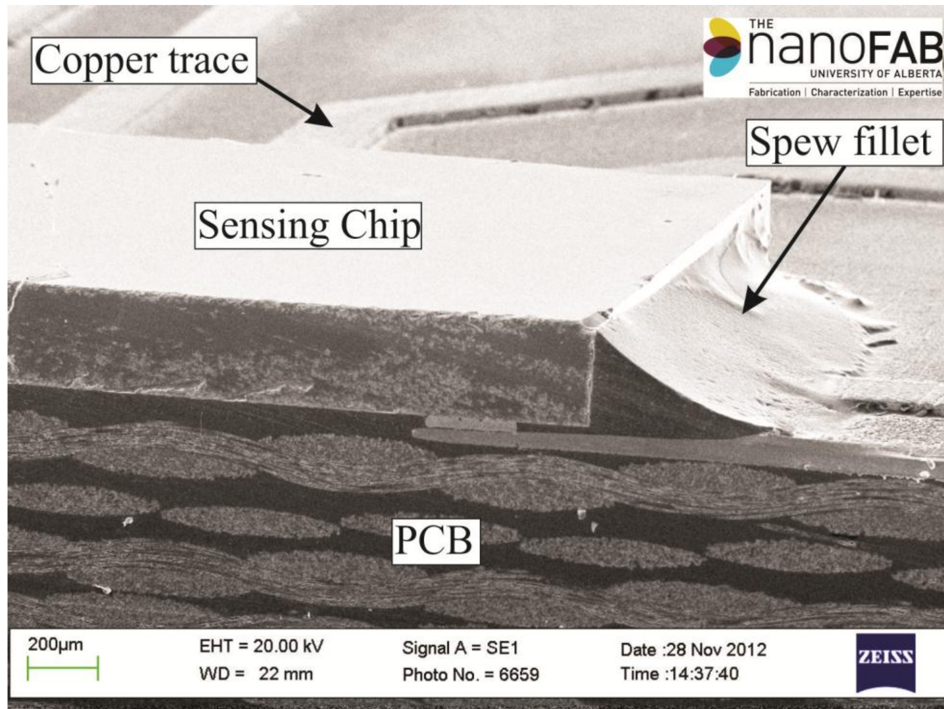

Figure 6-16 SEM image of the PCB/Chip cross-section showing ACA spew fillet

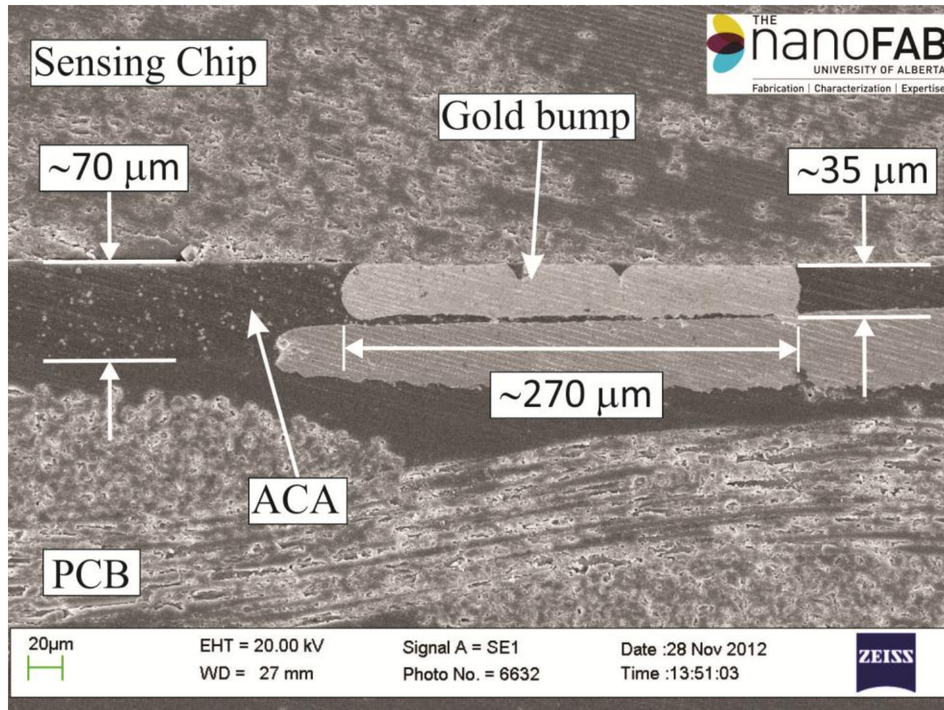

Figure 6-17 SEM image of the PCB/Chip cross-section showing the ACA, gold bump and copper trace thicknesses

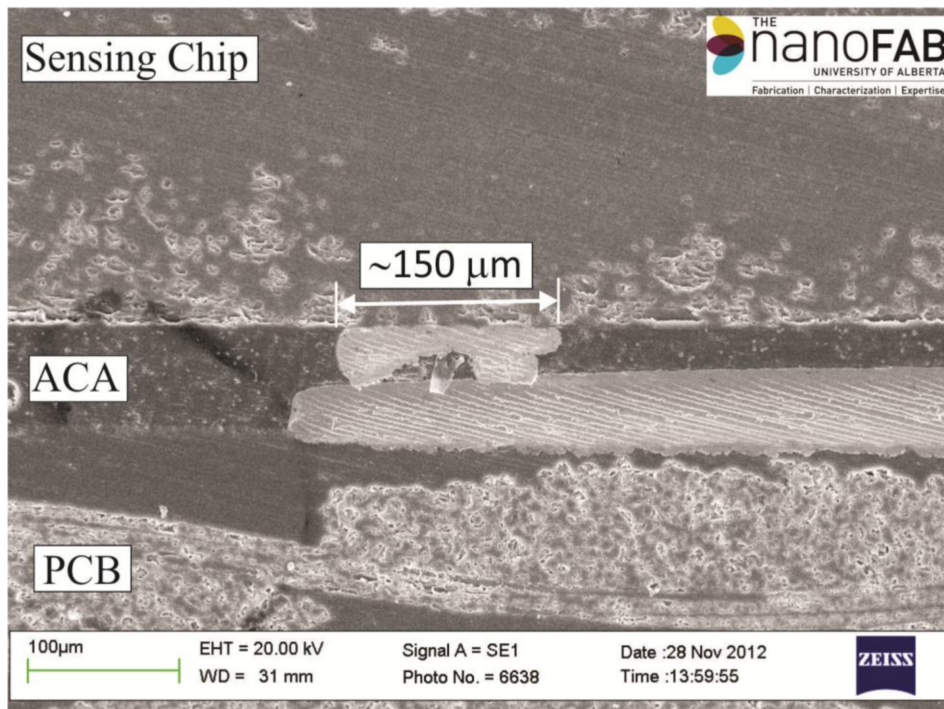

Figure 6-18 SEM image of the PCB/Chip cross-section showing the width of one coined gold bump

The resulting SEM images are shown in Figure 6-14 to Figure 6-16. The spew fillet in Figure 6-14 and Figure 6-15 for two different specimens is shown to completely cover the edge of the chip, but the angle varies from 49 to 57 degrees. Also, the angled view of the spew fillet in Figure 6-16 shows the variation of the flowed ACA around the chip's periphery, where at the corners almost no coverage is present. Closer inspection of the interface in Figure 6-17 and Figure 6-18 reveals the ACA layer with conductive particles, which has a thickness of around 70 μm. The gold bump has a thickness of around 35 μm and a width of 270 μm for the combined 5 bumps shown in Figure 6-17 and 150 μm for a single bump shown in Figure 6-18. The images also show the composite structure of the FR-4 material of the PCB, which is made out of fiberglass cloth fibers in an epoxy resin binder.

6.7 Finite Element Model

An FEM was developed using ANSYS® multiphysics release 13 software to study the stresses generated on the chip-on-beam under four-point bending. Also, it models the 3 rosettes on the chip surface to compare their output stresses to the average stress fields over the rosette-sites to determine the effect of the stress non-uniformity on the rosette output. This FEM is not intended as verification for the experimental results, rather it provides a range of expected stress values at the rosette-sites. The overall model is shown in Figure 6-19 showing the mesh and boundary conditions. The ACA was modeled with the gold stud bumps at the contact pads locations to include their effect in the load transfer between the PCB and the sensing chip. The thickness of the ACA layer was taken from the inspected SEM images in section 6.6 to be 70 μm. The gold stud bumps were modeled as cylinders with diameter and height equal to the size of the contact pad (350 μm) and ACA thickness (70 μm), respectively. The copper traces on the PCB were not modeled due to their relatively small thickness to the PCB thickness (~1:45). The spew fillet created from the flowing ACA during assembly was modeled as shown in Figure 6-20. The spew fillet was modeled to include its

effect in lowering the edge stresses compared to a square end. Adams *et al*. discovered that a spew fillet covering the edge of an adherend in a double-lap joint reduces the maximum shear stress at the edges by 30 % compared to a square end [3]. The angle of the spew fillet was selected to be 45 degrees for modeling simplicity and as a rounded average to the inspected fillet's angle at different points on the chip's periphery from the SEM images. The close-up view of the mesh at the chip/PCB interface is shown in Figure 6-21.

The piezoresistors were modeled at each rosette-site as volumes with length, width, and thickness measuring 200 μm x 20 μm x 5 μm, respectively as shown Figure 6-22. Three models were analyzed for the 0, 45, and 90 degrees oriented chips. Therefore, a full 3D model was utilized to capture the stress fields due to the non-symmetrical positions of the stud bumps over the chip periphery and the three different chip orientations.

The materials for the PCB, ACA, and gold bumps were considered isotropic, while that of the silicon chip was considered anisotropic with the stiffness constants along the crystallographic directions shown in Table 6-1. The silicon stiffness constants were transformed along the (111) direction to simulate the actual chip orientation. The PCB material (FR-4) is made up of layers of fiberglass and epoxy and is considered orthotropic since the properties over its plane is different than through its thickness. Assuming an isotropic material for the PCB will affect the values of the calculated out-of-plane shear stresses, where the shear modulus in the in-plane (G_{12}) and out-of-plane (G_{13} and G_{23}) differs from 3.0 GPa to 2.4 GPa [143]. However, the normal stresses generated in the beam are mainly in-plane due to the applied uni-axial stress on the beam with little normal out-of-plane stress. Therefore, for simplicity and since the objective of the FEM is to provide a guidance for the expected range of stresses from the experimental testing rather than verification, it is assumed that the PCB material is isotropic with its properties corresponding to the in-plane directions. The dimensions of the FEM and its material properties are given in Table 6-1.

Table 6-1 Material properties and geometry of the chip-on-beam FEM

	Dimensions, mm	Material properties
Sensing chip (Silicon)	7x7x0.3	C_{11}= 165.7 GPa
		C_{12}= 63.9 GPa
		C_{44}= 79.6 GPa
ACA (AC265) [142]	7x7x0.07	E=3.3 GPa, ν= 0.3
PCB beam (FR-4) [144]	180x22.73x1.57	E=23.73 GPa, ν= 0.117
Gold Bumps [145]	ϕ 0.35 x 0.07	E=77.2 GPa, ν= 0.3

E = elastic modulus, ν = poisson's ratio, C_{11}, C_{12}, and C_{44} = stiffness constants

The FEM was based on a static structural-piezoresistive analysis and was developed using SOLID187 10-noded tetrahedral elements for the structural components and SOLID226 10-noded structural-piezoresistive coupled tetrahedral elements for the piezoresistive sensing elements. Each piezoresistor was connected in a Wheatstone bridge configuration with three matching CIRCU124 resistor elements to measure the differential output voltage due to the applied load and 5 V input voltage to the bridge. The nodes at the terminals of the piezoresistors were coupled in terms of voltage degree of freedom to obtain a uniform voltage value at the terminals. The change in resistance for each piezoresistor is calculated from the change in voltage from the Wheatstone bridge as follows [146]:

$$\frac{\Delta R}{R}=\frac{4\Delta V/V_s}{1-2\Delta V/V_s} \tag{6-2}$$

Where, V_s is the voltage source to the bridge, which equals 5 V and ΔV is the change in voltage from the initial state. The boundary conditions and meshing of the FEM are shown in Figure 6-19. The vertical loads and supports were located at 70 mm and 27.5 mm from the center of the beam, respectively. The beam was fixed in the x_3-direction along the supports and in the x_1-direction along the beam's center-line. To avoid rigid body motion, the beam was fixed in the x_2-direction at the center-points of the supports.

The ANSYS code for the FEM is presented in Appendix D for the 45 degrees oriented chip. Different orientations can be obtained by changing the rotation angle in the code.

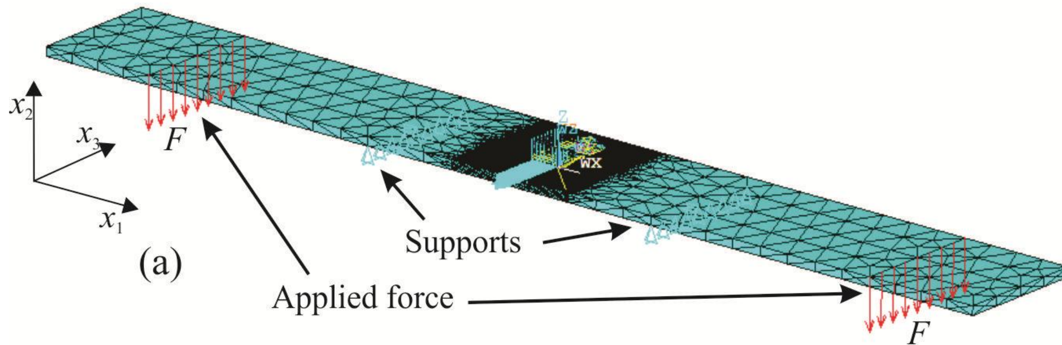

Figure 6-19 Overall mesh and boundary conditions of the finite element model

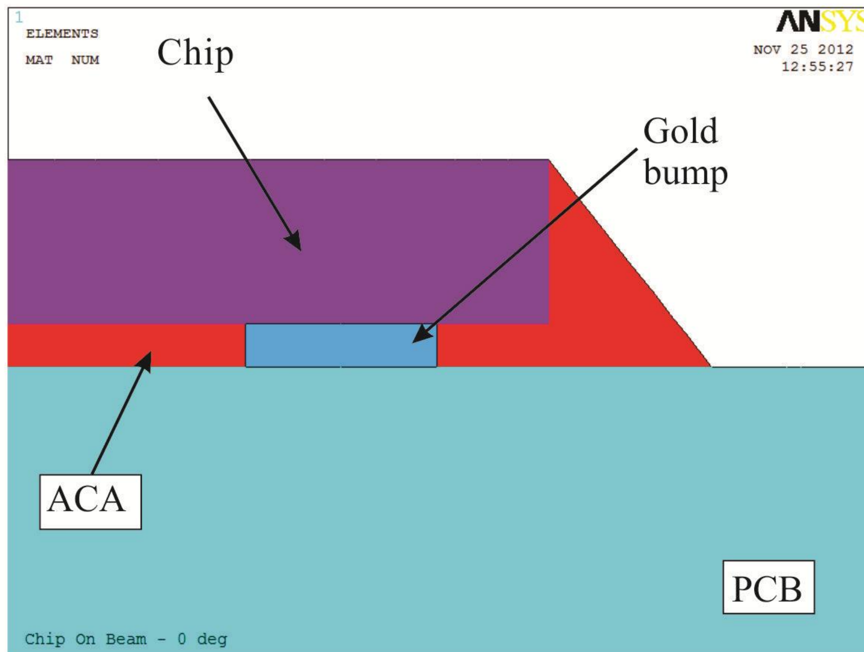

Figure 6-20 Cross-section view of the modeled chip/PCB interface

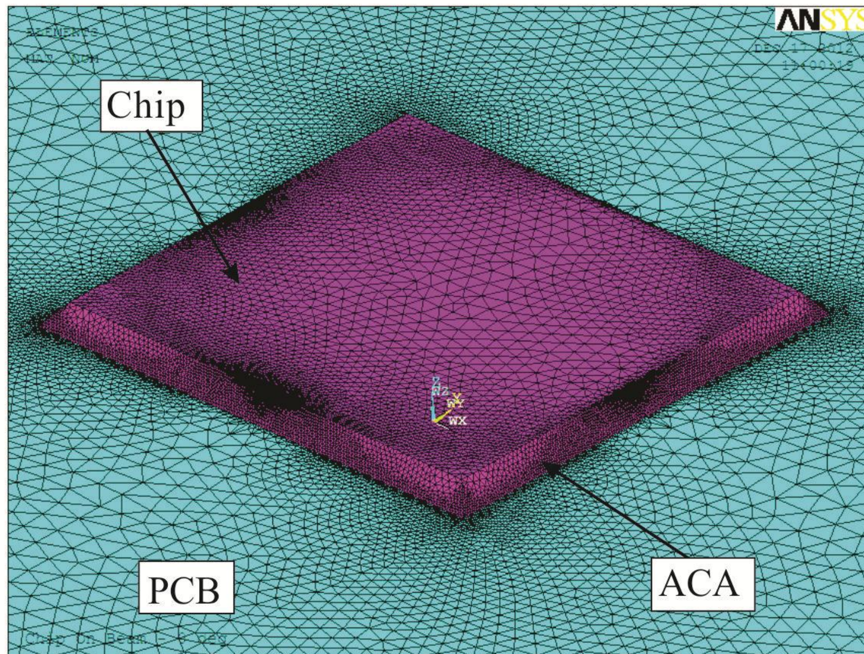

Figure 6-21 Finite element mesh of the chip, ACA and PCB

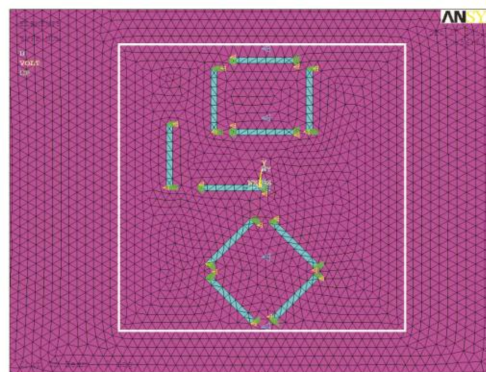

(a)

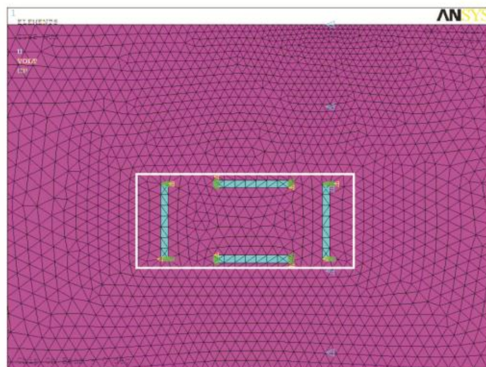

(b)

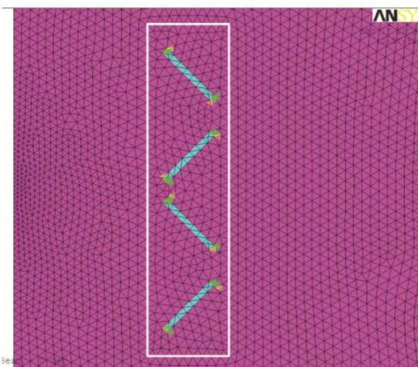

(c)

Figure 6-22 Planar view of the finite element mesh of the (a) center rosette, (b) edge rosette 1, and (c) edge rosette 2

6.8 Drift and Hysteresis

One of the major problems with stress or strain sensors is the load drift over time and hysteresis over loading/unloading cycles. Testing of these effects on the developed 10-element rosette requires extended loading time and a large number of loading/unloading cycles. However, a simple test has been performed through applying 10 cycles of loading/unloading for the rosette over an axial stress range from -10 MPa to 40 MPa. This test has been conducted in collaboration with the wireless electronics group at the Glenrose Rehabilitation Research Center at the University of Alberta. The sensing chip was bonded to a 127 μm thick stainless steel shim, which was spot welded to a 300 x 45 x 3.175 mm steel specimen. Measurement electronics was connected to the chip using ACA and the steel specimen was loaded using an MTS tensile machine under load P from -8 kN to 30 kN. The output signal from the chip was sent using a wireless system to a computer data logging station. A schematic of the loading assembly is shown in Figure 6-23.

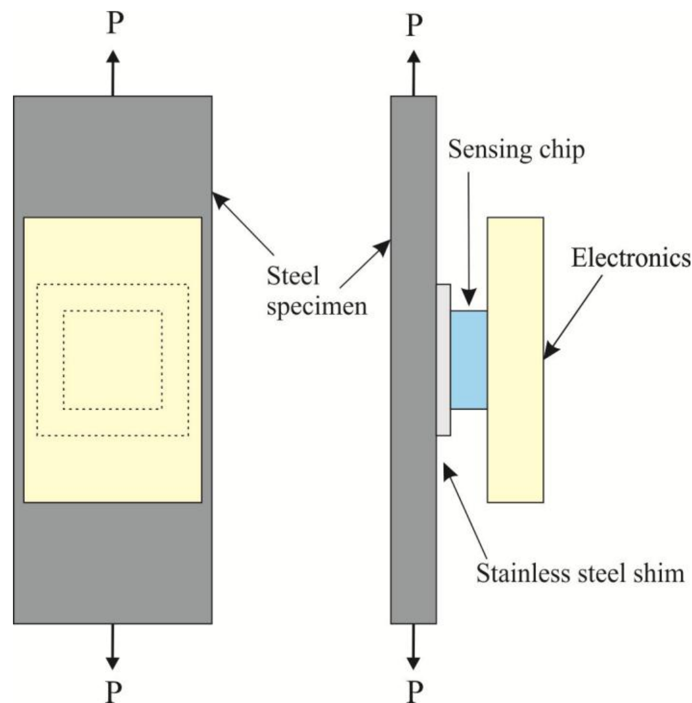

Figure 6-23 Loading setup for hysteresis testing (not to scale)

6.9 Results

The testing results are divided into four parts; the first is the resistance change output from each sensing element on the chip versus the applied load, the second is a comparison between the FEM and the stress output from the experimental testing at a certain applied load, and the third presents the experimental stress output at different loads. The last part of the testing results shows the output from the sensing chip while undergoing 10 loading/unloading cycles. For each applied tensile and compressive nominal axial stress in the beam, the vertical load (F) on the beam was applied at 5 increments, where at each increment, manual switching between the 18 piezoresistors was carried out to record the differential voltages. The vertical force ($2F$) on the beam, as recorded from the load-cell, is shown in Figure 6-24 over the time of the test.

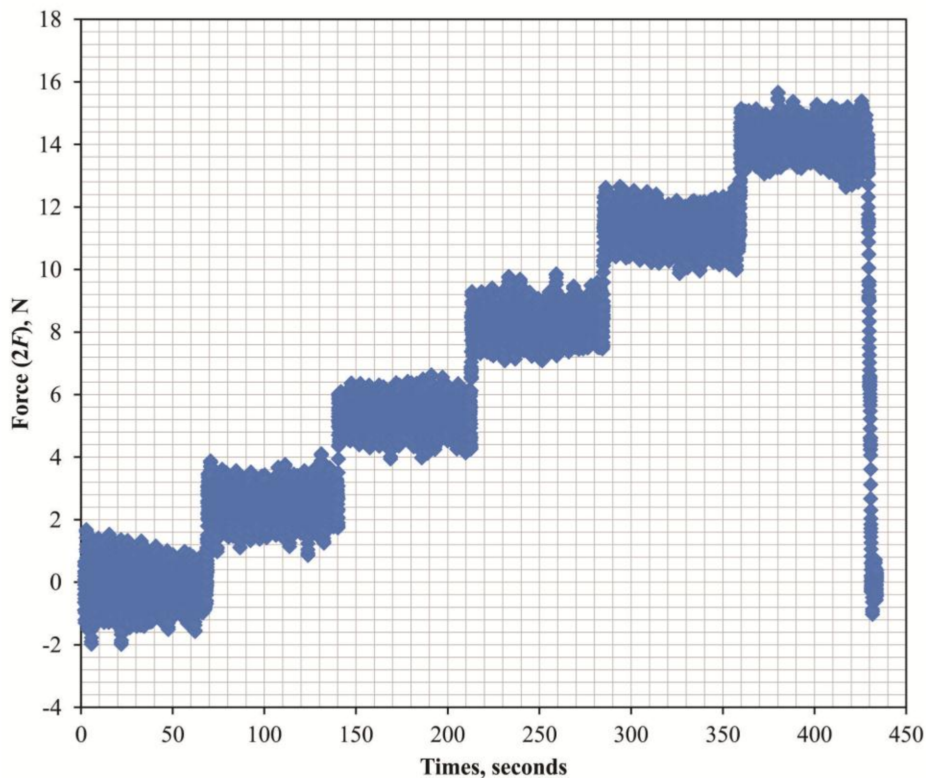

Figure 6-24 Typical output from the load-cell due to the applied vertical load increments on the beam

6.9.1 Resistance Change Output

The resistance changes output from each sensing element on the three specimens are shown in Figure 6-25 to Figure 6-33. The sensing elements are marked as C, E1, and E2 designating elements at the center rosette, edge rosette1, and edge rosette2, respectively. The results demonstrate an appropriate response of the sensing elements to the applied stress, especially at the center rosette, which has a controlled maximum stress direction for each specimen. For example, the maximum stress in the S0 specimen at the center rosette is the σ_{11}, which induced a maximum σ'_{11}. The output at the center rosette in S0 specimen in Figure 6-25 shows a negative change in resistance for the 0 degrees oriented sensing elements (i.e. R_1, R_5, and R_9), while a positive change in resistance for the 90 degrees oriented sensing elements (i.e. R_3, R_7, and R_{10}). Therefore, since σ'_{11} is the highest and most significant stress at the center rosette and assuming all other stresses are negligible, the change in resistance equations for the 0 and 90 degrees oriented elements are given by:

$$\left(\frac{\Delta R_0}{R_0}\right) = B_2 \sigma'_{11} \tag{6-3}$$

$$\left(\frac{\Delta R_{90}}{R_{90}}\right) = B_2 \sigma'_{11} \tag{6-4}$$

Where, the values of B_1 and B_2 are negative and positive, respectively. Similar conclusions are drawn for the S45 specimen results in Figure 6-28 and the S90 specimen results in Figure 6-31. The resistance changes of the sensing elements of the center rosette of the S45 specimen are shown in Figure 6-28. The highest stress at the center rosette is the in-plane shear stress σ'_{12}, while the in-plane normal stresses σ'_{11} and σ'_{22} are less in value and equal and the out-of-plane stresses are zero. Therefore, the ±45 degrees oriented sensing elements will encounter this stress in the form of resistance change as follows:

$$\left(\frac{\Delta R_{+45}}{R_{+45}}\right)=\left(\frac{B_1+B_2}{2}\right)\sigma'_{11}+\left(\frac{B_1+B_2}{2}\right)\sigma'_{22}+(B_1-B_2)\sigma'_{12} \tag{6-5}$$

$$\left(\frac{\Delta R_{-45}}{R_{-45}}\right)=\left(\frac{B_1+B_2}{2}\right)\sigma'_{11}+\left(\frac{B_1+B_2}{2}\right)\sigma'_{22}-(B_1-B_2)\sigma'_{12} \tag{6-6}$$

Where, the coefficients of σ'_{11}, σ'_{22}, and σ'_{12} are given in Table 5-3 indicating a very small sensitivity to σ'_{11} and σ'_{22} and a high sensitivity to σ'_{12}. Therefore, the ±45 sensing elements have relatively high sensitivity to σ'_{12} than the normal in-plane stresses. Since, (B_1 - B_2) has a negative value for the three groups, then the resistance changes of the +45 degrees elements (i.e. R_2 and R_6) are negative and of the -45 degrees elements (i.e. R_4 and R_8) are positive with an applied positive σ'_{12} load as shown in Figure 6-28. Similarly, the ±45 degrees elements in the center rosettes of the S0 and S90 specimens show a nearly zero resistance changes due to the zero in-plane shear stress and their low sensitivity to the normal in-plane stresses.

The stress fields at the edge rosettes are more complicated because they involve more than one stress component. Also, due to the fact that the resistance change of each sensing element is an effective combination of a number of stress components, it is more difficult to correlate the resistance changes plots to the type of the applied stresses. However, the resistance change at the edge rosette 2 can be directly correlated to the shear stresses σ'_{12} and/or σ'_{13} as shown in Figure 6-27 for the S0, Figure 6-30 for the S45, and Figure 6-33 for the S90. It is noticed that the behavior of the resistance changes for edge rosette 2 in the S90 indicate a non-linear behavior with values in the $1\text{x}10^{-4}$ range. The ±45 degrees sensing elements in the edge rosette 2 are sensitive to the normal stresses as well as to σ'_{12} and σ'_{13}. Subtracting the resistance changes of R_2 from R_4 and R_6 from R_8 eliminates the normal stress components and only the shear σ'_{12} and σ'_{13} are

present in the equation, which is demonstrated in the set of linear equations (3-18) in Chapter 3. The resulting subtraction is shown in Figure 6-34, which shows a linear relationship with the applied load. This indicates that the non-linearity in Figure 6-33 is due to the normal stress components, which might be due to non-linear changes of the stress field over the rosette area during loading.

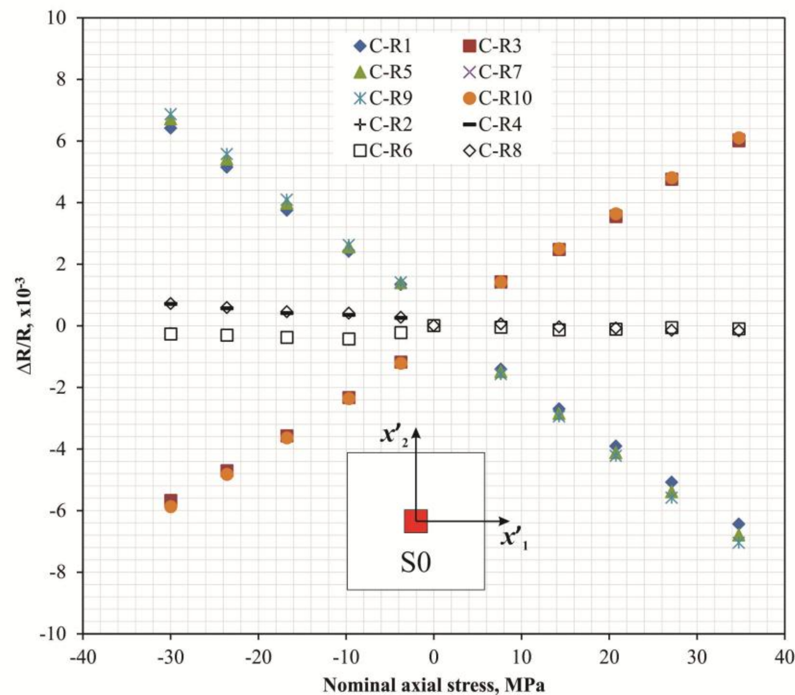

Figure 6-25 Resistance changes in the sensing elements of the center 10-element rosette in the S0-speciemen

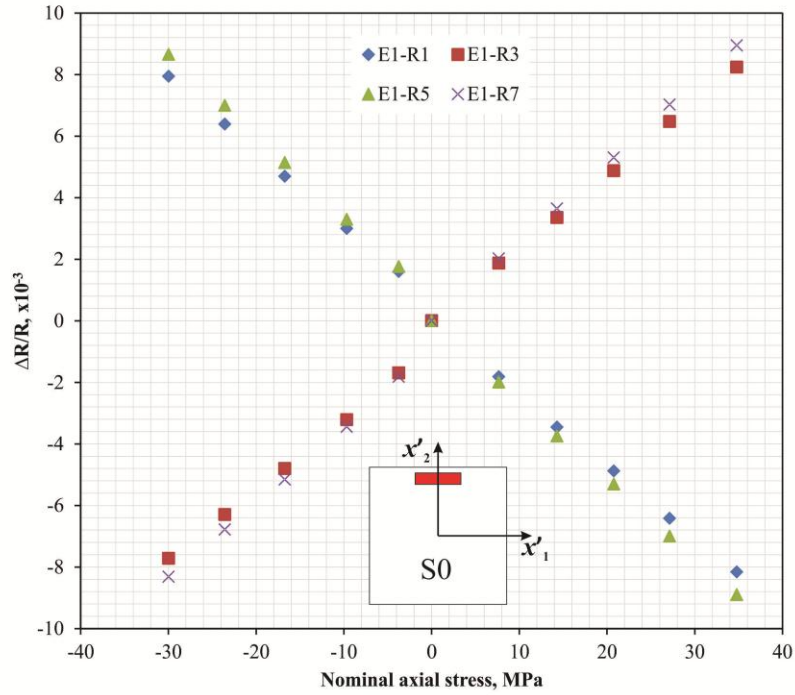

Figure 6-26 Resistance changes in the sensing elements of the edge1 4-element rosette in the S0-speciemen

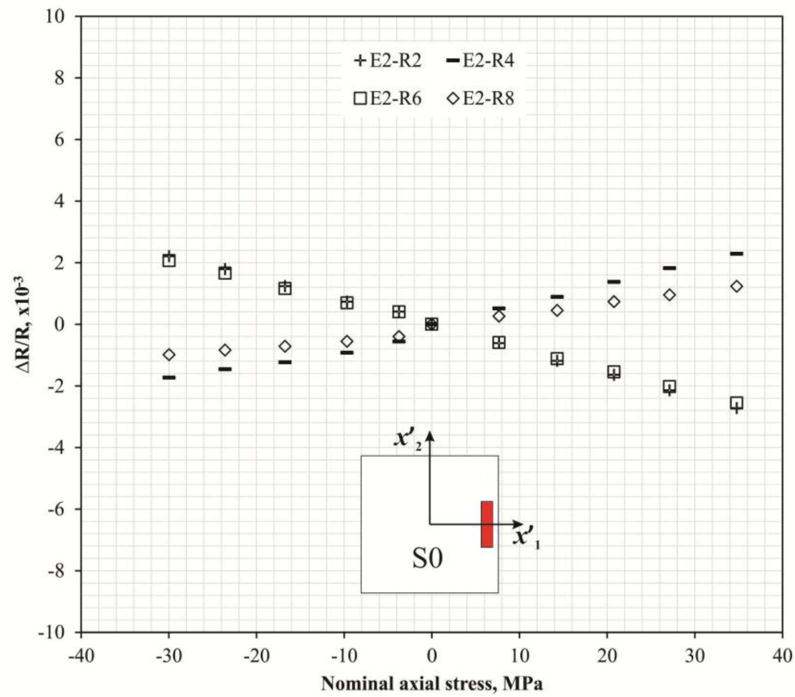

Figure 6-27 Resistance changes in the sensing elements of the edge2 4-element rosette in the S0-speciemen

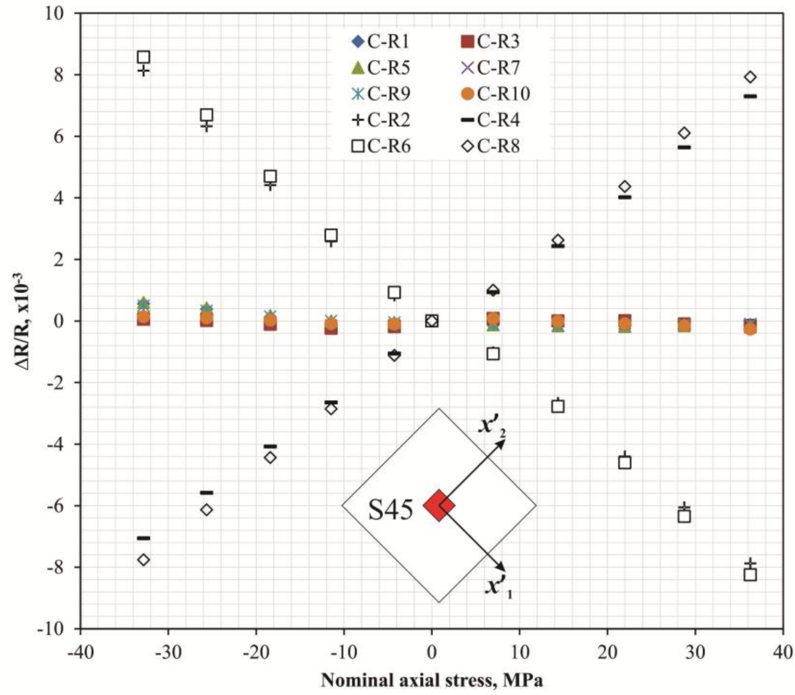

Figure 6-28 Resistance changes in the sensing elements of the center 10-element rosette in the S45-speciemen

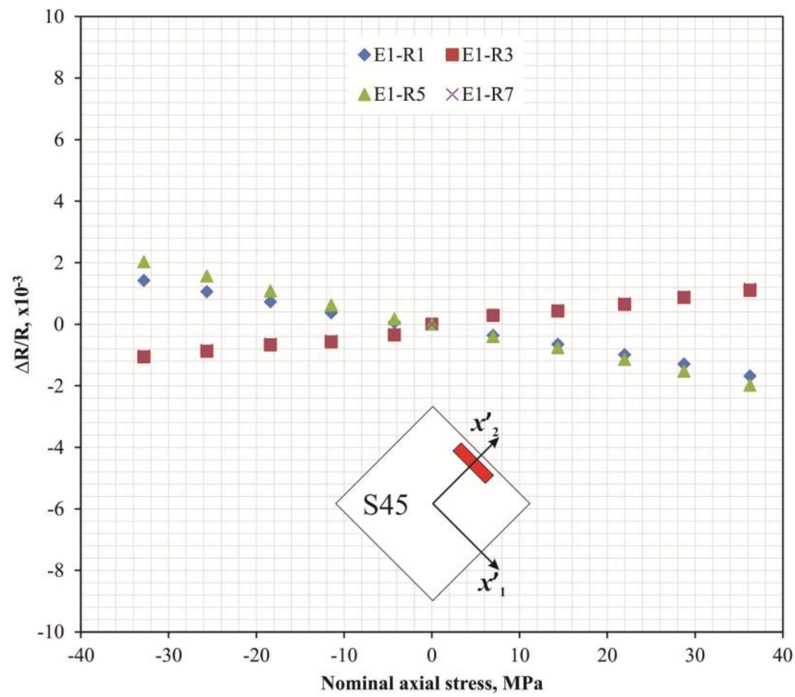

Figure 6-29 Resistance changes in the sensing elements of the edge1 4-element rosette in the S45-speciemen

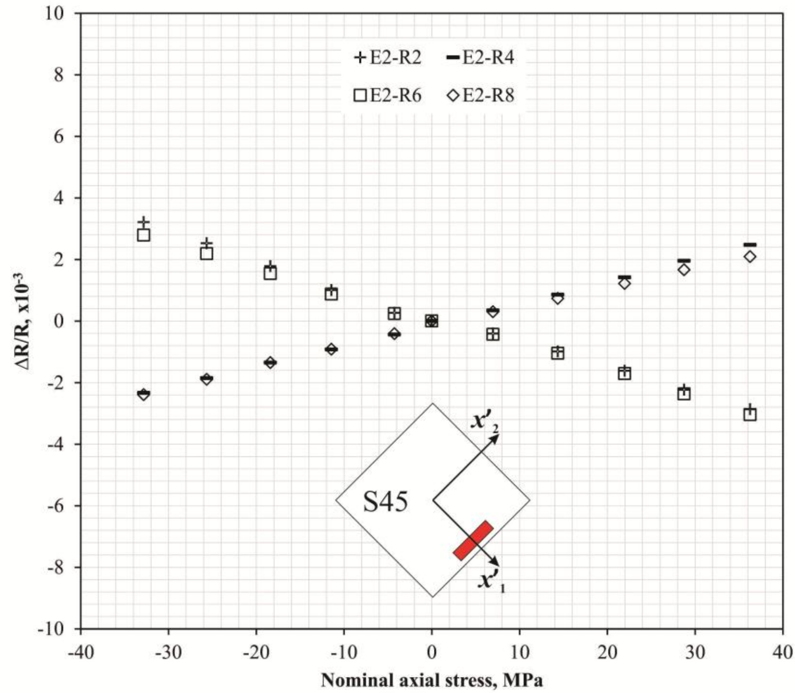

Figure 6-30 Resistance changes in the sensing elements of the edge2 4-element rosette in the S45-speciemen

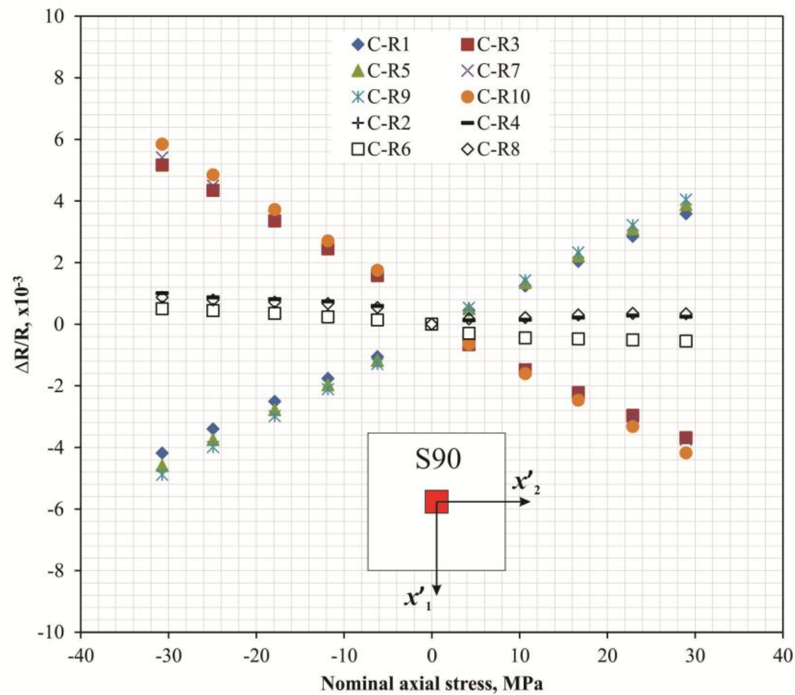

Figure 6-31 Resistance changes in the sensing elements of the center 10-element rosette in the S90-speciemen

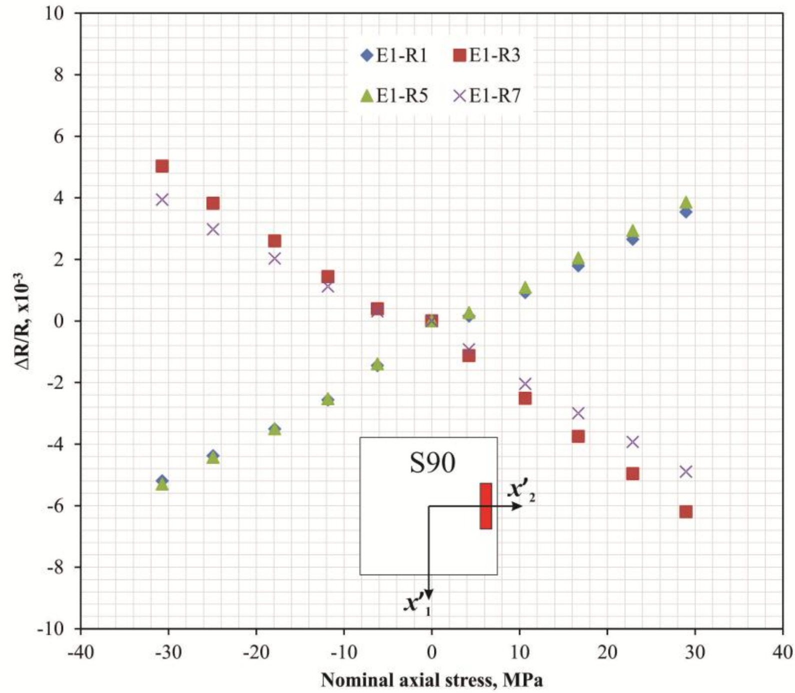

Figure 6-32 Resistance changes in the sensing elements of the edge1 4-element rosette in the S90-speciemen

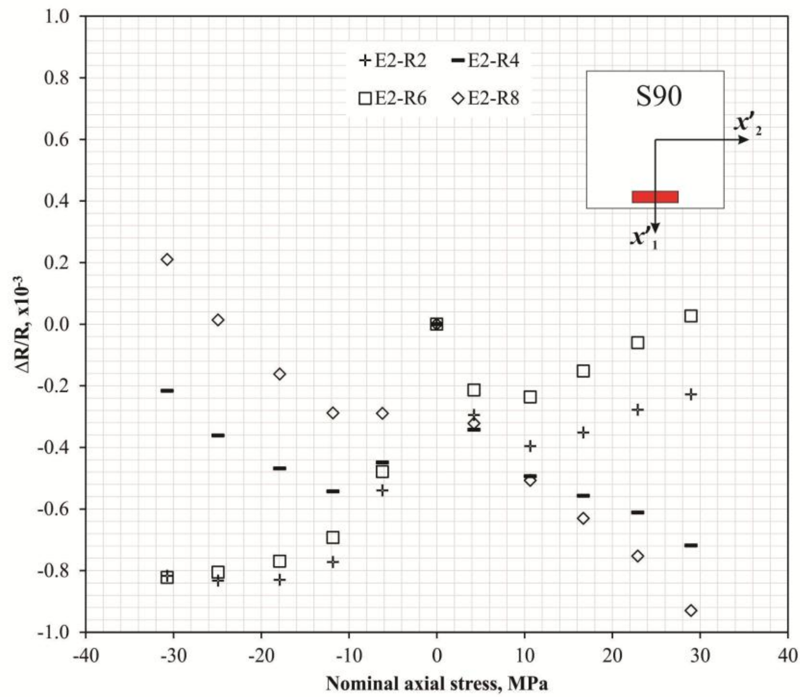

Figure 6-33 Resistance changes in the sensing elements of the edge2 4-element rosette in the S90-speciemen

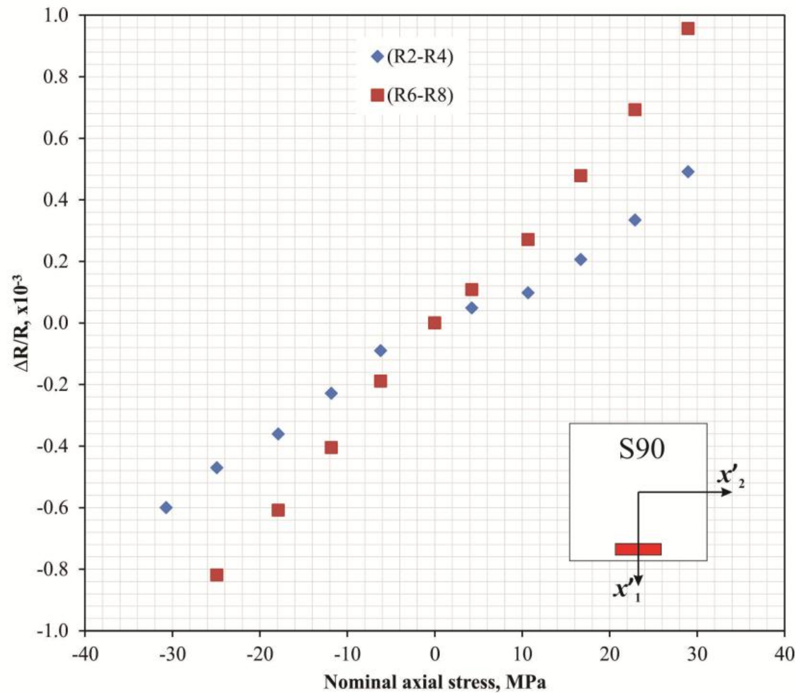

Figure 6-34 Difference between the change in resistance from (R_2 and R_4) and (R_6 and R_8) due to applied load for the edge2 4-element rosette in the S90-speciemen

6.9.2 Sensing chip output versus FEM

The results from the FEM along the beam's axes demonstrate high in-plane stress σ_{11} at the center of the chip, while the out-of-plane stresses peak at the edges. The gold bumps induce stress concentrations around the areas of the contact pads, but does not affect the uniformity of the stress fields at the location of the edge rosettes. For each chip orientation, the stress components with the highest values are presented to compare with the corresponding experimental output as shown in the contour plots over the sensing surface in Figure 6-35 to Figure 6-39 with respect to the x'-co-ordinate system. In these plots, AVG_N refers to the average stress over the surface area of the rosette calculated from the FEM with the difference between the maximum and minimum stresses (range) shown between parentheses as an indication of stress non-uniformity. S_N refers to the calculated

stress from the FEM rosette and S_E refers to the extracted stress from the experimental rosette.

In the S0 specimen, σ'_{11} is maximum at the center rosette, while σ'_{13} is almost zero at the center of the chip and increases at the edge rosette 2 as shown in Figure 6-35 and Figure 6-36, respectively. In the S45 specimen, σ'_{12} is maximized at the center of the chip and decreases at the edge rosette 2 as shown in Figure 6-37. Finally, in the S90 specimen σ'_{22} is maximum at the center rosette as shown in Figure 6-38. On the other, σ'_{23} is almost zero at the center of the chip and increases at the edge rosette 2 as shown in Figure 6-39.

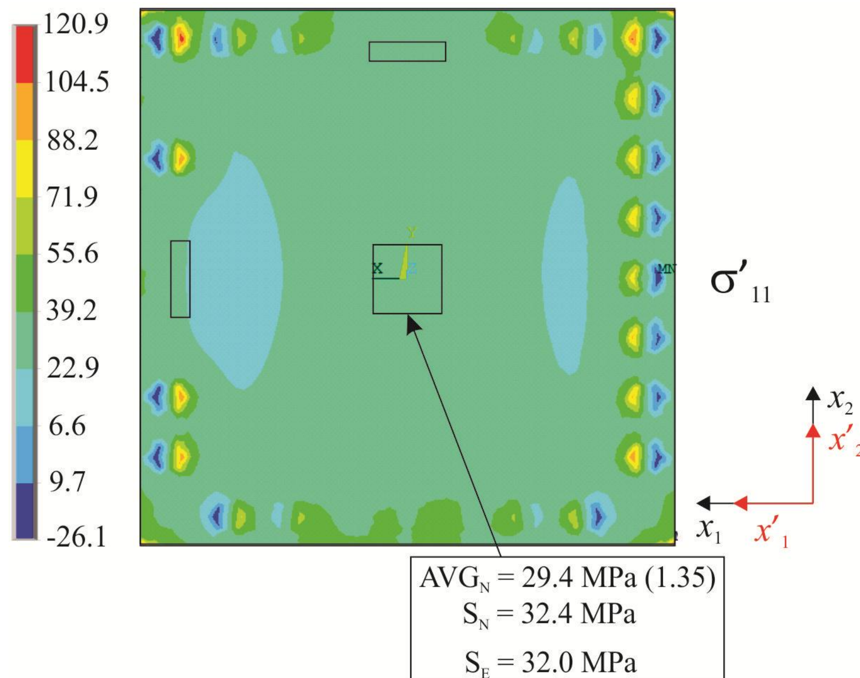

Figure 6-35 Specimen S0 - Stress field of σ'_{11} on chip surface at a nominal axial stress of 27.1 MPa

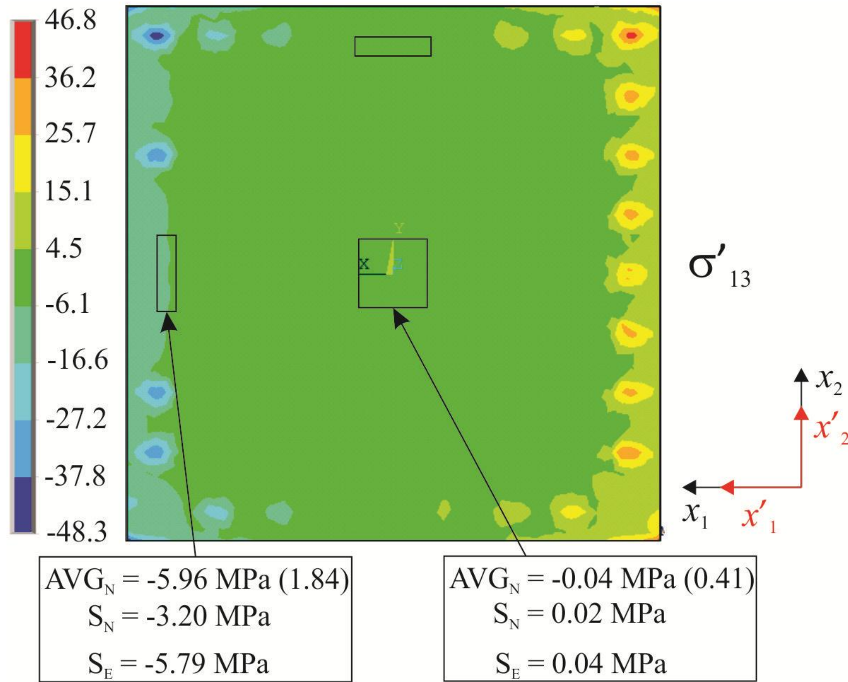

Figure 6-36 Specimen S0 - Stress field of σ'_{13} on chip surface at a nominal axial stress of 27.1 MPa

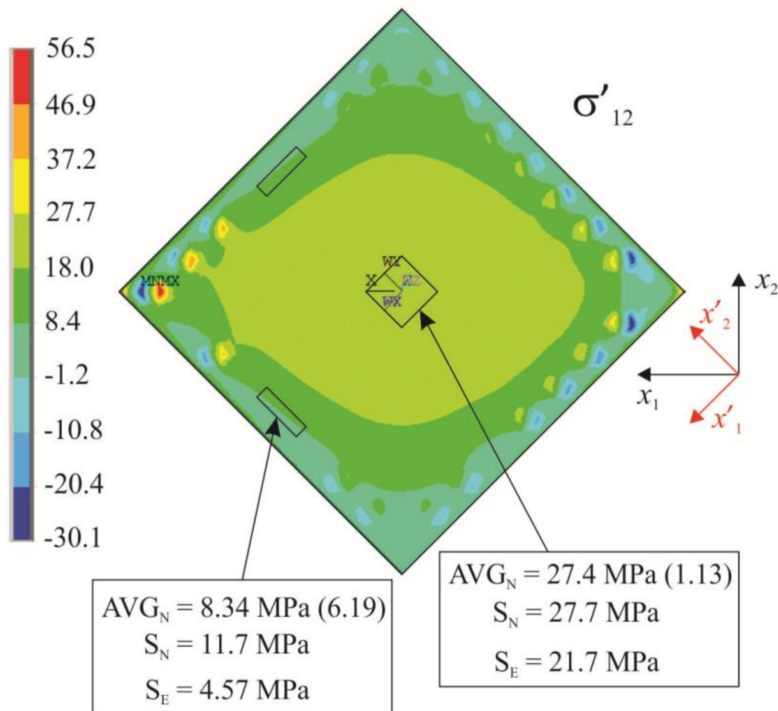

Figure 6-37 Specimen S45 - Stress field of σ'_{12} on chip surface at a nominal axial stress of 28.7 MPa

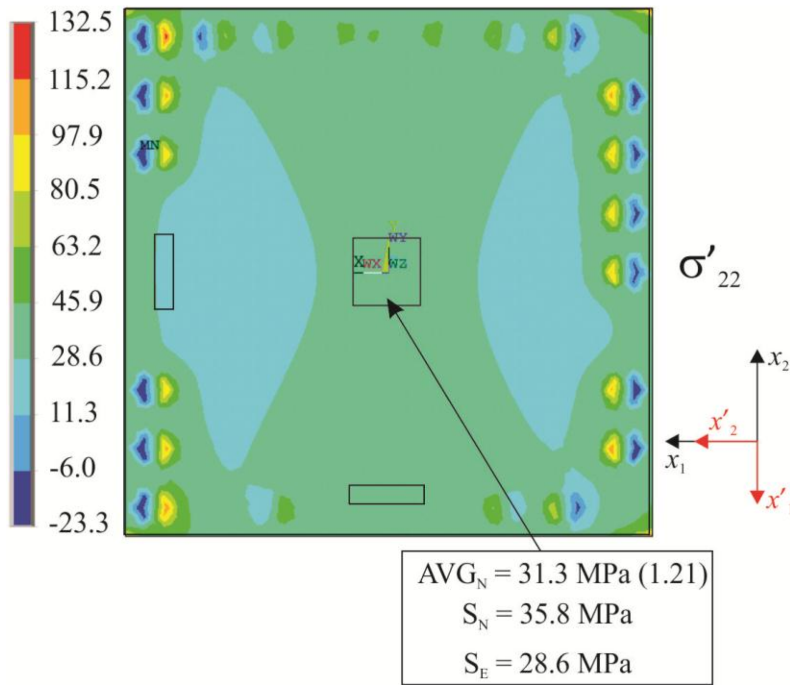

Figure 6-38 Specimen S90 - Stress field of σ'_{22} on chip surface at a nominal axial stress of 29.0 MPa

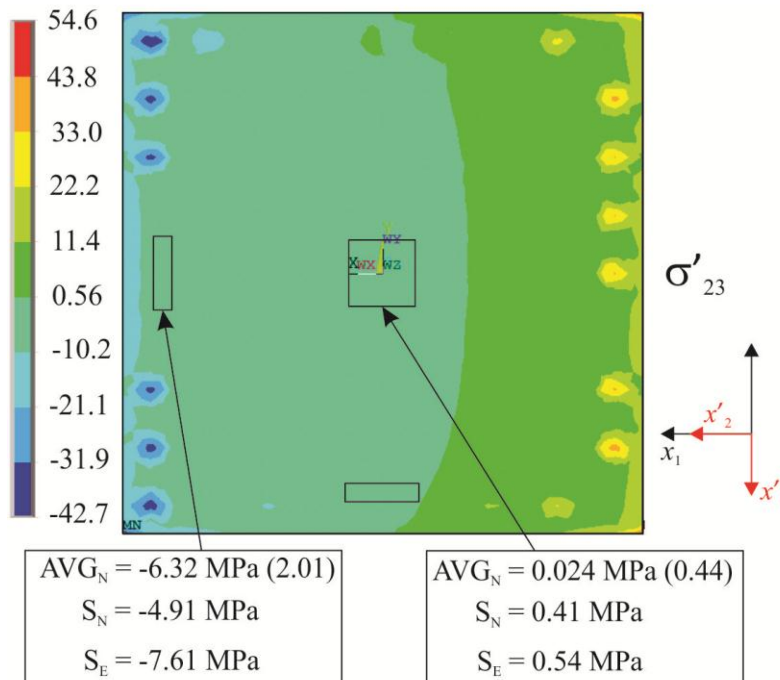

Figure 6-39 Specimen S90 - Stress field of σ'_{23} on chip surface at a nominal axial stress of 29.0 MPa

It is noticed that the difference between the FEM extracted stresses (S_N) and the average stresses (AVG_N) is higher at the edge rosettes compared to the center, which is evident in the results of σ'_{12} in Figure 6-37. This is due to the higher stress non-uniformity at the edges of the sensing chip compared to the center. In this case, each sensing element of the rosette is sensing a slightly different stress than the others in the rosette. This indicates the importance of locating the rosettes at areas of uniform stress fields or reducing the footprint of the rosette to be less sensitive to stress non-uniformities.

6.9.3 Experimental stress output at different loads

The extracted stresses from the sensing chip under tensile and compressive loads generated from the four-point bending are plotted in Figure 6-40 to Figure 6-48 for each chip orientation. The nominal uni-axial stress applied to the beam ranged from around -30 MPa to 30 MPa. The extracted six stress components and $\left(\sigma'_{11}-\sigma'_{22}\right)$ are presented at the center rosette, the shear stresses and $\left(\sigma'_{11}-\sigma'_{22}\right)$ are presented at the edge rosettes, and *T* (the difference between the current temperature and reference (room) temperature) is presented at the center rosette.

The results at the center rosette show different highest in-plane stress (σ'_{11} , σ'_{22} , and σ'_{12}) based on the chip orientation. In the S0 specimen, the highest stress at the center rosette is σ'_{11} which almost matches $\left(\sigma'_{11}-\sigma'_{22}\right)$ indicating a small value for σ'_{22} as shown in Figure 6-40, while all other stress components are lying within the zero boundaries. The 45 degrees dashed line in the graph is intended for comparison between the extracted σ'_{11} in the chip and the nominal axial stress in the PCB beam, which are shown to be close.

In the S45 specimen, the highest stress at the center rosette is the in-plane shear stress (σ'_{12}) as shown in Figure 6-43. From the FEM for the S45 specimen at a

nominal axial stress of 28.7 MPa, the average stresses generated at the center rosette along the beam's coordinate system, i.e. x-directions are given as σ_{11} = 41.5 MPa and σ_{11} = -11.4 MPa, while σ_{12} is zero. When these stresses are transformed along the x'-directions oriented at 45 degrees, the resulting normal stresses are σ'_{11} = σ'_{22} = 15 MPa, while the maximum generated σ'_{12} is 26.5 MPa. A Mohr's circle has been plotted using these results as shown in Figure 6-44 to represent the stress transformation from the beam's coordinate system to that of the 45 degrees oriented chip. From the experimental results in Figure 6-43, it is noticed that the maximum normal stress components σ'_{11} and σ'_{22} are around 3 MPa compared to the expected 15 MPa. Also, the linearity of σ'_{11} and σ'_{22} is not as good as the other orientations. This is mainly due to the small resistance change measurement extracted from the 0 and 90 degrees oriented sensing elements. In the case of a bi-axial in-plane stress, the equations of the 0 and 90 degrees elements reduce to:

$$\left(\frac{\Delta R_0}{R_0}\right) = B_1\,\sigma'_{11} + B_2\sigma'_{22} \tag{6-7}$$

$$\left(\frac{\Delta R_{90}}{R_{90}}\right) = B_2\sigma'_{11} + B_1\,\sigma'_{22} \tag{6-8}$$

Since the values of B_1 and B_2 are close with a sign difference, the resulting resistance changes are small as shown in the R_1, R_3, R_5, R_7, R_9, and R_{10} curves in Figure 6-28 which is affected by the measurement errors. The effect of the measurement errors has been studied earlier by Hussain *et al*. [65] for their 8-element rosette and they showed that σ'_{11} and σ'_{22} are among the stress components that are highly affected by measurement and calibration errors. One way to enhance the measurements is to maximize the resistance values of the sensing elements in order to increase the measured voltage change due to the same applied load. These inaccuracies in the resulting σ'_{11} and σ'_{22} does not affect the results for σ'_{12} since it uses different sensing elements and equations than those for σ'_{11} and σ'_{22}.

In the S90 specimen, the highest stress at the center rosette is σ'_{22} as shown in Figure 6-47, with $\left(\sigma'_{11} - \sigma'_{22}\right)$ showing close negative magnitudes indicating a small σ'_{11}. Also, the 45 degrees dashed line indicates that the extracted σ'_{22} is close to the nominal axial stress in the beam.

Regarding the stresses at the edge rosettes, the highest values for the shear stresses σ'_{13} and σ'_{23} occur in the S0 and S90 specimens as shown in Figure 6-41 and Figure 6-48, respectively. In the S45 specimen, all shear stress components are induced with maximum σ'_{12} due to the direction of loading as shown in Figure 6-45. Also, $\left(\sigma'_{11} - \sigma'_{22}\right)$ is present at the edge rosettes for all specimens indicating that normal in-plane stresses are induced at the chip edges.

The temperature difference *T* extracted from the center rosette is shown in Figure 6-42, Figure 6-46, and Figure 6-49 for the S0, S45, and S90 specimens, respectively. The values of *T* lay within the zero boundaries indicating a no-change in the temperature during testing. The highest error in the extracted *T* is found in the S90 specimen, which reaches around 0.4 °C.

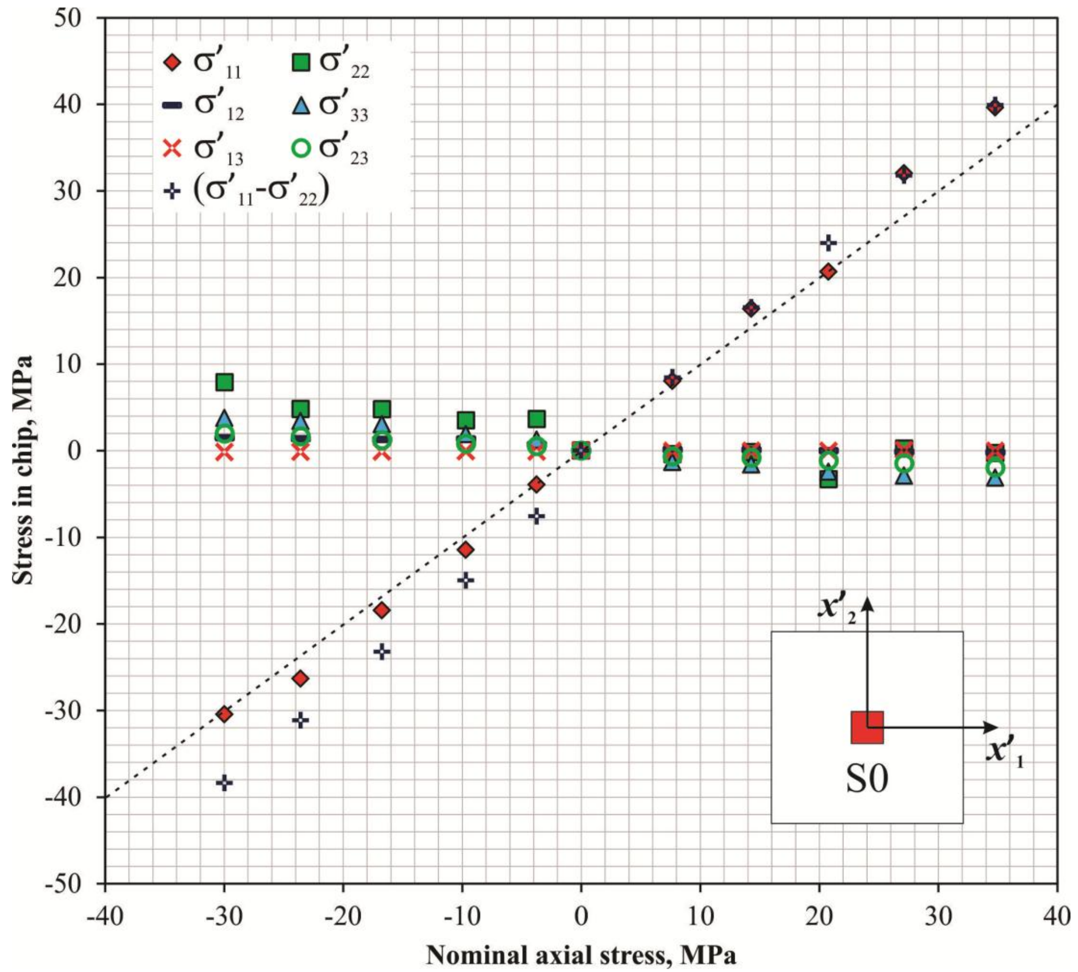

Figure 6-40 Extracted stresses from the 0 degrees oriented chip at the center rosette

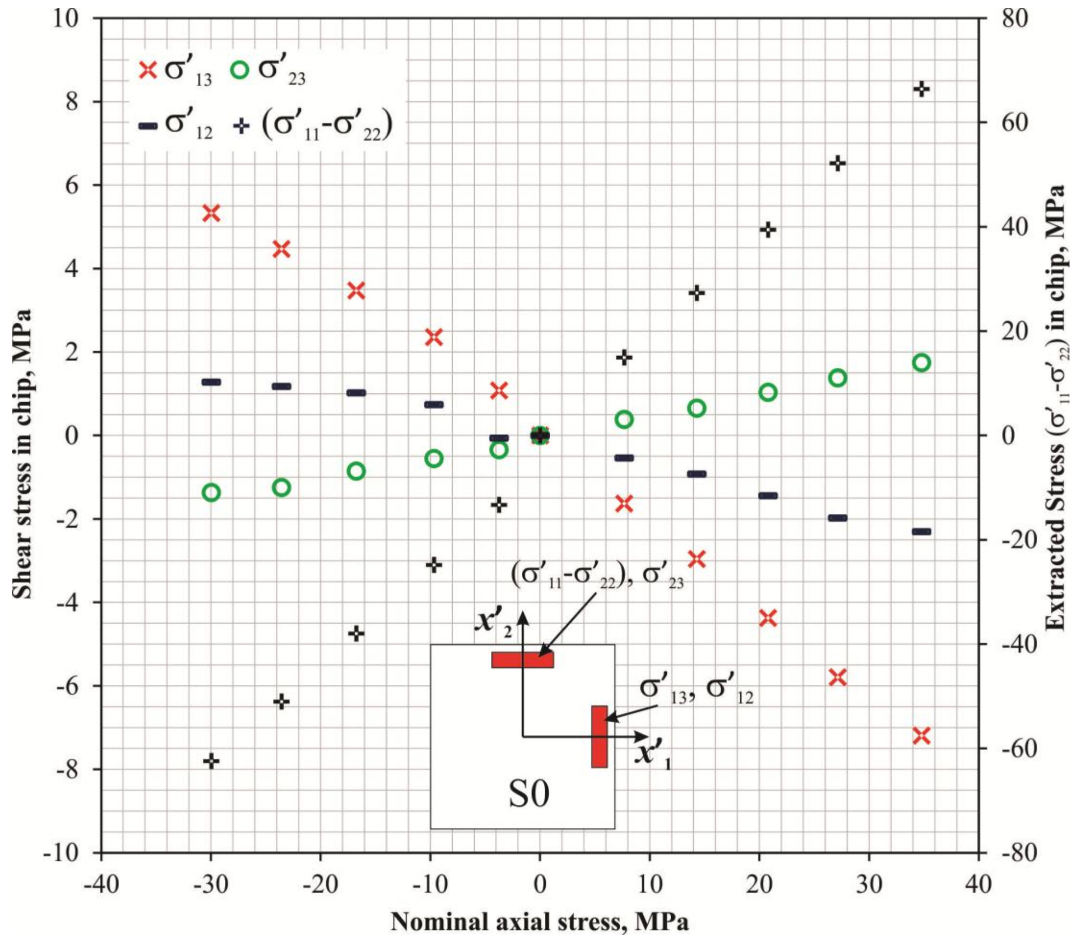

Figure 6-41 Extracted stresses from the 0 degrees oriented chip at the edge rosettes

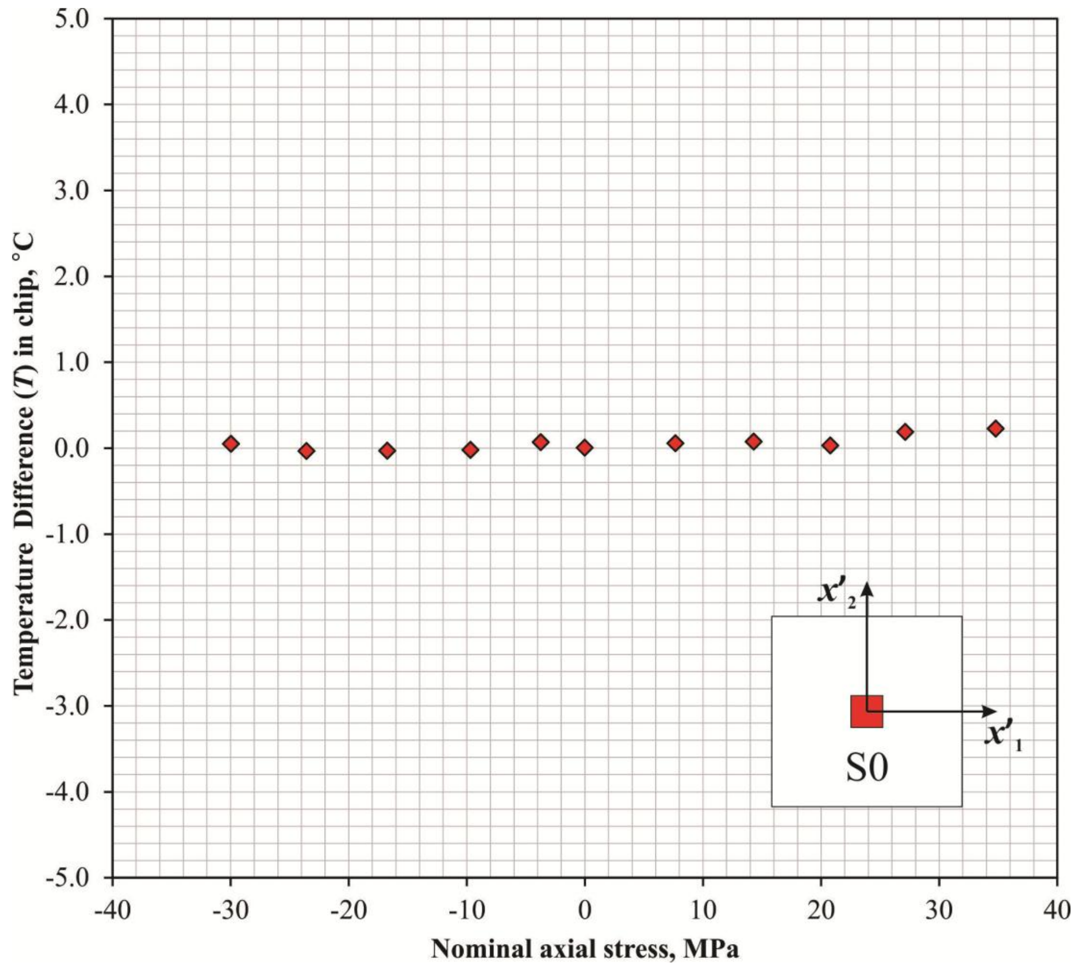

Figure 6-42 Extracted temperature from the 0 degrees oriented chip at the center rosette

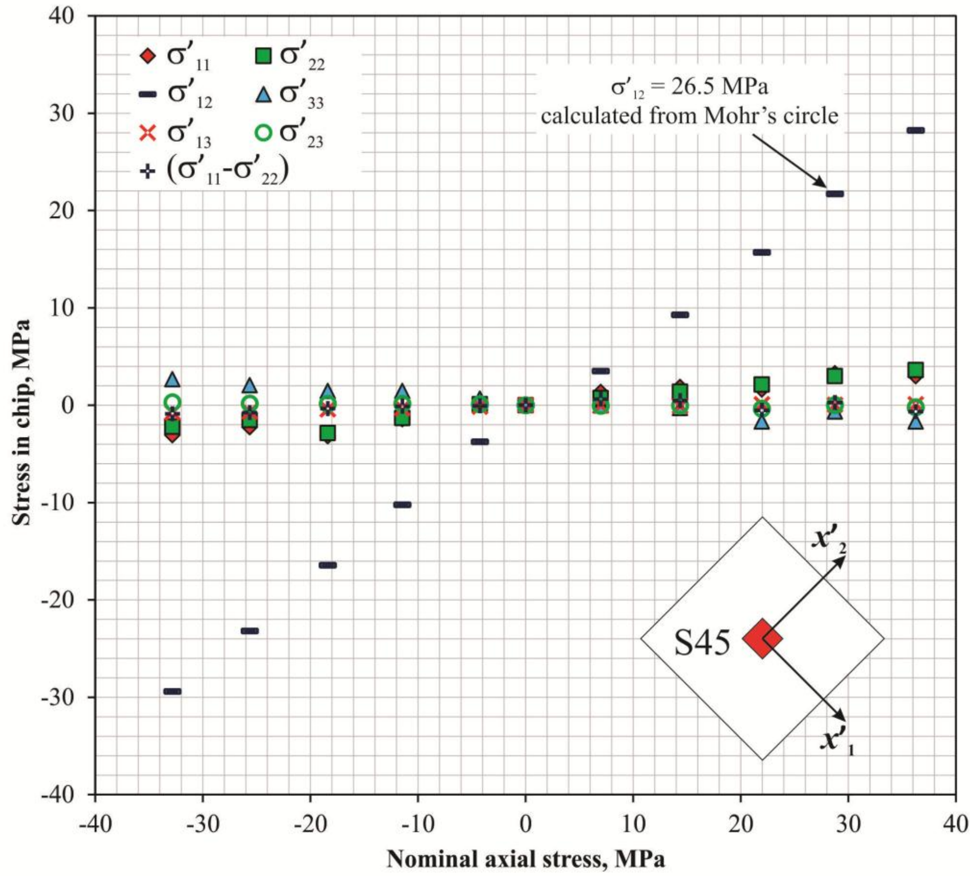

Figure 6-43 Extracted stresses from the 45 degrees oriented chip at the center rosette

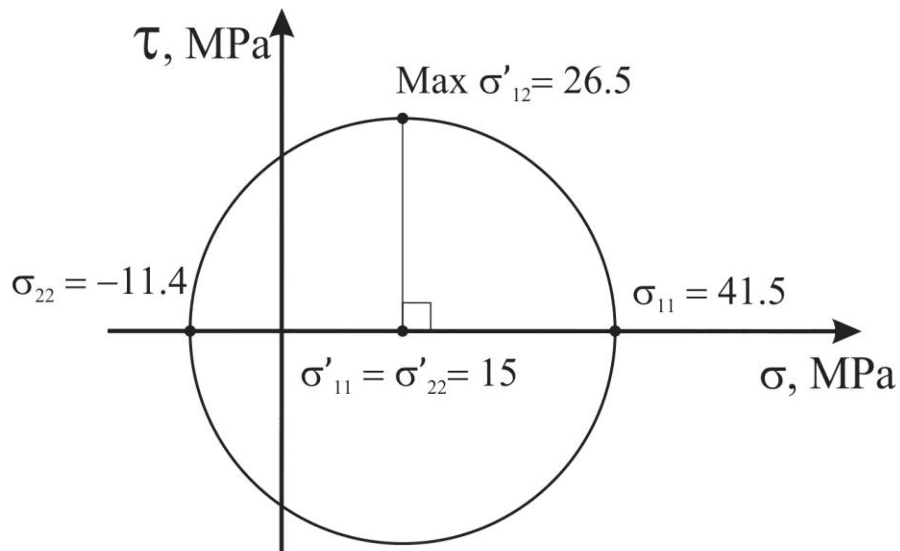

Figure 6-44 Mohr's circle representing the stress transformation for the S45 Specimen

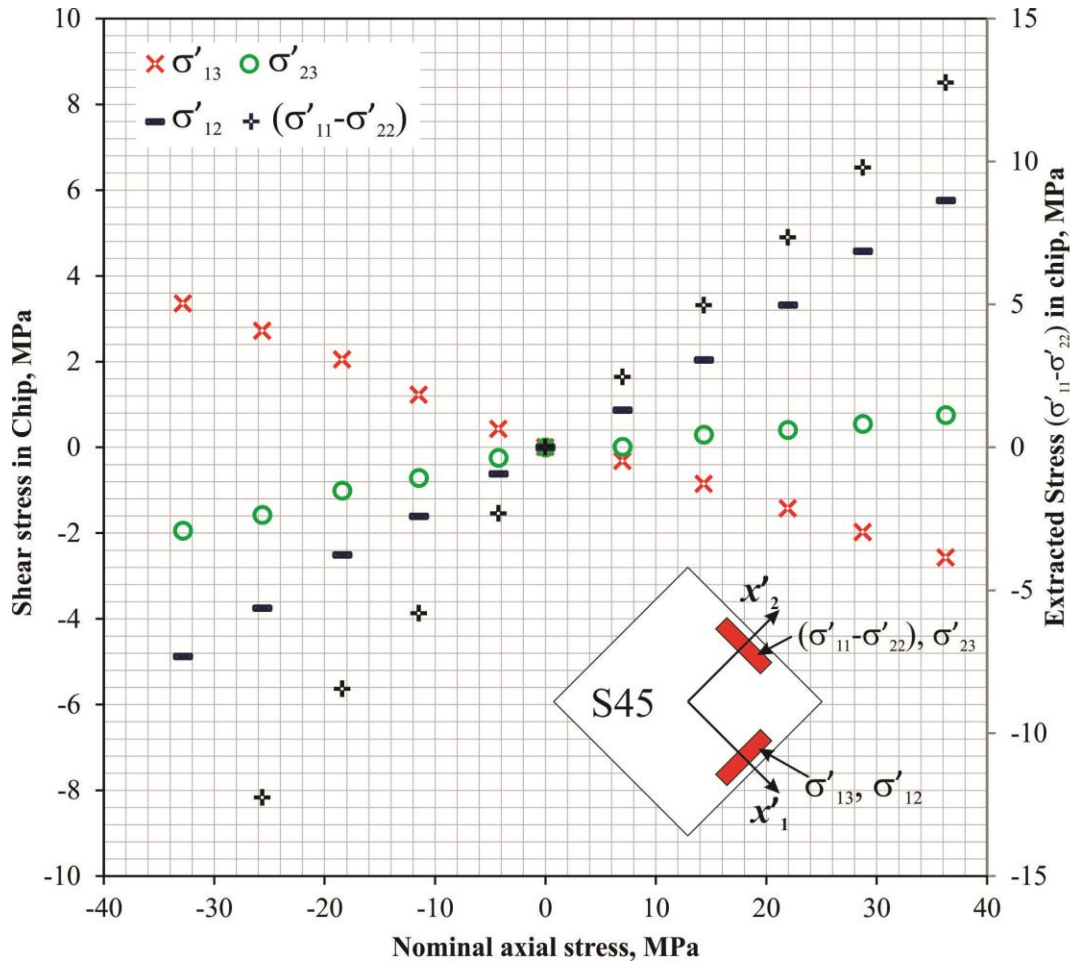

Figure 6-45 Extracted stresses from the 45 degrees oriented chip at the edge rosettes

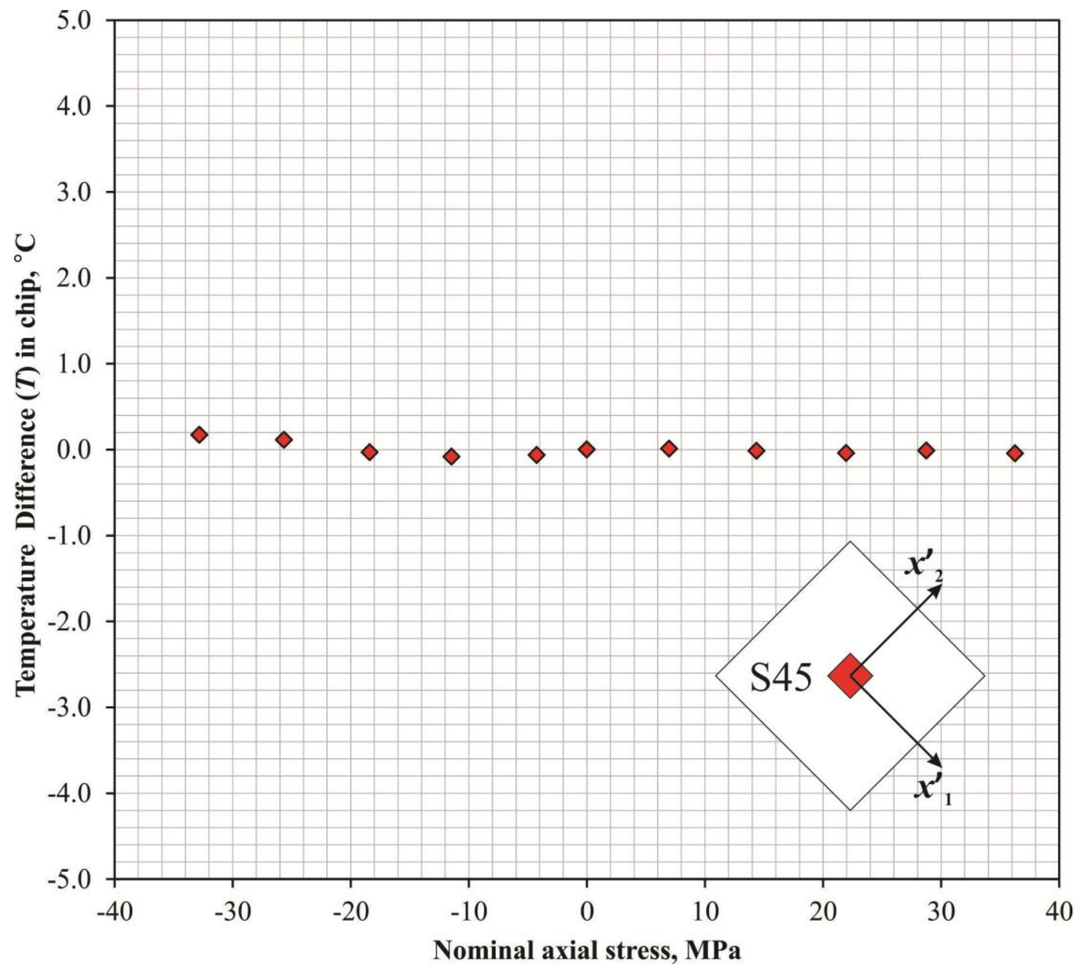

Figure 6-46 Extracted temperature from the 45 degrees oriented chip at the center rosette

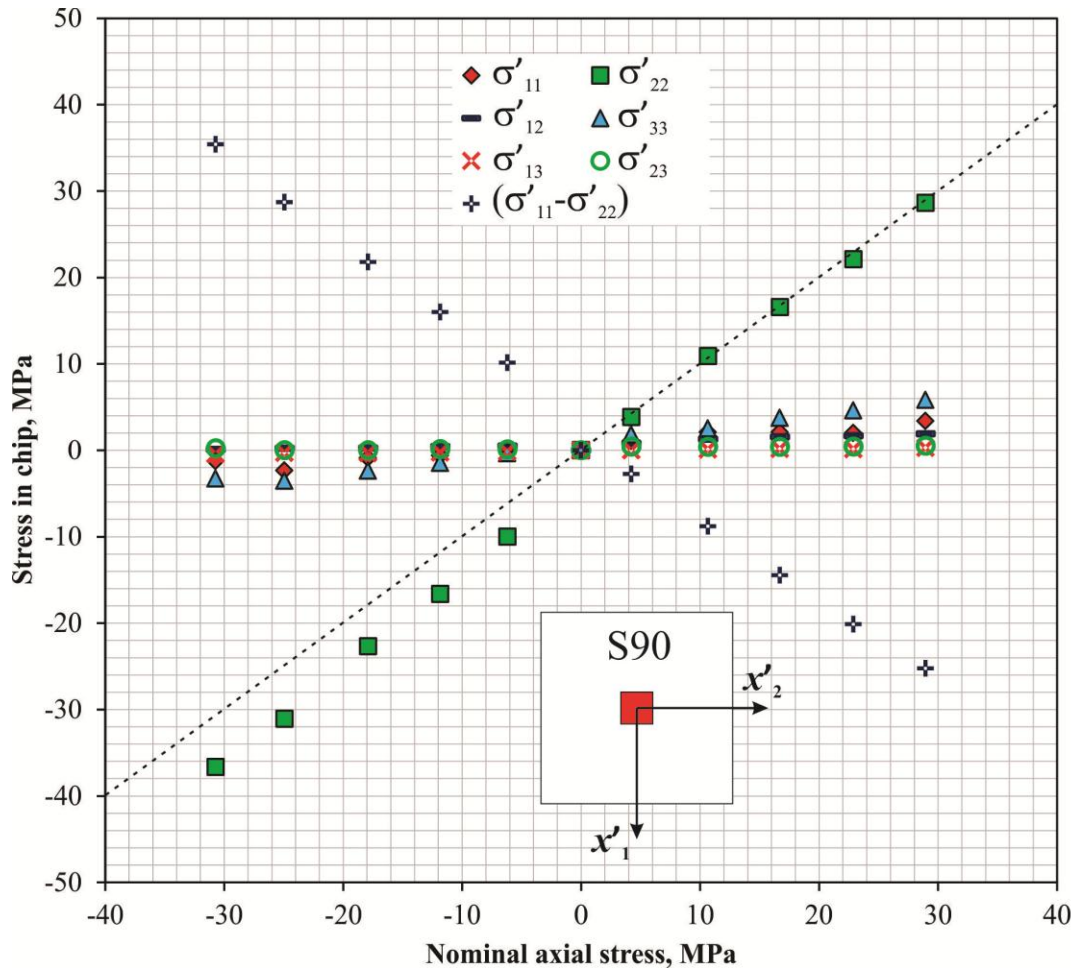

Figure 6-47 Extracted stresses from the 90 degrees oriented chip at the center rosette

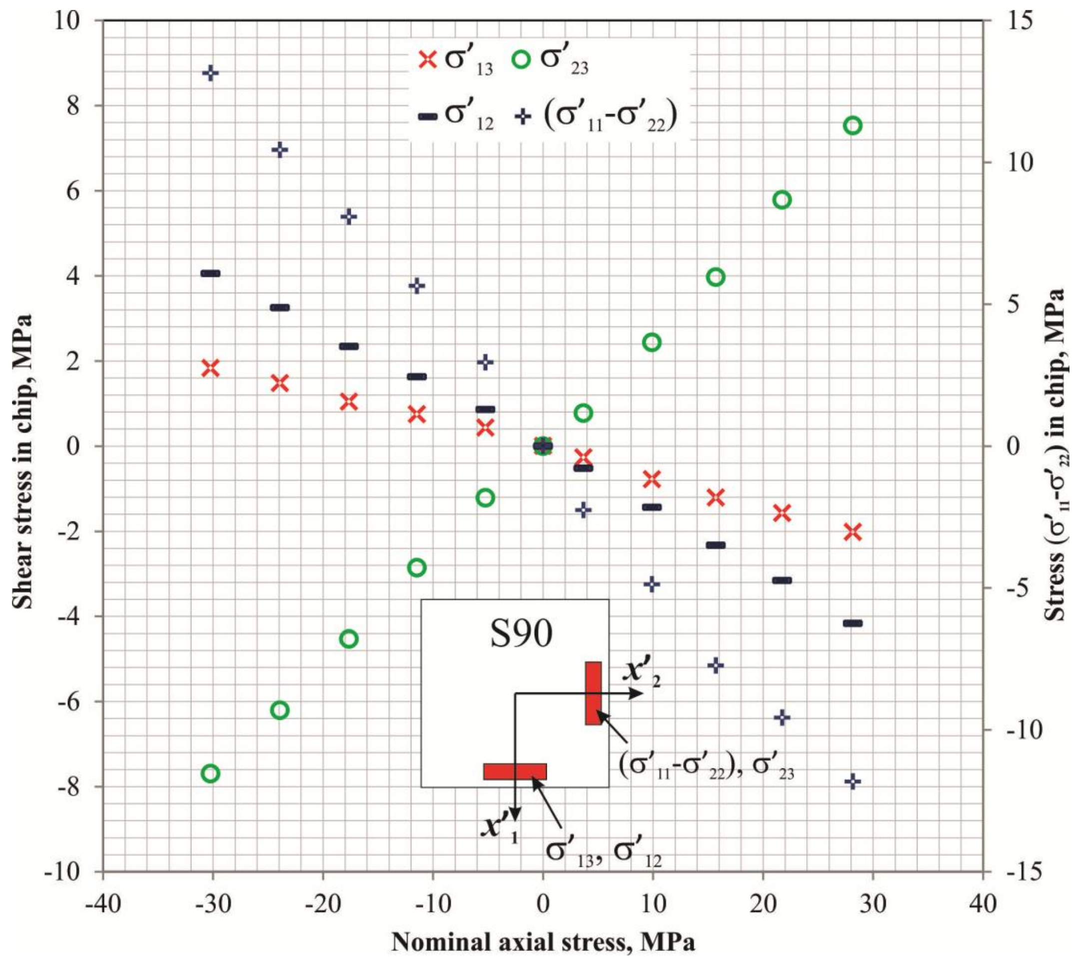

Figure 6-48 Extracted stresses from the 90 degrees oriented chip at the edge rosettes

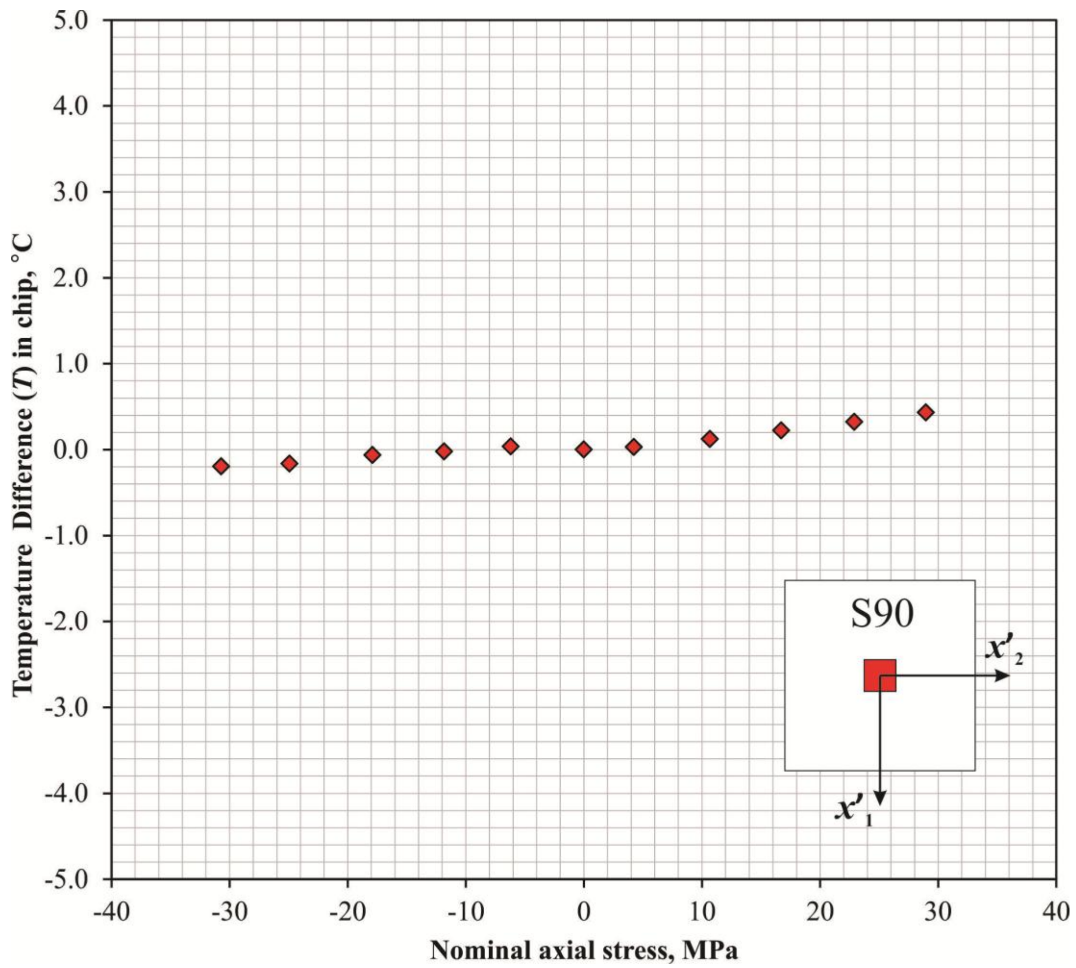

Figure 6-49 Extracted temperature from the 90 degrees oriented chip at the center rosette

The presented results demonstrate a proper response of the single-polarity 10-element sensing rosette to the applied stresses in tension and compression. Also, it presents a good linearity of the stress output over the applied load range, which is expected due to the linear elastic properties of the Chip/PCB assembly. All tests in this study were conducted at room temperature. Future work should focus on testing under thermal loads. However, the high impurity concentration (above 2×10^{19} cm^{-3}) of the sensing elements used in this study provides piezoresistive coefficients that are less sensitive to temperature than other levels of concentrations as studied experimentally by Tufte *et al*. [23] and analytically by Kanda [26]. Therefore, the response from the rosette will not be significantly affected by thermal loads. Moreover, accurate calibration of the piezoresistive coefficients can be carried out at different temperatures to capture any changes in their values over the operating temperature range. Cho *et al*. calibrated the piezoresistive coefficients over the range from -150 °C to 125 °C for n-Si piezoresistors doped at 4×10^{18} cm^{-3} and showed that a linear response exists between the coefficients and temperature [64].

6.9.4 Loading/Unloading Cycles

The stress output results from 10 cycles of tensile/compressive loadings are shown in Figure 6-50. These results correspond to $\left(\sigma'_{11} - \sigma'_{22}\right)$ extracted from the center rosette and correspond to an axial normal stress σ'_{11} of -10 MPa to 40 MPa at the center rosette. The results show good linearity and no hysteresis or load drifts over the loading cycles. This test is considered a preliminary analysis of the fabricated rosette under cyclic loading. If higher cyclic loading is of an interest towards a specific application, further tests are required to apply higher number of cycles and under prolonged periods to study any possible load drifts.

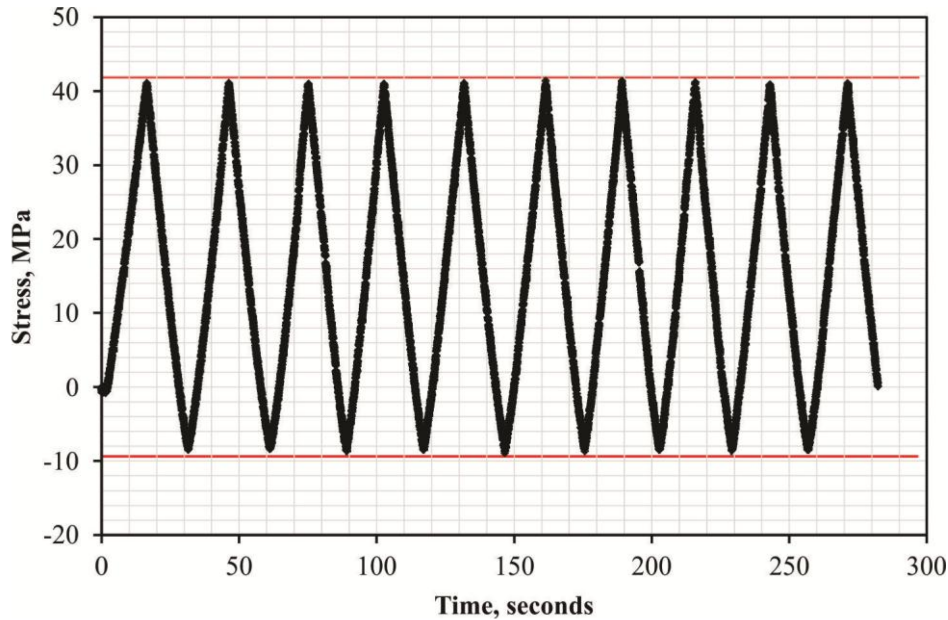

Figure 6-50 Stress $\left(\sigma'_{11} - \sigma'_{22}\right)$ from the center rosette under 10 cycles tensile/compressive loading

6.10 Conclusions

The 10-element single-polarity piezoresistive rosette was experimentally tested through a four-point bending of a PCB beam with a bonded sensing chip that has three rosette-sites. This chip-on-beam assembly oriented the sensing chip at three angles over the beam to induce five stress components at the three rosette-sites in a controlled manner. An FEM was developed to study the stress fields over the sensing chip surface to determine the range of expected stress output from the experimental testing. Also, the FEM modeled the piezoresistive sensing elements in the three rosette-sites to compare their stress output to the average stresses. The output from the experimental rosette showed comparable range of stress values to the FEM. The extracted stresses from the experimental testing showed good stress linearity from the rosette under tensile and compressive loads. Moreover, a simple hysteresis test of the rosette was performed under 10 cycles of tensile and compressive loads, which demonstrated no load drifts.

Independent testing of the normal out-of-plane stress σ'_{33} was not conducted in the current research due to its low sensitivity, where the low B_3 in the current microfabrication run limits the ability of the rosette to monitor small values of σ'_{33}. A controlled testing of σ'_{33} requires applying a normal pressure on the chip surface. Maximizing B_3 in n-Si is possible through changing the impurity concentrations; however, B_1 and B_2 will always be at least two times larger than B_3, thus the sensitivity to σ'_{11} and σ'_{22} will be higher than σ'_{33}. However, if a higher sensitivity to σ'_{33} is anticipated, the 10-element *dual-polarity* rosette can be used to take advantage of the high B_3 in p-Si as presented in Chapter 3.

The output results for the out-of-plane shear stresses at the edges of the chip indicate its potential use for monitoring delamination of bonded structures. The stress non-uniformities present at the edges of the chip indicate the importance of minimizing the rosette size to avoid their effect on the stress output. Fabrication of a smaller rosette size is possible by minimizing the feature sizes of the piezoresistors to obtain an equivalent sheet resistance.

CHAPTER 7: CONCLUSION AND FUTURE WORK

7.1 Research Contributions

The current research deals with the development of a new piezoresistive sensing rosette capable of 3D stress measurements. The research work involved the design, microfabrication, calibration, and testing of a silicon chip utilizing the developed 3D stress sensing rosette. 3D stress monitoring is important for SHM applications that require out-of-plane stress measurement to detect potential delamination of bonded structures. Some examples include bonded patches, bio-implants, and electronic packaging. There has been limited research towards the development of a 3D piezoresistive stress sensor, which was mainly focused on two types; the rosette design and the MOSFET design. Both designs were not able to extract stress components separately with temperature compensation. The rosette design was able to extract the three shear stresses and the difference of the in-plane normal stresses with temperature compensation. The current research was able to develop a new 3D stress rosette to extract all stress components with temperature compensation. The following are the major research contributions:

1. The piezoresistive 8-elment 3D stress sensing rosette developed in the literature was studied to determine how the six stress components with temperature compensation can be extracted instead of the limited 4 temperature-compensated components available in the literature. A new 10-element piezoresistive rosette was devised that can extract the six stress components with temperature compensation. The unique behavior of the shear piezoresistive coefficient (π_{44}) in n-Si with impurity concentration reported in the literature is the main feature that helps in the operation of the new 10-element rosette.

2. Two types of the proposed rosette were analytically studied; one using single-polarity and the other using dual-polarity sensing elements. An analytical study involving the analysis of the effect of impurity concentration on the determinants of the resistance change versus stress equations was conducted. Full extraction of the six stress components with temperature compensation was found possible with both types of rosettes.
3. Temperature drift effects on the stress output were controlled through two approaches; the first is using high doping concentrations and the other through mathematical subtraction. The high doping concentrations provide PR coefficients and TCR that is unaffected by thermal variations. On the other hand, elimination of the temperature effects on the change in resistance through the TCR is eliminated by subtraction of the resistance change equations from two sets of equations and solving for the temperature from the third set of equations.
4. A new calibration approach utilizing ZIF connectors was adopted to calibrate the 10-element single-polarity rosette. The connector, which has been utilized by Richter *et al*. [112] for four-point bending has been extended to the calibration process in an environmental chamber and pressure vessel. This expedited and facilitated the calibration process compared to the previous approach which involved wire-bonding the calibration chip to a PCB before placing in the environmental chamber and pressure vessel. Moreover, it eliminated the uncontrolled forces applied on the sensing elements from the contacting probes during calibration. This approach can also be used for quick characterization of micro-fabricated devices instead of packaging through wire-bonding or flip-chipping.
5. In order to test the sensing chip under 3D stresses, a new setup was devised to induce five controlled stress components. The testing was conducted by applying a four-point bending on a chip-on-beam specimen. Three specimens made up of the sensing chip bonded to a PCB beam were prepared, where the chip on each of the three specimens was oriented at a

different angle to induce a different known stress component at three rosette-sites.

6. The results from the experimental testing demonstrated correct response for the five induced stress components under tensile and compressive loading on the fibers of the beam. The results of the test setup present a potential approach for monitoring delamination of bonded structure from the induced shear stresses at the edges of the chip.

7.2 Future Work

The current research dealt with a number of study areas ranging from devising a new approach to a full experimental study. However, there are a number of development areas that will definitely improve the proposed approach and extend its use.

1. The limitation with the low sensitivity of the out-of-plane normal stress (σ'_{33}) will need to be investigated by micro-fabricating a new test chip with higher B_3. This should be accompanied by preparing a test setup to apply normal controlled pressure on the chip to induce enough σ'_{33} for testing.
2. The low resistance value of the sensing elements has an impact on the measurement errors. Therefore, it is suggested to maximize the resistance values to increase the voltage change from the sensing elements for the same applied load, thus reducing the need for high accuracy measurement equipment.
3. The 10-element dual-polarity rosette presented in Chapter 3 has not been experimentally investigated in this research. An experimental investigation of this rosette is valuable especially to determine its response to the σ'_{33} loads.
4. The current research did not involve testing under varying thermal loads. This is an important continuation to the proposed approach, where the

sensing chip will need to be tested at different temperatures to ensure the independence of the stress output from the applied temperature.

5. The presented approach of using single-polarity doping to create stress sensors can be investigated towards implantation in different sensing techniques like the van der Pauw stress sensor developed by Mian *et al*. [90]. The van der Pauw stress sensor can offer a smaller foot-print than the rosette design.

BIBLIOGRAPHY

[1] S. Sambursky, *Physical thought from the Presocratics to the quantum physicists : an anthology*. London,: Hutchinson, 1974.

[2] W. S. Johnson, ASTM Committee D-14 on Adhesives., and American Society for Testing and Materials., *Adhesively bonded joints : testing, analysis, and design*. Philadelphia: American Society for Testing and Materials, 1988.

[3] R. D. Adams and N. A. Peppiatt, "Stress analysis of adhesive-bonded lap joints," *The Journal of Strain Analysis for Engineering Design,* vol. 9, pp. 185-196, July 1 1974.

[4] A. R. Baker, LRF; Jones, R, *Advances in bonded composite repair of metallic aircraft structure*. United Kingdom: Elsevier, 2002.

[5] Z. L. Chaudhry, Frederic; Ganino, Anthony; Rogers, Craig A.; Chung, Jaycee, "Monitoring the integrity of composite patch structural repair via piezoelectric actuators/sensors," in *Proceedings of the 36th AIAA/ASME/ASCE/AHS/ASC Structures, Structural Dynamics, and Materials Conference and AIAA/ASME Adaptive Structures Forum. Part 4 (of 5)*, New Orleans, LA, USA, 1995, pp. 2243-2248.

[6] W. Baker, I. McKenzie, and R. Jones, "Development of life extension strategies for Australian military aircraft, using structural health monitoring of composite repairs and joints," ed, 2004.

[7] H. C. H. Li, F. Beck, O. Dupouy, I. Herszberg, P. R. Stoddart, C. E. Davis, *et al.*, "Strain-based health assessment of bonded composite repairs," *Composite Structures,* vol. 76, pp. 234-242, Nov 2006.

[8] I. McKenzie, R. Jones, I. H. Marshall, and S. Galea, "Optical fibre sensors for health monitoring of bonded repair systems," *Composite Structures,* vol. 50, pp. 405-416, Dec 2000.

[9] G. D. Davis, "Electrochemical impedance evaluation of aluminum/boron–epoxy composite bonds," *Journal of Adhesion Science and Technology,* vol. 19, pp. 1397-1408, 2005/01/01 2005.

[10] F. Alfaro, L. Weiss, P. Campbell, M. Miller, and G. K. Fedder, "Design of a multi-axis implantable MEMS sensor for intraosseous bone stress

monitoring," *Journal of Micromechanics and Microengineering,* vol. 19, pp. -, Aug 2009.

[11] K. Seidl, S. Herwik, T. Torfs, H. P. Neves, O. Paul, and P. Ruther, "CMOS-Based High-Density Silicon Microprobe Arrays for Electronic Depth Control in Intracortical Neural Recording," *IEEE Journal of Microelectromechanical Systems,* vol. 20, pp. 1439-1448, 2011.

[12] B. G. Lapatki, J. Bartholomeyczik, P. Ruther, I. E. Jonas, and O. Paul, "Smart bracket for multi-dimensional force and moment measurement," *J Dent Res,* vol. 86, pp. 73-8, Jan 2007.

[13] J. C. Suhling and R. C. Jaeger, "Silicon piezoresistive stress sensors and their application in electronic packaging," *Sensors Journal, IEEE,* vol. 1, pp. 14-30, 2001.

[14] C. Hautamaki, L. Cao, J. Zhou, S. C. Mantell, and T. S. Kim, "Calibration of MEMS strain sensors fabricated on silicon: Theory and experiments," *Journal of Microelectromechanical Systems,* vol. 12, pp. 720-727, Oct 2003.

[15] A. I. Sabra. (2003) Ibn al-Haytham. *Harvard Magazine*.

[16] C. Wheatstone, "The Bakerian Lecture: An Account of Several New Instruments and Processes for Determining the Constants of a Voltaic Circuit," *Philosophical Transactions of the Royal Society of London,* vol. 133, pp. 303-327, 1843.

[17] W. Thomson, "On the Electro-Dynamic Qualities of Metals:--Effects of Magnetization on the Electric Conductivity of Nickel and of Iron," *Proceedings of the Royal Society of London,* vol. 8, pp. 546-550, 1856.

[18] F. G. Tatnall, *Tatnall on testing : an autobiographical account of adventures under 13 vice presidents*. Metals Park, Ohio: American Society for Metals, 1966.

[19] C. S. Smith, "Piezoresistance Effect in Germanium and Silicon," *Physical Review,* vol. 94, pp. 42-49, 1954.

[20] W. Paul and G. L. Pearson, "Pressure Dependence of the Resistivity of Silicon," *Physical Review,* vol. 98, pp. 1755-1757, 1955.

[21] W. G. Pfann and R. N. Thurston, "Semiconducting Stress Transducers Utilizing the Transverse and Shear Piezoresistance Effects," *Journal of Applied Physics,* vol. 32, pp. 2008-2019, 10/00/ 1961.

[22] O. N. Tufte and E. L. Stelzer, "Piezoresistive Properties of Silicon Diffused Layers," *Journal of Applied Physics,* vol. 34, pp. 313-318, 1963.

[23] O. N. Tufte and E. L. Stelzer, "Piezoresistive Properties of Heavily Doped n-Type Silicon," *Physical Review,* vol. 133, p. A1705, 1964.

[24] F. J. Morin, T. H. Geballe, and C. Herring, "Temperature Dependence of the Piezoresistance of High-Purity Silicon and Germanium," *Physical Review,* vol. 105, pp. 525-539, 1957.

[25] J. Richter, O. Hansen, A. N. Larsen, J. L. Hansen, G. F. Eriksen, and E. V. Thomsen, "Piezoresistance of silicon and strained Si0.9Ge0.1," *Sensors and Actuators a-Physical,* vol. 123-24, pp. 388-396, Sep 23 2005.

[26] Y. Kanda, "A graphical representation of the piezoresistance coefficients in silicon," *Electron Devices, IEEE Transactions on,* vol. 29, pp. 64-70, 1982.

[27] Y. Kanda and K. Matsuda, "Piezoresistance effect in p-type silicon," *Physics of Semiconductors, Pts A and B,* vol. 772, pp. 79-80, 2005.

[28] Y. Kanda and K. Matsuda, "Piezoresistance Effect of n-type Silicon; Temperature and Concentration Dependencies, Stress Dependent Effective Masses," *AIP Conference Proceedings,* vol. 893, pp. 173-174, 2007.

[29] Y. Kanda and K. Suzuki, "Origin of the shear piezoresistance coefficient pi 44 of n-type silicon," *Physical Review B,* vol. 43, p. 6754, 1991.

[30] K. Matsuda, Y. Kanda, and K. Suzuki, "2nd-Order Piezoresistance Coefficients of N-Type Silicon," *Japanese Journal of Applied Physics Part 2-Letters,* vol. 28, pp. L1676-L1677, Oct 1989.

[31] K. Matsuda, Y. Kanda, K. Yamamura, and K. Suzuki, "2nd-Order Piezoresistance Coefficients of P-Type Silicon," *Japanese Journal of Applied Physics Part 2-Letters & Express Letters,* vol. 29, pp. L1941-L1942, Nov 1990.

[32] S. I. Kozlovskiy and I. I. Boiko, "First-order piezoresistance coefficients in silicon crystals," *Sensors and Actuators a-Physical,* vol. 118, pp. 33-43, Jan 31 2005.

[33] T. Toriyama and S. Sugiyama, "Analysis of piezoresistance in p-type silicon for mechanical sensors," *Journal of Microelectromechanical Systems,* vol. 11, pp. 598-604, Oct 2002.

[34] J. Richter, J. Pedersen, M. Brandbyge, E. V. Thomsen, and O. Hansen, "Piezoresistance in p-type silicon revisited," *Journal of Applied Physics,* vol. 104, pp. -, Jul 15 2008.

[35] D. R. Kerr and A. G. Milnes, "Piezoresistance of Diffused Layers in Cubic Semiconductors," *Journal of Applied Physics,* vol. 34, pp. 727-&, 1963.

[36] J. T. Lenkkeri, "Nonlinear Effects in the Piezoresistivity of p-Type Silicon," *physica status solidi (b),* vol. 136, pp. 373-385, 1986.

[37] W. M. Bullis, F. H. Brewer, C. D. Kolstad, and L. J. Swartzendruber, "Temperature coefficient of resistivity of silicon and germanium near room temperature," *Solid-State Electronics,* vol. 11, pp. 639-646, 1968.

[38] P. Norton and J. Brandt, "Temperature-Coefficient of Resistance for P-Type and N-Type Silicon," *Solid-State Electronics,* vol. 21, pp. 969-974, 1978.

[39] A. Boukabache and R. Pons, "Doping effects on thermal behaviour of silicon resistor," *Electronics Letters,* vol. 38, pp. 342-343, 2002.

[40] Y. Kanda and K. Matsuda, "Shear Piezoresistance Coefficient pi44 of n-type Silicon," in *NASTI Nanotech 2007*, 2007.

[41] K. Nakamura, Y. Isono, T. Toriyama, and S. Sugiyama, "Simulation of piezoresistivity in n-type single-crystal silicon on the basis of the first-principles band structure," *Physical Review B,* vol. 80, pp. -, Jul 2009.

[42] X. Li, Q. Liu, S. Pang, K. Xu, H. Tang, and C. Sun, "High-temperature piezoresistive pressure sensor based on implantation of oxygen into silicon wafer," *Sensors and Actuators A: Physical,* vol. 179, pp. 277-282, 6// 2012.

[43] C.-T. Peng, J.-C. Lin, C.-T. Lin, and K.-N. Chiang, "Performance and package effect of a novel piezoresistive pressure sensor fabricated by front-side etching technology," *Sensors and Actuators A: Physical,* vol. 119, pp. 28-37, 3/28/ 2005.

[44] S. Sugiyama, M. Takigawa, and I. Igarashi, "Integrated piezoresistive pressure sensor with both voltage and frequency output," *Sensors and Actuators,* vol. 4, pp. 113-120, // 1983.

[45] A. A. Barlian, W. T. Park, J. R. Mallon, A. J. Rastegar, and B. L. Pruitt, "Review: Semiconductor Piezoresistance for Microsystems," *Proceedings of the IEEE,* vol. 97, pp. 513-552, 2009.

[46] D. Li, T. Zhao, Z. C. Yang, and D. C. Zhang, "Monolithic integration of a micromachined piezoresistive flow sensor," *Journal of Micromechanics and Microengineering,* vol. 20, Mar 2010.

[47] M. A. Schmidt, R. T. Howe, S. D. Senturia, and J. H. Haritonidis, "Design and Calibration of a Microfabricated Floating-Element Shear-Stress Sensor," *Ieee Transactions on Electron Devices,* vol. 35, pp. 750-757, Jun 1988.

[48] S. S. Li and W. R. Thurber, "Dopant Density and Temperature-Dependence of Electron-Mobility and Resistivity in N-Type Silicon," *Solid-State Electronics,* vol. 20, pp. 609-616, 1977.

[49] B. David, L. Edmond, and A. M. Walied, "A packaging solution utilizing adhesive-filled TSVs and flip–chip methods," *Journal of Micromechanics and Microengineering,* vol. 22, p. 065009, 2012.

[50] T. C. Duc, J. F. Creemer, and P. M. Sarro, "Piezoresistive Cantilever Beam for Force Sensing<newline/>in Two Dimensions," *Sensors Journal, IEEE,* vol. 7, pp. 96-104, 2007.

[51] A. Tibrewala, A. Phataralaoha, and S. Büttgenbach, "Simulation, fabrication and characterization of a 3D piezoresistive force sensor," *Sensors and Actuators A: Physical,* vol. 147, pp. 430-435, 10/3/ 2008.

[52] A. Partridge, J. K. Reynolds, B. W. Chui, E. M. Chow, A. M. Fitzgerald, L. Zhang*, et al.*, "A high-performance planar piezoresistive accelerometer," *Microelectromechanical Systems, Journal of,* vol. 9, pp. 58-66, 2000.

[53] I. K. Hung, G. Jun, and W. H. Ko, "High Performance Piezoresistive Micro Strain Sensors," in *Nano/Micro Engineered and Molecular Systems, 2007. NEMS '07. 2nd IEEE International Conference on*, 2007, pp. 1052-1055.

[54] A. A. S. Mohammed, W. A. Moussa, and E. Lou, "Optimization of geometric characteristics to improve sensing performance of MEMS piezoresistive strain sensors," *Journal of Micromechanics and Microengineering,* vol. 20, pp. -, Jan 2010.

[55] M. Baumann, P. Ruther, and O. Paul, "Modeling and Characterization of a Cmos Sensor with Surface Trenches for High-Pressure Applications," *2011 Ieee 24th International Conference on Micro Electro Mechanical Systems (Mems),* pp. 601-604, 2011.

[56] P. J. French and A. G. R. Evans, "Polycrystalline Silicon Strain Sensors," *Sensors and Actuators,* vol. 8, pp. 219-225, Nov 1985.

[57] C. Li, K. Tae Song, Z. Jia, S. C. Mantell, and D. L. Polla, "Calibration technique for MEMS membrane type strain sensors," in *University/Government/Industry Microelectronics Symposium, 1999. Proceedings of the Thirteenth Biennial*, 1999, pp. 204-210.

[58] L. Cao, T. S. Kim, S. C. Mantell, and D. L. Polla, "Simulation and fabrication of piezoresistive membrane type MEMS strain sensors," *Sensors and Actuators a-Physical,* vol. 80, pp. 273-279, Mar 15 2000.

[59] M. A. Fraga, H. Furlan, S. M. Wakavaiachi, and M. Massi, "Fabrication and characterization of piezoresistive strain sensors for high temperature applications," in *Industrial Technology (ICIT), 2010 IEEE International Conference on*, 2010, pp. 513-516.

[60] H. Miura, A. Nishimura, S. Kawai, and G. Murakami, "Structural Effect of Ic Plastic Package on Residual-Stress in Silicon Chips," *40th Electronic Components and Technology Conference, Vols 1 and 2,* pp. 316-321, 1990.

[61] D. A. Bittle, J. C. Suhling, R. E. Beaty, and R. C. Jaeger, "Piezoresistive stress sensors for structural analysis of electronic packages," *Journal of Electronic Packaging,* vol. 113, pp. 203-215, 1991.

[62] R. A. Cordes, J. C. Suhling, Y. L. Kang, and R. C. Jaeger, "Optimal temperature compensated piezoresistive stress sensor rosettes," in *Proceedings of the 1995 ASME International Mechanical Engineering Congress and Exposition*, San Francisco, CA, USA, 1995, pp. 109-116.

[63] R. C. Jaeger, J. C. Suhling, and R. Ramani, "Errors Associated with the Design, Calibration and Application of Piezoresistive Stress Sensors in Silicon(100)," *Ieee Transactions on Components Packaging and Manufacturing Technology Part B-Advanced Packaging,* vol. 17, pp. 97-107, Feb 1994.

[64] C. H. Cho, R. C. Jaeger, and J. C. Suhling, "Characterization of the temperature dependence of the piezoresistive coefficients of silicon from-150 degrees C to+125 degrees C," *IEEE Sensors Journal,* vol. 8, pp. 1455-1468, Jul-Aug 2008.

[65] S. Hussain, R. C. Jaeger, J. C. Suhling, J. C. Roberts, M. A. Motalab, and C. H. Cho, "Error Analysis for Piezoresistive Stress Sensors Used in Flip Chip Packaging," in *2010 12th Ieee Intersociety Conference on Thermal and Thermomechanical Phenomena in Electronic Systems*, 2010, p. 12pp.

[66] J. C. Suhling, R. C. Jaeger, P. Lall, M. K. Rahim, J. C. Roberts, and S. Hussain, "Application of Stress Sensing Test Chips to Area Array Packaging," *Eurosime 2009: Thermal, Mechanical and Multi-Physics*

Simulation and Experiments in Micro-Electronics and Micro-Systems, pp. 13-24, 2009.

[67] B. J. Lwo, T. S. Chen, C. H. Kao, and Y. L. Lin, "In-plane packaging stress measurements through piezoresistive sensors," *Journal of Electronic Packaging,* vol. 124, pp. 115-121, Jun 2002.

[68] B. J. Lwo, C. H. Kao, T. S. Chen, and Y. S. Chen, "On the study of piezoresistive stress sensors for microelectronic packaging," *Journal of Electronic Packaging,* vol. 124, pp. 22-26, Mar 2002.

[69] B. J. Lwo and C. S. Lin, "Measurement of moisture-induced packaging stress with piezoresistive sensors," *Ieee Transactions on Advanced Packaging,* vol. 30, pp. 393-401, Aug 2007.

[70] B.-J. Lwo, J.-S. Su, and H. Chung, "In Situ Chip Stress Extractions for LFBGA Packages Through Piezoresistive Sensors," *Journal of Electronic Packaging,* vol. 131, pp. 031003-9, 09/00/ 2009.

[71] Z. Y. Wang, K. Tian, Y. Z. Zhou, L. Y. Pan, C. H. Hu, and L. T. Liu, "A high-temperature silicon-on-insulator stress sensor," *Journal of Micromechanics and Microengineering,* vol. 18, Apr 2008.

[72] K. Tian, Z. Y. Wang, M. Zhang, and L. T. Liu, "Design, Fabrication, and Calibration of a Piezoresistive Stress Sensor on SOI Wafers for Electronic Packaging Applications," *Ieee Transactions on Components and Packaging Technologies,* vol. 32, pp. 513-520, Jun 2009.

[73] P. J. Tzeng, J. H. Lau, M. J. Dai, S. T. Wu, H. C. Chien, Y. L. Chao*, et al.*, "Design, Fabrication, and Calibration of Stress Sensors Embedded in a TSV Interposer in a 300mm Wafer," *2012 Ieee 62nd Electronic Components and Technology Conference (Ectc),* pp. 1731-1737, 2012.

[74] Z. Xiaowu, R. Rajoo, C. S. Selvanayagam, A. Kumar, V. S. Rao, N. Khan, *et al.*, "Application of piezoresistive stress sensor in wafer bumping and drop impact test of embedded ultra thin device," in *Electronic Components and Technology Conference (ECTC), 2011 IEEE 61st*, 2011, pp. 1276-1282.

[75] J. Schwizer, M. Mayer, and O. Brand, *Force sensors for microelectronic packaging applications*. Berlin ; London: Springer, 2005.

[76] L. Seung Seoup, B. Jong Whan, K. Jin Soo, J. Hyung Jin, and Y. Sung, "Wafer Level Packaging by residual stress evaluation using piezoresistive stress sensors for the enhancement of reliability," in *Electronic*

Manufacturing Technology Symposium (IEMT), 2008 33rd IEEE/CPMT International, 2008, pp. 1-5.

[77] S. Jie, S. Jing, and T. Jieying, "A novel piezoresistive stress sensing method in flip chip technology," in *Electronic Packaging Technology & High Density Packaging (ICEPT-HDP), 2010 11th International Conference on*, 2010, pp. 675-678.

[78] Y. H. Luo and D. K. Nayak, "Enhancement of CMOS performance by process-induced stress," *Ieee Transactions on Semiconductor Manufacturing,* vol. 18, pp. 63-68, Feb 2005.

[79] S. E. Thompson, M. Armstrong, C. Auth, S. Cea, R. Chau, G. Glass*, et al.*, "A logic nanotechnology featuring strained-silicon," *Ieee Electron Device Letters,* vol. 25, pp. 191-193, Apr 2004.

[80] Y. Sun, S. E. Thompson, and T. Nishida, "Physics of strain effects in semiconductors and metal-oxide-semiconductor field-effect transistors," *Journal of Applied Physics,* vol. 101, pp. 104503-22, 05/15/ 2007.

[81] M. Baumann, P. Gieschke, B. Lemke, and O. Paul, "CMOS SENSOR CHIP WITH A 10x10 ARRAY OF UNIT CELLS FOR MAPPING FIVE STRESS COMPONENTS AND TEMPERATURE," *Mems 2010: 23rd Ieee International Conference on Micro Electro Mechanical Systems, Technical Digest,* pp. 604-607, 2010.

[82] A. T. Bradley, R. C. Jaeger, J. C. Suhling, and Y. Zou, "Die stress characterization using arrays of CMOS sensors," in *Solid-State Circuits Conference, 1998. ESSCIRC '98. Proceedings of the 24th European*, 1998, pp. 472-475.

[83] Y. Chen, R. C. Jaeger, and J. C. Suhling, "High Resolution Die Stress Mapping Using Arrays of CMOS Sensors," *ASME Conference Proceedings,* vol. 2007, pp. 285-295, 01/01/ 2007.

[84] R. C. Jaeger, R. Ramani, J. C. Suhling, and Y. Kang, "CMOS stress sensor circuits using piezoresistive field-effect transistors (PIFETs)," in *VLSI Circuits, 1995. Digest of Technical Papers., 1995 Symposium on*, 1995, pp. 43-44.

[85] R. C. Jaeger, J. C. Suhling, R. Ramani, A. T. Bradley, and J. P. Xu, "CMOS stress sensors on (100) silicon," *Ieee Journal of Solid-State Circuits,* vol. 35, pp. 85-95, Jan 2000.

[86] M. Baumann, B. Lemke, P. Ruther, and O. Paul, "Piezoresistive CMOS sensors for out-of-plane shear stress," in *Sensors, 2009 IEEE*, 2009, pp. 441-444.

[87] B. Lemke, R. Baskaran, and O. Paul, "Piezoresistive CMOS sensor for the localized measurement of five independent stress components," in *Micro Electro Mechanical Systems (MEMS), 2010 IEEE 23rd International Conference on*, 2010, pp. 596-599.

[88] B. Lemke, R. Baskaran, and O. Paul, "Piezoresistive CMOS sensor for out-of-plane normal stress," *Sensors and Actuators A: Physical,* vol. 176, pp. 10-18, 4// 2012.

[89] O. Paul, P. Gieschke, and B. Lemke, "CMOS-Integrated Stress Sensor Systems for Mechanical Sensing and Packaging Reliability Testing," *Microelectromechancial Systems - Materials and Devices Ii,* vol. 1139, pp. 201-209, 2009.

[90] A. Mian, J. C. Suhling, and R. C. Jaeger, "The van der Pauw stress sensor," *IEEE Sensors Journal,* vol. 6, pp. 340-356, Apr 2006.

[91] H. S. Choi, H. Konishi, H. F. Xu, and X. C. Li, "Embedding of micro thin film strain sensors in sapphire by diffusion bonding," *Journal of Micromechanics and Microengineering,* vol. 17, pp. 2248-2252, Nov 2007.

[92] X. Li and F. Prinz, "Embedded Fiber Bragg Grating Sensors in Polymer Structures Fabricated by Layered Manufacturing," *Journal of Manufacturing Processes,* vol. 5, pp. 78-86, 2003.

[93] X. C. Li, "Embedded Sensors in Layered Manufacturing," PhD, Mechanical Engineering, Stanford University, Stanford, 2001.

[94] L. Xiaochun, Z. Xugang, D. Werschmoeller, C. Hongseok, and C. Xudong, "Embedded micro/nano sensors for harsh engineering environments," Piscataway, NJ, USA, 2008, pp. 1273-6.

[95] H. Du and B. E. Klamecki, "Characterization of force sensors embedded in surfaces for manufacturing process monitoring," New Orleans, LA, USA, 1993, pp. 207-216.

[96] H. Du and B. E. Klamecki, "Force sensors embedded in surfaces for manufacturing and other tribological process monitoring," *Journal of Manufacturing Science and Engineering-Transactions of the Asme,* vol. 121, pp. 739-748, Nov 1999.

[97] C. A. Rogers, C. Liang, and J. Jia, "Behavior of Shape Memory Alloy Reinforced Composite Plates .1. Model Formulations and Control Concepts," *Aiaa/Asme/Asce/Ahs/Asc 30th Structures, Structural Dynamics and Materials Conference, Pts 1-4,* pp. 2011-2017, 1989.

[98] T. Ogisu, M. Nomura, N. Andou, J. Takaki, D.-Y. Song, and N. Takeda, "Development of damage suppression system using embedded SMA foil sensor and actuator," Newport Beach, CA, USA, 2000, pp. 62-73.

[99] T. Ogisu, M. Shimanuki, S. Kiyoshima, and N. Takeda, "A basic study of CFRP laminates with embedded prestrained SMA foils for aircraft structures," *Journal of Intelligent Material Systems and Structures,* vol. 16, pp. 175-185, Feb 2005.

[100] K. C. Kuang, WJ, "Use of conventional optical fibers and fiber Bragg gratings for damage detection in advanced composite structures: A review," *Applied Mechanics Reviews,* vol. 56, pp. 493-513, 2003.

[101] V. M. Murukeshan, P. Y. Chan, L. S. Ong, and A. Asundi, "Intracore fiber Bragg gratings for strain measurement in embedded composite structures," *Applied Optics,* vol. 40, pp. 145-149, 2001.

[102] J. S. Sirkis, C. C. Chang, and B. T. Smith, "Low-Velocity Impact of Optical-Fiber Embedded Laminated Graphite-Epoxy Panels .1. Macroscale," *Journal of Composite Materials,* vol. 28, pp. 1347-1370, 1994.

[103] C. A. Paget and K. Levin, "Structural integrity of composites with embedded piezoelectric ceramic transducer," *Proceedings of SPIE - The International Society for Optical Engineering,* vol. 3668, pp. 306-313, 1999.

[104] K. S. Kim, M. Breslauer, and G. S. Springer, "The Effect of Embedded Sensors on the Strength of Composite Laminates," *Journal of Reinforced Plastics and Composites,* vol. 11, pp. 949-958, Aug 1992.

[105] K. Shivakumar and A. Bhargava, "Failure mechanics of a composite laminate embedded with a fiber optic sensor," *Journal of Composite Materials,* vol. 39, pp. 777-798, 2005.

[106] C. Hautamaki, S. Zurn, S. C. Mantell, and D. L. Polla, "Experimental evaluation of MEMS strain sensors embedded in composites," *Microelectromechanical Systems, Journal of,* vol. 8, pp. 272-279, 1999.

[107] N. Mahayotsanun, S. Sah, J. Cao, M. Peshkin, R. X. Gao, and C. T. Wang, "Tooling-integrated sensing systems for stamping process monitoring,"

International Journal of Machine Tools & Manufacture, vol. 49, pp. 634-644, Jun 2009.

[108] L. Moore and J. Barrett, "Embedded Module for 3-D Mechanical Strain Measurement," *Components, Packaging and Manufacturing Technology, IEEE Transactions on,* vol. 2, pp. 1002-1011, 2012.

[109] S. Chaparala, F. Andros, W. Infantolino, and B. Sammakia, "A new technique for calibrating piezoresistive stress sensor chips," in *11th IEEE Intersociety Conference on Thermal and Thermomechanical Phenomena in Electronic Systems*, 2008, pp. 720-725.

[110] B. J. Lwo and S. Y. Wu, "Calibrate piezoresistive stress sensors through the assembled structure," *Journal of Electronic Packaging,* vol. 125, pp. 289-293, Jun 2003.

[111] W. H. Ko, D. J. Young, J. Guo, M. Suster, H. I. Kuo, and N. Chaimanonart, "A high-performance MEMS capacitive strain sensing system," *Sensors and Actuators a-Physical,* vol. 133, pp. 272-277, Feb 12 2007.

[112] J. Richter, M. B. Arnoldus, O. Hansen, and E. V. Thomsen, "Four point bending setup for characterization of semiconductor piezoresistance," *Review of Scientific Instruments,* vol. 79, Apr 2008.

[113] C. H. Cho, R. C. Jaeger, J. C. Suhling, Y. Kang, and A. Mian, "Characterization of the temperature dependence of the pressure coefficients of n- and p-type silicon using hydrostatic testing," *IEEE Sensors Journal,* vol. 8, pp. 392-400, Mar-Apr 2008.

[114] W. L. W. Hau, M. M. F. Yuen, G. Z. Yan, and P. C. H. Chan, "A new stress chip design for electronic packaging applications," in *Electronic Materials and Packaging, 2000. (EMAP 2000). International Symposium on*, 2000, pp. 457-463.

[115] H. H. Gharib and W. A. Moussa, "On the Feasibility of a New Approach for Developing a Piezoresistive 3D Stress Sensing Rosette," *IEEE Sensors Journal,* vol. 11, pp. 1861-1871, 2011.

[116] H. H. Gharib and W. A. Moussa, "A Single-Polarity Piezoresistive Three-Dimensional Stress-Sensing Rosette," *IEEE Journal of MEMS,* vol. 20, pp. 555-557, 2011.

[117] J. Suhling, R. Beaty, R. Jaeger, and R. Johnson, "Piezoresistive sensors for measurement of thermally-induced stresses in microelectronics," in *1991 SEM Spring Conference on Experimental Mechanics*, 1991, pp. 683-694.

[118] W. P. Mason and R. N. Thurston, "Use of Piezoresistive Materials in the Measurement of Displacement, Force, and Torque," *Journal of the Acoustical Society of America,* vol. 29, pp. 1096-1101, 1957.

[119] A. Boukabache, P. Pons, G. Blasquez, and Z. Dibi, "Characterisation and modelling of the mismatch of TCRs and their effects on the drift of the offset voltage of piezoresistive pressure sensors," *Sensors and Actuators a-Physical,* vol. 84, pp. 292-296, Sep 1 2000.

[120] M. Olszacki, C. Maj, M. Al Bahri, J. C. Marrot, A. Boukabache, P. Pons*, et al.*, "Experimental verification of temperature coefficients of resistance for uniformly doped P-type resistors in SOI," *Journal of Micromechanics and Microengineering,* vol. 20, pp. -, Jun 2010.

[121] D. Tanaskovic, Z. Djuric, and Z. Lazic, "Influence of impurity distribution on thermal coefficients of resistivity and piezoresistivity of diffused layers in silicon," in *Microelectronics, 1995. Proceedings., 1995 20th International Conference on*, 1995, pp. 573-576 vol.2.

[122] H. H. Gharib and W. A. Moussa, "Microfabrication and calibration of a single-polarity piezoresistive three-dimensional stress sensing chip," *Journal of Micromechanics and Microengineering,* vol. 23, p. 035019, 2013.

[123] R. C. Jaeger, *Introduction to microelectronic fabrication*, 2nd ed. Upper Saddle River, N.J.: Prentice Hall, 2002.

[124] S. A. Campbell, *The science and engineering of microelectronic fabrication*, 2nd ed. New York: Oxford University Press, 2001.

[125] R. S. Muller, T. I. Kamins, and M. Chan, *Device electronics for integrated circuits*, 3rd ed. New York, N.Y.: John Wiley & Sons, 2003.

[126] R. S. Popovic, "Metal-N-Type Semiconductor Ohmic Contact with a Shallow N+ Surface-Layer," *Solid-State Electronics,* vol. 21, pp. 1133-1138, 1978.

[127] R. B. Fair and J. C. C. Tsai, "A Quantitative Model for the Diffusion of Phosphorus in Silicon and the Emitter Dip Effect," *Journal of The Electrochemical Society,* vol. 124, pp. 1107-1118, // 1977.

[128] H. Ryssel and I. Ruge, *Ion implantation*. Chichester [West Sussex] ; New York: Wiley, 1986.

[129] G. S. May and S. M. Sze, *Fundamentals of semiconductor fabrication*. New York: John Wiley & Sons, 2004.

[130] J. R. Mallon, A. J. Rastegar, A. A. Barlian, M. T. Meyer, T. H. Fung, and B. L. Pruitt, "Low 1/f noise, full bridge, microcantilever with longitudinal and transverse piezoresistors," *Applied Physics Letters,* vol. 92, Jan 21 2008.

[131] F. Bordoni and A. Damico, "Noise in Sensors," *Sensors and Actuators a-Physical,* vol. 21, pp. 17-24, Feb 1990.

[132] R. Dieme, "Characterization of Noise in MEMS Piezoresistive Microphones," MSc, University of Florida, 2005.

[133] R. E. Beaty, R. C. Jaeger, J. C. Suhling, R. W. Johnson, and R. D. Butler, "Evaluation of Piezoresistive Coefficient Variation in Silicon Stress Sensors Using a 4-Point Bending Test Fixture," *Ieee Transactions on Components Hybrids and Manufacturing Technology,* vol. 15, pp. 904-914, Oct 1992.

[134] R. E. Beaty, J. C. Suhling, C. A. Moody, D. A. Bittle, R. W. Johnson, R. D. Butler, *et al.*, "Calibration Considerations for Piezoresistive-Based Stress Sensors," *40th Electronic Components and Technology Conference, Vols 1 and 2,* pp. 797-806, 1990.

[135] W. X. Song and E. Ristolainen, "Calibration improvement for piezoresistive coefficients of stress sensors on (100) silicon," *Physica Scripta,* vol. T114, pp. 205-208, 2004.

[136] C. H. Cho, R. C. Jaeger, and J. C. Suhling, "The Effect of the Transverse Sensitivity on Measurement of the Piezoresistive Coefficients of Silicon," *Japanese Journal of Applied Physics,* vol. 47, pp. 3647-3656, May 2008.

[137] S. Chaparala, F. Andros, W. Infantolino, and B. Sammakia, "A new technique for calibrating piezoresistive stress sensor chips," *2008 11th Ieee Intersociety Conference on Thermal and Thermomechanical Phenomena in Electronic Systems, Vols 1-3,* pp. 720-725, 2008.

[138] H. H. Gharib and W. A. Moussa, "Testing of a Single-Polarity Piezoresistive Three-Dimensional Piezoresistive Sensing Chip," *Journal of Micromechanics and Microengineering,* vol. In review, 2013.

[139] R. D. Adams and W. C. Wake, *Structural Adhesive Joints in Engineering*: Elsevier applied science publishers, 1984.

[140] J. T. Lin, D. Jackson, J. Aebersold, K. M. Walsh, J. Naber, and W. Hnat, "A High Gauge Factor Capacitive Strain Sensor and its Telemetry Application in Biomechanics," in *University/Government/Industry Micro/Nano Symposium, 2008. UGIM 2008. 17th Biennial*, 2008, pp. 98-101.

[141] B. Lee, "Review of the present status of optical fiber sensors," *Optical Fiber Technology,* vol. 9, pp. 57-79, Apr 2003.

[142] *DELO Industrial Adhesives*. Available: http://www.delo-adhesives.com

[143] D. B. Barker and A. Dasgupta, "Thermal Stress Issues in Plated-Through-hole Reliability," in *Thermal stress and strain in microelectronics packaging*, J. H. Lau, Ed., ed New York: Van Nostrand Reinhold, 1993, pp. xxii, 883 p.

[144] C. H. Cho, "Experimental Characterization of the Temperature Dependence of the Piezoresistive Coefficients of Silicon," PhD, Graduate Faculty of Auburn University, Auburn University, Auburn, Alabama, 2007.

[145] X. Bin, S. Xun Qing, and D. Han, "Understanding of Delamination Mechanism of Anisotropic Conductive Film (ACF) Bonding in Thin Liquid Crystal Display (LCD) Module," *Components and Packaging Technologies, IEEE Transactions on,* vol. 30, pp. 509-516, 2007.

[146] A. S. Kobayashi, *Handbook on experimental mechanics*, 2nd rev. ed. New York, N.Y. Bethel, CT, USA: VCH; SEM, 1993.

[147] L. Onsager, "Reciprocal Relations in Irreversible Processes. I," *Physical Review,* vol. 37, pp. 405-426, 02/15/ 1931.

[148] L. Onsager, "Reciprocal Relations in Irreversible Processes. II," *Physical Review,* vol. 38, pp. 2265-2279, 12/15/ 1931.

APPENDIX A: DERIVATION OF THE GENERAL CHANGE IN RESISTANCE RELATIONS OF A FILAMENTARY CONDUCTOR

The following mathematical account is based on the works of Suhling *et al*. [117] to derive the general theory of conduction in a piezoresistive material subjected to stress and temperature change. The presented derivations are valid for cubic symmetry crystals with diamond lattice structure such as silicon. The current density vector is related to the electric field vector as follows:

$$\vec{J} = \vec{J}(\vec{E}) \tag{A-1}$$

Or

$$J_i = J_i(E_1, E_2, E_3) \tag{A-2}$$

Where, J_i and E_i are the Cartesian components of the current density and electric field vectors, respectively. In most solid conductors, this relationship has been noticed to be linear over a wide range of electric field magnitudes, thus known as Ohmic materials. In an anisotropic Ohmic conductor:

$$J_i = k_{ij} E_j \tag{A-3}$$

Or

$$E_i = \rho_{ij} J_j \tag{A-4}$$

Where, k_{ij} and ρ_{ij} are the components of the conductivity and resistivity tensors, respectively. Based on the reciprocity theorem by Onsager [147, 148], the conductivity and resistivity tensors are symmetric and can be written as:

$$k_{ij} = k_{ji} \text{ and } \rho_{ij} = \rho_{ji} \tag{A-5}$$

A.1 Formulation at Fixed Temperature

The piezoresistive effect is a stress-induced change in the components of the resistivity tensor, which is realized in piezoresistive materials. The piezoresistive effect can be modeled mathematically using the following series expansion at a fixed reference temperature:

$$\rho_{ij} = \rho_{ij}^{0} + \Pi_{ijkl}\sigma_{kl} + \Lambda_{ijklmn}\sigma_{kl}\sigma_{mn} + \ldots \tag{A-6}$$

Where, ρ_{ij}^{0} = resistivity components for the stress free material

Π_{ijkl} , Λ_{ijklmn} = components of the fourth, sixth, and higher order tensors which characterize the stress-induced resistivity change

The higher order piezoresistivity tensors constitute small fractional effects in mono-crystalline silicon. Then, for small stress levels, the above relation is simplified as:

$$\rho_{ij} = \rho_{ij}^{0} + \Pi_{ijkl}\sigma_{kl} \tag{A-7}$$

And the change in resistivity is given by:

$$\Delta\rho_{ij} = \Pi_{ijkl}\sigma_{kl} \tag{A-8}$$

A.2 Formulation at Variable Temperature

The effect of temperature on piezoresistivity is demonstrated by: (1) the thermally-induced change in the unstressed resistivity components (TCR) and (2) the thermally-induced change in the coefficients which characterize the piezoresistive effect. Using Taylor series to include the effect of temperature in

electric field/current density relationship in equation (A-4), the electric field is related to 3 current density components, nine stress components, and temperature:

$$E_i = E_i\left(J_j, \sigma_{kl}, T\right) \tag{A-9}$$

Where T is the change in temperature from a reference temperature and given by:

$$T = \Delta\theta = \theta - \theta_{ref} \tag{A-10}$$

Taylor series is used to expand the electric field equation taking into consideration the following:

- The material must possess an Ohmic behavior. Therefore, only the terms which have a linear dependence on the current density components are considered.
- The piezoresistive effect possesses a linear relationship with the applied stress at all temperatures. Therefore, all higher order tems in the stress components are neglected.
- For crystalline silicon, which is a cubic crystal with diamond structure, the components of all odd order material property tensors must be identically zero.

Therefore, the electric field vector is given by:

$$\begin{aligned} E_i = \frac{\partial E_i}{\partial J_j} J_j &+ \left[\frac{\partial^2 E_i}{\partial J_j \partial \sigma_{kl}} J_j \sigma_{kl} + \frac{\partial^2 E_i}{\partial J_j \partial T} J_j T \right] \\ &+ \left[\frac{1}{2} \frac{\partial^3 E_i}{\partial J_j \partial T^2} J_j T^2 + \frac{\partial^3 E_i}{\partial J_j \partial \sigma_{kl} \partial T} J_j \sigma_{kl} T \right] + \ldots \end{aligned} \tag{A-11}$$

By introducing specific notations for each material property tensor, equation (A-11) is reduced to:

$$E_i = \left[\rho_{ij}^0 + \left(\alpha_{ij}^{(1)} T + \alpha_{ij}^{(2)} T^2 + \ldots \right) + \Pi_{ijkl} \sigma_{kl} + \left(\beta_{ijkl}^{(1)} T + \beta_{ijkl}^{(2)} T^2 + \ldots \right) \sigma_{kl} \right] J_j \tag{A-12}$$

The term $\left[\rho_{ij}^{0}+\left(\alpha_{ij}^{(1)}T+\alpha_{ij}^{(2)}T^{2}+\ldots\right)\right]J_{j}$ is the *unstressed* portion of the electric field vector, while the term $\left[\Pi_{ijkl}\sigma_{kl}+\left(\beta_{ijkl}^{(1)}T+\beta_{ijkl}^{(2)}T^{2}+\ldots\right)\sigma_{kl}\right]J_{j}$ is the *stressed* portion. The notations given in equation (A-12) are designated as:

The unstressed resistivity tensor at reference temperature:

$$\rho_{ij}^{0}=\frac{\partial E_{i}}{\partial J_{j}}, \tag{A-13}$$

The temperature coefficient or resistance (TCR):

$$\alpha_{ij}^{(N)}=\frac{1}{N!}\frac{\partial^{N+1}E_{i}}{\partial J_{j}\partial T^{N}}, \tag{A-14}$$

The 4th order piezoresistivity tensor:

$$\Pi_{ijkl}=\frac{\partial^{2}E_{i}}{\partial J_{j}\partial\sigma_{kl}}, \tag{A-15}$$

The 4th order tensor which characterize the dependence of the piezoresistive effect on temperature:

$$\beta_{ijkl}^{(N)}=\frac{1}{N!}\frac{\partial^{N+2}E_{i}}{\partial J_{j}\partial\sigma_{kl}\partial T^{N}}, \tag{A-16}$$

Where, N = 1, 2, 3, …

Combining equation (A-12) with equation (A-4), the resistivity components are related to the stress and temperature by:

$$\rho_{ij}=\left[\rho_{ij}^{0}+\left(\alpha_{ij}^{(1)}T+\alpha_{ij}^{(2)}T^{2}+\ldots\right)\right]+\left[\Pi_{ijkl}\sigma_{kl}+\left(\beta_{ijkl}^{(1)}T+\beta_{ijkl}^{(2)}T^{2}+\ldots\right)\sigma_{kl}\right] \tag{A-17}$$

Based on the reciprocity theorem indicated in the conductivity and resistivity tensors in equation (A-5) and due to the stress tensor symmetry, the following applies:

$$\alpha_{ij}^{(N)} = \alpha_{ji}^{(N)}, \text{ for N=1,2,3,...} \tag{A-18}$$

$$\Pi_{ijkl} = \Pi_{jikl} \text{ and } \beta_{ijkl}^{(N)} = \beta_{jikl}^{(N)}, \text{ for N=1,2,3,...} \tag{A-19}$$

$$\Pi_{ijkl} = \Pi_{ijlk} \text{ and } \beta_{ijkl}^{(N)} = \beta_{ijlk}^{(N)}, \text{ for N=1,2,3,...} \tag{A-20}$$

Silicon is a cubic crystal that belongs to the crystal class 32 or m3m (O_h). This class of crystals has its components of the odd order material property tensors identically zero. The second order symmetric material property tensors have only one unique component in this class, which have the following form for arbitrary components:

$$A_{ij} = \begin{bmatrix} A & 0 & 0 \\ 0 & A & 0 \\ 0 & 0 & A \end{bmatrix} \tag{A-21}$$

Therefore, the resistivity (ρ_{ij}) and TCR (α_{ij}) components behave similarly to the A_{ij} in equation (A-21). On the other hand, the fourth order material property tensor for cubic crystals with diamond structure with symmetry in the first two and last two indices possesses only three unique coefficients. The simplified form of this tensor is given by:

$$\begin{bmatrix} B_{1111} & B_{1122} & B_{1133} & 2B_{1113} & 2B_{1123} & 2B_{1112} \\ B_{2211} & B_{2222} & B_{2233} & 2B_{2213} & 2B_{2223} & 2B_{2212} \\ B_{3311} & B_{3322} & B_{3333} & 2B_{3313} & 2B_{3323} & 2B_{3312} \\ B_{1311} & B_{1322} & B_{1333} & 2B_{1313} & 2B_{1323} & 2B_{1312} \\ B_{2311} & B_{2322} & B_{2333} & 2B_{2313} & 2B_{2323} & 2B_{2312} \\ B_{1211} & B_{1222} & B_{1233} & 2B_{1213} & 2B_{1223} & 2B_{1212} \end{bmatrix} = \begin{bmatrix} B_{11} & B_{12} & B_{12} & 0 & 0 & 0 \\ B_{12} & B_{11} & B_{12} & 0 & 0 & 0 \\ B_{12} & B_{12} & B_{11} & 0 & 0 & 0 \\ 0 & 0 & 0 & B_{44} & 0 & 0 \\ 0 & 0 & 0 & 0 & B_{44} & 0 \\ 0 & 0 & 0 & 0 & 0 & B_{44} \end{bmatrix}$$

(A-22)

Where, B_{11}, B_{12}, and B_{44} are the coefficients of the fourth order tensor. Then, Π_{ijkl} and $\beta_{ijkl}^{(N)}$ behave similar to B_{ijkl} in equation (A-22).

Taking into account the tensors' components symmetry given in equations (A-18), (A-19), and (A-20) and the unique components for the second and fourth order tensors in equations (A-21) and (A-22), respectively, equation (A-17) is re-formulated to represent the most general formulas for conduction relations in silicon as:

$$\begin{aligned} \frac{E_1}{\rho} = &\Big[\left(1+\alpha_1 T+\alpha_2 T^2+\ldots\right)+\left(\Pi_{11}+\beta_{11}^{(1)}T+\beta_{11}^{(2)}T^2+\ldots\right)\sigma_{11} \\ &\quad +\left(\Pi_{12}+\beta_{12}^{(1)}T+\beta_{12}^{(2)}T^2+\ldots\right)\left(\sigma_{22}+\sigma_{33}\right)\Big]J_1 \\ &+\Big[\left(\Pi_{44}+\beta_{44}^{(1)}T+\beta_{44}^{(2)}T^2+\ldots\right)\sigma_{12}\Big]J_2 \\ &+\Big[\left(\Pi_{44}+\beta_{44}^{(1)}T+\beta_{44}^{(2)}T^2+\ldots\right)\sigma_{13}\Big]J_3 \end{aligned}$$

$$\begin{aligned} \frac{E_2}{\rho} = &\Big[\left(1+\alpha_1 T+\alpha_2 T^2+\ldots\right)+\left(\Pi_{11}+\beta_{11}^{(1)}T+\beta_{11}^{(2)}T^2+\ldots\right)\sigma_{22} \\ &\quad +\left(\Pi_{12}+\beta_{12}^{(1)}T+\beta_{12}^{(2)}T^2+\ldots\right)\left(\sigma_{11}+\sigma_{33}\right)\Big]J_2 \\ &+\Big[\left(\Pi_{44}+\beta_{44}^{(1)}T+\beta_{44}^{(2)}T^2+\ldots\right)\sigma_{12}\Big]J_1 \\ &+\Big[\left(\Pi_{44}+\beta_{44}^{(1)}T+\beta_{44}^{(2)}T^2+\ldots\right)\sigma_{23}\Big]J_3 \end{aligned}$$

(A-23)

$$\frac{E_3}{\rho} = \Big[\left(1+\alpha_1 T+\alpha_2 T^2+\ldots\right)+\left(\Pi_{11}+\beta_{11}^{(1)}T+\beta_{11}^{(2)}T^2+\ldots\right)\sigma_{33}$$
$$+\left(\Pi_{12}+\beta_{12}^{(1)}T+\beta_{12}^{(2)}T^2+\ldots\right)\left(\sigma_{11}+\sigma_{22}\right)\Big]J_3$$
$$+\Big[\left(\Pi_{44}+\beta_{44}^{(1)}T+\beta_{44}^{(2)}T^2+\ldots\right)\sigma_{13}\Big]J_1$$
$$+\Big[\left(\Pi_{44}+\beta_{44}^{(1)}T+\beta_{44}^{(2)}T^2+\ldots\right)\sigma_{23}\Big]J_2$$

A.3 Resistance Change Equations for One-Dimensional (1D) Filament along Crystallographic Directions

The 1D filamentary conductor shown in Figure 3-1 has a general orientation with respect to the principal crystallographic directions; $X_1 = [100]$, $X_2 = [010]$, and $X_3 = [001]$. The orientation is defined by the unit vector:

$$\vec{n} = l\vec{e}_1 + m\vec{e}_2 + n\vec{e}_3 \qquad \text{(A-24)}$$

Where, *l*, *m*, and *n* are the direction cosines of the orientation of the conductor with respect to the crystallographic directions. For a flowing current in the conductor, the net flow is along the length of the conductor, such that:

$$\vec{J} = J\vec{n} \qquad \text{(A-25)}$$

Or in indicial form, where *J* is the magnitude of the current density,

$$J_1 = lJ\,,\ J_2 = mJ\,,\ \text{and}\ J_3 = nJ \qquad \text{(A-26)}$$

The current (*I*) flowing in a conductor is given by:

$$I = JA \qquad \text{(A-27)}$$

Where, A is the cross-sectional area of the unstressed conductor. The potential drop (*V*) along the conductor is given by:

$$V = \left(E_1 l + E_2 m + E_3 n\right)L \qquad \text{(A-28)}$$

Where, L is the length of the unstressed conductor. Then, the general relationship between the resistance change and the stress and temperature is found by substituting equations (A-23), (A-26), and (A-27) into equation (A-28) and using the relationship for the resistance, $R = V/I$:

$$\begin{aligned} R^{\sigma,T} = \frac{\rho L}{A}\Big[1 &+ \left(\alpha_1 T + \alpha_2 T^2 + \ldots\right) \\ &+ \Big[\left(\Pi_{11} + \beta_{11}^{(1)} T + \beta_{11}^{(2)} T^2 + \ldots\right)\sigma_{11} \\ &\quad + \left(\Pi_{12} + \beta_{12}^{(1)} T + \beta_{12}^{(2)} T^2 + \ldots\right)\left(\sigma_{22} + \sigma_{33}\right)\Big] l^2 \\ &+ \Big[\left(\Pi_{11} + \beta_{11}^{(1)} T + \beta_{11}^{(2)} T^2 + \ldots\right)\sigma_{22} \\ &\quad + \left(\Pi_{12} + \beta_{12}^{(1)} T + \beta_{12}^{(2)} T^2 + \ldots\right)\left(\sigma_{11} + \sigma_{33}\right)\Big] m^2 \\ &+ \Big[\left(\Pi_{11} + \beta_{11}^{(1)} T + \beta_{11}^{(2)} T^2 + \ldots\right)\sigma_{33} \\ &\quad + \left(\Pi_{12} + \beta_{12}^{(1)} T + \beta_{12}^{(2)} T^2 + \ldots\right)\left(\sigma_{11} + \sigma_{22}\right)\Big] n^2 \\ &+ 2\left(\Pi_{44} + \beta_{44}^{(1)} T + \beta_{44}^{(2)} T^2 + \ldots\right)\left(\sigma_{12} lm + \sigma_{13} ln + \sigma_{23} mn\right)\Big] \end{aligned} \tag{A-29}$$

A filamentary conductor at zero stress and temperature is written from equation (A-29) as:

$$R = \frac{\rho L}{A} \tag{A-30}$$

The piezoresistivity tensor (Π_{ij}) and the dependence of the piezoresistive effect on temperature tensor ($\beta_{ij}^{(N)}$) are combined into one piezoresistivity tensor that includes the effect of temperature, which is given by:

$$\pi_{ij} = \Pi_{ij} + \beta_{ij}^{(1)} T + \beta_{ij}^{(2)} T^2 + \ldots \tag{A-31}$$

Therefore, the general equation for the change in resistance due to the applied stress and temperature is given by:

$$\begin{aligned}\frac{\Delta R}{R} &= \left(\alpha_1 T + \alpha_2 T^2 + \ldots\right)\\ &\quad + \left[\pi_{11}\sigma_{11} + \pi_{12}\left(\sigma_{22} + \sigma_{33}\right)\right] l^2 + \left[\pi_{11}\sigma_{22} + \pi_{12}\left(\sigma_{11} + \sigma_{33}\right)\right] m^2\\ &\quad + \left[\pi_{11}\sigma_{33} + \pi_{12}\left(\sigma_{11} + \sigma_{22}\right)\right] n^2 + 2\pi_{44}\left[\sigma_{12} lm + \sigma_{13} ln + \sigma_{23} mn\right]\\ &= \frac{R^{\sigma,T} - R^{0,0}}{R^{0,0}}\end{aligned} \tag{A-32}$$

A.4 Resistance Change Equations for One-Dimensional (1D) Filament along Off-axis Coordinate System

For an off-axis coordinate system, the orientation is defined by the unit vector:

$$\vec{n}' = l'\vec{e}_1' + m'\vec{e}_2' + n'\vec{e}_3' \tag{A-33}$$

Where, *l'*, *m'*, and *n'* are the direction cosines of the conductor with respect to the x_1' , x_2', and x_3' axes. Since, equation (A-23) is form invariant and valid in all coordinate systems, then:

$$\begin{aligned}\frac{E_1'}{\rho} &= \left[\pi_{11}'\sigma_{11}' + \pi_{12}'\left(\sigma_{22}' + \sigma_{33}'\right) + \left(1 + \alpha_1 T + \alpha_2 T^2 + \ldots\right)\right] J_1\\ &\quad + \pi_{44}'\sigma_{12}' J_2 + \pi_{44}'\sigma_{13}' J_3\end{aligned}$$

$$\begin{aligned}\frac{E_2'}{\rho} &= \left[\pi_{11}'\sigma_{22}' + \pi_{12}'\left(\sigma_{11}' + \sigma_{33}'\right) + \left(1 + \alpha_1 T + \alpha_2 T^2 + \ldots\right)\right] J_2\\ &\quad + \pi_{44}'\sigma_{12}' J_1 + \pi_{44}'\sigma_{23}' J_3\end{aligned}$$

$$\begin{aligned}\frac{E_3'}{\rho} &= \left[\pi_{11}'\sigma_{33}' + \pi_{12}'\left(\sigma_{11}' + \sigma_{22}'\right) + \left(1 + \alpha_1 T + \alpha_2 T^2 + \ldots\right)\right] J_3\\ &\quad + \pi_{44}'\sigma_{13}' J_1 + \pi_{44}'\sigma_{23}' J_2\end{aligned} \tag{A-34}$$

Writing the current density components in the x' -directions:

$J_1 = l'J$, $J_2 = m'J$, and $J_3 = n'J$ (A-35)

Substituting for the current density in terms of the current flow (I) and cross-sectional area of the conductor (A), the general conduction relations for the conductor along the off-axis directions are formulated as:

$$\frac{E_1'A}{\rho I} = \left[\pi_{11}'\sigma_{11}' + \pi_{12}'\left(\sigma_{22}' + \sigma_{33}'\right) + \left(1 + \alpha_1 T + \alpha_2 T^2 + \ldots\right)\right]l' + \pi_{44}'\sigma_{12}'m' + \pi_{44}'\sigma_{13}'n'$$

$$\frac{E'A_2}{\rho I} = \left[\pi_{11}'\sigma_{22}' + \pi_{12}'\left(\sigma_{11}' + \sigma_{33}'\right) + \left(1 + \alpha_1 T + \alpha_2 T^2 + \ldots\right)\right]m' + \pi_{44}'\sigma_{12}'l' + \pi_{44}'\sigma_{23}'n'$$

$$\frac{E_3'A}{\rho I} = \left[\pi_{11}'\sigma_{33}' + \pi_{12}'\left(\sigma_{11}' + \sigma_{22}'\right) + \left(1 + \alpha_1 T + \alpha_2 T^2 + \ldots\right)\right]n' + \pi_{44}'\sigma_{13}'l' + \pi_{44}'\sigma_{23}'m' \quad \text{(A-36)}$$

The above equation is formulated in terms of the change in resistance for a general off-axis conductor:

$$\begin{aligned}\frac{\Delta R}{R} &= \frac{R(\sigma,T) - R(0,0)}{R(0,0)} \\ &= \left[\pi_{11}'\sigma_{11}' + \pi_{12}'\left(\sigma_{22}' + \sigma_{33}'\right)\right]l'^2 + \left[\pi_{11}'\sigma_{22}' + \pi_{12}'\left(\sigma_{11}' + \sigma_{33}'\right)\right]m'^2 \\ &\quad + \left[\pi_{11}'\sigma_{33}' + \pi_{12}'\left(\sigma_{11}' + \sigma_{22}'\right)\right]n'^2 \\ &\quad + 2\pi_{44}'\left(\sigma_{12}'l'm' + \sigma_{13}'l'n' + \sigma_{23}'m'n'\right) \\ &\quad + [\alpha_1 T + \alpha_2 T^2 + \ldots]\end{aligned} \quad \text{(A-37)}$$

Combining terms with common direction cosine components and writing the stress components in reduced index notations, the following final equation is realized, which is stated in Chapter 3 as equation (3-1) :

$$
\begin{aligned}
\frac{\Delta R}{R} &= \frac{R(\sigma,T)-R(0,0)}{R(0,0)} \\
&= \left(\pi'_{1\beta}\sigma'_{\beta}\right)l'^{2} + \left(\pi'_{2\beta}\sigma'_{\beta}\right)m'^{2} + \left(\pi'_{3\beta}\sigma'_{\beta}\right)n'^{2} \\
&\quad + 2\left(\pi'_{4\beta}\sigma'_{\beta}\right)l'n' + 2\left(\pi'_{5\beta}\sigma'_{\beta}\right)m'n' + 2\left(\pi'_{6\beta}\sigma'_{\beta}\right)l'm' \\
&\quad + [\alpha_1 T + \alpha_2 T^2 + ...]
\end{aligned}
\qquad \text{(A-38)}
$$

Where,

$R(\sigma, T)$ = resistor value with applied stress and temperature change

$R(0, 0)$ = reference resistor value without applied stress and temperature change

$\pi'_{\gamma\beta}$ = off-axis temperature dependent piezoresistive coefficients with γ, β = 1,2,…6

σ'_{β} = stress in the primed coordinate system, β = 1,2,..,6

α_1, α_2, … = first and higher order temperature coefficients of resistance (*TCR*)

$T=T_c-T_{ref}$ = difference between the current measurement temperature (T_c) and reference temperature (T_{ref})

l', m', n' = direction cosines of the filament orientation with respect to the x'_1, x'_2, and x'_3 axes

APPENDIX B: FORMULATION OF THE RESISTANCE-STRAIN EQUATIONS ON THE (111) SILICON PLANE

To reformulate the resistance change equation (3-1) in terms of strain, the elastic stress-strain relation is used:

Unprimed C.S.: $\sigma_{ij} = C_{ijkl}\varepsilon_{kl}$

Primed C.S.: $\sigma'_{ij} = C'_{ijkl}\varepsilon'_{kl}$ (B-1)

Where the following are based on the primed coordinate system,

ε'_{kl} = Strain components

C'_{ijkl} = Stiffness constants

Since, the stress and strain tensors are symmetric, the 4th order tensor C_{ijkl} is symmetric and can be written as a 2nd order tensor $C_{\alpha\beta}$ using the reduced summation convention. Then, due to the cubic symmetry of crystalline silicon, the elasticity tensor of silicon in the unprimed coordinate system is given by:

$$C_{\alpha\beta} = \begin{bmatrix} C_{11} & C_{12} & C_{12} & 0 & 0 & 0 \\ C_{12} & C_{11} & C_{12} & 0 & 0 & 0 \\ C_{12} & C_{12} & C_{11} & 0 & 0 & 0 \\ 0 & 0 & 0 & C_{44} & 0 & 0 \\ 0 & 0 & 0 & 0 & C_{44} & 0 \\ 0 & 0 & 0 & 0 & 0 & C_{44} \end{bmatrix} \quad \text{(B-2)}$$

The transformed elasticity tensor along the primed coordinate system is given by:

$$C'_{\alpha\beta} = T_{\alpha\gamma} C_{\gamma\delta} T^{-1}_{\delta\beta} \quad \text{(B-3)}$$

Where, the transformation matrix is presented in equation (3-8) with the direction cosines along the (111) plane given by equation (3-10) in Chapter 3. The

resistance change equation (3-11) can be re-formulated in terms of strains by using the stress-strain relation (B-1). The substituted elasticity matrix for silicon is given by (in GPa):

$$C_{\alpha\beta} = \begin{bmatrix} C_{11} & C_{12} & C_{12} & 0 & 0 & 0 \\ C_{12} & C_{11} & C_{12} & 0 & 0 & 0 \\ C_{12} & C_{12} & C_{11} & 0 & 0 & 0 \\ 0 & 0 & 0 & C_{44} & 0 & 0 \\ 0 & 0 & 0 & 0 & C_{44} & 0 \\ 0 & 0 & 0 & 0 & 0 & C_{44} \end{bmatrix}$$
$$= \begin{bmatrix} 165.6 & 63.9 & 63.9 & 0 & 0 & 0 \\ 63.9 & 165.6 & 63.9 & 0 & 0 & 0 \\ 63.9 & 63.9 & 165.6 & 0 & 0 & 0 \\ 0 & 0 & 0 & 79.5 & 0 & 0 \\ 0 & 0 & 0 & 0 & 79.5 & 0 \\ 0 & 0 & 0 & 0 & 0 & 79.5 \end{bmatrix} \tag{B-4}$$

Then, transforming the elasticity matrix along the (111) silicon plane using equation (B-3) gives (in GPa):

$$C'_{\alpha\beta} = \begin{bmatrix} C'_{11} & C'_{12} & C'_{13} & C'_{14} & 0 & 0 \\ C'_{12} & C'_{11} & C'_{13} & -C'_{14} & 0 & 0 \\ C'_{13} & C'_{13} & C'_{33} & 0 & 0 & 0 \\ C'_{14} & -C'_{14} & 0 & C'_{44} & 0 & 0 \\ 0 & 0 & 0 & 0 & C'_{44} & C'_{14} \\ 0 & 0 & 0 & 0 & C'_{14} & C'_{66} \end{bmatrix}$$
$$= \begin{bmatrix} 194.3 & 54.4 & 44.8 & 13.5 & 0 & 0 \\ 54.4 & 194.3 & 44.8 & -13.5 & 0 & 0 \\ 44.8 & 44.8 & 203.9 & 0 & 0 & 0 \\ 13.5 & -13.5 & 0 & 60.4 & 0 & 0 \\ 0 & 0 & 0 & 0 & 60.4 & 13.5 \\ 0 & 0 & 0 & 0 & 13.5 & 70 \end{bmatrix} \tag{B-5}$$

Substituting the stress-strain relation (B-1) into equation (3-11) yields:

$$
\begin{aligned}
\frac{\Delta R}{R} = & \Big[(B_1\cos^2\phi + B_2\sin^2\phi)C'_{11} + (B_2\cos^2\phi + B_1\sin^2\phi)C'_{12} + B_3C'_{13} \\
& + 2\sqrt{2}(B_2 - B_3)(\cos^2\phi - \sin^2\phi)C'_{14}\Big]\varepsilon'_{11} \\
& + \Big[(B_1\cos^2\phi + B_2\sin^2\phi)C'_{12} + (B_2\cos^2\phi + B_1\sin^2\phi)C'_{11} + B_3C'_{13} \\
& - 2\sqrt{2}(B_2 - B_3)(\cos^2\phi - \sin^2\phi)C'_{14}\Big]\varepsilon'_{22} \\
& + \Big[\left(B_1 + B_2\right)\left(\cos^2\phi + \sin^2\phi\right)C'_{13} + B_3C'_{33}\Big]\varepsilon'_{33} \\
& + \Big[\left(B_1 - B_2\right)\left(\cos^2\phi - \sin^2\phi\right)C'_{14} + 2\sqrt{2}(B_2 - B_3)(\cos^2\phi - \sin^2\phi)C'_{44}\Big]\varepsilon'_{23} \\
& + \Big[2\sqrt{2}(B_2 - B_3)\sin\left(2\phi\right)C'_{44} + (B_1 - B_2)\sin\left(2\phi\right)C'_{14}\Big]\varepsilon'_{13} \\
& + \Big[2\sqrt{2}(B_2 - B_3)\sin\left(2\phi\right)C'_{14} + (B_1 - B_2)\sin\left(2\phi\right)C'_{66}\Big]\varepsilon'_{12} \\
& + \alpha T
\end{aligned}
\tag{B-6}
$$

Substituting the stiffness constants along the primed coordinate system, equation (B-4) is written in terms of strain components:

$$
\begin{aligned}
\frac{\Delta R}{R} = & \Big[(194.3\cos^2\phi + 54.4\sin^2\phi)B_1 + (54.4\cos^2\phi + 194.3\sin^2\phi)B_2 + 44.8B_3 \\
& + 27\sqrt{2}(B_2 - B_3)(\cos^2\phi - \sin^2\phi)\Big]\varepsilon'_{11} \\
& + \Big[(54.4\cos^2\phi + 194.3\sin^2\phi)B_1 + (194.3\cos^2\phi + 54.4\sin^2\phi)B_2 + 44.8B_3 \\
& - 27\sqrt{2}(B_2 - B_3)(\cos^2\phi - \sin^2\phi)\Big]\varepsilon'_{22} \\
& + \Big[44.8\left(B_1 + B_2\right)\left(\cos^2\phi + \sin^2\phi\right) + 203.9B_3\Big]\varepsilon'_{33} \\
& + \Big[13.5\left(B_1 - B_2\right)\left(\cos^2\phi - \sin^2\phi\right) + 120.8\sqrt{2}(B_2 - B_3)(\cos^2\phi - \sin^2\phi)\Big]\varepsilon'_{23} \\
& + \Big[120.8\sqrt{2}(B_2 - B_3)\sin\left(2\phi\right) + 13.5(B_1 - B_2)\sin\left(2\phi\right)\Big]\varepsilon'_{13} \\
& + \Big[27\sqrt{2}(B_2 - B_3)\sin\left(2\phi\right) + 70(B_1 - B_2)\sin\left(2\phi\right)\Big]\varepsilon'_{12} \\
& + \alpha T
\end{aligned}
\tag{B-7}
$$

Orientation of equation (B-7) along the angles defining the ten-element rosette generates the following equations defining the resistance change with strain for the ten sensing elements:

$$\left(\frac{\Delta R_1}{R_1}\right) = \left[194.3B_1^a + 54.4B_2^a + 44.8B_3^a + 27\sqrt{2}\left(B_2^a - B_3^a\right)\right]\varepsilon'_{11}$$
$$+\left[54.4B_1^a + 194.3B_2^a + 44.8B_3^a - 27\sqrt{2}\left(B_2^a - B_3^a\right)\right]\varepsilon'_{22}$$
$$+\left[44.8\left(B_1^a + B_2^a\right) + 203.9B_3^a\right]\varepsilon'_{33} + \left[13.5\left(B_1^a - B_2^a\right) + 120.8\sqrt{2}\left(B_2^a - B_3^a\right)\right]\varepsilon'_{23}$$
$$+\alpha^a \mathrm{T}$$

$$\left(\frac{\Delta R_2}{R_2}\right) = \left[124.35\left(B_1^a + B_2^a\right) + 44.8B_3^a\right]\varepsilon'_{11} + \left[124.35\left(B_1^a + B_2^a\right) + 44.8B_3^a\right]\varepsilon'_{22}$$
$$+\left[44.8\left(B_1^a + B_2^a\right) + 203.9B_3^a\right]\varepsilon'_{33}$$
$$+\left[120.8\sqrt{2}\left(B_2^a - B_3^a\right) + 13.5\left(B_1^a - B_2^a\right)\right]\varepsilon'_{13}$$
$$+\left[27\sqrt{2}\left(B_2^a - B_3^a\right) + 70\left(B_1^a - B_2^a\right)\right]\varepsilon'_{12} + \alpha^a \mathrm{T}$$

$$\left(\frac{\Delta R_3}{R_3}\right) = \left[54.4B_1^a + 194.3B_2^a + 44.8B_3^a - 27\sqrt{2}\left(B_2^a - B_3^a\right)\right]\varepsilon'_{11}$$
$$+\left[194.3B_1^a + 54.4B_2^a + 44.8B_3^a + 27\sqrt{2}\left(B_2^a - B_3^a\right)\right]\varepsilon'_{22}$$
$$+\left[44.8\left(B_1^a + B_2^a\right) + 203.9B_3^a\right]\varepsilon'_{33} - \left[13.5\left(B_1^a - B_2^a\right) + 120.8\sqrt{2}\left(B_2^a - B_3^a\right)\right]\varepsilon'_{23}$$
$$+\alpha^a \mathrm{T}$$

$$\left(\frac{\Delta R_4}{R_4}\right) = \left[124.35\left(B_1^a + B_2^a\right) + 44.8B_3^a\right]\varepsilon'_{11} + \left[124.35\left(B_1^a + B_2^a\right) + 44.8B_3^a\right]\varepsilon'_{22}$$
$$+\left[44.8\left(B_1^a + B_2^a\right) + 203.9B_3^a\right]\varepsilon'_{33}$$
$$-\left[120.8\sqrt{2}\left(B_2^a - B_3^a\right) + 13.5\left(B_1^a - B_2^a\right)\right]\varepsilon'_{13}$$
$$-\left[27\sqrt{2}\left(B_2^a - B_3^a\right) + 70\left(B_1^a - B_2^a\right)\right]\varepsilon'_{12} + \alpha^a \mathrm{T}$$

$$\left(\frac{\Delta R_5}{R_5}\right)=\left[194.3B_1^b+54.4B_2^b+44.8B_3^b+27\sqrt{2}\left(B_2^b-B_3^b\right)\right]\varepsilon'_{11}$$
$$+\left[54.4B_1^b+194.3B_2^b+44.8B_3^b-27\sqrt{2}\left(B_2^b-B_3^b\right)\right]\varepsilon'_{22}$$
$$+\left[44.8\left(B_1^b+B_2^b\right)+203.9B_3^b\right]\varepsilon'_{33}+\left[13.5\left(B_1^b-B_2^b\right)+120.8\sqrt{2}\left(B_2^b-B_3^b\right)\right]\varepsilon'_{23}$$
$$+\alpha^b\mathrm{T}$$

$$\left(\frac{\Delta R_6}{R_6}\right)=\left[124.35\left(B_1^b+B_2^b\right)+44.8B_3^b\right]\varepsilon'_{11}+\left[124.35\left(B_1^b+B_2^b\right)+44.8B_3^b\right]\varepsilon'_{22}$$
$$+\left[44.8\left(B_1^b+B_2^b\right)+203.9B_3^b\right]\varepsilon'_{33}$$
$$+\left[120.8\sqrt{2}\left(B_2^b-B_3^b\right)+13.5\left(B_1^b-B_2^b\right)\right]\varepsilon'_{13}$$
$$+\left[27\sqrt{2}\left(B_2^b-B_3^b\right)+70\left(B_1^b-B_2^b\right)\right]\varepsilon'_{12}+\alpha^b\mathrm{T}$$

$$\left(\frac{\Delta R_7}{R_7}\right)=\left[54.4B_1^b+194.3B_2^b+44.8B_3^b-27\sqrt{2}\left(B_2^b-B_3^b\right)\right]\varepsilon'_{11}$$
$$+\left[194.3B_1^b+54.4B_2^b+44.8B_3^b+27\sqrt{2}\left(B_2^b-B_3^b\right)\right]\varepsilon'_{22}$$
$$+\left[44.8\left(B_1^b+B_2^b\right)+203.9B_3^b\right]\varepsilon'_{33}$$
$$-\left[13.5\left(B_1^b-B_2^b\right)+120.8\sqrt{2}\left(B_2^b-B_3^b\right)\right]\varepsilon'_{23}+\alpha^b\mathrm{T}$$

$$\left(\frac{\Delta R_8}{R_8}\right)=\left[124.35\left(B_1^b+B_2^b\right)+44.8B_3^b\right]\varepsilon'_{11}+\left[124.35\left(B_1^b+B_2^b\right)+44.8B_3^b\right]\varepsilon'_{22}$$
$$+\left[44.8\left(B_1^b+B_2^b\right)+203.9B_3^b\right]\varepsilon'_{33}$$
$$-\left[120.8\sqrt{2}\left(B_2^b-B_3^b\right)+13.5\left(B_1^b-B_2^b\right)\right]\varepsilon'_{13}$$
$$-\left[27\sqrt{2}\left(B_2^b-B_3^b\right)+70\left(B_1^b-B_2^b\right)\right]\varepsilon'_{12}+\alpha^b\mathrm{T}$$

$$\left(\frac{\Delta R_9}{R_9}\right)=\left[194.3B_1^c+54.4B_2^c+44.8B_3^c+27\sqrt{2}\left(B_2^c-B_3^c\right)\right]\varepsilon'_{11}$$
$$+\left[54.4B_1^c+194.3B_2^c+44.8B_3^c-27\sqrt{2}\left(B_2^c-B_3^c\right)\right]\varepsilon'_{22}$$
$$+\left[44.8\left(B_1^c+B_2^c\right)+203.9B_3^c\right]\varepsilon'_{33}+\left[13.5\left(B_1^c-B_2^c\right)+120.8\sqrt{2}\left(B_2^c-B_3^c\right)\right]\varepsilon'_{23}$$
$$+\alpha^c\mathrm{T}$$

$$\begin{aligned}\left(\frac{\Delta R_{10}}{R_{10}}\right) &= \left[124.35\left(B_1^c + B_2^c\right) + 44.8B_3^c\right]\varepsilon'_{11} + \left[124.35\left(B_1^c + B_2^c\right) + 44.8B_3^c\right]\varepsilon'_{22} \\ &+ \left[44.8\left(B_1^c + B_2^c\right) + 203.9B_3^c\right]\varepsilon'_{33} \\ &+ \left[120.8\sqrt{2}\left(B_2^c - B_3^c\right) + 13.5\left(B_1^c - B_2^c\right)\right]\varepsilon'_{13} \\ &+ \left[27\sqrt{2}\left(B_2^c - B_3^c\right) + 70\left(B_1^c - B_2^c\right)\right]\varepsilon'_{12} + \alpha^c \mathrm{T}\end{aligned} \tag{B-8}$$

APPENDIX C: ANSYS FINITE ELEMENT CODE FOR THE FOUR-POINT BENDING OF THE CALIBRATION BEAM

```
/prep7

!PARAMETERS
!############
Ld=56       !Length of Dead Weights location, mm
Lc=70.7     !Total length of beam, mm
W=7         !Width of beam, mm
t=0.3       !Thickness of beam, mm
Lz=2        !Length of ZIF connector contact, mm
thz1=0*3.14/180     !misalignment angle (rad) of ZIF connector right
thz2=0*3.14/180     !misalignment angle (rad) of ZIF connector left
Ls=28               !Length of Supports location, mm
terr=0              !Translational error, mm

F=12*9.81/1000      !Dead weight load, mN
FE=1.1*9.81/1000!End connector load, mN
n=29                !Number of nodes at dead weight
!GEOEMTRY
!##########
Block,-Lc/2,Lc/2,-W/2,W/2,0,t
WPLANE, 1, Ls/2, 0, 0, Ls/2, W/2, 0, Ls/2, 0, t      ! Partitioning at Supports
VSBW, all
WPLANE, 1, -Ls/2, 0, 0, -Ls/2, W/2, 0, -Ls/2, 0, t      ! Partitioning at Supports
VSBW, all
WPLANE, 1, Ld/2, 0, 0, Ld/2, W/2, 0, Ld/2, 0, t      ! Partitioning at Dead Weights
VSBW, all
WPLANE, 1, -Ld/2, 0, 0, -Ld/2, W/2, 0, -Ld/2, 0, t ! Partitioning at Dead Weights
VSBW, all
WPLANE, 1, 3, 0, 0, 3, W/2, 0, 3, 0, t      ! Partitioning Center Area
VSBW, all
WPLANE, 1, 4, 0, 0, 4, W/2, 0, 4, 0, t      ! Partitioning Center Area
VSBW, all
WPLANE, 1, 0, -0.5, 0, 7, -0.5, 0, 0, -0.5, t      ! Partitioning Center Area
VSBW, all
WPLANE, 1, 0, 0.5, 0, 7, 0.5, 0, 0, 0.5, t      ! Partitioning Center Area
VSBW, all
WPLANE, 1, Lc/2-Lz, 0, 0, (W/2)*tan(thz1)+Lc/2-Lz, W/2, 0, Lc/2-Lz, 0, t      ! Partitioning at Dead Weights
VSBW, all
WPLANE, 1, -Lc/2+Lz, 0, 0, -(W/2)*tan(thz2)-Lc/2+Lz, W/2, 0, -Lc/2+Lz, 0, t      ! Partitioning at Dead Weights
VSBW, all
VGLUE,all

CSYS,0
WPCSYS, 1, 0     ! Global CS
!ELEMENT TYPE
!#############
ET,1,SOLID186
!MATERIAL PROPERTIES
!#####################
!Silicon
MP,EX,1,169E3
MP,PRXY,1,0.3
!MESHING
!########
ESIZE, 0.25
VMESH,all
/solu
!CONSTRAINTS
!#############
!Center Constraint in x-direction
nsel,s,loc,x,terr
D,ALL,UX,terr
allsel,all
!Supports
nsel,s,loc,x,Ls/2+terr
nsel,a,loc,x,-Ls/2+terr
nsel,r,loc,z,0
D, ALL, UZ,0
allsel,all
!Constraint in Y-direction
nsel,s,loc,x,Ls/2+terr
nsel,a,loc,x,-Ls/2+terr
nsel,r,loc,y,0
nsel,r,loc,z,0
D,ALL,UY,0
allsel,all
!LOADING
!########
vsel,s,loc,x,Lc/2-Lz-(W/2)*tan(thz1),Lc/2
eslv,s
nsle,s
nsel,r,loc,z,t
SF,all,PRES,FE/(7*2)
allsel,all
vsel,s,loc,x,-Lc/2+Lz+(W/2)*tan(thz2),-Lc/2
eslv,s
nsle,s
nsel,r,loc,z,t
SF,all,PRES,FE/(7*2)
allsel,all
SOLVE
FINISH
/post1
```

APPENDIX D: ANSYS FINITE ELEMENT CODE FOR THE FOUR-POINT BENDING OF THE TEST BEAM

```
/title, Chip On Beam - 45 deg
/com, Geometrical Parameters (mm)
/com,

!MONITORED STRUCTURE
!######################
lm = 180000 !Length of monitored structure (um)
wm = 22730 !Width of monitored structure (um)
tm = 1574.8 !Thickness of monitored structure (um)
Standard PCB thickness 0.062inch
!SENSOR
!#######
ls = 7000 !Length of sensor (um)
ws = 7000 !Width of sensor (um)
ts = 300 !Thickness of sensor (um)
!ACF Flip Chip Bond
!#################
lb = 1.00*ls !Length of Bond (um)
wb = 1.00*ws !Width of Bond (um)
tb = 70 !Thickness of Bond (um)
!Four point bending
!###############
L=140000/2
D=55000/2
!Sensing Rosette
!#############
c=50
r=200
a=100           ! length of piezoresistors, um
b=20            ! width of piezoresistors, um
TP=6            ! depth of doping, um
pi=3.14
phi=pi/4
!Sensing Rosette positions
! ####################
!1) Center Rosette
!Element 1
xc1=0
yc1=400
sc1=0
!Element 2
xc2=-75
yc2=-200
sc2=45
!Element 3
xc3=-150
yc3=275
sc3=90
!Element 4
xc4=-75
yc4=-375
sc4=135
!Element 5
xc5=0
yc5=175
sc5=180
!Element 6
xc6=75
yc6=-375
sc6=225
!Element 7
xc7=150
yc7=275
sc7=270
!Element 8
xc8=75
yc8=-200
sc8=315
!Element 9
xc9=100
yc9=0
sc9=0
!Element 10
xc10=290
yc10=100
sc10=90

!2) Edge Rosette 1
xedge23=0
yedge23=ws/2-525
!Element 1
xe1=200
ye1=-100
se1=sc1
!Element 3
xe3=430
ye3=0
se3=sc3
!Element 5
xe5=200
ye5=100
se5=sc5
!Element 7
xe7=0
ye7=0
se7=sc7
! !Element 9
! xe9=-350
! ye9=0
! se9=sc9
! !Element 10
! xe10=-150
! ye10=0
! se10=sc10

!3)  Edge Rosette 2
xedge13=ls/2-525
yedge=0
!Element 2
xe2=0
ye2=325
se2=sc2
!Element 4
```

```
xe4=0
ye4=70
se4=sc4
!Element 6
xe6=0
ye6=-70
se6=sc6
!Element 8
xe8=0
ye8=-325
se8=sc8
!LOADING
!#########
/COM, LOADING CONDITIONS
F=12.71e6/2 !Check number of nodes along line of
applied load
/com, Supply voltage, Volt
Vs=5
/NOPR
!MATERIAL PROPERTIES
!######################
/COM,
/COM,  MATERIAL PROPERTIES (Si):
/COM,
/COM,  Young's modulus, MPa
E=165e3
/COM,  Poisson's ratio
nu=0.25
/COM,
/com,  Stiffness,  MN/m^2
/com,   [c11 c12 c12  0  0    0 ]
/com,   [c12 c11 c12  0  0    0 ]
/com,   [c12 c12 c11  0  0    0 ]
/com,   [ 0     0  0  c44  0    0 ]
/com,   [ 0    0    0  0  c44   0 ]
/com,   [ 0    0  0  0  0   c44]
c11= 16.57e4
c12= 6.39e4
c44= 7.96e4
/com,
!Piezoresistive properties of group a
/COM,  Resistivity (group a), TOhm*um
rhoa= 1.493e-8
/COM,
/COM,  Piezoresistive coefficients (n-Si), (MPa)^-1
/COM,   [p11 p12 p12  0  0  0 ]
/COM,   [p12 p11 p12  0  0  0 ]
/COM,   [p12 p12 p11  0  0  0 ]
/COM,   [ 0    0    0   p44  0  0 ]
/COM,   [ 0    0    0    0  p44 0 ]
/COM,   [ 0    0    0    0   0 p44]
/COM,
p11a=-547.6e-6
p12a=286.1e-6
p44a=-150.9E-6
!Piezoresistive properties of group b
/COM,  Resistivity (group b), TOhm*um
rhob= 5.435e-8
/COM,  Piezoresistive coefficients (n- Si), (MPa)^-1
/COM,   [p11 p12 p12  0  0  0 ]
/COM,   [p12 p11 p12  0  0  0 ]
/COM,   [p12 p12 p11  0  0  0 ]
/COM,   [ 0    0    0   p44  0  0 ]
/COM,   [ 0    0    0    0  p44 0 ]
/COM,   [ 0    0    0    0   0 p44]
/COM,
p11b=-873.3e-6
p12b=456.3e-6
p44b=-131.5e-6
!Piezoresistive properties of group c
/COM,  Resistivity (group c), TOhm*um
rhoc= 8.746e-8
/COM,  Piezoresistive coefficients (n-Si), (MPa)^-1
/COM,   [p11 p12 p12  0  0  0 ]
/COM,   [p12 p11 p12  0  0  0 ]
/COM,   [p12 p12 p11  0  0  0 ]
/COM,   [ 0    0   0   p44  0   0 ]
/COM,   [ 0    0   0    0  p44  0 ]
/COM,   [ 0    0   0    0   0  p44]
/COM,
p11c=-948.3e-6
p12c=495.5e-6
p44c=-128.4e-6
!################################
/PREP7
! Specify material orientation
!^^^^^^^^^^^^^^^^^^^^^^^^^^^^^^
LOCAL,11,0
K,1000,0,0,0
K,1001,-1/sqrt(2),-1/sqrt(6),1/sqrt(3)
K,1002,1/sqrt(2),-1/sqrt(6),1/sqrt(3)
CSKP, 12, 0, 1000, 1001, 1002
!Geommetry Modeling
################################
block, -wm/2, wm/2, -wm/2, wm/2, 0, tm
block, -lm/2, -wm/2, -wm/2, wm/2, 0, tm
block, wm/2, lm/2, -wm/2, wm/2, 0, tm
!WPLANE, 1, 0, 0, 0, ls*cos(phi), ws*sin(phi), 0, -
ls*cos(phi), ws*sin(phi), 0        ! Silicon Chip Working
Plane
!CHIP ORIENTATION
LOCAL,14,0,0,0,0,-45,0,0
CSYS,14
WPCSYS,1,14
block, -lb/2, lb/2, -wb/2, wb/2, tm, tm+tb               !
ACF bonding layer
block, -ls/2, ls/2, -ws/2, ws/2, tm+tb, tm+tb+ts           !
Silicon Chip
block, -lb/2, lb/2, -wb/2, wb/2, 0, tm+tb          !
Adhesive - Volume 2
VSBV,all,4
block, -lb/2, lb/2, -wb/2, wb/2, 0, tm+tb          !
Adhesive
!Sensing Rosette CS
CSYS,14
CLOCAL, 21, 0, xc1,yc1,tm+tb,sc1, 0, 0
CSYS,14
CLOCAL, 22, 0, xc2,yc2,tm+tb,sc2, 0, 0
CSYS,14
CLOCAL, 23, 0, xc3,yc3,tm+tb,sc3, 0, 0
CSYS,14
CLOCAL, 24, 0, xc4,yc4,tm+tb,sc4, 0, 0
CSYS,14
CLOCAL, 25, 0, xc5,yc5,tm+tb,sc5, 0, 0
CSYS,14
CLOCAL, 26, 0, xc6,yc6,tm+tb,sc6, 0, 0
CSYS,14
CLOCAL, 27, 0, xc7,yc7,tm+tb,sc7, 0, 0
CSYS,14
CLOCAL, 28, 0, xc8,yc8,tm+tb,sc8, 0, 0
CSYS,14
CLOCAL, 29, 0, xc9,yc9,tm+tb,sc9, 0, 0
CSYS,14
CLOCAL, 30, 0, xc10,yc10,tm+tb,sc10, 0, 0
CSYS,14
CLOCAL, 31, 0, xedge23+xe1,yedge23+ye1,tm+tb,se1,
0, 0
CSYS,14
```

```
CLOCAL, 33, 0, xedge23+xe3,yedge23+ye3,tm+tb,se3,
0, 0
CSYS,14
CLOCAL, 35, 0, xedge23+xe5,yedge23+ye5,tm+tb,se5,
0, 0
CSYS,14
CLOCAL, 37, 0, xedge23+xe7,yedge23+ye7,tm+tb,se7,
0, 0
CSYS,14
CLOCAL, 39, 0, xedge23+xe9,yedge23+ye9,tm+tb,se9,
0, 0
CSYS,14
CLOCAL, 40, 0,
xedge23+xe10,yedge23+ye10,tm+tb,se10, 0, 0
CSYS,14
CLOCAL, 32, 0, xedge13+xe2,yedge13+ye2,tm+tb,se2,
0, 0
CSYS,14
CLOCAL, 34, 0, xedge13+xe4,yedge13+ye4,tm+tb,se4,
0, 0
CSYS,14
CLOCAL, 36, 0, xedge13+xe6,yedge13+ye6,tm+tb,se6,
0, 0
CSYS,14
CLOCAL, 38, 0, xedge13+xe8,yedge13+ye8,tm+tb,se8,
0, 0
CSYS,0
WPCSYS,1,0

!Stud Bumps CS
CSYS,14
CLOCAL, 51, 0, -3120, 3120-780, tm, 0, 0, 0 !LG
CSYS,14
CLOCAL, 52, 0, -3120, 3120-780*2, tm, 0, 0, 0 !L1
CSYS,14
CLOCAL, 53, 0, -3120, 3120-780*3, tm, 0, 0, 0 !L3
CSYS,14
CLOCAL, 54, 0, -3120, 3120-780*4, tm, 0, 0, 0 !L5
CSYS,14
CLOCAL, 55, 0, -3120, 3120-780*5, tm, 0, 0, 0 !L7
CSYS,14
CLOCAL, 56, 0, -3120, 3120-780*6, tm, 0, 0, 0 !L9
CSYS,14
CLOCAL, 57, 0, -3120, 3120-780*7, tm, 0, 0, 0 !L10
CSYS,14
CLOCAL, 58, 0, -3120+780, -3120, tm, 0, 0, 0 !L2
CSYS,14
CLOCAL, 59, 0, -3120+780*2, -3120, tm, 0, 0, 0 !L4
CSYS,14
CLOCAL, 60, 0, -3120+780*3, -3120, tm, 0, 0, 0 !L6
CSYS,14
CLOCAL, 61, 0, -3120+780*4, -3120, tm, 0, 0, 0 !L8
CSYS,14
CLOCAL, 62, 0, -3120+780*6, -3120, tm, 0, 0, 0 !R2
CSYS,14
CLOCAL, 63, 0, -3120+780*7, -3120, tm, 0, 0, 0 !R4
CSYS,14
CLOCAL, 64, 0, 3120, 3120-780*7, tm, 0, 0, 0 !R6
CSYS,14
CLOCAL, 65, 0, 3120, 3120-780*6, tm, 0, 0, 0 !R8
CSYS,14
CLOCAL, 66, 0, 3120, 3120-780*2, tm, 0, 0, 0 !RG
CSYS,14
CLOCAL, 67, 0, 3120, 3120, tm, 0, 0, 0        !R1
CSYS,14
CLOCAL, 68, 0, 3120-780, 3120, tm, 0, 0, 0  !R3
CSYS,14
CLOCAL, 69, 0, 3120-780*2, 3120, tm, 0, 0, 0 !R5
CSYS,14
CLOCAL, 70, 0, 3120-780*6, 3120, tm, 0, 0, 0 !R7
CSYS,14
CLOCAL, 71, 0, 3120-780*7, 3120, tm, 0, 0, 0 !R9
CSYS,14
CLOCAL, 72, 0, 3120-780*8, 3120, tm, 0, 0, 0 !R10

WPCSYS,1,0
CSYS,0

!Central Sensing Rosette
!######################
! Sensing Element 1
WPCSYS, , 21
CSYS,21
Block,-a/2,a/2,-b/2,b/2,0,TP                ! Resistor 1
K,1011,-a/2,-b,0
K,1012,a/2,-b,0
! Sensing Element 2
WPCSYS, , 22
CSYS,22
Block,-a/2,a/2,-b/2,b/2,0,TP                ! Resistor 2
K,2011,-a/2,-b,0
K,2012,a/2,-b,0
! Sensing Element 3
WPCSYS, , 23
CSYS,23
Block,-a/2,a/2,-b/2,b/2,0,TP                ! Resistor 3
K,3011,-a/2,-b,0
K,3012,a/2,-b,0
! Sensing Element 4
WPCSYS, , 24
CSYS,24
Block,-a/2,a/2,-b/2,b/2,0,TP                ! Resistor 4
K,4011,-a/2,-b,0
K,4012,a/2,-b,0
! Sensing Element 5
WPCSYS, , 25
CSYS,25
Block,-a/2,a/2,-b/2,b/2,0,TP                ! Resistor 5
K,5011,-a/2,-b,0
K,5012,a/2,-b,0
! Sensing Element 6
WPCSYS, , 26
CSYS,26
Block,-a/2,a/2,-b/2,b/2,0,TP                ! Resistor 6
K,6011,-a/2,-b,0
K,6012,a/2,-b,0
! Sensing Element 7
WPCSYS, , 27
CSYS,27
Block,-a/2,a/2,-b/2,b/2,0,TP                ! Resistor 7
K,7011,-a/2,-b,0
K,7012,a/2,-b,0
! Sensing Element 8
WPCSYS, , 28
CSYS,28
Block,-a/2,a/2,-b/2,b/2,0,TP                ! Resistor 8
K,8011,-a/2,-b,0
K,8012,a/2,-b,0
! Sensing Element 9
WPCSYS, , 29
CSYS,29
Block,-a/2,a/2,-b/2,b/2,0,TP                ! Resistor 9
K,9011,-a/2,-b,0
K,9012,a/2,-b,0
! Sensing Element 10
WPCSYS, , 30
CSYS,30
```

```
Block,-a/2,a/2,-b/2,b/2,0,TP                ! Resistor 10
K,10011,-a/2,-b,0
K,10012,a/2,-b,0

!Edge Sensing Rosette
!####################
! Sensing Element 1
WPCSYS, , 31
CSYS,31
Block,-a/2,a/2,-b/2,b/2,0,TP               ! Resistor 2
K,1021,-a/2,-b,0
K,1022,a/2,-b,0
! Sensing Element 2
WPCSYS, , 32
CSYS,32
Block,-a/2,a/2,-b/2,b/2,0,TP               ! Resistor 2
K,2021,-a/2,-b,0
K,2022,a/2,-b,0
! Sensing Element 3
WPCSYS, , 33
CSYS,33
Block,-a/2,a/2,-b/2,b/2,0,TP                ! Resistor 4
K,3021,-a/2,-b,0
K,3022,a/2,-b,0
! Sensing Element 4
WPCSYS, , 34
CSYS,34
Block,-a/2,a/2,-b/2,b/2,0,TP                ! Resistor 4
K,4021,-a/2,-b,0
K,4022,a/2,-b,0
! Sensing Element 5
WPCSYS, , 35
CSYS,35
Block,-a/2,a/2,-b/2,b/2,0,TP                ! Resistor 6
K,5021,-a/2,-b,0
K,5022,a/2,-b,0
! Sensing Element 6
WPCSYS, , 36
CSYS,36
Block,-a/2,a/2,-b/2,b/2,0,TP                ! Resistor 6
K,6021,-a/2,-b,0
K,6022,a/2,-b,0
! Sensing Element 7
WPCSYS, , 37
CSYS,37
Block,-a/2,a/2,-b/2,b/2,0,TP                ! Resistor 8
K,7021,-a/2,-b,0
K,7022,a/2,-b,0
! Sensing Element 8
WPCSYS, , 38
CSYS,38
Block,-a/2,a/2,-b/2,b/2,0,TP                ! Resistor 8
K,8021,-a/2,-b,0
K,8022,a/2,-b,0
! Sensing Element 9
WPCSYS, , 39
CSYS,39
!Block,-a/2,a/2,-b/2,b/2,0,TP                ! Resistor 9
Block,-b,b,-b,b,0,10*TP                 ! Resistor 9
K,9021,-a/2,-b,0
K,9022,a/2,-b,0
! Sensing Element 10
WPCSYS, , 40
CSYS,40
!Block,-a/2,a/2,-b/2,b/2,0,TP                ! Resistor 10
Block,-b,b,-b,b,0,10*TP
            ! Resistor 10
K,10021,-a/2,-b,0
K,10022,a/2,-b,0
WPCSYS, 1, 0
CSYS,0
VOVLAP,all


!Modeling Stud Bumps
WPCSYS,,51
CSYS,51
CYL4, 0, 0, 175, 0, 175, 360, tb
WPCSYS,,52
CSYS,52
CYL4, 0, 0, 175, 0, 175, 360, tb
WPCSYS,,53
CSYS,53
CYL4, 0, 0, 175, 0, 175, 360, tb
WPCSYS,,54
CSYS,54
CYL4, 0, 0, 175, 0, 175, 360, tb
WPCSYS,,55
CSYS,55
CYL4, 0, 0, 175, 0, 175, 360, tb
WPCSYS,,56
CSYS,56
CYL4, 0, 0, 175, 0, 175, 360, tb
WPCSYS,,57
CSYS,57
CYL4, 0, 0, 175, 0, 175, 360, tb
WPCSYS,,58
CSYS,58
CYL4, 0, 0, 175, 0, 175, 360, tb
WPCSYS,,59
CSYS,59
CYL4, 0, 0, 175, 0, 175, 360, tb
WPCSYS,,60
CSYS,60
CYL4, 0, 0, 175, 0, 175, 360, tb
WPCSYS,,61
CSYS,61
CYL4, 0, 0, 175, 0, 175, 360, tb
WPCSYS,,62
CSYS,62
CYL4, 0, 0, 175, 0, 175, 360, tb
WPCSYS,,63
CSYS,63
CYL4, 0, 0, 175, 0, 175, 360, tb
WPCSYS,,64
CSYS,64
CYL4, 0, 0, 175, 0, 175, 360, tb
WPCSYS,,65
CSYS,65
CYL4, 0, 0, 175, 0, 175, 360, tb
WPCSYS,,66
CSYS,66
CYL4, 0, 0, 175, 0, 175, 360, tb
WPCSYS,,67
CSYS,67
CYL4, 0, 0, 175, 0, 175, 360, tb
WPCSYS,,68
CSYS,68
CYL4, 0, 0, 175, 0, 175, 360, tb
WPCSYS,,69
CSYS,69
CYL4, 0, 0, 175, 0, 175, 360, tb
WPCSYS,,70
CSYS,70
CYL4, 0, 0, 175, 0, 175, 360, tb
WPCSYS,,71
CSYS,71
CYL4, 0, 0, 175, 0, 175, 360, tb
```

```
WPCSYS,,72
CSYS,72
CYL4, 0, 0, 175, 0, 175, 360, tb
WPCSYS, 1, 0
CSYS,0
WPCSYS,,14
CSYS,14
block, -450, 450, -450, 450, tm+tb, tm+tb+ts   ! Center Rosette
block, 2850, 3100, -500, 500, tm+tb, tm+tb+ts   ! Edge Rosette 13
block, -75, 500, 2850, 3100, tm+tb, tm+tb+ts   ! Edge Rosette 23

!Modeling Spew Fillet
k,2001,3800,3800,tm
k,2002,-3800,3800,tm
k,2003,-3800,-3800,tm
k,2004,3800,-3800,tm
k,2005,3500,3500,tm+tb+ts
k,2006,-3500,3500,tm+tb+ts
k,2007,-3500,-3500,tm+tb+ts
k,2008,3500,-3500,tm+tb+ts

V,2001,2002,2003,2004,2005,2006,2007,2008


WPCSYS, 1, 0
CSYS,0

! Partition Structure
WPLANE, 1, 0, 0, 0, lm/2, 0, 0, 0, 0, tm       ! Partitioning the Sheet
vsel,s,loc,z,0,tm
VSBW, all
WPLANE, 1, 0, 0, 0, 0, wm/2, 0, 0, 0, tm       ! Partitioning the Sheet
VSBW, all
vsel,all

!Location of Four Point Bending
WPLANE, 1, -L, 0, 0, -L, wm/2, 0, -L,0,tm
vsbw,all
WPLANE, 1, L, 0, 0, L, wm/2, 0, L,0,tm
vsbw,all
WPLANE, 1, -D, 0, 0, -D, wm/2, 0, -D,0,tm
vsbw,all
WPLANE, 1, D, 0, 0, D, wm/2, 0, D,0,tm
vsbw,all
WPCSYS, 1, 0
CSYS,0

VOVLAP,all
VGLUE,all


! ELEMENT TYPE
!###############
ET,1,SOLID227,101      ! piezoresistive element type, Tetrahedron - 10 Noded
ET,2,SOLID187          ! structural element type
ET,3,CIRCU124,0        ! electrical resistance element

R,1,(a/(b*TP))*rhoa       ! resistance of constant resistors - TOhm
R,2,(a/(b*TP))*rhob       ! resistance of constant resistors - TOhm
R,3,(a/(b*TP))*rhoc          ! resistance of constant resistors - TOhm
```

```
!################################
! MATERIAL PROPERTIES
!################################
! 1) Anisotropic elasticity matrix of Silicon
!^^^^^^^^^^^^^^^^^^^^^^^^^^^^^^^^^^^^^
!a) Group a
tb,ANEL,2,,,0
tbdata,1,c11,c12,c12
tbdata,7,c11,c12
tbdata,12,c11
tbdata,16,c44
tbdata,19,C44,0,C44

!b) Group b
tb,ANEL,3,,,0
tbdata,1,c11,c12,c12
tbdata,7,c11,c12
tbdata,12,c11
tbdata,16,c44
tbdata,19,C44,0,C44

!c) Group c
tb,ANEL,4,,,0
tbdata,1,c11,c12,c12
tbdata,7,c11,c12
tbdata,12,c11
tbdata,16,c44
tbdata,19,C44,0,C44

!2) Resistivity
!^^^^^^^^^^^^^^
!a) Group a
MP,RSVX,2,rhoa               ! Resistivity

TB,PZRS,2                   ! piezoresistive stress matrix
TBDATA,1,p11a,p12a,p12a
TBDATA,7,p12a,p11a,p12a
TBDATA,13,p12a,p12a,p11a
TBDATA,22,p44a
TBDATA,29,p44a
TBDATA,36,p44a

!b) Group b
MP,RSVX,3,rhob               ! Resistivity

TB,PZRS,3                   ! piezoresistive stress matrix
TBDATA,1,p11b,p12b,p12b
TBDATA,7,p12b,p11b,p12b
TBDATA,13,p12b,p12b,p11b
TBDATA,22,p44b
TBDATA,29,p44b
TBDATA,36,p44b

!b) Group c
MP,RSVX,4,rhoc               ! Resistivity

TB,PZRS,4                   ! piezoresistive stress matrix
TBDATA,1,p11c,p12c,p12c
TBDATA,7,p12c,p11c,p12c
TBDATA,13,p12c,p12c,p11c
TBDATA,22,p44c
TBDATA,29,p44c
TBDATA,36,p44c

MP,EX,5,3.3E3                              ! Anisotropic Conductive Adhesive (ACA) Delo Industrial Adhesives LLC
!ACF, E= 3.3GPa, v=0.3 [Delo Technical Information - Delomonopox AC265 ]
```

```
MP,PRXY,5,0.3
MP,EX,1,23.73E3       ! PCB -FR4
!FR4, E= 23.73GPa, v=0.117 [Cho, PhD thesis 2007,
p43]
MP,PRXY,1,0.117
MP,EX,6,77.2E3        ! Gold Bumps
MP,PRXY,6,0.3

!################################
!MESHING #
!#########
NUMSTR, NODE, 300
WPCSYS,,14
CSYS,14
VATT,6,1,2 !Gold Bumps
esize,0.25*ts
vsel,s,loc,z,tm,tm+tb
vsel,r,loc,x,-3300,-2900
!esize,easize,
vmesh,all
vsel,s,loc,z,tm,tm+tb
vsel,r,loc,x,2900,3300
!esize,easize,
vmesh,all
vsel,s,loc,z,tm,tm+tb
vsel,r,loc,y,-3300,-2900
!esize,easize,
vmesh,all
vsel,s,loc,z,tm,tm+tb
vsel,r,loc,y,2900,3300
!esize,easize,
vmesh,all
vsel,all

WPCSYS,1,0
CSYS,0

!Chip
VATT,2,1,2,12         !Sensor
vsel,s,volu,,80
vsel,a,volu,,81
vsel,a,volu,,83
aslv,s
asel,r,loc,z,tm+tb
lsla,s
lesize,all,8*TP
allsel,all
vsel,s,loc,z,tm+tb,tm+tb+ts
vsel,u,volu,,79
vsel,u,volu,,80
vsel,u,volu,,81
vsel,u,volu,,83
vsel,u,volu,,4
vsel,u,volu,,6
vsel,u,volu,,9
vsel,u,volu,,10
vsel,u,volu,,17,20,1
vsel,u,volu,,11,14,1
vsel,u,volu,,21,24,1
vsel,u,volu,,15,16,1

LESIZE, 45,12*TP ,,,-0.1
LESIZE, 46,12*TP ,,,-0.1
LESIZE, 47,12*TP ,,,-0.1
LESIZE, 48,12*TP ,,,-0.1
LESIZE, 53,12*TP ,,,-0.1
LESIZE, 54,12*TP ,,,-0.1
LESIZE, 55,12*TP ,,,-0.1
LESIZE, 56,12*TP ,,,-0.1
esize,2*ts
MOPT,TETEXPND,2
VMESH,all
vsel,all

!Sensing Rosette
VATT,2,1,1,12
ESIZE,3*TP
VMESH,4                ! mesh group a resistor areas
VMESH,6
VMESH,9
VMESH,10
VMESH,17,20,1

VATT,3,1,1,12
ESIZE,3*TP
VMESH,11,14,1          ! mesh group b resistor areas
VMESH,21,24,1
VATT,4,1,1,12
ESIZE,3*TP
VMESH,15,16,1          ! mesh group c resistor areas
! VMESH,25,26,1
!Volume Surrounding Rosette
VATT,2,1,2,12
vsel,s,volu,,80
vsel,a,volu,,81
vsel,a,volu,,83
esize,10*TP
VMESH,all
vsel,all
VATT, 5, 1, 2          !ACF
vsel,s,loc,z,tm,tm+tb
vsel,a,volu,,79
!esize,tb*3
MOPT,TETEXPND,2
VMESH,all
vsel,all
WPCSYS,1,0
CSYS,0
VATT,1,1,2                    !Monitored Structure
vsel,s,loc,z,0,tm
vsel,r,loc,x,-wm/2,wm/2
esize,0.3*tm
MOPT,TETEXPND,2
VMESH,all
vsel,all
vsel,s,loc,x,-lm/2,-wm/2
vsel,a,loc,x,wm/2,lm/2
esize,5*tm
MOPT,TETEXPND,2
VMESH,all
vsel,all

!##########################
! BOUNDARY CONDITIONS #
!##########################

NKPT,11, 1011
NKPT,12, 1012

NKPT,21, 2011
NKPT,22, 2012

NKPT,31, 3011
NKPT,32, 3012

NKPT,41, 4011
NKPT,42, 4012
```

```
NKPT,51, 5011
NKPT,52, 5012

NKPT,61, 6011
NKPT,62, 6012

NKPT,71, 7011
NKPT,72, 7012

NKPT,81, 8011
NKPT,82, 8012

NKPT,91, 9011
NKPT,92, 9012

NKPT,101, 10011
NKPT,102, 10012


NKPT,111, 1021
NKPT,112, 1022

NKPT,121, 2021
NKPT,122, 2022

NKPT,131, 3021
NKPT,132, 3022

NKPT,141, 4021
NKPT,142, 4022

NKPT,151, 5021
NKPT,152, 5022

NKPT,161, 6021
NKPT,162, 6022

NKPT,171, 7021
NKPT,172, 7022

NKPT,181, 8021
NKPT,182, 8022

NKPT,191, 9021
NKPT,192, 9022

NKPT,201, 10021
NKPT,202, 10022

!##########
!LOADING #
!##########

!FOUR POINT BENDING
!##################
!Edge Supports
nsel,s,loc,x,-D
nsel,a,loc,x,D
nsel,r,loc,z,0
D,all,UZ,0
allsel,all

nsel,s,loc,x,-D
nsel,a,loc,x,D
nsel,r,loc,z,0
nsel,r,loc,y,0
D,all,UY,0
allsel,all
nsel,s,loc,x,0
nsel,r,loc,z,0
D,all,UX,0
allsel,all

!Applied Force
lsel,s,loc,x,-L
lsel,a,loc,x,L
lsel,r,loc,z,tm
nsll,s,1
F, all, FZ, -F/9
allsel,all

!1) Apply electrical BC:
!^^^^^^^^^^^^^^^^^^^^
!##########################
!2) Central Rosette
!##########################
!Bridge 1 - at 0 degrees
!+++++++++++++++++++++++

ASEL,S,AREA,,42             ! define supply voltage
contact
NSLA,S,1
CP,11,VOLT,ALL
*GET,ns1,NODE,0,NUM,MIN
D,ns1,VOLT,Vs
ALLSEL,ALL
NSEL,S,NODE,,11             ! define ground contact
!CP,12,VOLT,ALL
*GET,ng1,NODE,0,NUM,MIN
D,ng1,VOLT,0
ALLSEL,ALL
NSEL,S,NODE,,12             ! define first output contact
!CP,13,VOLT,ALL
*GET,no11,NODE,0,NUM,MIN
ALLSEL,ALL
ASEL,S,AREA,,36             ! define second output
contact
NSLA,S,1
CP,14,VOLT,ALL
*GET,no12,NODE,0,NUM,MIN
ALLSEL,ALL
Type, 3                     ! define constant resistors
!MAT, 4
REAL, 1
ESYS,11
E,ns1,no11
E,no11,ng1
E,ng1,no12

!Bridge 2 - at 45 degrees
!+++++++++++++++++++++++
ASEL,S,AREA,,48             ! define supply voltage
contact
NSLA,S,1
CP,21,VOLT,ALL
*GET,ns2,NODE,0,NUM,MIN
D,ns2,VOLT,Vs
ALLSEL,ALL
NSEL,S,NODE,,21             ! define ground contact
*GET,ng2,NODE,0,NUM,MIN
D,ng2,VOLT,0
ALLSEL,ALL

NSEL,S,NODE,,22             ! define first output contact
*GET,no21,NODE,0,NUM,MIN
ALLSEL,ALL
```

```
ASEL,S,AREA,,47          ! define second output contact
NSLA,S,1
CP,24,VOLT,ALL
*GET,no22,NODE,0,NUM,MIN
ALLSEL,ALL
Type, 3                  ! define constant resistors
!MAT, 4
REAL, 1
ESYS,11
E,ns2,no21
E,no21,ng2
E,ng2,no22

!Bridge 3 - at 90 degrees
!++++++++++++++++++++++
ASEL,S,AREA,,54          ! define supply voltage contact
NSLA,S,1
CP,31,VOLT,ALL
*GET,ns3,NODE,0,NUM,MIN
D,ns3,VOLT,Vs
ALLSEL,ALL
NSEL,S,NODE,,31          ! define ground contact
*GET,ng3,NODE,0,NUM,MIN
D,ng3,VOLT,0
ALLSEL,ALL
NSEL,S,NODE,,32          ! define first output contact
*GET,no31,NODE,0,NUM,MIN
ALLSEL,ALL
ASEL,S,AREA,,53          ! define second output contact
NSLA,S,1
CP,34,VOLT,ALL
*GET,no32,NODE,0,NUM,MIN
ALLSEL,ALL
Type, 3                  ! define constant resistors
!MAT, 4
REAL, 1
ESYS,11
E,ns3,no31
E,no31,ng3
E,ng3,no32

!Bridge 4 - at 135 degrees
!++++++++++++++++++++++
ASEL,S,AREA,,60          ! define supply voltage contact
NSLA,S,1
CP,41,VOLT,ALL
*GET,ns4,NODE,0,NUM,MIN
D,ns4,VOLT,Vs
ALLSEL,ALL
NSEL,S,NODE,,41          ! define ground contact
*GET,ng4,NODE,0,NUM,MIN
D,ng4,VOLT,0
ALLSEL,ALL
NSEL,S,NODE,,42          ! define first output contact
*GET,no41,NODE,0,NUM,MIN
ALLSEL,ALL
ASEL,S,AREA,,59          ! define second output contact
NSLA,S,1
CP,44,VOLT,ALL
*GET,no42,NODE,0,NUM,MIN
ALLSEL,ALL
Type, 3                  ! define constant resistors
!MAT, 4
REAL, 1
ESYS,11
E,ns4,no41
E,no41,ng4
E,ng4,no42

!Bridge 5 - at 180 degrees
!++++++++++++++++++++++
ASEL,S,AREA,,66          ! define supply voltage contact
NSLA,S,1
CP,51,VOLT,ALL
*GET,ns5,NODE,0,NUM,MIN
D,ns5,VOLT,Vs
ALLSEL,ALL
NSEL,S,NODE,,51          ! define ground contact
*GET,ng5,NODE,0,NUM,MIN
D,ng5,VOLT,0
ALLSEL,ALL
NSEL,S,NODE,,52          ! define first output contact
*GET,no51,NODE,0,NUM,MIN
ALLSEL,ALL
ASEL,S,AREA,,65          ! define second output contact
NSLA,S,1
CP,54,VOLT,ALL
*GET,no52,NODE,0,NUM,MIN
ALLSEL,ALL
Type, 3                  ! define constant resistors
!MAT, 4
REAL, 2
ESYS,11
E,ns5,no51
E,no51,ng5
E,ng5,no52

!Bridge 6 - at 225 degrees
!++++++++++++++++++++++
ASEL,S,AREA,,72          ! define supply voltage contact
NSLA,S,1
CP,61,VOLT,ALL
*GET,ns6,NODE,0,NUM,MIN
D,ns6,VOLT,Vs
ALLSEL,ALL
NSEL,S,NODE,,61          ! define ground contact
*GET,ng6,NODE,0,NUM,MIN
D,ng6,VOLT,0
ALLSEL,ALL
NSEL,S,NODE,,62          ! define first output contact
*GET,no61,NODE,0,NUM,MIN
ALLSEL,ALL
ASEL,S,AREA,,71          ! define second output contact
NSLA,S,1
CP,64,VOLT,ALL
*GET,no62,NODE,0,NUM,MIN
ALLSEL,ALL
Type, 3                  ! define constant resistors
!MAT, 4
REAL, 2
ESYS,11
E,ns6,no61
E,no61,ng6
E,ng6,no62

!Bridge 7 - at 270 degrees
!++++++++++++++++++++++
ASEL,S,AREA,,78          ! define supply voltage contact
```

```
NSLA,S,1
CP,71,VOLT,ALL
*GET,ns7,NODE,0,NUM,MIN
D,ns7,VOLT,Vs
ALLSEL,ALL
NSEL,S,NODE,,71             ! define ground contact
!CP,12,VOLT,ALL
*GET,ng7,NODE,0,NUM,MIN
D,ng7,VOLT,0
ALLSEL,ALL
NSEL,S,NODE,,72             ! define first output contact
!CP,13,VOLT,ALL
*GET,no71,NODE,0,NUM,MIN
ALLSEL,ALL
ASEL,S,AREA,,77             ! define second output
contact
NSLA,S,1
CP,74,VOLT,ALL
*GET,no72,NODE,0,NUM,MIN
ALLSEL,ALL
Type, 3                     ! define constant resistors
!MAT, 4
REAL, 2
ESYS,11
E,ns7,no71
E,no71,ng7
E,ng7,no72

!Bridge 8 - at 315 degrees
!++++++++++++++++++++++
ASEL,S,AREA,,84             ! define supply voltage
contact
NSLA,S,1
CP,81,VOLT,ALL
*GET,ns8,NODE,0,NUM,MIN
D,ns8,VOLT,Vs
ALLSEL,ALL
NSEL,S,NODE,,81             ! define ground contact
!CP,12,VOLT,ALL
*GET,ng8,NODE,0,NUM,MIN
D,ng8,VOLT,0
ALLSEL,ALL
NSEL,S,NODE,,82             ! define first output contact
!CP,13,VOLT,ALL
*GET,no81,NODE,0,NUM,MIN
ALLSEL,ALL
ASEL,S,AREA,,83             ! define second output
contact
NSLA,S,1
CP,84,VOLT,ALL
*GET,no82,NODE,0,NUM,MIN
ALLSEL,ALL
Type, 3                     ! define constant resistors
!MAT, 4
REAL, 2
ESYS,11
E,ns8,no81
E,no81,ng8
E,ng8,no82

!Bridge 9 - at 0 degrees
!++++++++++++++++++++++
ASEL,S,AREA,,90             ! define supply voltage
contact
NSLA,S,1
CP,91,VOLT,ALL
*GET,ns9,NODE,0,NUM,MIN
D,ns9,VOLT,Vs
ALLSEL,ALL
NSEL,S,NODE,,91             ! define ground contact
!CP,12,VOLT,ALL
*GET,ng9,NODE,0,NUM,MIN
D,ng9,VOLT,0
ALLSEL,ALL
NSEL,S,NODE,,92             ! define first output contact
!CP,13,VOLT,ALL
*GET,no91,NODE,0,NUM,MIN
ALLSEL,ALL
ASEL,S,AREA,,89             ! define second output
contact
NSLA,S,1
CP,94,VOLT,ALL
*GET,no92,NODE,0,NUM,MIN
ALLSEL,ALL
Type, 3                     ! define constant resistors
!MAT, 4
REAL, 3
ESYS,11
E,ns9,no91
E,no91,ng9
E,ng9,no92

!Bridge 10 - at 90 degrees
!++++++++++++++++++++++
ASEL,S,AREA,,96             ! define supply voltage
contact
NSLA,S,1
CP,101,VOLT,ALL
*GET,ns10,NODE,0,NUM,MIN
D,ns10,VOLT,Vs
ALLSEL,ALL
NSEL,S,NODE,,101            ! define ground contact
!CP,12,VOLT,ALL
*GET,ng10,NODE,0,NUM,MIN
D,ng10,VOLT,0
ALLSEL,ALL
NSEL,S,NODE,,102            ! define first output
contact
!CP,13,VOLT,ALL
*GET,no101,NODE,0,NUM,MIN
ALLSEL,ALL
ASEL,S,AREA,,95             ! define second output
contact
NSLA,S,1
CP,104,VOLT,ALL
*GET,no102,NODE,0,NUM,MIN
ALLSEL,ALL
Type, 3                     ! define constant resistors
!MAT, 4
REAL, 3
ESYS,11
E,ns10,no101
E,no101,ng10
E,ng10,no102

ALLSEL,ALL

!###############
!2) Edge Rosette
!###############
!Bridge 1 - at 0 degrees
!++++++++++++++++++++++

ASEL,S,AREA,,102            ! define supply voltage
contact
NSLA,S,1
CP,111,VOLT,ALL
*GET,nse1,NODE,0,NUM,MIN
```

```
D,nse1,VOLT,Vs
ALLSEL,ALL
NSEL,S,NODE,,111          ! define ground contact
*GET,nge1,NODE,0,NUM,MIN
D,nge1,VOLT,0
ALLSEL,ALL
NSEL,S,NODE,,112          ! define first output
contact
*GET,noe11,NODE,0,NUM,MIN
ALLSEL,ALL
ASEL,S,AREA,,101          ! define second output
contact
NSLA,S,1
CP,114,VOLT,ALL
*GET,noe12,NODE,0,NUM,MIN
ALLSEL,ALL
Type, 3                   ! define constant resistors
!MAT, 4
REAL, 1
ESYS,11
E,nse1,noe11
E,noe11,nge1
E,nge1,noe12

!Bridge 2 - at 45 degrees
!++++++++++++++++++++++
ASEL,S,AREA,,108          ! define supply voltage
contact
NSLA,S,1
CP,121,VOLT,ALL
*GET,nse2,NODE,0,NUM,MIN
D,nse2,VOLT,Vs
ALLSEL,ALL
NSEL,S,NODE,,121          ! define ground contact
*GET,nge2,NODE,0,NUM,MIN
D,nge2,VOLT,0
ALLSEL,ALL
NSEL,S,NODE,,122          ! define first output
contact
*GET,noe21,NODE,0,NUM,MIN
ALLSEL,ALL
ASEL,S,AREA,,107          ! define second output
contact
NSLA,S,1
CP,124,VOLT,ALL
*GET,noe22,NODE,0,NUM,MIN
ALLSEL,ALL
Type, 3                   ! define constant resistors
!MAT, 4
REAL, 1
ESYS,11
E,nse2,noe21
E,noe21,nge2
E,nge2,noe22

!Bridge 3 - at 90 degrees
!++++++++++++++++++++++
ASEL,S,AREA,,114          ! define supply voltage
contact
NSLA,S,1
CP,131,VOLT,ALL
*GET,nse3,NODE,0,NUM,MIN
D,nse3,VOLT,Vs
ALLSEL,ALL
NSEL,S,NODE,,131          ! define ground contact
*GET,nge3,NODE,0,NUM,MIN
D,nge3,VOLT,0
ALLSEL,ALL
NSEL,S,NODE,,132          ! define first output
contact
*GET,noe31,NODE,0,NUM,MIN
ALLSEL,ALL
ASEL,S,AREA,,113          ! define second output
contact
NSLA,S,1
CP,134,VOLT,ALL
*GET,noe32,NODE,0,NUM,MIN
ALLSEL,ALL
Type, 3                   ! define constant resistors
!MAT, 4
REAL, 1
ESYS,11
E,nse3,noe31
E,noe31,nge3
E,nge3,noe32

!Bridge 4 - at 135 degrees
!++++++++++++++++++++++
ASEL,S,AREA,,120          ! define supply voltage
contact
NSLA,S,1
CP,141,VOLT,ALL
*GET,nse4,NODE,0,NUM,MIN
D,nse4,VOLT,Vs
ALLSEL,ALL
NSEL,S,NODE,,141          ! define ground contact
*GET,nge4,NODE,0,NUM,MIN
D,nge4,VOLT,0
ALLSEL,ALL
NSEL,S,NODE,,142          ! define first output
contact
*GET,noe41,NODE,0,NUM,MIN
ALLSEL,ALL
ASEL,S,AREA,,119          ! define second output
contact
NSLA,S,1
CP,144,VOLT,ALL
*GET,noe42,NODE,0,NUM,MIN
ALLSEL,ALL
Type, 3                   ! define constant resistors
!MAT, 4
REAL, 1
ESYS,11
E,nse4,noe41
E,noe41,nge4
E,nge4,noe42


!Bridge 5 - at 180 degrees
!++++++++++++++++++++++
ASEL,S,AREA,,126          ! define supply voltage
contact
NSLA,S,1
CP,151,VOLT,ALL
*GET,nse5,NODE,0,NUM,MIN
D,nse5,VOLT,Vs
ALLSEL,ALL
NSEL,S,NODE,,151          ! define ground contact
*GET,nge5,NODE,0,NUM,MIN
D,nge5,VOLT,0
ALLSEL,ALL

NSEL,S,NODE,,152          ! define first output
contact
*GET,noe51,NODE,0,NUM,MIN
ALLSEL,ALL
```

```
ASEL,S,AREA,,125            ! define second output
contact
NSLA,S,1
CP,154,VOLT,ALL
*GET,noe52,NODE,0,NUM,MIN
ALLSEL,ALL
Type, 3                     ! define constant resistors
!MAT, 4
REAL, 2
ESYS,11
E,nse5,noe51
E,noe51,nge5
E,nge5,noe52

!Bridge 6 - at 225 degrees
!+++++++++++++++++++++++
ASEL,S,AREA,,132            ! define supply voltage
contact
NSLA,S,1
CP,161,VOLT,ALL
*GET,nse6,NODE,0,NUM,MIN
D,nse6,VOLT,Vs
ALLSEL,ALL
NSEL,S,NODE,,161            ! define ground contact
*GET,nge6,NODE,0,NUM,MIN
D,nge6,VOLT,0
ALLSEL,ALL
NSEL,S,NODE,,162            ! define first output
contact
*GET,noe61,NODE,0,NUM,MIN
ALLSEL,ALL
ASEL,S,AREA,,131            ! define second output
contact
NSLA,S,1
CP,164,VOLT,ALL
*GET,noe62,NODE,0,NUM,MIN
ALLSEL,ALL
Type, 3                     ! define constant resistors
!MAT, 4
REAL, 2
ESYS,11
E,nse6,noe61
E,noe61,nge6
E,nge6,noe62

!Bridge 7 - at 270 degrees
!+++++++++++++++++++++++
ASEL,S,AREA,,138            ! define supply voltage
contact
NSLA,S,1
CP,171,VOLT,ALL
*GET,nse7,NODE,0,NUM,MIN
D,nse7,VOLT,Vs
ALLSEL,ALL
NSEL,S,NODE,,171            ! define ground contact
!CP,12,VOLT,ALL
*GET,nge7,NODE,0,NUM,MIN
D,nge7,VOLT,0
ALLSEL,ALL
NSEL,S,NODE,,172            ! define first output
contact
!CP,13,VOLT,ALL
*GET,noe71,NODE,0,NUM,MIN
ALLSEL,ALL

ASEL,S,AREA,,137            ! define second output
contact
NSLA,S,1
CP,174,VOLT,ALL
*GET,noe72,NODE,0,NUM,MIN
ALLSEL,ALL
Type, 3                     ! define constant resistors
!MAT, 4
REAL, 2
ESYS,11
E,nse7,noe71
E,noe71,nge7
E,nge7,noe72

!Bridge 8 - at 315 degrees
!+++++++++++++++++++++++
ASEL,S,AREA,,144            ! define supply voltage
contact
NSLA,S,1
CP,181,VOLT,ALL
*GET,nse8,NODE,0,NUM,MIN
D,nse8,VOLT,Vs
ALLSEL,ALL
NSEL,S,NODE,,181            ! define ground contact
!CP,12,VOLT,ALL
*GET,nge8,NODE,0,NUM,MIN
D,nge8,VOLT,0
ALLSEL,ALL
NSEL,S,NODE,,182            ! define first output
contact
!CP,13,VOLT,ALL
*GET,noe81,NODE,0,NUM,MIN
ALLSEL,ALL
ASEL,S,AREA,,143            ! define second output
contact
NSLA,S,1
CP,184,VOLT,ALL
*GET,noe82,NODE,0,NUM,MIN
ALLSEL,ALL
Type, 3                     ! define constant resistors
!MAT, 4
REAL, 2
ESYS,11
E,nse8,noe81
E,noe81,nge8
E,nge8,noe82

ALLSEL,all

/PBC,u,,1
/PBC,volt,,1
/PBC,cp,,1
/PNUM,TYPE,1
/NUMBER,1
EPLOT
FINISH

!#########
! Solution #
!#########
/SOLU
ANTYPE,STATIC
CNVTOL,VOLT,1,1E-3
autots,on             ! auto time stepping
nsubst,5,1000,1                      ! Size of first
substep=1/5 of the total load, max # substeps=1000,
min # substeps=1


SOLVE
FINISH

/post1
```

```
!Calculate Results
!###############
/com, Results at Central Rosette
/com, VOA=%(volt(no11)-volt(no12))*1.e3%, mV     !
Calculate ANSYS Result - Bridge1
/com, VOA=%(volt(no21)-volt(no22))*1.e3%, mV     !
Calculate ANSYS Result - Bridge2
/com, VOA=%(volt(no31)-volt(no32))*1.e3%, mV     !
Calculate ANSYS Result - Bridge3
/com, VOA=%(volt(no41)-volt(no42))*1.e3%, mV     !
Calculate ANSYS Result - Bridge4
/com, VOA=%(volt(no51)-volt(no52))*1.e3%, mV     !
Calculate ANSYS Result - Bridge5
/com, VOA=%(volt(no61)-volt(no62))*1.e3%, mV     !
Calculate ANSYS Result - Bridge6
/com, VOA=%(volt(no71)-volt(no72))*1.e3%, mV     !
Calculate ANSYS Result - Bridge7
/com, VOA=%(volt(no81)-volt(no82))*1.e3%, mV     !
Calculate ANSYS Result - Bridge8
/com, VOA=%(volt(no91)-volt(no92))*1.e3%, mV     !
Calculate ANSYS Result - Bridge9
/com, VOA=%(volt(no101)-volt(no102))*1.e3%, mV
! Calculate ANSYS Result - Bridge10

/com, Results at Edge Rosette
/com, VOA=%(volt(noe11)-volt(noe12))*1.e3%, mV
! Calculate ANSYS Result - Bridge1
/com, VOA=%(volt(noe21)-volt(noe22))*1.e3%, mV
! Calculate ANSYS Result - Bridge2
/com, VOA=%(volt(noe31)-volt(noe32))*1.e3%, mV
! Calculate ANSYS Result - Bridge3
/com, VOA=%(volt(noe41)-volt(noe42))*1.e3%, mV
! Calculate ANSYS Result - Bridge4
/com, VOA=%(volt(noe51)-volt(noe52))*1.e3%, mV
! Calculate ANSYS Result - Bridge5
/com, VOA=%(volt(noe61)-volt(noe62))*1.e3%, mV
! Calculate ANSYS Result - Bridge6
/com, VOA=%(volt(noe71)-volt(noe72))*1.e3%, mV
! Calculate ANSYS Result - Bridge7
/com, VOA=%(volt(noe81)-volt(noe82))*1.e3%, mV
! Calculate ANSYS Result - Bridge8
```